

AD-A283 774
■■■■■■■■■■

Global Acoustic Mapping of Ocean Temperatures

GAMOT



DTIC
1094
G

Woods Hole Oceanographic Institution
The Pennsylvania State University
Naval Research Laboratory—Stennis
The Florida State University
University of Alaska
University of Texas at Austin

DTIC QUALITY INSPECTED 8

QUARTERLY PROGRESS REPORTS vol. III

Approved for public release
Distribution is unlimited

SERDP
Strategic Environmental Research
Development Program
A Partnership to Improve the Environment

Global Acoustic Mapping of Ocean Temperatures

GAMOT



Accession For	
NTIS	CRA&I <input checked="" type="checkbox"/>
DTIC	TAB <input type="checkbox"/>
Unannounced <input type="checkbox"/>	
Justification	
By	
Distribution/	
Availability Codes	
Dist	Availability or Special
A-1	

Woods Hole Oceanographic Institution
The Pennsylvania State University
Naval Research Laboratory—Stennis
The Florida State University
University of Alaska
University of Texas at Austin

QUARTERLY PROGRESS REPORT
April-June 1994

94-27157
■■■■■■■■■■
20607

94 8 24 176



August 1, 1994

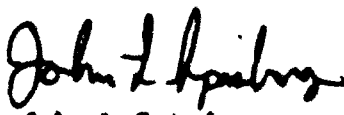
Dr. Ralph Alewine
Advanced Research Projects Agency
3701 North Fairfax Drive
Arlington, VA 22203-1714

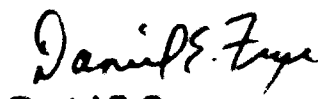
Dear Dr. Alewine,


The attached report fulfills the fifth quarterly progress report requirement for the period from April 1 to June 30 1994 as contained in the ARPA Grant No: MDA972-93-1-0004 entitled "Real Time System for Practical Acoustic Monitoring of Global Ocean Temperature" issued by the Contracts Management Office. The United States Government has a royalty-free license throughout the world in all copy rightable material contained herein. This report is approved for unlimited distribution and public release. Copies of this report are also mailed to the distribution list contained in Attachment Number 2 of the Grant.

Financial status reports will be submitted separately from this report. Woods Hole Oceanographic Institution, as the Grantee, will submit all financial reports directly to you.

The information contained in this report represents the inputs and opinions of the entire GAMOT team; the Woods Hole Oceanographic Institution, the Pennsylvania State University, the Florida State University, University of Alaska, University of Texas at Austin and NRL-Stennis. If this report generates any questions, please do not hesitate to direct your questions or comments to the Principal Investigators or the Program Manager.


John L. Spiesberger
Principal Investigator
WHOI/PSU


Daniel E. Frye
Principle Investigator
WHOI


John M. Kenny
Program Manager
ARL/PSU

August 15, 1994

GAMOT EXECUTIVE SUMMARY

Work continues on all GAMOT Tasks as described in ARPA Grant No: MDA972-93-1-0004.

• **Task A.** Task A work remains on schedule and we have completed the following work:

We are writing a new eigenray finder for use in identifying the paths which sound take from sources to the surface suspended acoustic receivers.

A theoretical investigation has been conducted which has found that it is possible "ray theory can be extended to acoustic frequencies below 100 Hz.

A new parabolic approximation to the acoustic wave equation has been developed. Unlike all previous parabolic approximations, the new approximation predicts delays of acoustic pulses with little error.

The acoustic multipaths from the Kaneohe source have been identified at one SOSUS station using a ray tracing algorithm called ZRAY. This was a breakthrough since this is the furthest, 4000 km, that ray theory has been successfully used to understand acoustic propagation in the ocean.

We have ported the first version of the tomography signal processing software to the SSAR.

We have perfected the encoding and decoding algorithms for transmission and reception from ARGOS satellites.

One paper has been submitted for review to the U. S. Navy prior to publication: Spiesberger, J.L., Kaneohe acoustic thermometer further validated with rays over 3700 km and the demise of the idea of axially trapped energy, to be submitted to the J. Acoust. Soc. Am., (1994).

Three papers are contained in this report:

Draganov, A. and Spiesberger, J., Diffraction and modeling pulse delays in structured media, submitted to J. Acoust. Soc. Am., (1994).

Einfalt, B., and Ackerman, C., "Utilization of ARGOS in a SSAR drifting buoy," to be published in the Proceedings of the Marine Technology Society (MTS) Conference, September 7-9, (1994).

Tappert, F., Spiesberger, J., and Boden, L., New full-wave approximation for ocean acoustic travel time predictions, submitted to J. Acoust. Soc. Am., (1994).

• **Task B.** Task B tasks and deliverables are on schedule. We have completed writing of a manuscript detailing the travel time anomaly estimates using a reduced gravity model of the northeast Pacific. We have designed an acoustic tomography assimilation method for a similar model but with spatially variable

density. The plan for monitoring the Pacific Ocean for long term change is contained in the Task B section.

NRL has plotted the five year tracks of 194 SSARs simulated by the 1/8° NRL Pacific model. A revised paper on the discovery of a decadal impact of the 1982-83 El Niño was completed and is now in press in *Nature*. This paper also received other favorable press and was featured on the front page of the *New York Times*.

The University of Alaska continues the work on interannual and seasonal variability and a report of that work is contained in the Task B section.

- **Task C.** Fabrication of ten operational SSARs is continuing. Two units are being prepared for a test cruise at the AUTECH Range in August and two units are being prepared for testing in the Pacific in November. No significant delays or problems have been encountered.

The SSAR design is complete and a Design and Test Report is in preparation. A new conductor assembly for the SSAR hose has been developed and ordered. It consists of a custom made coil cord assembly with a straight section and a coiled section. Tests of a stock coil cord are underway and the design appears to function well in an environment simulating the action of surface waves.

The hydrophone array was tested at Hazeltine Corporation's facility to determine the effects of vertical motions on the hydrophone output signals. This test demonstrated that the SSAR electronic filters effectively removed the heave signal. It also revealed a problem with acoustic coupling between the hydrophones and the array cabling. The method used to attach the hydrophones to the cable is being modified to minimize this problem.

Planning is underway on three new tasks. 1) A low power receiver for the SSAR is being designed so that future SSARs will be able to update their source transmit schedules after deployment. 2) A second test cruise at the AUTECH Range is planned for August to further test the USBL navigation system and to compare acoustic data from the SSAR hydrophone array with data from a subsurface, moored hydrophone array. Tomographic processing algorithms will also be tested on this cruise as well as GPS positioning, ARGOS telemetry, and all other SSAR subsystems. 3) A test cruise to the Pacific in November is in the planning stage.

- **Task D.** The 70 Hz source proposal was submitted to ARPA on April 19, 1994. No action has yet been taken on the proposal. Because there have been no changes to the status of Task D, the Task D section has not been included in this report.

- **Meetings.** Members of the GAMOT team attended several conferences and presented work on their work. John Spiesberger and John Kenny attended a

meeting to discuss the transition of this program to NOAA and met with the Executive Director of SERDP.

- **Issues and Concerns.** Three issues are addressed:
 - Acoustic interaction of cabled sources with the bottom slope, and
 - Identification of a source for the autonomous mooring.
 - An at-sea test with a suitable source transmitting M sequences over long range is desirable to fully verify SSAR operation. A short range tomography test will be performed at the AUTECH Range in August, but a long range test in the Pacific should be scheduled following the AUTECH work.

TASK A

TOMOGRAPHIC DATA ANALYSIS

In the last quarter we have accomplished the following tasks.

We are writing a new eigenray finder for use in identifying the paths which sound take from sources to the surface suspended acoustic receivers. This eigenray finder is designed to find eigenrays faster than our previous version. The increase in speed is based on the fact that the SSARs do not move much during a day, so the ray angles will not change much during a day from one ray trace to another ray trace. However, it is necessary to re-trace rays for each different SSAR position to obtain an accurate estimate of the ray path and ray travel time.

A theoretical investigation has been conducted which has found that it is possible that ray theory can be extended to acoustic frequencies below 100 Hz. Previously, it has been believed by the acoustic oceanography community that ray theory was not an accurate method for computing travel times below 100 Hz. A manuscript of this finding has been submitted to the J. Acoust. Soc. Am. (Draganov and Spiesberger, 1994).

A new parabolic approximation to the acoustic wave equation has been developed. Unlike all previous parabolic approximations, the new approximation predicts delays of acoustic pulses with little error. The new approximation is insensitive to any twiddle factors that plague previous parabolic approximations. For example, the impulse response is insensitive to a reference speed of sound. The new approximation is valid for range dependent fields and does not require that the propagation of sound be adiabatic. This new parabolic approximation also is valid for high grazing angles. A manuscript describing these findings has been submitted to the J. Acoust. Soc. Am. (Tappert, Spiesberger, and Boden, 1994). Tappert's involvement in this project was funded through Task A, under subcontract to Penn State University.

The acoustic multipaths from the Kaneohe source have been identified at one SOSUS station using a ray tracing algorithm called ZRAY. This was a breakthrough since this is the furthest, 4000 km, that ray theory has been successfully used to understand acoustic propagation in the ocean. The acoustic source was centered at 133 Hz. Travel times from this section have been compared to an eddy resolving section taken in July 1988 by NAVOCEANO. We find that ray travel times through the CTD section are consistent with measured travel times. A manuscript describing this finding has been written and is under review by the SOSUS program office before submission to a journal (Spiesberger, 1994).

We demonstrated that there is no such thing as axially trapped energy at 133 Hz and 4000 km distance in the northeast Pacific. This surprising finding comes from analysis of the Kaneohe acoustic thermometer experiments in the 1980's. We find that ocean fluctuations scatter otherwise axially trapped energy, more than 1000 m in the vertical near the receiver. The ocean fluctuations responsible for the demise of axially trapped energy have spatial scales smaller than the mesoscale, and may be in part associated with internal waves. A manuscript describing this finding has been written and is under review by the SOSUS program office before submission to a journal (Spiesberger, 1994).

We have ported the first version of the tomography signal processing software to the SSAR. This software performs Doppler correction, circulating sums, matched filtering and pulse compression, estimation of multipath arrival angle, and peak-picking. At the present time, all of this processing can be performed in nine minutes per each reception on the SSAR hardware. Quicker processing time is expected as we continue to refine the software. The tomography processing software will be used at to test the SSAR at AUTECH this August.

We have perfected the encoding and decoding algorithms for transmission and reception from ARGOS satellites. A paper describing this processing has been accepted for publication (Einfalt and Ackerman, 1994).

REFERENCES

Spiesberger, J.L., Kaneohe acoustic thermometer further validated with rays over 3700 km and the demise of the idea of axially trapped energy, to be submitted to the J. Acoust. Soc. Am., (1994).

ENCLOSURES

Draganov, A. and Spiesberger, J., Diffraction and modeling pulse delays in structured media, submitted to J. Acoust. Soc. Am., (1994).

Einfalt, B., and Ackerman, C., "Utilization of ARGOS in a SSAR drifting buoy," to be published in the Proceedings of the Marine Technology Society (MTS) Conference," September 7-9, (1994).

Tappert, F., Spiesberger, J., and Boden, L., New full-wave approximation for ocean acoustic travel time predictions, submitted to J. Acoust. Soc. Am., (1994).

Figures

Fig. 1 Task A Schedule

TASK A

TOMOGRAPHIC DATA ANALYSIS

In the last quarter we have accomplished the following tasks.

We are writing a new eigenray finder for use in identifying the paths which sound take from sources to the surface suspended acoustic receivers. This eigenray finder is designed to find eigenrays faster than our previous version. The increase in speed is based on the fact that the SSARs do not move much during a day, so the ray angles will not change much during a day from one ray trace to another ray trace. However, it is necessary to re-trace rays for each different SSAR position to obtain an accurate estimate of the ray path and ray travel time.

A theoretical investigation has been conducted which has found that it is possible that ray theory can be extended to acoustic frequencies below 100 Hz. Previously, it has been believed by the acoustic oceanography community that ray theory was not an accurate method for computing travel times below 100 Hz. A manuscript of this finding has been submitted to the J. Acoust. Soc. Am. (Draganov and Spiesberger, 1994).

A new parabolic approximation to the acoustic wave equation has been developed. Unlike all previous parabolic approximations, the new approximation predicts delays of acoustic pulses with little error. The new approximation is insensitive to any twiddle factors that plague previous parabolic approximations. For example, the impulse response is insensitive to a reference speed of sound. The new approximation is valid for range dependent fields and does not require that the propagation of sound be adiabatic. This new parabolic approximation also is valid for high grazing angles. A manuscript describing these findings has been submitted to the J. Acoust. Soc. Am. (Tappert, Spiesberger, and Boden, 1994). Tappert's involvement in this project was funded through Task A, under subcontract to Penn State University.

The acoustic multipaths from the Kaneohe source have been identified at one SOSUS station using a ray tracing algorithm called ZRAY. This was a breakthrough since this is the furthest, 4000 km, that ray theory has been successfully used to understand acoustic propagation in the ocean. The acoustic source was centered at 133 Hz. Travel times from this section have been compared to an eddy resolving section taken in July 1988 by NAVOCEANO. We find that ray travel times through the CTD section are consistent with measured travel times. A manuscript describing this finding has been written and is under review by the SOSUS program office before submission to a journal (Spiesberger, 1994).

We demonstrated that there is no such thing as axially trapped energy at 133 Hz and 4000 km distance in the northeast Pacific. This surprising finding comes from analysis of the Kaneohe acoustic thermometer experiments in the 1980's. We find that ocean fluctuations scatter otherwise axially trapped energy, more than 1000 m in the vertical near the receiver. The ocean fluctuations responsible for the demise of axially trapped energy have spatial scales smaller than the mesoscale, and may be in part associated with internal waves. A manuscript describing this finding has been written and is under review by the SOSUS program office before submission to a journal (Spiesberger, 1994).

We have ported the first version of the tomography signal processing software to the SSAR. This software performs Doppler correction, circulating sums, matched filtering and pulse compression, estimation of multipath arrival angle, and peak-picking. At the present time, all of this processing can be performed in nine minutes per each reception on the SSAR hardware. Quicker processing time is expected as we continue to refine the software. The tomography processing software will be used at to test the SSAR at AUTC this August.

We have perfected the encoding and decoding algorithms for transmission and reception from ARGOS satellites. A paper describing this processing has been accepted for publication (Einfalt and Ackerman, 1994).

REFERENCES

Spiesberger, J.L., Kaneohe acoustic thermometer further validated with rays over 3700 km and the demise of the idea of axially trapped energy, to be submitted to the J. Acoust. Soc. Am., (1994).

Spiesberger, J.L., Kaneohe acoustic thermometer further validated with rays over 3700 km and the demise of the idea of axially trapped energy, to be submitted to the J. Acoust. Soc. Am., (1994).

ENCLOSURES

Draganov, A. and Spiesberger, J., Diffraction and modeling pulse delays in structured media, submitted to J. Acoust. Soc. Am., (1994).

Einfalt, B., and Ackerman, C., "Utilization of ARGOS in a SSAR drifting buoy," to be published in the Proceedings of the Marine Technology Society (MTS) Conference," September 7-9, (1994).

Tappert, F., Spiesberger, J., and Boden, L., New full-wave approximation for ocean acoustic travel time predictions, submitted to J. Acoust. Soc. Am., (1994).

Figures

Fig. 1 Task A Schedule

June 8, 1994

Diffraction and pulse delay in a structured ocean

A. Draganov and J. Spiesberger

Abstract

In many media, the wave speed can be decomposed into a smoothed field in space plus a residual, with a spatial average of zero, that contains structure at shorter scales. Because of diffraction, the smoothing scale plays a key role in determining which approximation of the wave equation yields the most accurate estimate of pulse delay. For oceanic sound speed profiles which are smoothed to suppress fine structure, and at 4000 km and acoustic frequencies near 50 Hz, the difference in pulse delay predicted with rays and exact solutions of the wave equation is of order 0.1 s. This difference occurs because ray theory ignores diffraction whereas the wave equation incorporates diffraction. The difference in pulse delay accumulates primarily from focusing regions where the scale of the focusing region is about the same as the acoustic wavelength and diffraction effects come into play. Due to scattering from fine structure in the ocean, the scale of focusing regions may sometimes be enlarged to be much larger than an acoustic wavelength. Then, diffraction may not significantly affect pulse delay, and rays traced through a smoothed sound speed profile may yield more accurate estimates of pulse delay than exact solutions of the wave equation which represent the ocean with the same smoothed sound speed profile.

I. INTRODUCTION

In many media such as the ocean, atmosphere, and the solid Earth, the speed of sound can be decomposed into a smoothly varying field in space plus a residual which contains structure at shorter wavelengths. Typically, the smooth field is formed from a spatial or temporal average, and the fine structure is characterized statistically. The question we address is how to compute the travel times of pulses in these structured media. What errors are introduced when the speed of sound is modelled as a smoothly varying function in space? Can the fine structure of the sound speed field be ignored to advantage for some approximations of the wave equation but not ignored for other approximations?

When a finely structured sound speed field is modelled as a smoothed function, we find that ray approximations might yield more accurate travel times for the propagation time in the real medium than more computationally intensive solutions such as based on the exact wave equation or based on parabolic or normal mode approximations. Using ray theory with a smoothed sound speed profile implies (i) diffraction effects are neglected, and (ii) the effects of the fine structure are ignored. In turn, using any "exact" method for solving the wave equation, such as via normal modes, often means using the latter approximation only. "Exact" methods, when applied to a smoothed media, may overestimate the effects of diffraction on travel times, as compared to a structured medium, and therefore may be less accurate, than ray theory. Understanding our finding relies on understanding the role of diffraction on the delay of an acoustic pulse.

Classical ray theory does not include the effects of diffraction. Because diffraction affects each constituent wavelength of a pulse in a different manner, diffraction changes the propagation delay of a pulse. For example, consider a wave packet which is propagating toward a narrow opening along an otherwise impenetrable boundary. If the opening is large compared with the wavelengths making up the packet, then diffraction is negligible and the travel time will be close to that given by ray theory. If the opening size is of the same or smaller size than any of the wavelengths in the pulse, then diffraction will modify the wave field for each wavelength on the far side of the opening. After each constituent wavelength is Fourier transformed into the time domain, the pulse shape and delay may change compared to

that predicted from rays. Whether diffractive effects are significant depends on the ratio of geometrical, sound speed, and focusing region scales to the acoustic wavelengths.

Our work on this problem is based on an oceanographic application. To map climatic changes in the ocean's temperature with acoustic tomography,¹ it is necessary to compute the travel times of pulses from a reference field of sound speed. The corresponding reference travel times are compared with measured travel times and their differences are used to modify the reference field using tomography.² How important is diffraction in this application? The two obvious scales to consider are the depth of the ocean, and the vertical scale of the sound speed duct. In addition, wave packets from a source undergo focusing in the sound speed duct, thus creating a third geometrical scale associated with the dimensions of focusing regions. In the deep ocean, the first two scales are about 1 km or greater, so diffraction can be ignored for acoustic wavelengths much less than 1 km or equivalently for acoustic frequencies much greater than $(1.5 \text{ km s}^{-1})/1 \text{ km} = 1.5 \text{ Hz}$. The dimensions of focusing regions depend on the central frequency of the pulse and on the scattering of the sound from fine structure in the ocean. Since frequencies used in acoustic tomography to date^{1,2,4,5,6} are much greater than 1.5 Hz, the dimensions of the focusing regions are probably the key scales controlling diffraction in our application. When scattering effects are small, then focusing regions may be on the order of a wavelength and diffraction is important to consider. When scattering processes blur out the spatial scales of focusing regions, then diffraction may not affect the travel times much.

At present, no definitive theory or experiment allows us to reliably predict the dimensions of focusing regions for acoustic pulses in the ocean. For acoustic pulses between 100 and 300 Hz and distances between 3000 and 4000 km, experiments suggest that caustics are blurred out over much greater scales than the acoustic wavelengths due to scattering from fine structure.⁷ Effects of diffraction should then be small and ray theory could provide an accurate method to predict travel times using a smoothed sound speed field.

Given a smoothed model of sound speed in the ocean, travel times from ray theory differ from exact solutions of the wave equation by increasing amounts as the center frequency decreases. At a center frequency of 50 Hz and a distance of 4000 km, the difference is about 0.1 s.⁸ We ascribe this difference to diffraction which is not present in ray theory but is present in

exact solutions of the wave equation. This discrepancy does not mean that ray theory should not be used in tomography experiments. Rather, we have to consider effects of both smoothing the sound speed field and diffraction. Diffraction may not effect travel times considerably in a structured medium. Therefore, ray theory, which neglects diffraction, may provide good estimates for travel times when the sound speed field is smoothed. Solutions to the wave equation containing diffractive effects could provide accurate estimates of the travel time if a smoothed model of sound speed is *not* used.

There are other causes for errors in predicted travel times unrelated to the effects of diffraction^{9,10,11} They are not discussed further in this paper.

II. ANALYTICAL FORMULATION

In this section an analytical formulation is presented for the travel times of acoustic pulses in the ocean accounting for diffraction. Diffraction affects travel times, and this effect may be significant at low acoustic frequency.

We start from the wave equation for the pressure field $\mathcal{P}(\vec{r}, t)$.

$$c^2(\vec{r})\nabla^2\mathcal{P}(\vec{r}, t) - \frac{\partial^2\mathcal{P}(\vec{r}, t)}{\partial t^2} = 0, \quad (1)$$

where $c(\vec{r})$ is the sound speed in the inhomogeneous ocean, and the variables t and \vec{r} denote time and position respectively. The sound speed is assumed to not depend on time. The ray approach to the solution of (1) is to separate fast and slow variables assuming that wavelengths are short compared with the characteristic scale of inhomogeneity in the medium.¹² In order to use this approximation, we seek a solution in the form,

$$\mathcal{P}(\vec{r}, t) = \int d\omega P_0(\vec{r}, \omega) \exp(i\frac{\omega}{c_0}\psi) \exp(-i\omega t), \quad (2)$$

where P_0 is a slowly varying complex function of \vec{r} and depends on frequency ω , and c_0 is a constant of order of the sound speed, introduced for convenience. The exponents in (2) are assumed to vary much faster than P_0 . Substitution of (2) into (1) yields,

$$c^2\nabla^2 P_0 + c^2 i \nabla^2 \psi \frac{\omega}{c_0} P_0 + 2ic^2 \vec{\nabla} P_0 \cdot \vec{\nabla} \psi \frac{\omega}{c_0} - c^2 (\vec{\nabla} \psi)^2 (\frac{\omega}{c_0})^2 P_0 + \omega^2 P_0 = 0. \quad (3)$$

Equation (2) has two unknown functions, ψ and P_0 , describing the pressure field P . One of these functions can be chosen arbitrarily for simplicity, so that the other one is determined by equation (2). We note that for large frequencies, the two terms containing ω^2 in the left hand side of (2) are dominant. Therefore, it is convenient to choose ψ in such a way that these two large terms cancel out,

$$(\vec{\nabla}\psi)^2 \left(\frac{c}{c_0}\right)^2 - 1 = 0. \quad (4)$$

This is the eiconal equation for the wave phase.¹² A solution of (4), ray paths, can be obtained by the method of characteristics.¹² We introduce a curve in space $\vec{r}(\tau)$ which is parametrically described by the equation,

$$\frac{d\vec{r}(\tau)}{d\tau} = \frac{\partial D(\vec{\kappa}, \vec{r})}{\partial \vec{\kappa}}, \quad (5)$$

where $\vec{\kappa} = \vec{\nabla}\psi$ is the dimensionless wave vector, τ is a parameter, and $D(\vec{\kappa}, \vec{r}) = (\vec{\nabla}\psi)^2 \left(\frac{c}{c_0}\right)^2 - 1$ is the left hand side of (4). The equation, $D(\vec{\kappa}, \omega) = 0$, is the dispersion relation describing the local wave parameters. Since the integral of $\vec{\kappa}$ along the ray trajectory is linked to the phase of P , a simple way to understand the physical meaning of the quantity $\vec{\kappa}$ is to link it to the local value of the wave vector $\vec{\kappa} = \frac{\partial \psi}{\partial \vec{r}}$. The wave energy propagates along $\vec{r}(\tau)$. Since D is identically equal to zero for all $\vec{r}(\tau)$, the full derivative of D with respect to τ must be identically equal to zero. This condition yields the equation for $\vec{\kappa}$,

$$\frac{d\vec{\kappa}(\tau)}{d\tau} = -\frac{\partial D(\vec{\kappa}, \vec{r})}{\partial \vec{r}}. \quad (6)$$

Equations (5), (6) determine the value of $\vec{\kappa}$ in the illuminated region. Integration of $\vec{\kappa}$ along a ray trajectory determines the phase, $\psi(\vec{r})$.

The solution for $\vec{\kappa}$ and ψ , given by ray theory, can be substituted in (3) to determine P_0 ,

$$\vec{\nabla}P_0 \cdot \vec{\kappa} + \frac{1}{2}P_0 \text{div} \vec{\kappa} - \frac{ic_0}{2\omega} \nabla^2 P_0 = 0. \quad (7)$$

After solving (7) with respect to $P_0(\vec{r}, \omega)$, we perform the inverse Fourier transform to determine the pressure field in the time domain at any point in the illuminated region.

A. Travel time of acoustic pulses at the limit of high frequencies

Equation (7) is solved in the limit of high frequencies $\omega \rightarrow \infty$. In this case we neglect the ω^{-1} term on the left hand side of (7). Using the identity, $\vec{\nabla} P_0 \cdot \vec{\kappa} = \frac{dP_0}{ds} \kappa$, where s is the distance along the ray, the high frequency limit of equation (7) is reduced to an ordinary differential equation for P_0 along the ray,

$$\frac{dP_0}{ds} = -\frac{1}{2\kappa} P_0 \operatorname{div} \vec{\kappa}. \quad (8)$$

The solution of (8) is,

$$P_g(s, \omega) = P_g(s_0, \omega) \exp \left(-\frac{1}{2} \int_{s_0}^s \frac{\operatorname{div} \vec{\kappa}(\xi)}{\kappa(\xi)} d\xi \right), \quad (9)$$

where the subscript g denotes that $P_0(s, \omega)$ is calculated in the geometrical ray limit $\omega \rightarrow \infty$, and $P_g(s_0, \omega)$ is the value of the Fourier component of the pressure field at some given point s_0 along the ray trajectory. We assume that the point s_0 lies close to the source, so that $P_g(s_0, \omega)$ is the Fourier transform of the pressure impulse created by the source.

The most important feature in (9) is that the dependence of P_g on ω is in the same form at any point along the ray trajectory due to the fact that $\vec{\kappa}$ does not depend on ω (see equations (5), (6) for $\vec{\kappa}$). The only effect of the position of the observation point, s , is the exponent in (9) which does not depend on frequency and can be viewed as a focusing factor governing the amplitude of the wave. Therefore, upon substitution of P_g into the formula for the inverse Fourier transform we get,

$$P_g(s, t) = \frac{1}{2\pi} \exp \left(-\frac{1}{2} \int_{s_0}^s \frac{\operatorname{div} \vec{\kappa}(\xi)}{\kappa(\xi)} d\xi \right) \int d\omega P(s_0, \omega) \exp \left(-i\omega \left(t - \frac{\psi}{c_0} \right) \right). \quad (10)$$

The integral in (10) is similar to that of the inverse Fourier transform of the pulse at $s = s_0$, with time shifted by $T = \frac{\psi}{c_0}$. Therefore, the shape of the acoustic pulse does not change along the ray, and the travel time of the acoustic pulse is,

$$T = \frac{\psi}{c_0} = \frac{1}{c_0} \int_{s_0}^s \vec{\kappa} \cdot d\vec{s}. \quad (11)$$

In a locally isotropic media the infinitesimal element of the ray trajectory, $d\vec{s}$, is always parallel to $\vec{\kappa}$ so at any given point the ray propagates in the direction of the wave vector. Substituting the expression for $\vec{\kappa}$ from the dispersion equation, $D = 0$, we get,

$$T = \int_{s_0}^s \frac{ds}{c(\vec{r}(s))}. \quad (12)$$

This is a classic formula for the travel time of an acoustic pulse.¹² The treatment of this section allows us to pinpoint the approximations used in the derivation of (12). We neglected the last term in (7), which is a good approximation at high frequencies. In the next section, we investigate how this last term influences pulse delay.

B. Travel time of acoustic pulses at finite frequencies

The case of finite frequency is more complicated and in some respects more interesting. If we do not neglect the ω^{-1} term in the left hand side of (7), the solution for the focusing factor for $P_0(\vec{r}, \omega)$ will depend on frequency in contrast to the case of geometric rays. As a result of the dependence of the focusing factor on ω , the shape of the acoustic pulse at the receiver will be different from that at the source. Moreover, there may be a change in the travel time of an acoustic pulse associated with the effect of finite frequencies.

Qualitatively, we can understand the change in the travel time by considering the propagation of an acoustic wave in a rectangular waveguide with the refractive index constant and with purely reflecting walls.¹³ In this case, the bounded transverse structure of the wave packet is equivalent to the existence of a transverse component of the wave vector $k_{\perp} = \frac{\pi}{L}$ where L is the width of the waveguide, and $\epsilon \sim 1$ is a constant. Since the total magnitude of the wave vector, $k = \frac{\omega}{c}$, is determined by the refractive index of the media, the parallel component of the wave vector,

$$k_{\parallel} = \frac{\omega}{c} \left(1 - \left(\frac{\epsilon c}{L\omega} \right)^2 \right)^{\frac{1}{2}}, \quad (13)$$

has a slightly different value from that of the case of propagation in a free media. Therefore, the transverse structure of the wave packet results in a

dispersion for the parallel component of the wave vector. This dispersion is not due to the medium, but is due to geometrical constraints. Since the group velocity of the wave packet is determined by its dispersion, the geometrical constraints of the wave guide change the travel time of an acoustic pulse by ΔT as compared to a free medium,

$$\frac{\Delta T}{T} \approx \left(\frac{\epsilon c}{L\omega} \right)^2. \quad (14)$$

The change in the parallel component of the wave speed depends on the wave frequency. In contrast, travel time evaluated from ray theory is independent of frequency and is computed by dividing the distance between the source and receiver by the sound speed in the wave guide. The error in travel time from the ray theory decreases for large ω and for large L .

It is understandable that this geometric effect also manifests itself for sound which propagates in the ocean's sound channel. To demonstrate this, equation (7) is integrated exactly and yields,

$$P_0(s, \omega) = P_g(s, \omega) \left(1 + \frac{ic_0}{2\omega} \int_{s_0}^s \frac{d\xi}{\kappa} \frac{\nabla^2 P_0(\xi, \omega)}{P_g(\xi, \omega)} \right), \quad (15)$$

where P_g is defined by (9), and constants of integration are chosen in a way that P_0 reduces to P_g in the limit $\omega \rightarrow \infty$ or $s \rightarrow s_0$. For large enough ω and limited values of the integral in (15) we treat the ω -dependent term as a perturbation, and use an iteration technique to find the asymptotic expansion of P_0 with respect to powers of the small parameter $\frac{1}{\omega}$. As stated above, the zero order approximation, i.e., one corresponding to $\frac{1}{\omega} \rightarrow 0$, is $P_0 = P_g$. In order to find the next approximation to P_0 , we substitute the zero order approximation in the right hand side of (15) to get,

$$P_0(s, \omega) \approx P_g(s, \omega) \left(1 + \frac{ic_0}{2\omega} \int_{s_0}^s \frac{d\xi}{\kappa} \frac{\nabla^2 P_g(\xi, \omega)}{P_g(\xi, \omega)} \right). \quad (16)$$

This approximation is valid if the integral is small compared to unity. Effectively, it means that two conditions must be met: (1) the frequency ω is sufficiently high; and (2) the integral itself is not prohibitively large. If we define a new variable δ as,

$$\delta \equiv \frac{c_0}{2} \int_{s_0}^s \frac{d\xi}{\kappa} \frac{\nabla^2 P_g(\xi, \omega)}{P_g(\xi, \omega)}, \quad (17)$$

the criterion for the validity of the perturbation technique is,

$$\frac{|\delta|}{\omega} \ll 1. \quad (18)$$

Though the perturbation technique has limited applicability, it provides a qualitative insight of the phenomena.

Throughout this section we assume that the integration in (16) is performed over a relatively small extent of the ray trajectory, so that the absolute value of the integral is small, and (18) is valid. Equation (16) can then be rewritten in the form which simplifies further treatment,

$$P_0(s, \omega) \simeq P_s(s, \omega) \exp\left(\frac{i\delta}{\omega}\right). \quad (19)$$

In order to estimate the travel time of acoustic pulses, we substitute this solution into the formula for the inverse Fourier transform. For the sake of simplicity, the initial acoustic pulse is assumed to have a Gaussian envelope and a narrow spectrum centered at frequency ω_0 ,

$$P(s_0, \omega) = \bar{P} \exp\left(-\frac{(\omega - \omega_0)^2}{\Delta\omega^2}\right), \quad (20)$$

where $\Delta\omega$ is the bandwidth of the spectrum. Upon substitution of (20) and (19) in (2) we get

$$P(s, t) \simeq \bar{P} \int d\omega \exp\left(-\frac{(\omega - \omega_0)^2}{\Delta\omega^2}\right) \exp\left(i\frac{\omega}{c_0}\psi - i\omega t\right) \exp\left(\frac{i\delta}{\omega}\right). \quad (21)$$

If the spectrum of the initial pulse is narrow (i.e, for small $\Delta\omega$), the argument of the exponent is a fast varying function of ω . It allows us to estimate (21) by the method of stationary phase.¹⁵ This method yields the value of the integral for the pressure,

$$P(s, t) \simeq \text{const} \Delta\omega^2 \exp\left[i\omega_0\left(\frac{\psi}{c_0} - t\right) + \frac{i\delta}{\omega_0}\right] \times \exp\left[-\frac{\Delta\omega^2}{4}\left(\frac{\psi}{c_0} - t - \frac{\delta}{\omega_0^2}\right)^2\right], \quad (22)$$

(Appendix A). The first exponent corresponds to oscillations of pressure at the center frequency ω_0 of the initial pulse. The second exponent determines

the shape of the pulse and the time of its arrival. The maximum amplitude occurs at the time,

$$T_m = \frac{\psi}{c_0} - \frac{\delta}{\omega_0^2}. \quad (23)$$

Note that the time of arrival, defined as the time of the maximum amplitude, is changed as compared to the case $\omega \rightarrow \infty$ by the amount $\delta T = -\frac{\delta}{\omega_0^2}$ where δ is defined by (17). The change in the time of arrival of the pulse is inversely proportional to the square of the center frequency. The change in the travel time originates from the second-derivative term in (3), which describes the diffraction of acoustic waves. Qualitatively, the change in the travel time is associated with leakage of the wave energy between adjacent rays, so that at the observation point there is interference of waves coming from different directions.

An important feature of (23) is that the relative change in the travel time is of order,

$$\frac{\delta T}{T} \sim \left(\frac{c_0}{\omega L} \right)^2, \quad (24)$$

where,

$$L = \left(\frac{\nabla^2 P_g(\xi, \omega)}{P_g(\xi, \omega)} \right)^{-\frac{1}{2}}, \quad (25)$$

is the characteristic dimension of the spatial distribution of the pressure field. The form for the fractional change in travel time is similar to that for the wave guide, as given by equation (14). The width of the wave guide is analogous to the characteristic dimension of the spatial distribution of the pressure field envelope, P_g . In the case of large L , or equivalently, a smooth distribution of the pressure field, the derivatives from P_g are small, providing that values of δ are small. Then ray tracing yields accurate estimates for the delay of a pulse. The main contribution to the integral in (15) is near regions of large curvature of the pressure field envelope along the ray trajectory. Typically, these are focusing regions or regions of rapid variations in the sound speed near the ocean's surface. We believe that it is this effect which manifested itself in the comparison of travel times computed by the ray method and the normal mode method.⁸

C. Maximum change in travel time per focusing region.

Phase shifts in the form of (19) are inversely proportional to the wave frequency ω . In the derivation of (19), we implicitly assume that $\frac{\nabla^2 P_0}{P_0}$ has a finite limit when $\omega \rightarrow \infty$. While this is a valid assumption for extents of the ray curve in regions of a smooth spatial variation of P_0 , it may be not valid near focusing regions. The smallest possible dimension of a focusing region is of order of the wavelength, so the diffraction term $\frac{\nabla^2 P_0}{P_0}$ may be as large as $\frac{1}{\lambda^2}$. Thus $\frac{\nabla^2 P_0}{P_0}$ may not have a finite limit when $\omega \rightarrow \infty$, since $\lambda \rightarrow 0$. In this case, the integration distance may be estimated as $(s - s_0) \sim \lambda$, and the upper limit for the phase difference acquired during one pass through a focusing region due to diffraction can be estimated as (see (15))

$$\Delta\phi \sim \frac{c_0}{2\omega} \int_{s_0}^s \frac{d\xi}{\kappa} \frac{\nabla^2 P_0(\xi, \omega)}{P_0(\xi, \omega)} \sim \frac{1}{2}. \quad (26)$$

Note that this order of magnitude estimate does not exhibit the dependence on frequency which is characteristic of (19). Comprehensive study of diffraction at focusing regions is difficult due to the fact that location and structure of focusing regions depend on frequency in a complicated way.¹⁴ Appendix B gives detailed estimates of the phase shift due to diffraction at a focusing region. Formula (26) is the order of magnitude estimate only, so that phase shifts from different focusing regions may have different values and signs which sum constructively or destructively as the ray passes through the focusing regions.

During its propagation over thousands of kilometers, the acoustic wave packet encounters as many as $N \sim 10^2$ focusing regions. We assume that the coherence length for acoustic waves is larger or of the same order as the propagation distance.¹⁶ Then the maximum total phase shift accumulation due to constructive interference is $\Delta\phi \sim \frac{1}{2}10^2$ radians at each frequency. After an inverse Fourier transform, phase shifts transfer to a change in a travel time of about $\Delta T \sim \frac{\Delta\phi}{\omega} \sim 100$ ms at $\frac{\omega}{2\pi} = 70$ Hz. This is the upper limit estimate, based on the assumption that focusing regions have the smallest possible spatial dimensions $\sim \lambda$.

Random fluctuations affect the geometrical structure of the focusing regions, so that such regions are "blurred" as compared to an ideal model.

In this case, we can expect less sharp maxima of the wave intensity at the focusing region, and smaller values of the second derivative term $\frac{\nabla^2 P_0(\xi, \omega)}{P_0(\xi, \omega)}$ in (15). Therefore, larger dimensions of focusing regions should result in smaller effects from diffraction.

III. Scale of focusing regions and travel times

The spatial extent of a focusing region has a dominant influence on the manifestation of pulse delay due to diffraction. This is illustrated analytically by enlarging the size of a focusing region by increasing the size of an acoustic source. Given a sound speed profile, the medium creates images of the source, and larger dimensions of the source correspond to larger dimensions of focusing regions.

The wave equation, (1), is solved for a specific sound speed field,

$$\frac{1}{c^2(z)} = \frac{1}{c_0^2} (1 - \beta(z - z_b)^2). \quad (27)$$

Though this field is unrealistic, it allows an analytical treatment of the problem. In (27), z_b is the depth of the minimum of the sound speed profile. The Fourier transform of (1) is taken with respect to t ,

$$\nabla^2 P(\vec{r}, \omega) + \frac{\omega^2}{c^2(z)} P(\vec{r}, \omega) = 0. \quad (28)$$

The general solution of (28) can be represented via expansion over the normal modes (see Appendix C),

$$P(\vec{r}, \omega) = \sum_{n=0}^{\infty} \frac{C_n(\omega)}{2^{\frac{n}{2}} \pi^{\frac{1}{2}} (n!)^{\frac{1}{2}}} \exp\left(-\frac{\theta^2}{2}\right) H_n(\theta) H_0^{(1)}(k_z^{(n)} r), \quad (29)$$

where $H_0^{(1)}$ is the Hankel function of the first kind of zero order, $\theta = \gamma^{-1}(z - z_b)$, $\gamma = \left(\frac{c_0^2}{2\beta}\right)^{\frac{1}{2}}$, $H_n(\theta)$ are Hermitian polynomials, and $k_z^{(n)}$ is the horizontal component of the wave vector for the n -th mode given by (C6). Coefficients of the expansion C_n are determined by the source and/or by boundary conditions (Appendix C).

We assume that the acoustic wave is created by a source of small, but finite dimensions, centered at the minimum of the sound speed profile, i.e., at $z = z_b$. The pressure field created by a small source has regularly spaced focusing regions. The inhomogeneous media effectively acts as a lens, creating "images" of the source. At high frequencies, the "images" of the source at focusing regions have approximately the same shape and dimensions as the source (Appendix C). At lower frequencies these "images" are imperfect, because of diffraction.

For small r , we assume that the pressure field has a Gaussian profile,

$$P = \frac{P_s(\omega)}{\sigma_s \pi^{\frac{1}{2}}} \exp \left(-\frac{(z - z_b)^2}{\sigma_s^2} \right), \quad (30)$$

implying that the scale of the source is σ_s . For small dimensions of the source, one has to take into account large numbers of terms in the normal mode expansion (Appendix C). In the high-frequency approximation, the dependence of the pressure field P on r along the sound channel axis is characterized by periodically spaced minima and maxima. The latter correspond to focusing regions (Appendix C).

We evaluate (29) numerically. Figure 1 shows the magnitude of P as a function of range along the line $z = z_b$ for $f = 70$ Hz and for a source of size $\sigma_s = 30$ m. Figure 2 shows the same quantity for $\sigma_s = 60$ m. The maxima in the middle of the plots correspond to the focusing region at r defined by (C14) with $m = 30$. Note that the curve corresponding to the smaller source has more sharp features with small scale oscillations, and we expect larger effects associated with diffraction. Since the expansion converges very slowly for r corresponding to focusing regions, we limit our numerical calculations of the diffraction effects for r lying in between focusing regions, as defined by (C15). We compare the value of P to that in the approximation $\omega \rightarrow \infty$ (as defined by (C12)). Figure 3 shows the ratio $R = \frac{P}{P_\infty}$, where P is evaluated using the exact formulas for $k_z^{(n)}$, and P_∞ is calculated in the limit of large ω , when (C12) holds. For this calculation we choose $r \simeq 2140$ km, which corresponds to $m = 30$ in (C15). For frequencies less than ~ 140 Hz, the Fourier component of the pressure field is different from that calculated in the high frequency limit, and the ratio R is not close to 1. For a larger source of size $\sigma_s = 60$ m, diffraction might be neglected for $f > 70$ Hz. Thus, diffraction effects are less for large sizes of acoustic sources.

In Figures 3 and 4, diffraction effects can be modeled by multiplying P by an oscillating function of frequency, W , which can be roughly represented as,

$$W \simeq 1 + \chi(\omega) \exp(i\eta\omega). \quad (31)$$

If we assume that the acoustic pulse has a Gaussian shape, we can get a rough estimate for the change in the travel time associated with diffraction,

$$\Delta T \sim \chi(\omega_0)\eta. \quad (32)$$

Estimating graphically from Figure 3,

$$\begin{aligned} \chi &\sim 0.5, \\ \eta &\sim 0.15 \text{ s/rad}, \end{aligned}$$

for $f = 70$ Hz, we get $\Delta T \sim 120$ ms for $\sigma_z = 30$ m. For larger dimensions of the source (see Figure 4), we estimate

$$\begin{aligned} \chi &\sim 0.08, \\ \eta &\sim 0.15 \text{ s/rad}, \end{aligned}$$

and the effect at $f = 70$ Hz is only $\Delta T \sim 20$ ms.

Figure 5 shows the estimate for ΔT , from (32), as a function of frequency for $\sigma_z = 30$ m. For comparison, circles show the change in travel time obtained in the numerical experiment by Boden, et al.⁸ at the range $r = 2000$ km. There is no quantitative agreement between the results of Boden et al.⁸ and those of this section, due to the fact that we used a different model for the sound speed field. However, the change in travel time, ΔT , has the same order of magnitude and exhibits the same behavior with frequency ($\Delta T \sim \omega^{-2}$) as that in the numerical experiment. We also note that ΔT is predicted to be proportional to range for smoothed sound speed profiles. This is consistent with the numerical experiments conducted by Boden et al.⁸

IV. CONCLUSIONS

As was shown earlier,⁸ travel times of acoustic pulses modelled by ray tracing and normal modes are different, the difference being larger at lower

frequencies. Note that numerical experiments in Boden, et al.⁸ were performed in a smooth sound speed field. For smooth sound speed profiles, diffraction effects at focusing regions may be strong enough to cause changes in travel time by tens or hundreds of milliseconds for frequencies $f < 100$ Hz. Our estimates for diffraction suggest that the change in travel time rapidly decreases with frequency, typically $\Delta T \sim \omega^{-2}$, and linearly increase with range r (Figure 5).

The perturbation to the travel times associated with diffraction is determined by the small-scale details of the geometrical structure of the wave pressure field, in particular in the vicinity of focusing regions. Therefore, random fluctuations of the sound speed may determine the numerical value of the diffraction-associated changes of the travel times. This uncertainty of the travel times is not associated with a method of acoustic modeling, e.g., ray-tracing, or normal mode expansion, and is intrinsic to the sound speed model and to the level of fluctuations. If focusing regions are blurred by random fluctuations, so that their dimensions are larger than in smoothed models of the sound speed, the effect of diffraction on the travel times diminishes.

The normal mode method and parabolic approximation account for diffraction. Their applicability is not restricted to high frequencies. Therefore, if the fine spatial structure of the sound speed field was given, these methods might provide the most accurate estimate for the travel times of acoustic pulses. However, diffraction effects considered above are extremely sensitive to small scale features of the wave packet structure in the vicinity of focusing regions. Our ability to estimate travel time perturbations is necessarily restricted by the lack of knowledge of the wave magnitude distribution in the vicinity of focusing regions. In the ocean, the sound speed field has fine structure, which potentially results in the blurring of focusing regions. Under these circumstances, the normal mode and parabolic approximation methods overestimate the perturbations to the travel times, when applied to smoothed sound speed profiles. In contrast, the ray tracing method, which ignores diffraction, may give a more accurate estimate for measured travel times.

We expect, that if the numerical comparison between the normal mode method and ray theory in Boden, et al.⁸ was made in a structured ocean, the agreement between these two methods might have been better than that in a smooth sound speed profile.¹⁸ In the future, theoretical and numeri-

cal studies are required for estimating the spatial scales of focusing regions. Experimentally, effects of diffraction on travel times might be detected by simultaneously transmitting acoustic pulses at different center frequencies along the same path, using the same source and receiver. The measured difference in travel times at different frequencies may also serve as a tool for estimating the spatial dimensions of focusing regions in the ocean.

V. ACKNOWLEDGMENTS

This research was supported by the Advanced Research Projects Agency grant MDA972-93-1-0004 managed by Dr. Ralph Alewine, and the Strategic Environmental Research Defense Program (SERDP) headed by Dr. John Harrison.

Appendix A. Integration by the Method of Stationary Phase

The method of stationary phase is useful for estimating integrals in the form,

$$I = \int_{-\infty}^{+\infty} d\omega \exp(f(\omega)) g(\omega),$$

where $f(\omega)$ is a fast varying function of ω . From (21), we choose,

$$f(\omega) = -\frac{(\omega - \omega_0)^2}{\Delta\omega^2} + i\frac{\omega}{c_0}\psi - i\omega t + \frac{i\delta}{\omega}, \quad (A1)$$

$$g(\omega) = 1.$$

The equation for the point of the stationary phase is obtained by differentiating (A1) with respect to ω ,

$$\omega = \omega_0 + \frac{i\Delta\omega^2}{2} \left(\frac{\psi}{c_0} - t - \frac{\delta}{\omega^2} \right). \quad (A2)$$

In the approximation of narrow band signals (small $\Delta\omega$), the solution of (A2) is obtained by a perturbation method, substituting the lowest order approximation $\omega = \omega_0$ in the right hand side of (A2),

$$\omega \simeq \omega_0 + \frac{i\Delta\omega^2}{2} \left(\frac{\psi}{c_0} - t - \frac{\delta}{\omega_0^2} \right). \quad (A3)$$

With the point of the stationary phase defined by (A3), the stationary phase approximation yields (22).

Appendix B. Change of Wave Phase at a Focusing Region

We consider the travel time of an acoustic wave which encounters a caustic. Since we are interested in the wave near a caustic, we expand the sound speed profile in a Taylor series and retain only the linear term in the expansion,¹⁷

$$\frac{\omega^2}{c^2(z)} = \frac{\omega^2}{c_0^2} (1 - \alpha z). \quad (B1)$$

where α is a constant. We choose the point $z = 0$ at the caustic. We assume that the sound speed depends only on the depth z and that the dependence of the pressure on the coordinate x is in the form,

$$P = P_1(z) \exp(ik_x x). \quad (\text{B2})$$

The equation for the Fourier transformed pressure field follows from the wave equation,

$$\frac{\partial^2 P_1}{\partial z^2} + \frac{\omega^2}{c_0^2} (1 - \alpha z) P_1 - k_x^2 P_1 = 0. \quad (\text{B3})$$

If we choose $k_x = \frac{\omega}{c_0}$, a solution of (B3) can be expressed via a linear combination of Airy functions Ai and Bi.¹⁷ For the estimates below we use,

$$P_1 = C(\omega) (\text{Bi}(\zeta) + i\text{Ai}(\zeta)), \quad (\text{B4})$$

where C does not depend on the coordinates, but may depend on the frequency, and $\zeta = (\alpha \frac{\omega^2}{c_0^2})^{\frac{1}{3}} z$. We use this expression to estimate the phase shift associated with diffraction in the vicinity of the caustic (compare to (15) and (19)),

$$\Delta\phi = \frac{c_0}{2\omega} \int_{s_-}^{s_+} \frac{d\xi}{\kappa} \frac{\nabla^2 P_0(\xi, \omega)}{P_g(\xi, \omega)}, \quad (\text{B5})$$

where s_- , s_+ are points on the ray curve before and after the ray encounters the caustic, respectively.

We must substitute into (B5) the slowly varying amplitude P_0 as defined by (2), where P in the left hand side of (2) is obtained from the exact solution of the wave equation which accounts for diffraction. In contrast, the value of P_g in (B5) is defined by (9) and is determined only by the integral along the ray curve. Generally, P and P_g may have different values. In the derivation of the wave field magnitude (15) we required $P_0 \rightarrow P_g$ for $s \rightarrow s_0$. In this appendix, we consider a small extent of the ray curve in the vicinity of the caustic $s_- < s < s_+$, so that the limits of integration in (B5) can be viewed as a subset of the limits of integration in (15). In (B5) we may not assume that $P_0 \rightarrow P_g$, since the exact solution P_0 may have acquired an additional phase shift due to diffraction effects during wave propagation from s_0 to s_- . Therefore, throughout this appendix we will assume that the phases of P_0 and P_g are different.

If there is more than one ray intersecting at a given point in the illuminated region, we have to separate contributions from different rays in the full wave field P to determine P_0 associated with each of these rays. Rigorously speaking, the pressure field P_1 in the form (B4) is formed as a result of the interference of waves approaching the caustic and those which have already encountered the caustic. However, since we are interested in order of magnitude estimates, we will use P_1 to calculate P_0 in (B5), and will not estimate contributions of the two rays separately. Note that P_1 is linked with the pressure field by equation (B2), while P_0 in (B5) is defined by (2), where ψ must be determined from the solution of the ray tracing equations (5), (6). Therefore, to determine P_0 , one has to determine ψ by solving ray equations.

For the sound speed profile used throughout this section, the ray tracing equations may be derived from (5), (6) and are in the form,

$$\begin{aligned} k_x &= \text{const}, \\ \frac{\partial k_x}{\partial \tau} &= -\frac{\omega^2}{c_0^2} \alpha, \\ \frac{\partial z}{\partial \tau} &= 2k_x, \\ \frac{\partial x}{\partial \tau} &= 2k_z. \end{aligned} \quad (\text{B6})$$

Integration of these equations yields

$$\begin{aligned} z &= -\frac{\omega^2}{c_0^2} \alpha \tau^2, \\ x &= 2k_x \tau, \end{aligned} \quad (\text{B7})$$

which describes a parabolic trajectory for the ray. Integration of the wave phase expression for ψ yields,

$$\psi = x + \frac{2}{3} \alpha^{\frac{1}{2}} (-z)^{\frac{3}{2}}. \quad (\text{B8})$$

Substituting ψ in the definition of P_0 (see (2)), we estimate P_0 as,

$$P_0 = P \exp \left(-i \frac{\omega}{c_0} \psi \right) = C(\omega) (\text{Bi}(\zeta) + i \text{Ai}(\zeta)) \exp \left(-i \frac{2}{3} \frac{\omega}{c_0} \alpha^{\frac{1}{2}} (-z)^{\frac{3}{2}} \right). \quad (\text{B9})$$

Since we substitute second derivatives of P_0 in (B5), we have to differentiate (B9) with respect to z . Omitting some algebra, we note that the expression for the second derivative of P_0 has several terms, one of them having

a singularity in the vicinity of the caustic at $z = 0$. This term results from differentiating the exponent in (B9),

$$\frac{\partial^2 P_0}{\partial z^2} \simeq -\frac{1}{2} i k_x \alpha^{\frac{1}{2}} (-z)^{-\frac{1}{2}} P_0, \quad (\text{B10})$$

and is dominant.

To complete the evaluation of the integral in (B5), we must calculate P_g along the ray path. The focusing factor can be estimated from geometrical considerations, accounting for the fact that the distance between adjacent trajectories depends on z as $(-z)^{-\frac{1}{2}}$. Since the square of the magnitude of the pressure field must be inversely proportional to the distance between the adjacent trajectories, we find,

$$P_g \sim C_g(\omega)(-z)^{-\frac{1}{2}}, \quad (\text{B11})$$

where C_g is a coefficient which does not depend on z . As discussed above, P_g may have a phase different from that of P_0 in the limit $z \rightarrow -\infty$, but we assume that they are of the same order of magnitude, so that their ratio is a constant $U(\omega) \sim 1$. We can estimate C_g by comparing (B11) to the asymptotics of the exact solution (B4) for $z \rightarrow -\infty$. Substituting standard expressions for the asymptotics of Ai and Bi for $z \rightarrow -\infty$,

$$\begin{aligned} \text{Ai}(-\zeta) &= \pi^{-\frac{1}{2}} \zeta^{-\frac{1}{4}} \sin\left(\frac{2}{3}\zeta^{\frac{3}{2}} + \frac{\pi}{4}\right), \\ \text{Bi}(-\zeta) &= \pi^{-\frac{1}{2}} \zeta^{-\frac{1}{4}} \cos\left(\frac{2}{3}\zeta^{\frac{3}{2}} + \frac{\pi}{4}\right), \end{aligned} \quad (\text{B12})$$

into (B4) and comparing the result to (B11), we obtain for C_g ,

$$\frac{C(\omega)}{C_g(\omega)} \sim U \left(\alpha \frac{\omega^2}{c_0^2} \right)^{\frac{1}{2}}. \quad (\text{B13})$$

Since the pressure fields in the integral of (B5) are expressed in terms of z , it is convenient to change the integration variable from the element of the ray path ξ to z ,

$$d\xi \simeq \alpha^{-\frac{1}{2}} (-z)^{-\frac{1}{2}} dz. \quad (\text{B14})$$

We take into account that z spans the same range values before and after the ray encounters the caustic. This results in a factor of 2 multiplying the

entire expression. Substituting (B10), (B11) and (B14) into (B5), we get

$$\Delta\psi \sim \frac{1}{2}U \left(\alpha \frac{\omega^2}{c_0^2} \right)^{\frac{1}{2}} \int_{-z_0}^0 dz (-z)^{-\frac{1}{2}} = 2U \left(\alpha \frac{\omega^2}{c_0^2} \right)^{\frac{1}{2}} (-z_0)^{\frac{1}{2}}, \quad (\text{B15})$$

where z_0 is the maximum distance from the caustic. Since $\Delta\psi$ depends on the one-fourth power of z_0 , the result is not very sensitive to the correct choice of the limits of integration. We are interested in effects caused by the focusing at the caustic. Therefore we choose z_0 so that the integration limits cover the region of the most rapid fluctuations of the wave magnitude and/or phase. They correspond to $|\zeta_{\max}| \sim 1$ in the full solution (B4), which is equivalent to $z_0 \sim \left(\alpha \frac{\omega^2}{c_0^2} \right)^{-\frac{1}{2}}$. This yields the following expression for the phase shift of a wave packet due to diffraction in the vicinity of a caustic,

$$\Delta\psi \sim 2U, \quad (\text{B16})$$

where $|U| \sim 1$ may depend on ω and is determined by the wave propagation from the source to the region of the caustic. This formula is an order of magnitude estimate for the phase shift acquired by the wave at each focusing region along the ray path due to diffraction.

Appendix C. Normal Mode Solution of the Wave Equation

A solution of (28) is sought using separation of variables in cylindrical coordinates,

$$P = Z(z)X(r), \quad (\text{C1})$$

where r is the radial variable. The equation for $X(r)$ yields the equation for Bessel functions; the equation for $Z(z)$ yields,

$$\frac{d^2 Z}{dz^2} - \beta \frac{\omega^2}{c_0^2} (z - z_b)^2 Z + k_z^2 Z = 0, \quad (\text{C2})$$

where,

$$k_z^2 = \frac{\omega^2}{c_0^2} - k_r^2, \quad (\text{C3})$$

and k_z is the separation constant. Physically, k_z is the longitudinal component of the wave vector for a given mode. Equation (C2) is accompanied by boundary conditions, which we assume to be $Z(z) \rightarrow 0$ when $z \rightarrow \pm\infty$. The full set of solutions of (C2) can be expressed through the Hermitian polynomials as,

$$Z_n(z) = \frac{1}{2^{\frac{n}{2}} \pi^{\frac{1}{4}} (n!)^{\frac{1}{2}}} \exp\left(-\frac{\theta^2}{2}\right) H_n(\theta), \quad (C4)$$

where $\theta = \gamma^{-1}(z - z_0)$, $\gamma = \left(\frac{c_0^2}{\beta\omega^2}\right)^{\frac{1}{2}}$, and $n \geq 0$ is an integer. Eigenfunctions (C4) correspond to eigenvalues,

$$k_z^2 = \frac{(2n+1)\beta^{\frac{1}{2}}\omega}{c_0}. \quad (C5)$$

Substitution of k_z in (C3) determines the value of the horizontal component of the wave vector for the n -th mode,

$$k_x^{(n)} = \frac{\omega}{c_0} \left[1 - \frac{(2n+1)\beta^{\frac{1}{2}}c_0}{\omega} \right]^{\frac{1}{2}}. \quad (C6)$$

1. The coefficients for the normal mode expansion.

The coefficients C_n are determined by expanding the pressure field near the source. By integrating the product of (30) and eigenfunctions (C4) with respect to z , we evaluate C_n for even n ,

$$C_n = \frac{P_s(\omega)}{\sigma_z} \frac{(-1)^{\frac{n}{2}} (n!)^{\frac{1}{2}}}{\pi^{\frac{1}{4}} 2^{\frac{n}{2}} \left(\frac{n}{2}\right)!} \frac{(q-1)^{\frac{n}{2}}}{q^{\frac{n+1}{2}}}, \quad (C7)$$

where,

$$\begin{aligned} q &= \frac{1}{2} + \frac{1}{\sigma_z^2}, \\ \sigma &= \gamma^{-1}\sigma_z. \end{aligned} \quad (C8)$$

Due to the important role that higher order coefficients C_n play in the travel time of wave pulses, it is necessary to investigate the dependence of C_n on n . We assume that the dimensions of the source are small compared with the

characteristic scale of the sound speed profile. Then, $\sigma \ll 1$, $q \gg 1$. Normal modes with relatively small mode number n "feel" the narrow source as a point, while rapidly oscillating high order normal modes would "feel" the source as a smooth function of z . Therefore, we expect a different behavior of C_n for small and large values of n . For small σ we use the approximation,

$$\frac{\gamma (q-1)^{\frac{3}{2}}}{\sigma_s q^{\frac{n+1}{2}}} \simeq \left[\left(1 - \frac{1}{q} \right)^q \right]^{\frac{n}{2q}} \simeq \exp \left(-\frac{n}{2q} \right). \quad (C9)$$

Using Stirling's formula for $n!$, we get an approximate formula for C_n for even n ($n \neq 0$),

$$C_n \simeq \frac{2^{\frac{1}{2}} (-1)^{\frac{n}{2}} P_s(\omega)}{\gamma \pi^{\frac{1}{2}} n^{\frac{1}{2}}} \exp \left(-\frac{n}{2q} \right). \quad (C10)$$

Note that for small dimensions of the source, $q \gg 1$, $\sigma \ll 1$, the exponential factor in (C10) is close to 1 for not very large n , so that C_n decreases very slowly with n , namely as $n^{-\frac{1}{2}}$. For sufficiently large n , the exponent in (C10) starts to play its role, providing the convergence of the expansion in (29). Terms with n as large as $n \sim 2q$ make significant contributions to the solution. At a given frequency, these higher order modes have different the group velocity than at infinitely high frequency, and the pulse delay is thus a function of frequency.

The receiver is located at $z = z_b$, the same depth as the center of the source. At high frequencies, $\omega \rightarrow \infty$, the impulse response can be estimated with rays. The simplest solution corresponds to a ray propagating along a straight line connecting the center of the narrow source and the receiver. The travel time of the ray is $T = \frac{z}{c_0}$. Other rays, which have non-zero launch angle, oscillate around the plane $z = z_b$, forming focusing regions where they all arrive at the same point after executing a number of oscillations.

The same pattern can be obtained from (29). We use the asymptotic approximation for the Hankel function,

$$H_0^{(1)}(\rho) \simeq \left(\frac{2}{\pi \rho} \right)^{\frac{1}{2}} \exp \left(-i\rho - \frac{i\pi}{4} \right), \quad (C11)$$

We also expand the expression (C6) for $k_z^{(n)}$ in the Taylor series,

$$k_z^{(n)} \simeq \frac{\omega}{c_0} - \frac{(2n+1)\beta^{\frac{1}{2}}}{2}. \quad (C12)$$

This expression is valid when the second term is small compared to the first one, i.e. for large frequencies and not very large n .

Substitution of (C11) and (C12) in (29) yields the Fourier component of the pressure field,

$$P = \exp\left(-i\frac{\omega}{c_0}r\right) \exp\left(-i\frac{\pi}{4}\right) \sum_{n=0}^{\infty} C_n(\omega) Z_n(z) \left(\frac{2}{\pi k_z^{(n)} r}\right)^{\frac{1}{2}} \exp\left(-i\frac{(2n+1)\beta^{\frac{1}{2}}}{2}r\right). \quad (C13)$$

For points at $z = z_b$ (i.e., $\theta = 0$) we find that $Z_0(z_b) \simeq \pi^{-\frac{1}{4}}$, and $Z_n(z_b) \simeq (-1)^{\frac{n}{2}} 2^{\frac{1}{2}} \pi^{-\frac{1}{2}} n^{-\frac{1}{2}}$ for even n ($n \neq 0$). Depending on the value of r , subsequent terms in (C13) can either accumulate or nearly cancel each other. To show this, consider the value of the exponent $E_n = \exp\left(-i\frac{(2n+1)\beta^{\frac{1}{2}}}{2}r\right)$ for different n and r . For,

$$r = 2m\pi\beta^{-\frac{1}{2}}, \quad (C14)$$

where m is an integer, we get $E_{n+1} = E_n$, and subsequent terms add constructively. In contrast, if,

$$r = (2m+1)\pi\beta^{-\frac{1}{2}}, \quad (C15)$$

we get $E_{n+1} = -E_n$, and subsequent terms in (C13) are subtracted one from another. As determined above, a large number of terms, $\sim 2q$, make significant contribution to (C13), and the coefficients of the expansion decrease slowly with n for $n < 2q$. Therefore, the constructive adding of all terms for r defined by (C14) would form significantly larger magnitudes of the signal, as compared to the destructive interference if r is defined by (C15). The spatial distribution of the pressure magnitude along the line $z = z_b$ has maxima and minima defined by (C14) and (C15) respectively. The maxima correspond to focusing regions, and the minima correspond to the points in between the focusing regions.

If we differentiate (C12), we see that all modes in this approximation have the same group velocity c_0 . However, this approximation is not valid for modes of higher order. As we saw above, modes with $n \sim 2q$ make a significant contribution to the solution; the difference of the group velocity of these modes from c_0 is the physical phenomena responsible for the change in travel time as compared to the ray approximation.

2. Transverse dimensions of focusing regions

Dimensions of focusing regions in the transverse direction z are estimated from (C13), where we use $z \neq z_b$ as the argument of $Z_n(z)$. Since the coefficients of (C13) decrease slowly with n , we assume that terms with large $n \sim 2q$ make the main contribution in (C13). We use the standard asymptotic formula for Hermitian polynomials¹⁹ at large n to get,

$$Z_n(z) \approx \frac{2^{\frac{1}{2}} (-1)^{\frac{n}{2}}}{\pi^{\frac{1}{2}} n^{\frac{1}{2}}} \cos \left(\left(\frac{n}{2} \right)^{\frac{1}{2}} \theta \right), \quad (\text{C16})$$

We substitute (C16) and (C10) and estimate the result at the range of the m -th focusing region, defined by (C14),

$$P(z, \omega) \approx \frac{2}{(\pi k_z r)^{\frac{1}{2}}} \exp \left(-\frac{i\omega}{c_0} r \right) \exp \left(-\frac{i\pi}{4} + i\pi m \right) \gamma P_s(\omega) \sum_{n=0}^{\infty} \frac{1}{n^{\frac{1}{2}}} \exp \left(-\frac{n}{2q} \right) \cos \left(\left(\frac{n}{2} \right)^{\frac{1}{2}} \theta \right). \quad (\text{C17})$$

In (C17) we assumed that $k_z^{(n)}$ depends on n very slowly, and that $\theta \ll 1$, which corresponds to positions near the minimum of the sound speed profile. Since individual terms in (C17) are insensitive to n , we can estimate $P(z, \omega)$ by integration instead of summation with respect to n . The resulting integral for the profile of the pressure magnitude at the range of the focusing region is,

$$P(z, \omega) \sim \left(\frac{q}{2\pi k_z r} \right)^{\frac{1}{2}} \exp \left(-\frac{i\omega}{c_0} r - \frac{i\pi}{4} + i\pi m \right) \gamma P_s(\omega) \exp \left(\frac{-q\theta^2}{4} \right). \quad (\text{C18})$$

Characteristic dimensions of the focusing region are therefore defined by

$$\theta \sim \frac{2}{q^{\frac{1}{2}}},$$

which corresponds to $(z - z_b) \sim \sigma_z$, i.e. the focusing region has the dimensions of the source.

Glossary

Ai, Bi - The Airy functions

$C(\omega)$ - amplitude coefficient in (B4)

C_g - the amplitude coefficient in ray approach (B11)

$c(r)$ - sound speed

C_n - the coefficients of the normal mode expansion

c_0 - a constant of order of c

$D(\vec{k}, \omega)$ - the left hand side of the dispersion equation (4)

d - the distance between caustics

E_n - the value of the exponent in the n -th term of the normal mode expansion

f - frequency (Hz)

H_n - the Hermitian polynomials

$H_0^{(1)}$ - the Hankel function

\vec{k} - the wave vector

k_x - the horizontal component of the wave vector

k_z - the vertical component of the wave vector

L - the characteristic spatial scale of the acoustic wave packet

L_c - the coherence length L_t - the total distance of wave propagation

$\mathcal{P}(r, t)$ - pressure field of acoustic wave

$P(r, \omega)$ - the Fourier transform for $\mathcal{P}(r, t)$

$P_0(r, \omega)$ - slow varying amplitude of the Fourier transformed pressure field as defined by (2)

P_g - P_0 in the limit $\omega \rightarrow \infty$

P_s - P_0 near the source (at $s = s_0$)

$P_{\perp}(z)$ - the function characterizing the dependence of the pressure field on the depth in the vicinity of a caustic

q - a parameter defined by (C8)

\vec{r} - position

$R = P(r, \omega)/P_g$

s - the distance along the ray curve

s_0 - a point near the source where P_0 is assumed to be known

s_- - a point on the ray curve before a caustic

s_+ - a point on the ray curve after a caustic

T - the travel time of the acoustic pulse in the limit $\omega \rightarrow \infty$

T_m - the travel time of the acoustic pulse, accounting for effects of diffraction

t - time

U - a parameter, describing the ratio $\frac{C}{C_g}$, (defined by (B13))

W - the oscillating function of frequency which approximately describes the effects of the finite dimensions of the source in (31)

$X(r)$ - the function describing the dependence of the Fourier transformed pressure field P on r in the parabolic profile

x - the range

z - the depth

z_0 - the depth, corresponding to s_- , s_+

z_b - the depth at which the parabolic profile has minimum speed in (27)

$Z(z)$ - the function describing the dependence of the Fourier transformed pressure field P on z in the parabolic profile

α - a parameter describing the sound speed profile in the vicinity of a caustic (B1)
 β - a parameter describing the parabolic sound speed profile in (27)
 γ - a parameter linking the depth z and the dimensionless depth θ
 δ - a parameter characterizing the perturbation to P_0 due to diffraction, as defined by (17)
 $\Delta\phi$ - the change in the wave phase due to diffraction effects at a focusing region
 $\Delta\phi_t$ - the total phase difference due to diffraction effects accumulated over the ray path.
 $\Delta\omega$ - the spectral width of the acoustic pulse at the source
 ζ - the dimensionless depth,
 η - a parameter used in the definition of W'
 θ - the dimensionless depth as used in the normal mode expansion
 $\vec{\kappa} = \vec{\nabla}\psi$ - the dimensionless wave vector
 μ - the level of fluctuations
 ξ - the integration variable
 σ_s - the characteristic dimension of the source
 σ - the dimensionless characteristic dimension of the source
 τ - a parameter used in the definition of the ray curve
 χ - a parameter used in the definition of W'
 $\psi(\omega, r)$ - wave phase as defined by (2)
 ω_0 - the center frequency of the acoustic pulse at the source
 ω - frequency (rad/s)

Figure captions

Figure 1. The magnitude of the wave amplitude $P(r, \omega)$ as a function of range r . The maximum at $r \approx 2175$ km corresponds to a focusing region. Note many sharp features associated with $P(r, \omega)$. The values of parameters used for this calculation are: $\frac{\omega}{2\pi} = 70$ Hz, $c_0 = 1500$ m/s, $\beta = 2 \times 10^{-9} \text{ m}^{-\frac{1}{2}}$. The size of the source is $\sigma_s = 30$ m.

Figure 2. Same as Figure 1, but for a source of size $\sigma_s = 60$ m.

Figure 3. The relative change in the wave spectra $R = \frac{P}{P_0}$ due to diffraction as a function of frequency. P is the wave pressure including effects of diffraction. P_0 is the wave pressure from ray theory which ignores diffraction. The values of parameters used for this calculation are: $r = 2140$ km, $c_0 = 1500$ m/s, $\beta = 2 \times 10^{-9} \text{ m}^{-\frac{1}{2}}$. The size of the source is $\sigma_s = 30$ m.

Figure 4. Same as Figure 3, but for a source of size $\sigma_s = 60$ m. Diffraction affects the spectra at $\frac{\omega}{2\pi} \leq 70$ Hz.

Figure 5. The change in the travel time of acoustic pulses due to diffraction as a function of frequency (solid line). Solid circles are the results of a numerical experiment by *Boden et al*⁸ for 2000 km range. The values of parameters used for the solid line are: $r = 2140$ km, $c_0 = 1500$ m/s, $\beta = 2 \times 10^{-9} \text{ m}^{-\frac{1}{2}}$. The width of the source is $\sigma_s = 30$ m.

References

- ¹J. L. Spiesberger, and K. Metzger, "Basin scale ocean monitoring with acoustic thermometers," *Oceanography* **5**, 92-98 (1992).
- ²W. Munk, and C. Wunsch, "Ocean acoustic tomography: a scheme for large scale monitoring," *Deep-Sea Research* **26A**, 123-161 (1979).
- ³B. Cornuelle, C. Wunsch, D. Behringer, T. Birdsall, M. Brown, R. Heilmiller, R., Knox, K. Metzger, W. Munk, J. Spiesberger, R. Spindel, D. Webb, and P. Worcester, "Tomographic maps of the ocean mesoscale-1: pure acoustics," *J. Physical Oceanogr.* **15**, 133-152 (1985).
- ⁴B. M. Howe, "Multiple receivers in single vertical slice ocean acoustic tomography experiments," *J. Geophys. Res.*, **92**, 9479-9486 (1987).
- ⁵D. S. Ko, H. A. DeFerrari, and P. Malanotte-Rizzoli, "Acoustic tomography in the Florida Strait: temperature, current, and vorticity measurements," *J. Geophys. Res.*, **94**, 6197-6211, (1989).
- ⁶J. F. Lynch, R. C. Spindel, C-S. Chiu, J. H. Miller, and T. G. Birdsall, "Results from the 1984 marginal ice zone experiment preliminary tomography transmissions: implications for marginal ice zone, Arctic, and surface wave tomography," *J. Geophys. Res.*, **92**, 6869-6885 (1987).
- ⁷J. L. Spiesberger, E. Terray, and K. Prada, "Successful ray modelling of acoustic multipaths over a 3000 km section in the Pacific," in press, *J. Acoust. Soc. Am.* (1994).
- ⁸L. Boden, J. B. Bowlin, and J. L. Spiesberger, "Time domain analysis of normal mode, parabolic, and ray solutions of the wave equation," *J. Acoust. Soc. Am.* **90**, 954-958 (1991).
- ⁹J. L. Spiesberger, "Ocean acoustic tomography: travel time biases," *J. Acoust. Soc. Am.* **77**, 83-100 (1985).
- ¹⁰W. Munk, and C. Wunsch, "Bias in acoustic travel time through an ocean with adiabatic range-dependence," *Geophys. Astrophys. Fluid Dyn.*, **39**, 1-24 (1987).

- ¹¹E. C. Schang, and Y. Y. Wang, "The nonlinearity of modal travel time perturbation," in *Computational Acoustics - Vol. 1*, edited by R.L. Lau, D. Lee, and A.R. Robinson, (Elsevier Science Publishers B.V., New York, 1993) pp. 385-397.
- ¹²F. B. Jensen, W. A. Kuperman, M. B. Porter, and H. Schmidt, *Computational Ocean Acoustics* (American Institute of Physics, New York, 1994), 612 pp.
- ¹³A. D. Pierce, *Acoustics*, (McGraw Hill, New York, 1989), 678 pp.
- ¹⁴A. M. Plotkin, "Mode correction of a ray algorithm," *Sov. Phys. Acoust.* **38**, 583-1074 (1993).
- ¹⁵H. Jeffreys, and B. S. Jeffreys, *Methods of Mathematical Physics*, (University Press, Cambridge, 1966), 718 pp.
- ¹⁶J. A. Colosi, S. M. , Flatte, and C. Bracher, "Internal-wave effects on 1000-km oceanic acoustic pulse propagation: simulation and experiment," paper presented at the 1994 Ocean Sciences Meeting, San Diego, California, February 21-25 (1994).
- ¹⁷L. M. Brekhovskikh, and Y. P. Lysanov, *Fundamentals of Ocean Acoustics*, (Springer-Verlag, New York, 1991), 270 pp.
- ¹⁸Simmen, J., pers. comm., (1994).
- ¹⁹Handbook on Mathematical Functions, edited by M. Abramowitz, and I. Stegun, (Dover, New York, 1972) 1046 pp.

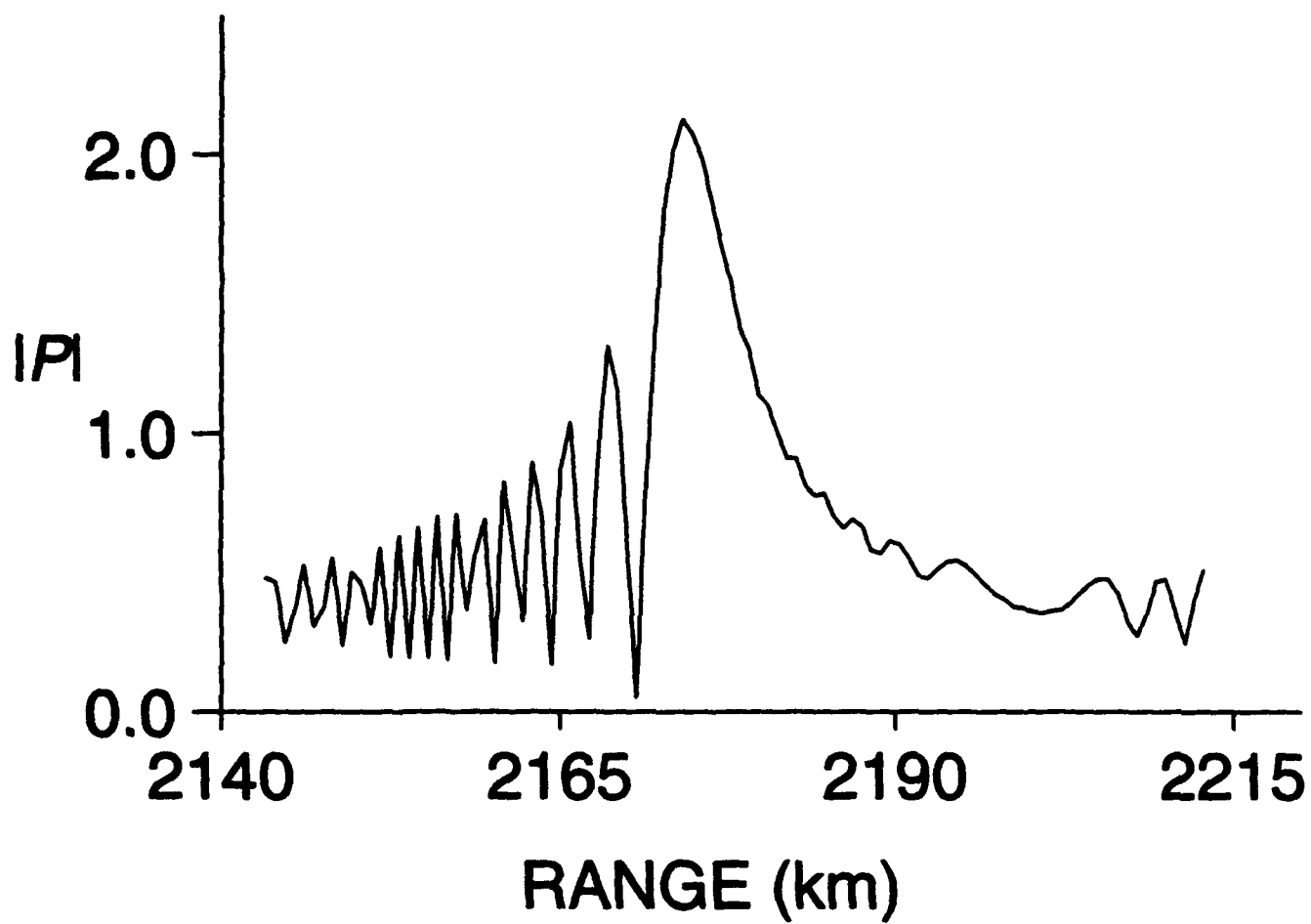


Figure 1

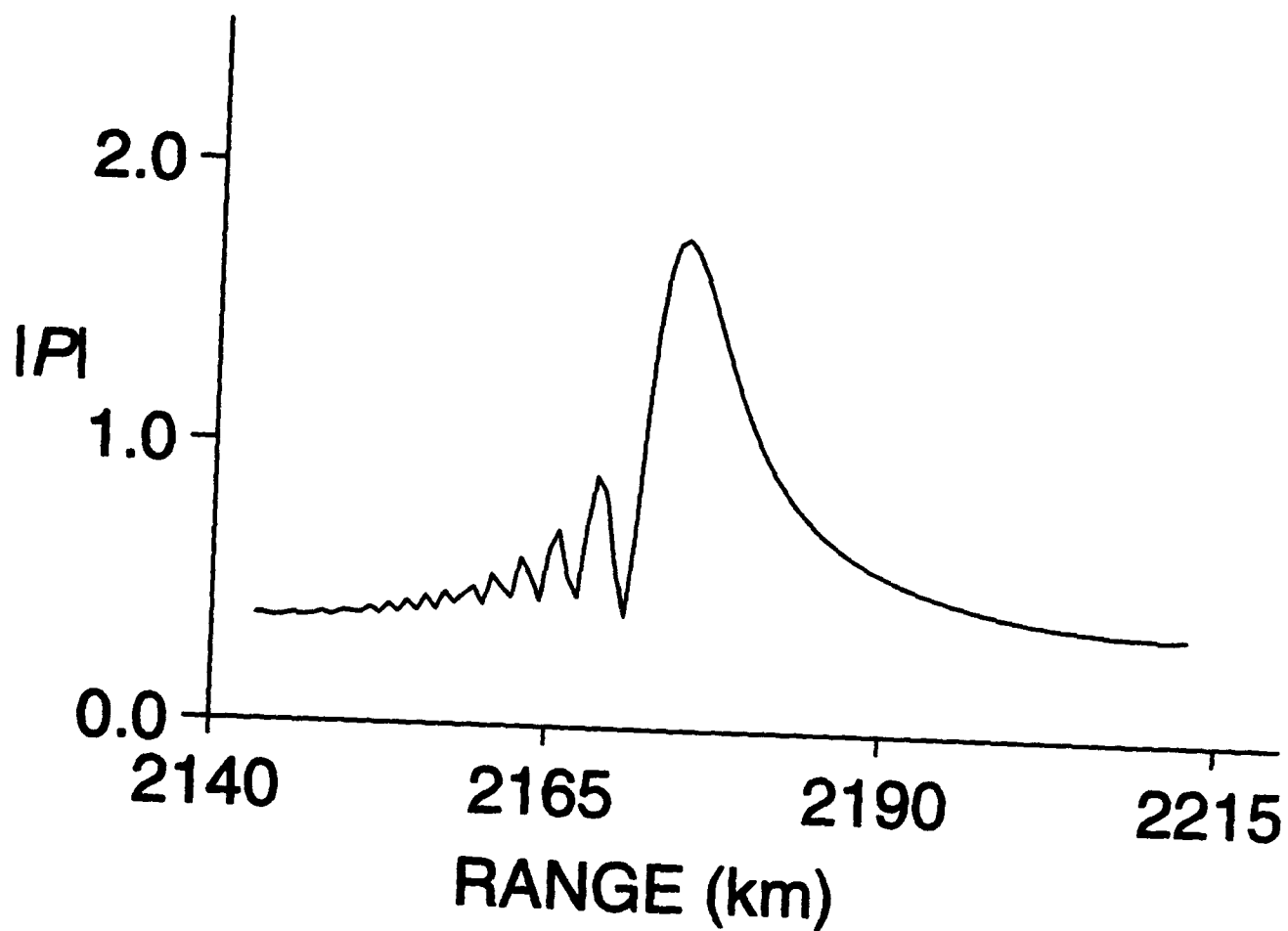


Figure 2

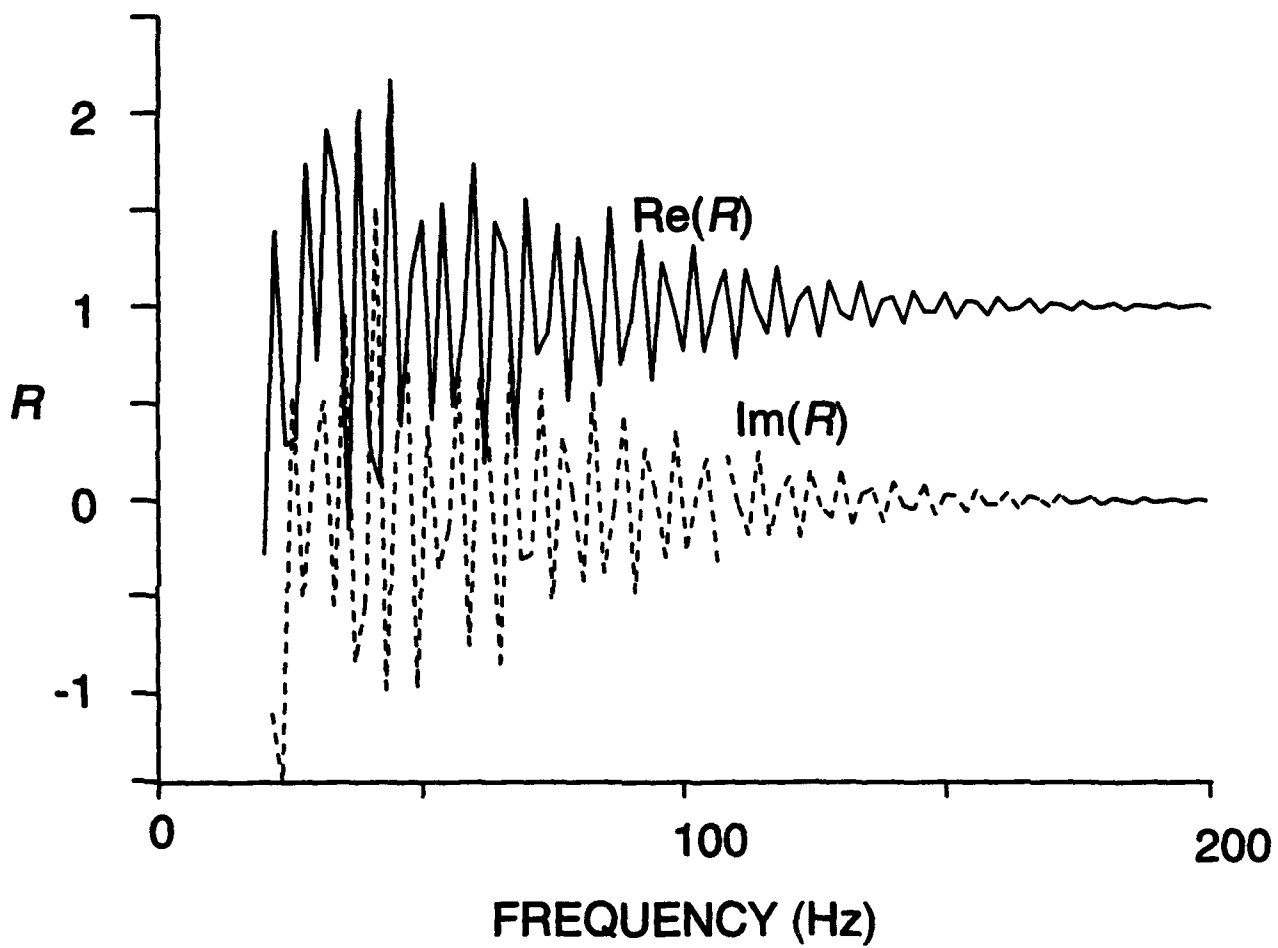


Figure 3

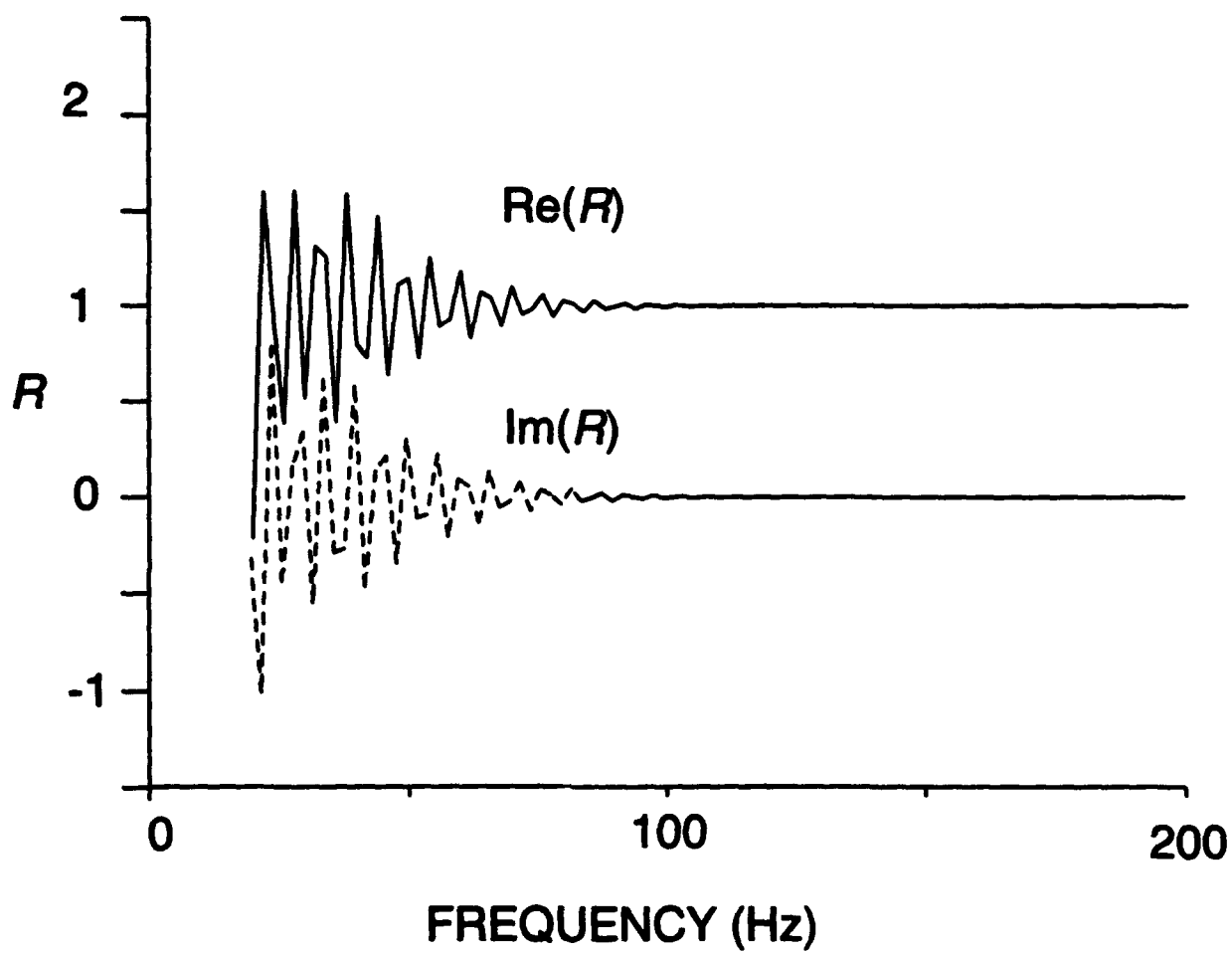


Figure 4

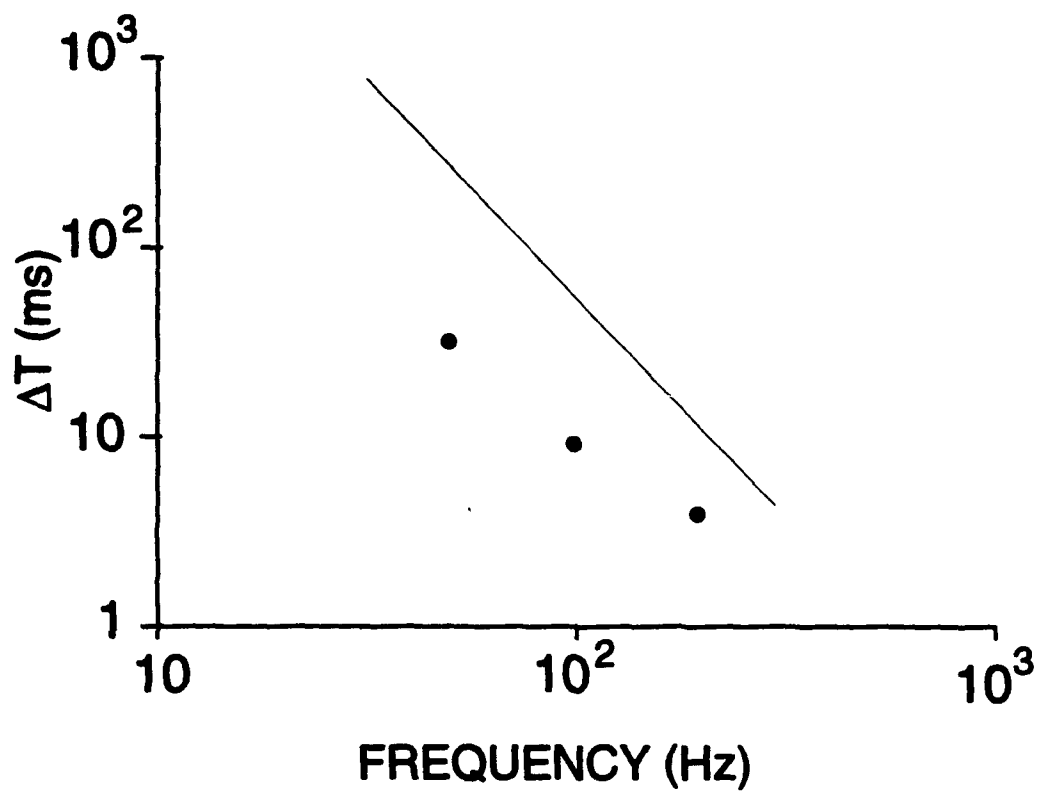


Figure 5

UTILIZATION OF ARGOS IN A SSAR DRIFTING BUOY

Bruce Einfalt
Carter Ackerman

Applied Research Laboratory
Pennsylvania State University
University Park, PA 16802

ABSTRACT

ARGOS satellite communication has been widely used as a method for transmitting environmental data. Today, many applications utilize this low-orbit, sun-synchronous satellite for ocean tracking experiments [4]. Detecting errors within the limited ARGOS bandwidth and understanding the effect of the environment and other variables on the transmitted data in a SSAR drifting buoy are key issues discussed in this paper. A design is described that utilizes the maximum bandwidth of the ARGOS satellite with minimal loss of data. Measured error rates from SSAR buoys are discussed, and strategies are presented for optimal retrieval. These strategies were developed and implemented in the GAMOT (Global Acoustic Mapping of Ocean Temperatures) program [6].

GAMOT

The characterization of ocean temperatures on a global scale can provide us with valuable insight into climate variability and global climate change [2]. In 1983, John Spiesberger demonstrated that the temperature along the travel path could be derived from the measurement of travel times of acoustic pulses across basin-scales [5]. GAMOT (Global Acoustic Mapping of Ocean Temperatures) was proposed by Spiesberger to Advanced Research Projects Agency (ARPA) as an economical and efficient way to monitor the global ocean by using autonomously moored sources and drifting receivers. The proposal was funded by the Strategic Environmental Research and Development Program (SERDP) and sponsored by ARPA.

GAMOT seeks to achieve the goal of useful ocean temperature measurements by developing an acoustic thermometer that can be deployed in the ocean. This acoustic thermometer is an instrument called the SSAR (Surface Suspended Acoustic Receiver). The SSAR is a drifting receiver in which a hydrophone is submersed at the end of a 500 meter cable beneath a freely drifting buoy (see Figure 1). The SSAR is inexpensive, battery powered, and designed to last one year [7].

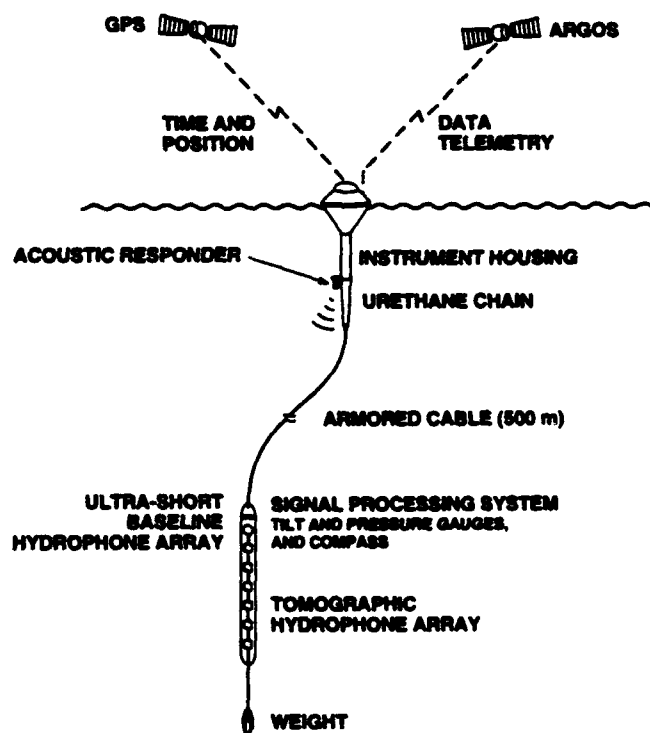


Figure 1. Surface Suspended Acoustic Receiver (SSAR) transmits compressed data to ARGOS satellites.

The SSAR determines the arrival of an acoustic signal by utilizing an acoustic database combined with the buoy position gathered from the Global Positioning Satellites (GPS). Navigation of the subsurface hydrophone array is accomplished with an ultra-short baseline acoustic navigation system. Tomography processing is performed on the received acoustic signal and is sent, along with the GPS and sensor data, to the ARGOS satellites.

Because of the amount of data that are being sent to ARGOS by the SSAR, a key issue is the effect of the environment and other variables on the transmitted data, specifically the error rates that can be expected. Another issue is the type of error control scheme that is needed to overcome these errors.

ARGOS

The ARGOS system consists of two NOAA satellites in simultaneous low-earth orbit. Each satellite receives and records, on a random-access basis, transmissions from the platforms that are visible during a pass. The recorded data are downloaded whenever a satellite passes over one of the system ground stations.

The general orbit of the satellite is polar and sun-synchronous. A summary of the ARGOS satellite characteristics is described below [4]:

• General Orbit	Circular, Polar
• Altitude	830 +/- 18 Km and 870 +/- 18 Km
• Period	Approximately 101 minutes
• Revs per Day	Approximately 14 for each satellite
• Visibility zone	5000 Km diameter footprint for a minimum elevation angle of 5 degrees.

Since ARGOS is polar-orbiting the number of daily passes over a given platform increases with latitude. At the poles, the satellite sees all platforms on each pass or 28 times a day [4].

Platforms transmit to ARGOS through a certified Platform Transmitter Terminal (PTT). Each PTT outputs a short message packet by modulating a carrier frequency. The PTT does not receive any acknowledgment from the satellite to indicate that the packet was received. Furthermore, the satellite may reject the packet due to bad signal quality, multiple PTT interference, or satellite receiver channels being unavailable [9]. The time between packets is typically set to 90 seconds for a drifting buoy and is assigned by Service Argos [4]. The maximum length of an ARGOS packet is 32 bytes (256 bits), also known as the packet data. In order to improve the probability of receiving a packet and to improve the bit error rate, ARGOS recommends that you repeat the packet. The packet is received by the satellite when the platform is in view.

BERMUDA EXPERIMENT

Two tests were performed by GAMOT researchers to monitor the operation of the SSAR and to characterize ARGOS bit errors in a SSAR buoy. These tests were conducted during a test deployment of a SSAR buoy off the coast of Bermuda (approximate position 33 N 63 E). The data that were received by ARGOS were compared with the data that were sent by the SSAR. The data consisted of approximately 120 packets or 3840 bytes per day. The transmission instrument consisted of a SmartCat PTT with a 60 second repetition rate. A GAMOT-designed patch antenna was used for the first Bermuda tests, and a Webb two foot whip antenna was used for the second test.

The first test, lasting four days, was used to gather statistics on the frequency and location of the bit errors in an ARGOS packet. This information is used to determine the type of error scheme needed by the SSAR. Each data packet used in this test contained a known data pattern. The second test, lasting over 2 months, was used to determine bit error statistics over a longer duration. Because data packets contained varying data, an 8-bit checksum was used to determine whether a bit-error occurred in the packet.

The results from both tests (see Figure 2 and Table 2) suggest that approximately 80 percent of the packets received each day did not contain any bit errors. This does not include packets rejected by the ARGOS satellite. Of important note is that in Table 1, 12.8% of the packets had 10 or more bit errors. These "burst errors" could be caused by the environment, faulty hardware, or low signal to noise during the collection of the data.

Number of Bit Errors	Percentage of ARGOS Packets
0	80.2
1	2.5
2-5	3.0
6-10	1.5
10+	12.8

Table 1. Percentage of ARGOS packets that contained bit errors during a four day drifting buoy test off the coast of Bermuda.

The data error rate can be reduced by utilizing redundancy (i.e. repeated transmissions of the same data). If Q is the probability that a packet contains one or more errors on a single reception, then the probability, P , of obtaining a packet with no bit errors in N repeated transmissions is given by:

$$P = 1 - Q^N$$

Table 2 lists P versus N for the value of $Q = 0.199$ from Table 1.

Number of Identical ARGOS Transmissions	Probability of Obtaining an Error-Free Data Packet
N	P
1	0.801
2	0.960
3	0.992
4	0.998

Table 2. Improvement in bit error rates utilizing redundant transmissions.

Figure 3 illustrates the measured location of the bit errors in an ARGOS packet. These data were gathered during the four day Bermuda test. The

results indicate that the error rate increases as a function of bit position. This means that an error in the packet is usually followed by additional errors. Sherman [9] also observed these results. The fact that more bit errors occur at the end of the packet suggests that any error control scheme should use the beginning of the packet to store vital packet information.

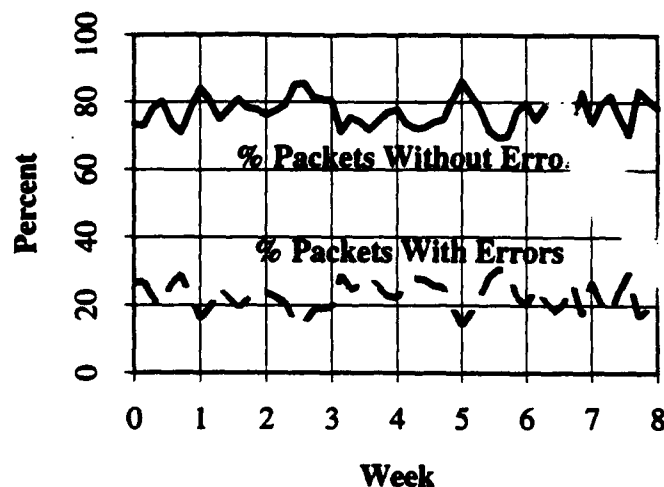


Figure 2. Daily ARGOS Packet Error Statistics taken over a two month period in Bermuda. This does not include packets rejected by the ARGOS satellite.

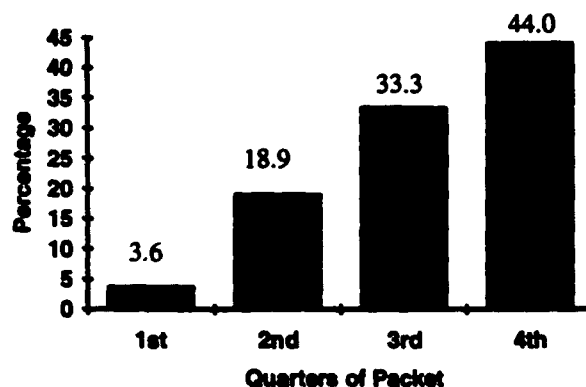


Figure 3. Location of bit error in an ARGOS packet taken from four day test using the SSAR buoy off the coast of Bermuda.

ERROR CONTROL SCHEMES

In determining the type of error control scheme to be used for the ARGOS transmission, one must characterize the errors as single bit or burst (multiple

bit) errors. It is meaningless to develop an error control scheme that can detect and correct a single bit error if the burst errors are more common. The Bermuda experiment demonstrated that the burst errors are more frequent than single random errors. This is common for satellite communication systems since transmission errors are not usually mutually independent [3].

There are two basic strategies for effectively dealing with transmission errors:

- Include enough information with each packet of data to enable the receiver to detect and correct the errors.
- Include enough information with each packet of data to enable the receiver to detect but not correct the errors.

The former strategy uses error correcting codes and the latter uses error detection.

ERROR CORRECTING

Error correcting is based on the premise that all the information about the data is stored in the packet. Additional bits are added to each data field in a packet to determine what the transmitted data must have been in an event of an error. In other words, each data field consists of d data bits and r check bits for a total length of n (i.e. $n = d + r$). This is often referred to as an n -bit code word.

The number of bit positions in which two code words differ is called the Hamming distance. If two code words are a Hamming distance h apart, it will require h single-bit errors to convert one into the other. The error correcting properties of a code word depends on its Hamming distance [1].

To correct h errors, you need a distance $2h + 1$ code because that way the legal code words are so far apart that even with h changes, the original code word is still closer than any other code word so it can be uniquely identified. For example, to correct double-bit errors, the code must have a distance of

5, or 5 additional bits added to each code word. For further reference on error correcting, see Tanenbaum, 1981 [1].

Error correcting is advantageous for data transmissions that utilize simplex communication such as ARGOS since the data are not re-transmitted or acknowledged. However, utilizing an error correcting scheme in ARGOS has a huge disadvantage due to the inability to effectively correct burst errors. Burst error correction, such as code interleaving, is available but is very costly because of the amount of additional bits required to correct an error. For example, to correct a double-bit error in an ARGOS packet would nearly double the required data space. Due to the high message drop-out rate, it is actually more effective to repeat the same message rather than attempt to perform any error correcting [9]. The huge overhead required to correct burst errors, combined with more complex processing, makes error correcting in an ARGOS packet impractical at this time.

ERROR DETECTION

Error detection is based on the premise that the sender provides enough information with each packet of data to enable the receiver to determine that an error has occurred. Error detection schemes do not provide enough information to determine where the error occurred, only that an error has occurred. The error detection is often provided through a code word that is usually stored at the beginning or end of the packet. Error detection is very popular for ARGOS applications because it is efficient and simple to implement.

The choice of an error detecting scheme depends on the error characteristics of the transmission. False detection of an error, or a missed error, often leads to incorrect results. Therefore, choosing the correct error detection scheme is a key issue for the ARGOS network designers. The most popular error detecting schemes are the arithmetic checksum and cyclic redundancy check (CRC).

The arithmetic checksum is the simplest of the error detecting schemes, but it does not trap as many errors as the CRC. The checksum is often used for networks that do not produce a lot of errors. Its function is to simply sum the data fields of size c bits in a packet, where c is commonly 8, 16, or 32 bits. The results of the summation is the check code.

The CRC method is also based on the addition of a series of bits. In this case, the added bits guarantee that the code word plus the check bits is divisible by a given polynomial. The specific division method and the polynomial used determine the type and range of transmission errors that can be detected. The problem of designing a CRC code is to find a polynomial that traps the largest class of transmission errors [3].

To determine the optimal error detecting scheme for ARGOS, tests were performed by randomly distorting 100,000 packets of 256 bits each. The missed error rates were computed and compared for 8 and 16 bit arithmetic checksums using single bit errors and burst errors. A burst error is defined as consecutive bit errors. Likewise, missed error rates were performed for 12 and 16 bit CRCs using single bit errors and burst errors. Figure 4 illustrate the results. The generator polynomials used for the CRC test are listed below. Further details about the CRC and the class of generator polynomials are found in Holtzmann, 1992 [3].

CRC Size	Generator Polynomial
12 bit	$x^{12} + x^{11} + x^2 + x^1$
16 bit	$x^{16} + x^{15} + x^2 + x^1$

The results clearly show that the CRC is superior in both the single bit and burst error tests. Similar results were also found comparing an 8-bit CRC with an 8-bit checksum (not shown). Making the CRC even more attractive is the fact that, by using look-up tables, the execution time of the CRC algorithm is nearly identical to that of the checksum. Choosing the size of the CRC depends on the amount of protection you need for your data. Due to the large number of errors seen during the

Bermuda experiment (see Table 1 and Figures 2-3), it is recommended that, at a minimum, a 12-bit CRC be utilized using the generator polynomial described earlier.

MAXIMIZING BANDWIDTH UTILIZATION

Developing a good packet design will utilize all of the available bandwidth. This is especially important when using ARGOS because of the small packet size and limited visibility. There are several simple ways to efficiently utilize available ARGOS bandwidth. The first starts with an efficient packet design. The items below provide guidelines to develop a good packet design:

- **Data** Always encode data with minimum bits. Data that requires only 4-bits should use 4-bits instead of 8 or 16 bits.
- **Error Detection** Choose minimally a 12-bit CRC stored at the beginning of the packet.
- **Packet Header** Utilize a packet header that stores a packet number, and date and time of transfer (if possible). This aids in decoding the data.
- **Repeats** Repeat packets to improve the probability of obtaining zero bit errors.
- **Multiple Id's** Use multiple platform Id's (message buffers) with a single physical PTT.
- **Transmission** For fixed platforms and to platforms moving in a limited range, transmit data when ARGOS is in view by utilizing predictable pass times [8,9].

The first step in decoding a packet involves validating the data. This is accomplished by performing a CRC on the data received and comparing it with the CRC that was sent. Duplicate packets that also have errors could use a "majority

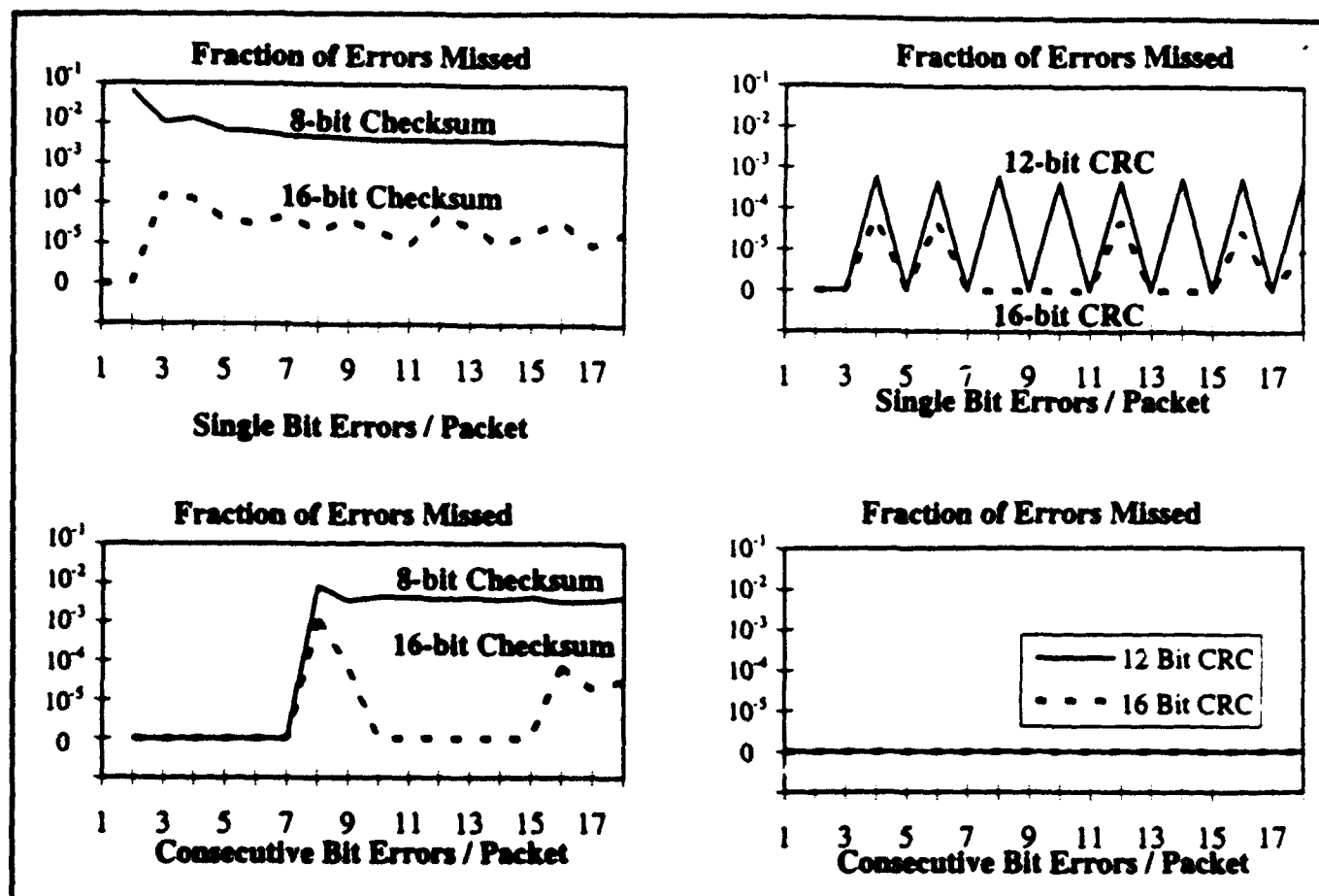


Figure 4. Comparison of arithmetic checksum and CRC for single and consecutive bit errors in an ARGOS packet. The data was simulated using 100,000 packets of 256 bits each.

rule" algorithm to retrieve some of the data fields in a packet. Under this rule, bits are used when they are common (same location and value) in each packet.

The packet number, date, and time field stored in each packet are used to group duplicate packets or identify lost packets. This is especially important when the data-repeat is delayed.

SUMMARY

This paper demonstrated the need for a good packet design when attempting to maximize throughput via ARGOS in a SSAR buoy. Tests conducted in Bermuda have shown that about 20% of the packets from ARGOS will contain bit errors. The error rate increased as a function of bit position indicating that

an error in the packet is usually followed by additional errors in the rest of the packet. The results from first Bermuda experiment indicate that 12.8% of the packets had 10 or more errors which means that errors normally occur in bursts rather than randomly.

The bit errors could be caused by the environment, faulty hardware, or bad signal quality during the collection of data. Another source of error could be due to the times when the ARGOS satellite is below the horizon or at a low elevation angle (< 5 degs). This results in packets being transmitted at large distances through the atmosphere, increasing the potential for interference.

Error correction is impractical due to the large number of burst errors and lost packets. To ensure

good error detection, an error detection algorithm, such as a 12-bit CRC, should be utilized in each packet and stored near the beginning of the packet. The CRC outperformed the checksum for both single and consecutive bit error tests on 100,000 simulated ARGOS packets. A good packet design is needed to efficiently utilize the available ARGOS bandwidth. This design should include data encoding, error detection, data repeats, and multiple PTT identifiers.

ACKNOWLEDGMENT

GAMOT is a coordinated research effort of scientists from the Applied Research Laboratory and the Meteorology Department at Penn State, the Woods Hole Oceanographic Institution, the Florida State University, the University of Alaska, the University of Texas at Austin, and the Naval Research Laboratory-Stennis. The authors would like to thank Woods Hole Oceanographic Institute, especially Dan Frye and Lee Freitag, for deploying and performing the SSAR buoy tests. The authors would also like to acknowledge the support of John Spiesberger and John Kenny of Pennsylvania State University.

REFERENCES

- [1] Andrew S. Tanenbaum, "Computer Networks", Prentice Hall, 1981.
- [2] John Spiesberger, "Inland Oceanography", *Earth & Mineral Sciences*, Vol. 62, no. 3, 1993, pp. 51-55.
- [3] G. Holtzmann, "Design and Validation of Computer Protocols", Prentice Hall Software Series, 1992.
- [4] "ARGOS System Guide", Issue 1, Service ARGOS, September 1989.
- [5] J. Spiesberger, K. Metzger, and J. Furgerson, "Listening for climatic temperature change in the northeast Pacific: 1983-1989", *Journal Acoustic Society of America*, Vol. 92, no. 1, 1992, pp. 384-396.
- [6] J. Spiesberger, D. Frye, J. O'Brien, H. Hurlburt, J. McCaffrey, M. Johnson, and J. Kenny, "Global Acoustic Mapping of Ocean Temperatures", *IEEE Oceans*, 1993, pp. 253-257.
- [7] D. Frye, L. Freitag, W. Paul, M. Grosenbaugh, and J. Spiesberger, "Surface Suspended Acoustic Receiver (SSAR) for Mapping Ocean Temperatures", *Oceanology International*, 1994.
- [8] P. Griffith, Personal Communication, March 1993.
- [9] J. Sherman, "Observations of Argos Performance", *Journal of Atmospheric and Oceanic Technology*, Vol. 9, June 1992.

New full-wave approximation for ocean acoustic travel time predictions

Frederick Tappert
Division of Applied Marine Physics
University of Miami, RSMAS
4600 Rickenbacker Causeway
Miami, FL 33149

John L. Spiesberger
Department of Meteorology and Applied Research Laboratory
512 Walker Building
Pennsylvania State University
University Park, PA 16802

Linda Boden
820 South Grant Street
Denver, CO 80209

5 July 1994

ABSTRACT

A new full-wave parabolic approximation is introduced that is valid for a wide range of grazing angles. By Fourier synthesis it yields travel times of ocean acoustic multipaths that are insensitive to a reference speed of sound. After depths and sound speeds are transformed to new coordinates, the highly efficient "split-step Fourier" algorithm is used to solve the new approximate wave equation for forward propagation. Accuracy of the new approximation has been tested by comparison to a broadband normal mode model in a range-independent environment. At 1000 km range and with a pulse of resolution 20 ms at center frequency 75 Hz, computed travel times of 24 multipaths agreed with maximum difference 3.4 ms, mean difference 0.9 ms, and rms difference 1.5 ms. This approximation may prove to be an efficient method for accurate travel time predictions of multipaths over a wide range of acoustic frequencies and for basin scale distances.

INTRODUCTION

Mapping temperatures in the global oceans with acoustic tomography requires a sufficiently accurate model for the propagation of sound waves in a reference model for the ocean. To date, tomographic methods^[1, 2, 3] have been used to map basin-wide temperatures at frequencies above 100 Hz. A reference field of sound speed is corrected by putting the difference between measured and predicted travel times of multipaths into a tomographic inverse. The predicted travel times are computed using the reference field of the speed of sound.

Previously, travel times in range dependent ocean environments have been computed with ray theory. Below about 100 Hz, however, phase errors in ray theory can accumulate to significant values at long ranges. For example, Boden et al.^[4] compared travel times of rays with delays computed from exact solutions of the wave equation. Their work represented the ocean with a smoothed profile of sound speed and no range dependence, which suppressed mesoscale structure for example. The difference in travel times between rays and exact solutions was about 0.09 seconds at 4000 km distance with center frequency of 50 Hz. The reference travel times should be as close as possible to the actual delays of pulses in the ocean so that the tomographic inverse is nearly linear.^[5]

An accurate and efficient algorithm to compute travel times for a sound speed field that depends on depth and distance between the acoustic source and receiver is required. The algorithm should be able to deal with a realistic bottom that is not flat. The algorithm would be more powerful if it does not depend on the questionable validity of the adiabatic approximation. An approach based on coupled normal modes is numerically inefficient.^[6] Parabolic approximations used to date yield travel times which are either sensitive to a reference speed of sound, or are not sufficiently accurate over a wide range of grazing angles at long distances.

We show that a new full-wave parabolic approximation has promise to compute accurate travel times without exhibiting a sensitivity to a reference speed of sound. This approximation is valid over a wide range of grazing angles, and is valid for sound speed and bottom profiles that depend on distance along an acoustic section.

I. FORWARD PROPAGATION WAVE EQUATION

Fourier synthesis is an efficient method for computing the travel time of an acoustic multipath from a full-wave solution.^[7] Thus, accurate predictions of travel time require accurate computations of the phase and amplitude for each acoustic frequency. The starting point is therefore the exact forward propagation wave equation at fixed bearing,^[8]

$$\frac{\partial \Psi}{\partial r} = ik_0 \hat{Q}(r) \Psi, \quad (1)$$

where the range dependent operator $\hat{Q}(r)$ is given by

$$\hat{Q}(r) = \sqrt{n^2(z, r) - \hat{p}^2}, \quad (2)$$

and the "momentum" operator is

$$\hat{p} = -ik_0^{-1} \partial_z. \quad (3)$$

Here c_0 is the reference sound speed, $k_0 = \omega/c_0$ is the reference wave number, $n(z, r) = c_0/c(z, r)$ is the acoustic index of refraction, $c(z, r)$ is the range dependent sound speed profile at fixed bearing, and the symbol ∂_z in the operator \hat{p} denotes the partial derivative with respect to depth z . The complex-valued acoustic field $\Psi(z, r)$ is defined by Eq.(5) below.

In the ray limit, the operator \hat{p} becomes the function $p = n \sin \theta$, where θ is the ray grazing angle. Thus small \hat{p} means small grazing angles, which is the usual situation in ocean acoustics for long range propagation. Also in the ray limit, the operator $\hat{Q}(r)$ becomes the function $Q(r) = \sqrt{(n^2 - p^2)} = n \cos \theta$. The travel time of a ray, in our notation, is given by

$$t_{\text{ray}} = \int_0^r \frac{n^2(z(r'), r')}{c_0 Q(r')} dr', \quad (4)$$

where the index of refraction $n(z, r)$ and the function $Q(r)$ are evaluated along the ray trajectory.

The full-wave acoustic pressure P at frequency $f = \omega/2\pi$ and at fixed bearing is given by,^[8]

$$P(f, z, r) = P_0(f) [rk_0 \hat{Q}(r)]^{-1/2} \Psi(z, r), \quad (5)$$

where $P_0(f)$ is the Fourier frequency representation of the transmitted signal time series. The time domain analytic signal at the receiver is obtained by Fourier synthesis as

$$\tilde{P}(t, z, r) = \int_0^\infty P(f, z, r) \exp(-i2\pi ft) df. \quad (6)$$

Many of the peaks of the function $|\tilde{P}(t)|^2$ correspond to ray multipaths, and the time at which a peak occurs yields a full-wave prediction of travel time that corresponds to t_{ray} given by Eq.(4).

The operator $k_0 \hat{Q}(r)$ may be interpreted physically as the radial (horizontal) component of wavenumber. It is easy to see that $k_0 \hat{Q}(r)$ does not depend on the reference sound speed c_0 , from which it follows that Ψ , P and \tilde{P} are also independent of c_0 . Another basic result is the conservation relation,^[8]

$$\int |\Psi|^2 dz = \text{const}, \quad (7)$$

which follows from the self-adjoint property of $\hat{Q}(r)$. This constant may be interpreted physically as proportional to the outgoing radial component of acoustical power W_r in the small constant bearing interval Δb , since Eq.(5) gives

$$\int |\Psi|^2 dz \propto r \Delta b \int P^* k_0 \hat{Q}(r) P dz \propto W_r. \quad (8)$$

Numerical solutions of Eq.(1) can in principle be obtained by a coupled mode model. The local normal modes are defined by

$$k_0 \hat{Q}(r) \phi_n = k_n(r) \phi_n, \quad (9)$$

with the orthonormality condition

$$\int \phi_n \phi_m dz = \delta_{n,m}. \quad (10)$$

The solution of Eq.(1) is then represented as

$$\Psi(z, r) = \sum_n a_n(r) \phi_n(z, r). \quad (11)$$

The following system of equations may be derived:

$$\dot{a}_n = ik_n(r)a_n + i \sum_m b_{nm}(r)a_m, \quad (12)$$

where overdots denote differentiation with respect to range r , and the mode coupling coefficients $b_{nm}(r)$ vanish if $m = n$, and if $m \neq n$ they are given by

$$b_{nm}(r) = -i \frac{k_0^2}{k_n^2 - k_m^2} \int \phi_n \frac{\partial n^2}{\partial r} \phi_m dz. \quad (13)$$

The mode coupling matrix is Hermitian (self-adjoint),

$$b_{nm}(r) = b_{mn}^*(r), \quad (14)$$

which implies from Eq.(12) that

$$\sum_n |a_n(r)|^2 = \text{const.} \quad (15)$$

This conservation relation is obviously equivalent to Eq.(7). Finally, the acoustic pressure is obtained from Eq.(5) as

$$P(f, z, r) = P_0(f) \sum_n a_n(r) \phi_n(z, r) / \sqrt{rk_n(r)}. \quad (16)$$

These coupled mode equations and relations are exact, and if Eq.(12) could be solved numerically by an accurate and efficient algorithm, then solutions of Eq.(1) could be obtained and parabolic approximations would not be needed. Unfortunately, accurate algorithms^[6] for solving Eq.(12) are inefficient, and broadband coupled mode computations are not feasible for general range dependent environments. At the present time, therefore, there is a need for better and improved parabolic approximations to Eq.(1).

II. PARABOLIC APPROXIMATIONS

The term "parabolic approximation" refers to the procedure of replacing the exact operator $\hat{Q}(r)$ with an approximate operator $\hat{Q}_a(r)$ and replacing the exact forward propagation wave equation with an approximate wave equation,^[8]

$$\frac{\partial \Psi_a}{\partial r} = ik_0 \hat{Q}_a(r) \Psi_a. \quad (17)$$

For many parabolic approximations, the highly efficient "split-step Fourier" algorithm,^[9] called the SSF algorithm in the following, may be used to solve Eq.(17). This is the primary reason for introducing such approximations.

Since $\hat{Q}_a(r)$ is not equal to $\hat{Q}(r)$, the solution $\Psi_a(z, r)$ of the approximate wave equation will not be equal to the solution $\Psi(z, r)$ of the exact wave equation, and some measure of the difference may be called the "error". Mathematical research on "operator approximations" remains in a undeveloped state, and the problem of accurately estimating the solution error in complicated range dependent environments appears to be intractable by theoretical methods. Even for benign range independent environments, the problem of estimating full-wave travel time errors due to various parabolic approximations has not yet been studied by theoretical methods. This makes the problem of obtaining a "better" parabolic approximation largely a matter of physical and mathematical intuition, to be tested by numerical computations, bearing in mind that a "better" approximation for one application may not be "good enough" for another application. The general conditions that $\hat{Q}_a(r)$ must satisfy are that it be self-adjoint, yielding a conservation relation, and that it obey the principle of reciprocity.^[7]

An operator approximation that preserves the self-adjointness of $\hat{Q}(r)$ and also preserves the c_0 -independence of $k_0\hat{Q}(r)$ was derived by Tappert.^[8] The resulting approximate wave equation is of parabolic type, and numerical solutions were later obtained using a finite difference method by Tappert and Lee.^[10] This c_0 -independent operator approximation is

$$\hat{Q}_{Ind}(r) = n - \hat{p}n^{-1}\hat{p}/2 + R, \quad (18)$$

where R is a remainder term given by

$$R = (k_0n)^{-2}(n_{zz} - n_z^2/n)/4, \quad (19)$$

where subscripts z denote partial differentiation with respect to z . This approximation is formally exact for all n , and to leading order in \hat{p} .

If n varies smoothly and slowly in depth on the scale b , and if n differs from unity by the small amount ϵ , then an order of magnitude estimate of R yields

$$R = O(\epsilon(k_0b)^{-2}). \quad (20)$$

Typically $b \approx 500$ m or more and $\epsilon \approx 0.05$ or less, which makes R negligibly small for acoustic frequencies above about 1 Hz. If $n(z, r)$ is known analytically and can be analytically differentiated, then R should be retained for greater accuracy; otherwise R should be neglected and the formally exact $\hat{Q}_{Ind}(r)$ replaced by

$$\hat{Q}_{Ind}(r) = n - \hat{p}n^{-1}\hat{p}/2. \quad (21)$$

This approximation is also self-adjoint and c_0 -independent, and will be used in what follows. The approximate wave equation is then

$$\frac{\partial \Psi_{Ind}}{\partial r} = ik_0\hat{Q}_{Ind}(r)\Psi_{Ind}. \quad (22)$$

The acoustic pressure is given by

$$P_{Ind}(f, z, r) = P_0[rk_0n(z, r)]^{-1/2}\Psi_{Ind}(z, r), \quad (23)$$

and the conservation relation becomes

$$\int |\Psi_{Ind}|^2 dz \propto r\Delta b \int k_0n(z, r)|P_{Ind}|^2 dz = \text{const.} \quad (24)$$

In order to solve this equation using the SSF algorithm, Tappert^[8] introduced the transformation (at each range r),

$$\tilde{z} = \int_0^z \sqrt{n(z', r)} dz'. \quad (25)$$

Also, the transformed index of refraction is

$$\tilde{n}(\tilde{z}, r) = n(z, r), \quad (26)$$

and the transformed wave function is

$$\tilde{\Psi}_{Ind}(\tilde{z}, r) = n^{-1/4}(z, r) \Psi_{Ind}(z, r). \quad (27)$$

With this "tilde" transformation, it was shown^[8] that

$$\hat{p} n^{-1} \hat{p} = \tilde{p}^2 + R', \quad (28)$$

where the "momentum" operator in the tilde coordinates is

$$\tilde{p} = -ik_0^{-1} \partial_{\tilde{z}}, \quad (29)$$

and the remainder term R' has the same form and order of magnitude as R and will henceforth be neglected. In tilde coordinates, the approximate operator becomes

$$\tilde{Q}_{Ind}(r) = \tilde{n}(\tilde{z}, r) - \tilde{p}^2/2, \quad (30)$$

and the approximate wave equation becomes

$$\frac{\partial \tilde{\Psi}_{Ind}}{\partial r} = ik_0 \tilde{Q}_{Ind}(r) \tilde{\Psi}_{Ind}. \quad (31)$$

The conservation relation is then

$$\int |\tilde{\Psi}_{Ind}|^2 d\tilde{z} = \text{const}, \quad (32)$$

which follows from the self-adjointness of $\tilde{Q}_{Ind}(r)$, and independently from Eq.(24) and the above tilde transformation.

The tilde transformed c_0 -independent approximate wave equation, Eq.(31) above, is tantalizingly close to, but different from, the CMOD approximation introduced by Brock, et al.^[11] The CMOD approximation uses the crude expression $\tilde{z} = \sqrt{n}z$ in place of the correct Eq.(25), does not rescale Ψ , and violates power conservation.

Numerical solutions of Eq.(31) are efficiently and easily obtained using the SSF algorithm. Implementation requires that source and receiver depths as well as the index of refraction profile be mapped into the \tilde{z} coordinate at each range step, for general range dependent environments. The extra computational work is minimal.

The above c_0 -independent approximation is valid to first order in \tilde{p}^2 , and its accuracy for steeper grazing angles (say, above 15°) is questionable, especially at long ranges due

to accumulated errors. Thomson and Chapman^[12] provided another approximation that replaces the modified standard parabolic approximation,^[8]

$$\hat{Q}_{Std}(r) = n - \hat{p}^2/2, \quad (33)$$

by the improved approximation,

$$\hat{Q}_{T-C}(r) = n + \sqrt{1 - \hat{p}^2} - 1, \quad (34)$$

that may also be written as

$$\hat{Q}_{T-C}(r) = n - \hat{p}^2/(1 + \sqrt{1 - \hat{p}^2}). \quad (35)$$

This Thomson-Chapman (T-C) approximation is exact when $n = 1$ and it is also exact when $\hat{p} = 0$. Since it reduces to the modified standard parabolic approximation for small \hat{p} to first order in \hat{p}^2 , the T-C approximation is considered an improvement for larger \hat{p} or steeper grazing angles, and a limited amount of numerical testing has confirmed this. Since it is easy to implement and is "free" when using the SSF algorithm, the T-C approximation has been nearly universally adopted as the new standard.

However, the T-C approximation depends on c_0 , and this leads to the vexing question of how to select c_0 . Since the T-C approximation is exact when both $n = 1$ and $\hat{p} = 0$, which gives $\hat{Q}(r) = \hat{Q}_{T-C}(r) = 1$, one should try to center the values of $\hat{Q}_{T-C}(r)$ as close to unity as possible in order to minimize the error. If c_0 is chosen to be the minimum sound speed, then $n \leq 1$ and Eq.(34) shows that $\hat{Q}_{T-C}(r) \leq 1$. This choice is clearly very poor because values of $\hat{Q}_{T-C}(r)$ will not be centered at unity, but will have a first order bias. The above expression for ray travel time, Eq.(4), indicates that if $\hat{Q}_{T-C}(r)$ is biased toward values that are too small, then predicted travel times will be too large, that is, later in time than they should be. Numerical results of Boden et al.^[4] and those presented below in Sect. V have confirmed this expectation.

A better way to select c_0 is to require that

$$\langle \hat{Q}_{T-C}(r) \rangle \approx 1, \quad (36)$$

where the angular brackets denote a depth average. In the small angle limit $\langle \hat{p}^2 \rangle \ll 1$, we obtain

$$c_0(r) = \langle c^{-1} \rangle^{-1}. \quad (37)$$

This harmonic average over depth is recognized to be the "fathometer correction" for depth sounders.

Although the above selection of c_0 mitigates the gross errors caused by selecting c_0 as the minimum sound speed, it does not overcome the fundamental limitation of the T-C approximation, namely, that the accuracy of results depends sensitively on c_0 . Just one value of c_0 , even though range dependent as above, is not as accurate as the c_0 -independent approximation described above that, in effect, allows c_0 to depend on depth as well as range. In the following Section, a new parabolic approximation is introduced that combines the excellent high angle capability of the T-C approximation with the excellent small angle capability of the c_0 -independent approximation.

III. NEW PARABOLIC APPROXIMATION

The c_0 -independent approximation, given by Eq.(21), is extended to steep angles by analogy to the way the T-C approximation extends the modified standard approximation, given by Eq.(33), to steep angles leading to Eq.(34). The result is the new parabolic approximation, called the c_0 -insensitive approximation,

$$\hat{Q}_{Ins}(r) = n + \sqrt{1 - \hat{p}n^{-1}\hat{p}} - 1, \quad (38)$$

that may also be written as

$$\hat{Q}_{Ins}(r) = n - \hat{p}n^{-1}\hat{p}/(1 + \sqrt{1 - \hat{p}n^{-1}\hat{p}}). \quad (39)$$

For small grazing angles (small \hat{p}), this reduces to the c_0 -independent approximation, and for steep angles it has the proper "spherical" wavefront property of the T-C approximation. Like the T-C approximation, it is exact if $n = 1$ and if $\hat{p} = 0$. Unlike the T-C approximation, it is insensitive to (but not independent of) the selected value of c_0 . The new approximate wave equation is

$$\frac{\partial \Psi_{Ins}}{\partial r} = ik_0 \hat{Q}_{Ins}(r) \Psi_{Ins}. \quad (40)$$

Implementation of this new c_0 -insensitive approximation using the SSF algorithm is done with the same tilde transformation discussed above in connection with the c_0 -independent approximation. Neglecting the small remainder terms, R and R' , as before, we obtain the following representation in the tilde coordinates,

$$\tilde{Q}_{Ins}(r) = \tilde{n} - \tilde{p}^2/(1 + \sqrt{1 - \tilde{p}^2}). \quad (41)$$

This has the same form as the $\hat{Q}_{T-C}(r)$ operator, and solutions of the approximate wave equation in the tilde representation,

$$\frac{\partial \tilde{\Psi}_{Ins}}{\partial r} = ik_0 \tilde{Q}_{Ins}(r) \tilde{\Psi}_{Ins}, \quad (42)$$

are efficiently computed with the SSF algorithm. The small extra computational work, as compared to the T-C approximation, is to compute \tilde{z} and \tilde{n} at each range step. For range independent cases, the extra computational work is practically zero.

This c_0 -insensitive approximation requires a value of c_0 at each range step. If $h(r)$ is the water depth at range r , we compute c_0 from the condition that the water depth be unchanged in the \tilde{z} coordinate. Then Eq.(25) gives

$$h(r) = \int_0^{h(r)} \sqrt{n(z, r)} dz, \quad (43)$$

which yields

$$c_0(r) = \left[\frac{1}{h(r)} \int_0^{h(r)} \frac{dz}{\sqrt{c(z, r)}} \right]^{-2}. \quad (44)$$

Writing this expression in the form of Eq.(37) gives

$$c_0(r) = \langle c^{-1/2} \rangle^{-2}. \quad (45)$$

The University of Miami PE/SSF acoustic model,^[13] called UMPE, was modified to implement the c_0 -insensitive approximation using the above formulas and the algorithms provided in the Appendix. An earlier version of this model was used to predict CW transmission loss for Porter's surface duct problem^[14] with good success.^[15] The new fully range dependent version was used to predict travel time as discussed in the next two Sections.

IV. SYNTHESIS OF TRAVEL TIMES

It is assumed that the transmitted signal is band-limited, with bandwidth B and center frequency f_c , with $f_c > B/2$. Then the desired time series at the receiver is given by the band-limited version of Eq.(6):

$$\tilde{P}(t, z, r) = \int_{f_c - B/2}^{f_c + B/2} P(f, z, r) \exp(-i2\pi ft) df. \quad (46)$$

Base-banding this Fourier transform gives

$$\tilde{P}(t, z, r) = \exp(-i2\pi f_c t) \tilde{P}_e(t, z, r), \quad (47)$$

where the envelope function is

$$\tilde{P}_e(t, z, r) = \int_{-B/2}^{B/2} P(f_c + f, z, r) \exp(-i2\pi ft) df. \quad (48)$$

Predictions of \tilde{P}_e are to be compared to a measured time series of complex demodulates at a receiver at depth z and range r , and at fixed bearing relative to the transmitter. The same formula is used to predict \tilde{P}_e when a parabolic approximation is made — one simply replaces the exact $P(f, z, r)$ by an approximate $P_a(f, z, r)$, where $P_a(f, z, r)$ is computed in terms of $\Psi_a(f, z, r)$ that satisfies an approximate forward wave equation.

Following Nghiem-Phu and Tappert,^[7] we normalize $|\tilde{P}_e|^2$ relative to the peak power at reference range $R_0 = 1$ m. At the given receiver location, we then compute and display the transmission loss time series given by

$$\tilde{TL}(t) = -10 \log(|\tilde{P}_e(t)|^2). \quad (49)$$

Peaks of this function correspond to travel times of acoustic multipaths that we want to predict as accurately and efficiently as possible.

It is also important to accurately predict the amplitudes of the peaks for the following reasons: 1) Knowledge of the amplitudes aids understanding of multipath propagation conditions and path identification for tomographic inversion; 2) It would be wasteful to spend excessive amounts of computer time to predict arrivals that have such low amplitudes that they are unobservable in a noisy background; 3) Knowledge of absolute amplitudes aids the design of experimental configurations — optimal placement of sources and receivers, optimal bandwidths and center frequencies, etc.

False peaks, or temporal sidelobes,^[7] are artifacts caused by excessively sharp or discontinuous windows in frequency space. To minimize such numerical artifacts, we use the Hann window (raised cosine) in frequency space, that goes smoothly to zero at the two end points of the passband. The first sidelobes (in time) are more than 30 dB down from the main peak, and the higher sidelobes are progressively farther down. The main peak in time of a single arrival is broadened somewhat (the effective bandwidth is only half of B), but this is a small price to pay for reducing the levels of false peaks. In addition, the Hann filter allows zero padding in frequency which gives better resolution in the time domain by Fourier interpolation. The numerical examples in the next Section make use of this technique.

If the number of frequency components used in a numerical computation is N_f and the bandwidth is B , then the width of one frequency bin is $\Delta f = B/N_f$. The period in time of the predicted time series is then $T = 1/\Delta f$, which should be chosen large enough to include all multipaths without overlap caused by "wraparound" due to periodicity. Generally T increases linearly with range, which means that N_f should also increase linearly with range. The sample interval in time is $\Delta t = T/N_f = 1/B$, which can be reduced to smaller values by Fourier interpolation using zero padding, although this does not really give more information. This is discussed further in the next Section, where numerical examples are described.

Let the method of Fourier synthesis be regarded as a numerical technique that solves a time dependent wave equation. The exact forward propagation wave equation, Eq.(1), when transformed to the time domain becomes,

$$\frac{\partial \Psi}{\partial r} = -\sqrt{\partial_t^2/c^2(z, r) + \partial_z^2} \Psi. \quad (50)$$

In principle, the solution $\Psi(t, z, r)$ could be computed by marching out in range and evaluating the partial derivatives with respect to time t by finite difference methods on a grid in time with some mesh size Δt . Obviously this method would be inefficient and would also be inaccurate unless Δt were extremely small. In contrast, the Fourier synthesis method is much more efficient and is also very accurate. This is because partial derivatives with respect to time are evaluated in the frequency domain which yields "infinite order" accuracy compared to finite difference schemes. In the frequency domain, Eq.(50) becomes

$$\frac{\partial \Psi}{\partial r} = i\sqrt{\omega^2/c^2(z, r) - \partial_z^2} \Psi, \quad (51)$$

which of course is exactly equivalent to Eq.(1). Thus this spectral method allows quite large time steps ($\Delta t = 1/B$) compared to finite difference schemes. Moreover, the time domain solution computed at these discrete times does not depend on the number of frequencies N_f used in the computation, provided that the time window T is large enough to contain all of the arrivals without overlap.

The same principle obviously applies to approximate wave equations, since they can also be written either in the frequency domain or in the time domain. For example, the co-independent parabolic approximation, which is given by Eq.(22) in the frequency domain, may be transformed into the time domain yielding

$$\frac{\partial \Psi_{Ind}}{\partial r} + \frac{1}{c} \frac{\partial \Psi_{Ind}}{\partial t} = \left(\frac{\partial}{\partial t} \right)^{-1} \frac{\partial}{\partial z} \left(c \frac{\partial \Psi_{Ind}}{\partial z} \right) / 2. \quad (52)$$

Depth (m)	Speed (km/s)	Depth (m)	Speed (km/s)
0	1.52084	800	1.47904
10	1.52066	900	1.47964
20	1.52028	1000	1.48027
30	1.51933	1100	1.48105
50	1.51244	1200	1.48189
75	1.50578	1300	1.48282
100	1.50317	1400	1.48374
125	1.50106	1500	1.48466
150	1.49831	1750	1.48746
200	1.49190	2000	1.49059
250	1.48908	2500	1.49799
300	1.48676	3000	1.50603
400	1.48214	3500	1.51442
500	1.47935	4000	1.52321
600	1.47851	4500	1.53223
700	1.47865	5000	1.54143

Table 1: Sound speed profile used in the test case

This time domain equation is efficiently solved by the Fourier synthesis technique, which also avoids the singularity of the right hand side at zero frequency ($\partial/\partial t = 0$) for band limited signals of the kind described above. Application of the finite difference technique in the time domain requires that the above equation be multiplied through by $\partial/\partial t$, yielding a linear partial differential equation of second order. The resulting equation is of hyperbolic type and has two characteristics, one of which is parasitic or spurious. For this reason, and also for efficiency, full-wave predictions of travel times should utilize the Fourier synthesis technique, and one should not even think of using the finite difference technique for such predictions.

V. NUMERICAL EXAMPLES AND COMPARISONS

Travel time is computed for the following idealized problem. The acoustic source and receiver are located near the sound channel axis over a flat lossy (fully absorbing) bottom at 5000 m depth. The speed of sound varies only with depth and not with distance along the section, and is taken from historical averages for summertime in the northeast Pacific. We use a temperature and salinity profile from Levitus^[16] and Del Grosso's sound speed formula.^[17] Tabulated values of depth and sound speed are listed in Table 1. Between these tabulated points, the sound speed is assumed to vary linearly with depth. For this profile, the minimum sound speed occurs at 600 m depth. Seawater absorption effects and earth curvature effects are neglected. To complete the specification of the problem, the center frequency is 75 Hz and the bandwidth is $B = 50$ Hz.

For this range independent problem, the reference prediction of travel time is computed using a normal mode model, which in principle solves the exact forward propagation wave

equation. We use the KRAKEN normal mode model developed by Porter,^[18] and the Fourier synthesis described in Sect. IV.

The new c_0 -insensitive parabolic approximation is implemented with the UMPE model as described above. Two broadband runs are made to the range 1000 km for source depths 600 m, on the axis, and 400 m. Fourier synthesis gives the wave fronts displayed in Fig.(1). The wave-equation-solving UMPE model automatically computes the data needed for these plots at each mesh point in depth with no extra computational burden.

The early arrivals seen in Fig.(1) are ray-like and correspond to steeper grazing angles. They occur in groups of four, except for a receiver at the same depth as the source in which case each group consists of three arrivals, the middle one being a doublet. We use a ray model to estimate the launch angles of these multipaths, and find that the first group of rays are inclined at about 15° with respect to horizontal. The late cluster of arrivals having a duration about 0.4 s correspond to near axial ray paths having shallow grazing angles. This cluster contains a large number of unresolved multipaths, and the peaks seen in Fig.(1) at late times represent a complicated full-wave description of multipath interference and caustics that would be difficult to predict with a ray model. In fact, these late arrivals clearly resemble normal modes of low order, with white spaces demarking the nulls of successive normal modes.

Frequency domain data are interpolated in depth to five selected receiver depths, and Fourier synthesis is used to compute the band-limited pulse response functions at these five depths. The results are shown in Fig.(2) for the 600 m source depth, and in Fig.(3) for the 400 m source depth. These computed pulse response functions are readily interpreted as horizontal slices of the wavefronts shown in Fig.(1). Of the ten pulse response functions shown in Figs.(2) and (3), nine are distinctly different and two are the same, namely, Fig.(2a) and Fig.(3c). Overlays show that these two pulse response functions are identical to within the resolution of the plots. This confirms that the broadband UMPE model is accurately reciprocal.

These runs with UMPE use a transform size in depth of $N_d = 1024$ and a range step of 400 m, for all frequencies ($N_f = 256$). Thus the UMPE runs have period $T = 5.12$ s, and resolution $\Delta t = 20$ ms, that is reduced to 10 ms by zero padding. Each run uses about 50 minutes of CPU time on a desktop computer: a DEC Alpha 3000/600S, or a Sun SparcStation 10 having one processor. This is about 4.5 times slower than real time. One must remember, however, that the broadband run time increases quadratically with increasing range since both the number of frequencies and the number of range steps increase linearly with range, for fixed bandwidth. Thus broadband runs to truly global ranges are considerably slower than real time on current desktop computers.

To determine the absolute accuracy of the new c_0 -insensitive parabolic approximation, we consider the pulse response function shown in Fig.(2c), where both the source and receiver were on the axis at depth 600 m and separated by 1000 km in range. An overlay comparison with the corresponding pulse response function computed with the KRAKEN normal mode model showed no discernable difference for the dynamic range plotted (40 dB). We therefore developed a "peak finding routine", using three point quadratic interpolation, that automatically computes values of transmission loss and corresponding travel times of all peaks that are down less than 30 dB from the highest peak.

Both acoustic models give twenty four peaks that can be seen in Fig.(2c). The first

Peak #	KRAKEN		NEW UMPE			
	Time(s)	TL(dB)	Time(s)	Time(ms)	TL(dB)	TL(dB)
1	672.4944	120.3	672.4929	(-1.5)	121.9	(1.6)
2	672.6941	112.2	672.6923	(-1.8)	112.8	(0.6)
3	672.8913	117.1	672.8890	(-2.3)	117.4	(0.3)
4	673.6713	116.7	673.6696	(-1.7)	117.1	(0.4)
5	673.8334	109.3	673.8316	(-1.8)	109.7	(0.4)
6	673.9897	115.7	673.9877	(-2.0)	116.0	(0.3)
7	674.5263	115.8	674.5255	(-0.8)	116.1	(0.3)
8	674.6547	109.1	674.6537	(-1.0)	109.4	(0.3)
9	674.7791	114.6	674.7773	(-1.8)	114.9	(0.3)
10	675.1134	117.7	675.1124	(-1.0)	117.9	(0.2)
11	675.2044	111.4	675.2035	(-0.9)	111.6	(0.2)
12	675.2941	116.8	675.2927	(-1.4)	117.1	(0.3)
13	675.5475	114.5	675.5468	(-0.7)	114.7	(0.2)
14	675.6216	108.0	675.6208	(-0.8)	108.2	(0.2)
15	675.6900	115.7	675.6896	(-0.4)	116.3	(0.6)
16	675.8059	116.0	675.8049	(-1.0)	116.0	(0.0)
17	675.8434	110.1	675.8438	(0.4)	109.8	(-0.3)
18	675.8834	117.6	675.8831	(-0.3)	117.4	(-0.2)
19	675.9934	104.4	675.9921	(-1.3)	104.5	(0.1)
20	676.0909	113.1	676.0875	(-3.4)	113.2	(0.1)
21	676.1619	104.3	676.1624	(0.5)	104.3	(0.0)
22	676.2191	110.5	676.2209	(1.8)	110.5	(0.0)
23	676.2609	119.2	676.2635	(2.6)	117.8	(-1.4)
24	676.3266	96.1	676.3255	(-1.1)	96.0	(-0.1)

Table 2: Interpolated values at peaks with differences in parentheses, for a source depth of 600 m, a receiver depth of 600 m, and a separation of 1000 km.

eighteen peaks occur in six groups of three that correspond to ray-like arrivals. The last six peaks correspond to interference of unresolved ray multipaths or to low order normal modes arrivals. Interpolated values of travel time in seconds and TL in units of dB re 1 m of these twenty four peaks are listed in Table 2. Differences between the two models are listed in parentheses with travel time differences in milliseconds.

From the values listed in Table 2, the mean travel time difference of the twenty four peaks is -0.9 ms, with UMPE predicting slightly earlier travel times on the average. The rms travel time difference is 1.5 ms. The mean amplitude difference is 0.2 dB, with UMPE predicting slightly smaller amplitudes, or greater transmission loss, on the average. The rms amplitude difference is 0.5 dB. Both the KRAKEN and UMPE models contain numerical errors due to truncation and round-off that may account for some of this difference. Thus the accuracy of the new c_0 -insensitive parabolic approximation may be good enough to satisfy the requirements for long range acoustic tomography.

In order to ensure numerical convergence of the UMPE model, the computational mesh is refined by halving the range step to 200 m and doubling the transform size in depth to 2048. Again halving the range step to 100 m, no change in travel time is found to the reported precision of 0.1 ms, and no change of amplitude is found to the reported precision of 0.1 dB. The values given in Table 2 for the UMPE model were obtained from the fully converged run. For the courser mesh values used to produce the figures and for which run times were reported above, travel time differences increased by about an additional ms on the average. The resulting travel time predictions are still within the accuracy limitations imposed by knowledge of the ocean environment.

It is instructive to compare the travel time of the last peak ($t = 676.326$ s, from Table 2) to that predicted by a ray model. For this axis-to-axis propagation problem, there is one eigenray that travels directly down the axis of the sound channel with the axial sound speed ($c_a = 1578.51$ m/s, from Table 1). At range 1000 km, the predicted travel time of the axial ray is $t = 676.357$ s, which is 31 ms greater than the full-wave prediction. Evidently, the last peak predicted by the full-wave models corresponds to the lowest normal mode that has a group speed greater than the axial sound speed. In fact, the inferred group speed is 1478.58 m/s, which is slightly greater than the axial sound speed.

We briefly studied sensitivity of the full-wave UMPE model predictions of travel time to small changes of the sound speed profile caused by smoothing the profile. Instead of assuming that the sound speed is piecewise linear as above, we employ the traditional smoothing filter applied to the fine PE mesh after interpolating values of sound speed between tabulated points. One iteration of this smoothing filter applies a running average of three neighboring mesh points with 1-2-1 relative weights. A second iteration gives a running average of five neighboring mesh points with 1-4-6-4-1 relative weights, and so forth. The effect of this low-pass "Pascal" filter is to increase values of sound speed near the minimum at the sound channel axis and to decrease them far away from the axis. Two iterations of this filter, the traditional UMPE default, gives a maximum change of sound speed on the PE mesh less than 0.02 m/s near the axis and much less farther away. This is well within the uncertainty of sound speed profile measurements.

An UMPE model run to range 1000 km with this smoothed profile, displayed in Fig. (4), is compared to an identical run with the unsmoothed profile, displayed in Fig. (2). For the receiver depth of 600 m, twenty two of the twenty four peaks are found to correspond;

one peak disappears and one new peak appears. Travel time differences of the twenty two corresponding peaks varied up to about ± 2 ms, with later peaks arriving predictably earlier and early peaks arriving predictably later. Since the smoothed profile is just as good if not better than the unsmoothed profile as a representation of the measured data, we conclude that it is futile to try to predict travel times with accuracy better than a few milliseconds to range 1000 km in the frequency band between 50 Hz and 100 Hz.

Possible errors introduced by the new c_0 -insensitive parabolic approximation certainly fall within this tolerance envelope. Thus the accuracy of travel time predictions made by the new UMPE acoustic model are limited by the accuracy and resolution of the environmental data that are put into the model, and not by possible errors introduced by the new parabolic approximation.

In order to demonstrate the efficiency, stability and robustness of the new broadband UMPE model, we make runs for the test case to ranges 2000 km, 4000 km, and 8000 km. In all cases the transform size in depth is $N_d = 1024$ and the range step is 400 m. For range 2000 km, the number of frequencies is doubled to $N_f = 512$; for range 4000 km, this is doubled again to $N_f = 1024$; and for range 8000 km, we use $N_f = 2048$. In all cases, the plots of pulse response functions are very "clean" down to more than 50 dB below the largest peak. For example, Fig. (5) displays the wavefronts produced by UMPE for range 4000 km and source depth of 600 m. No signs of numerical noise or "incoherence" are observed, in contrast to the report of Boden et al.^[4] for the same case. It appears that the "Navy Standard" PE model used by Boden et al.^[4] is not only inaccurate but also has other defects that cause the "incoherence" observed with that model.

Wavefronts of the UMPE run to range 8000 km (source depth 600 m) are shown in Fig.(6), and pulse response functions at five receiver depths are shown in Fig.(7). Travel times are seen to spread over thirty seconds with more than 150 clearly resolvable peaks. Early arrivals are again seen to be ray-like, while late arrivals are definitely mode-like. This run to range 8000 km requires about 52 hours of CPU time on the desktop computers mentioned above.

VI. DISCUSSION

A new parabolic approximation provides pulse responses computed with smooth sound speed profiles that are within a few milliseconds of the delays computed with an exact solution of the wave equation over a 1000 km section of the ocean for pulses centered at 75 Hz having a time resolution of 20 ms. The accuracy of the new parabolic approximation stems from the fact that, unlike other parabolic approximations, it is insensitive to a reference speed of sound and it is insensitive to the launch angles of acoustic multipaths from the source. In particular, the fact that the new operator approximation includes the second order "cross term", neglected in the T-C approximation, that combines the two first order operators, \hat{p}^2 and $n(z, r) - 1$, leads to the observed improvement in accuracy of predicted travel time. The new approximation obeys reciprocity and conserves energy.

The limits of accuracy of the new parabolic approximation need to be examined further. If the time delays and amplitudes are accurate for other acoustic frequencies and for longer distances of propagation through sound speed fields that also depend on range due to mesoscale structure for example, then this new model may be an effective method for computing finite frequency solutions of the wave equation for realistic oceanic conditions. The

new approximation, like other parabolic approximations, does not assume that the acoustic propagation be adiabatic. It may be applied to oceans with rough surfaces and uneven and lossy bottoms over a wide range of acoustic frequencies.

ACKNOWLEDGMENTS

This research was supported the Advanced Research Projects Agency grant MDA972-93-1-0004, managed by Dr. Ralph Alewine, the Strategic Environmental Research Development Program, managed by Dr. John Harrison, and by the Office of Naval Research grant N00014-93-1-0434. We thank Michael A. Wolfson for helpful assistance with numerical computations.

APPENDIX. IMPLEMENTATION ALGORITHMS

Explicit algorithms that were used to implement the tilde transformation are given in this appendix. At each of a set of ranges, $r = r_l$, the sound speed profile is given as a table containing the pairs (z_j, c_j) , $j = 1, \dots, N_s$. The depths z_j are constrained by $z_1 = 0$, $z_{j+1} > z_j$ and $z_{N_s} = h(r_l)$, where $h(r_l)$ is the water depth at range r_l . Also, N_s may depend on l . There is no constraint on the corresponding sound speeds c_j , except of course that they must be positive. The UMPE model, unlike many normal mode and ray-based models, has no difficulty with very complicated sound speed profiles. This has been a traditional strength of acoustic models based on parabolic approximations.

From Eq.(25), assuming that $c(z)$ is piece-wise linear between tabular points, we obtain

$$\tilde{z}_j = 2\sqrt{c_0} \sum_{i=2}^j (\sqrt{c_i} - \sqrt{c_{i-1}})(z_i - z_{i-1}) / (c_i - c_{i-1}). \quad (53)$$

Since this formula is singular if $c_i = c_{i-1}$, it is better to write it as

$$\tilde{z}_j = 2\sqrt{c_0} \sum_{i=2}^j (z_i - z_{i-1}) / (\sqrt{c_i} + \sqrt{c_{i-1}}), \quad (54)$$

that cannot be singular. A recursion formula is $\tilde{z}_1 = 0$, and

$$\tilde{z}_j = \tilde{z}_{j-1} + 2\sqrt{c_0}(z_j - z_{j-1}) / (\sqrt{c_j} + \sqrt{c_{j-1}}), \quad j = 2, \dots, N_s. \quad (55)$$

The reference sound speed at range r_l is computed from the condition that $\tilde{z}_{N_s} = h(r_l)$. This yields

$$c_0(r_l) = \left[\frac{2}{h(r_l)} \sum_{i=2}^{N_s} (z_i - z_{i-1}) / (\sqrt{c_i} + \sqrt{c_{i-1}}) \right]^{-2}. \quad (56)$$

The tilde transformation is completed by specifying

$$\tilde{c}_j = c_j. \quad (57)$$

Thus at each of the ranges r_l , we compute $c_0(r_l)$ and then construct the new table $(\tilde{z}_j, \tilde{c}_j)$.

Next we transform source and receiver depths. We do this by computing \tilde{z} that corresponds to the given z at each each range r_l and then linearly interpolating in range between

the two nearest ranges where the tabulated profiles are given. Suppose that $z_{j-1} \leq z < z_j$. Define the fraction

$$f_r = (z - z_{j-1}) / (z_j - z_{j-1}). \quad (58)$$

We then compute

$$\tilde{z} = \tilde{z}_{j-1} + (\sqrt{c_j} + \sqrt{c_{j-1}}) f_r (\tilde{z}_j - \tilde{z}_{j-1}) / (\sqrt{u_j} + \sqrt{c_{j-1}}), \quad (59)$$

where

$$u_j = f_r c_j + (1 - f_r) c_{j-1}. \quad (60)$$

Next we need to interpolate $\tilde{c}(\tilde{z})$ onto the PE mesh at each range r_l . We use the traditional staggered mesh:

$$\tilde{z}_k = (k - .5) \Delta z, \quad k = 1, 2, \dots, N_d/2, \quad (61)$$

where N_d is the total number of points in the DFT, and the other $N_d/2$ points are in the image that is used to satisfy the surface boundary condition. We want to compute

$$\tilde{c}_k = \tilde{c}(\tilde{z}_k) = c(z_k). \quad (62)$$

Suppose that

$$\tilde{z}_{j-1} \leq \tilde{z}_k < \tilde{z}_j. \quad (63)$$

Then

$$z_{j-1} \leq z_k < z_j. \quad (64)$$

Define the fraction

$$f_k = (\tilde{z}_k - \tilde{z}_{j-1}) / (\tilde{z}_j - \tilde{z}_{j-1}). \quad (65)$$

This quantity is known, and we invert the above mapping from z to \tilde{z} to obtain z_k and then $c(z_k) = \tilde{c}(\tilde{z}_k)$. The result is

$$\tilde{c}_k(r_l) = \tilde{c}_{j-1} + g_k (\tilde{c}_j - \tilde{c}_{j-1}), \quad (66)$$

where the fraction g_k is given in terms of the fraction f_k by

$$g_k = \frac{f_k}{\sqrt{c_j} + \sqrt{c_{j-1}}} [2\sqrt{c_{j-1}} + (\sqrt{c_j} - \sqrt{c_{j-1}}) f_k]. \quad (67)$$

It is amusing to note that the tilde transform requires that $\tilde{c}(\tilde{z})$ varies quadratically between tabular points if it is assumed that $c(z)$ varies linearly between tabular points.

Finally, we need to compute the transformed sound speeds on the fine PE mesh at range r , where $r_{l-1} \leq r < r_l$. We use the traditional linear interpolation in range at fixed depth. Define the fraction

$$f_v = (r - r_{l-1}) / (r_l - r_{l-1}). \quad (68)$$

Then we compute

$$\tilde{c}_k(r) = \tilde{c}_k(r_{l-1}) + f_v [\tilde{c}_k(r_l) - \tilde{c}_k(r_{l-1})], \quad k = 1, \dots, N_s/2. \quad (69)$$

Also the reference sound speed at range r is computed as

$$c_0(r) = c_0(r_{l-1}) + f_v [c_0(r_l) - c_0(r_{l-1})], \quad (70)$$

and the receiver depths at range r are computed as

$$\tilde{z}(r) = \tilde{z}(r_{l-1}) + f_v[\tilde{z}(r_l) - \tilde{z}(r_{l-1})]. \quad (71)$$

These algorithms have been implemented in the UMPE model. This model efficiently computes full-wave c_0 -insensitive predictions of travel times for long range propagation in very complicated range dependent environments.

References

- [1] W. Munk and C. Wunsch, "Ocean acoustic tomography: a scheme for large scale monitoring," *Deep-Sea Res.* **26**, 123-161 (1979).
- [2] J. L. Spiesberger and K. Metzger, "Basin-scale tomography: a new tool for studying weather and climate," *J. Geophys. Res.* **96**, 4869-4889 (1991).
- [3] J. L. Spiesberger, E. Terray, and K. Prada, "Successful ray modeling of acoustic multipaths over a 3000-km section in the Pacific," *J. Acoust. Soc. Am.* **95**, 3654-3657 (1994).
- [4] L. Boden, J.B. Bowlin, and J.L. Spiesberger, "Time domain analysis of normal mode, parabolic, and ray solutions of the wave equation," *J. Acoust. Soc. Am.* **90**, 954-958 (1991).
- [5] J. L. Spiesberger, K. Metzger, and J. A. Furgerson, "Listening for climatic temperature change in the northeast Pacific: 1983-1989," *J. Acoust. Soc. Amer.* **92**, 384-396 (1992).
- [6] L. B. Dozier and F. D. Tappert, "Statistics of normal mode amplitudes in a random ocean. II. Computations," *J. Acoust. Soc. Am.* **64**, 533-547 (1978).
- [7] Lan Nghiêm-Phu and Frederick Tappert, "Modeling of reciprocity in the time domain using the parabolic equation method," *J. Acoust. Soc. Am.* **78**, 164-171 (1985).
- [8] F. D. Tappert, "The parabolic approximation method," in *Wave Propagation and Underwater Acoustics*, Lecture Notes in Physics, Vol. 70, edited by J. B. Keller and J. S. Papadakis (Springer-Verlag, New York, 1977), Chap. V, pp. 224-287.
- [9] F. D. Tappert and R. H. Hardin, "Computer simulation of long-range ocean acoustic propagation using the parabolic equation method," in *Proc. 8th Intern. Cong. on Acoustics* (Goldcrest, London, 1974), Vol. 2, p. 452.
- [10] Frederick D. Tappert and Ding Lee, "A range refraction parabolic equation," *J. Acoust. Soc. Am.* **76**, 1797-1803 (1984).
- [11] H. K. Brock, R. N. Buchal, and C. W. Spofford, "Modifying the sound speed profile to improve the accuracy of the parabolic equation method," *J. Acoust. Soc. Am.* **62**, 543-552 (1977).

- [12] D. J. Thomson and N. R. Chapman, "A wide-angle split step algorithm for the parabolic equation," *J. Acoust. Soc. Am.* **74**, 1848-1854 (1983).
- [13] Kevin B. Smith and Frederick D. Tappert, "UMPE: The University of Miami Parabolic Equation Model, Version 1.0," *MPL Technical Memorandum* **432**, May 1993.
- [14] M. B. Porter and F. B. Jensen, "Anomalous parabolic equation results for propagation in leaky surface ducts," *J. Acoust. Soc. Am.* **94**, 1510-1516 (1993).
- [15] Lan Nghiem-Phu, Kevin B. Smith, and Fred D. Tappert, "FastPE, SlowPE, YourPE, MiPE: What are the real issues?," in *PE WORKSHOP II: Proceedings of the Second Parabolic Equation Workshop*, edited by S. A. Chin-Bing, D. B. King, J. A. Davis, and R. B. Evans (Naval Research Laboratory, Stennis Space Center, 1993), pp. 249-264.
- [16] S. Levitus, "Climatological atlas of the world ocean," NOAA Prof. Pap. **13**, (U.S. Government Printing Office, Washington, DC, 1982).
- [17] V. A. Del Grosso, "New equation for the speed of sound in natural waters (with comparisons to other equations)," *J. Acoust. Soc. Am.* **56**, 1084-1091 (1974).
- [18] Michael Porter, "The KRAKEN normal mode program," *SACLANTCEN Memorandum SM-245*, September 1991.

FIGURE CAPTIONS

FIG. 1. The wavefront at range 1000 km computed with the new UMPE model for: A) a source depth of 600 m; and B) a source depth of 400 m. The greyscale is TL between 90 dB (black) and 140 dB (white).

FIG. 2. The pulse response function at range 1000 km computed with the new UMPE model for a source depth of 600 m and a receiver depth of: a) 400m; b) 500 m; c) 600 m; d) 800 m; and e) 1000 m.

FIG. 3. The pulse response function at range 1000 km computed with the new UMPE model for a source depth of 400 m and a receiver depth of: a) 400m; b) 500 m; c) 600 m; d) 800 m; and e) 1000 m.

FIG. 4. The pulse response function at range 1000 km computed with the new UMPE model using a slightly smoothed profile for a source depth of 600 m and a receiver depth of: a) 400m; b) 500 m; c) 600 m; d) 800 m; and e) 1000 m.

FIG. 5. The wavefront at range 4000 km computed with the new UMPE model for source depth of 600 m. The greyscale is TL between 100 dB (black) and 150 dB (white).

FIG. 6. The wavefront at range 8000 km computed with the new UMPE model for source depth of 600 m. The greyscale is TL between 100 dB (black) and 150 dB (white).

FIG. 7. The pulse response function at range 8000 km computed with the new UMPE model for a source depth of 600 m and a receiver depth of: a) 400m; b) 500 m; c) 600 m; d) 800 m; and e) 1000 m.

Fig.(1)

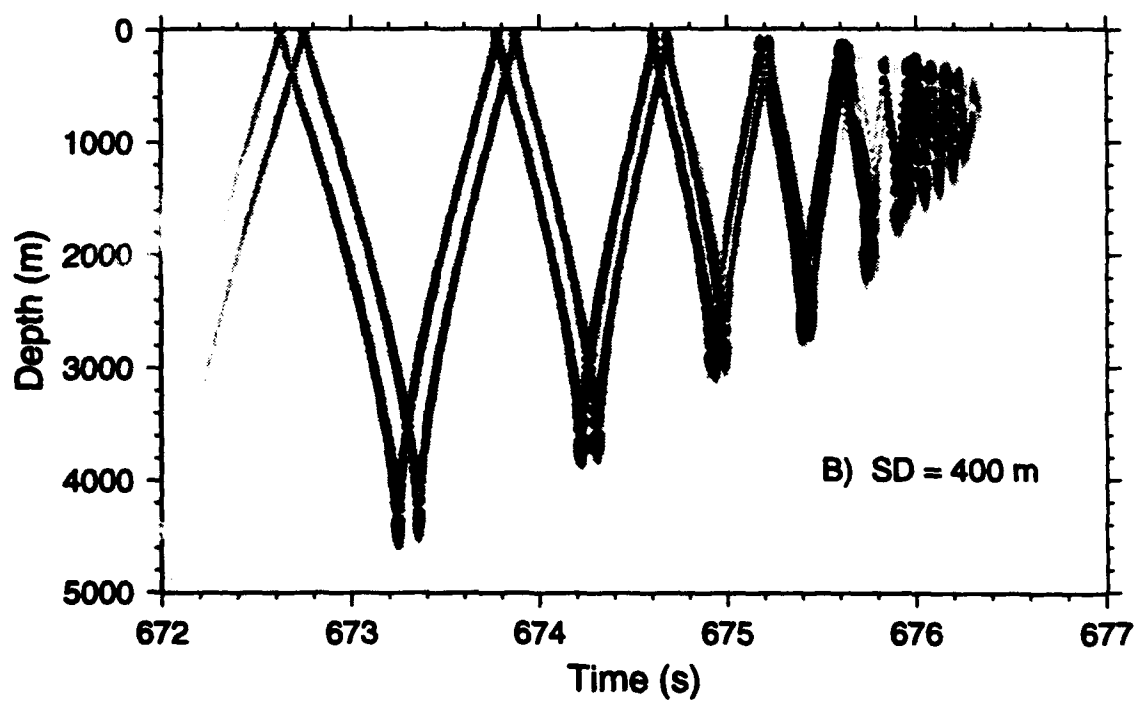
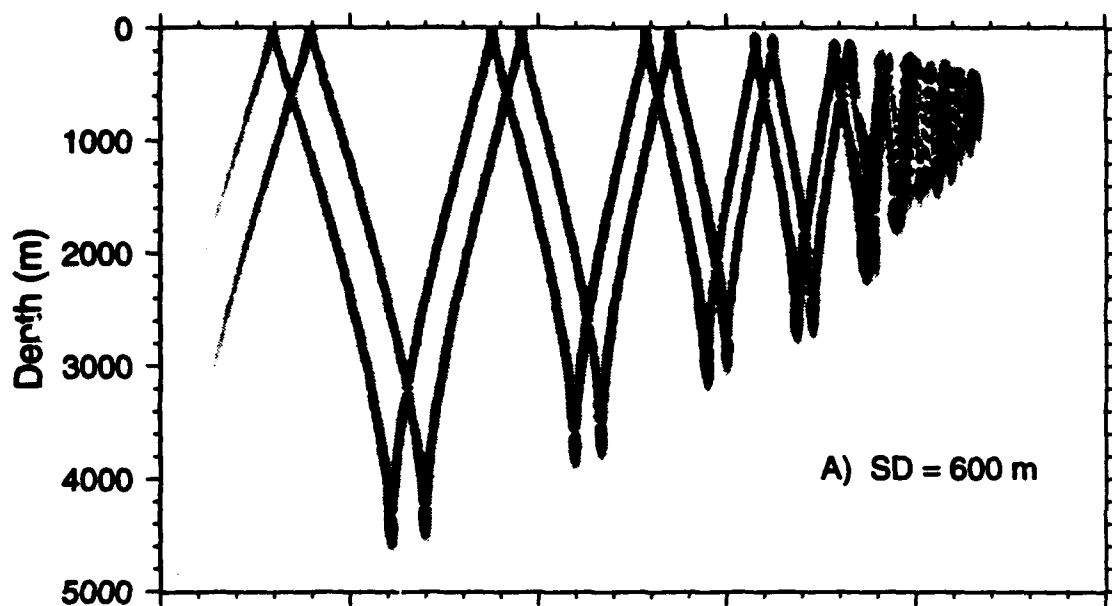


Fig (2)

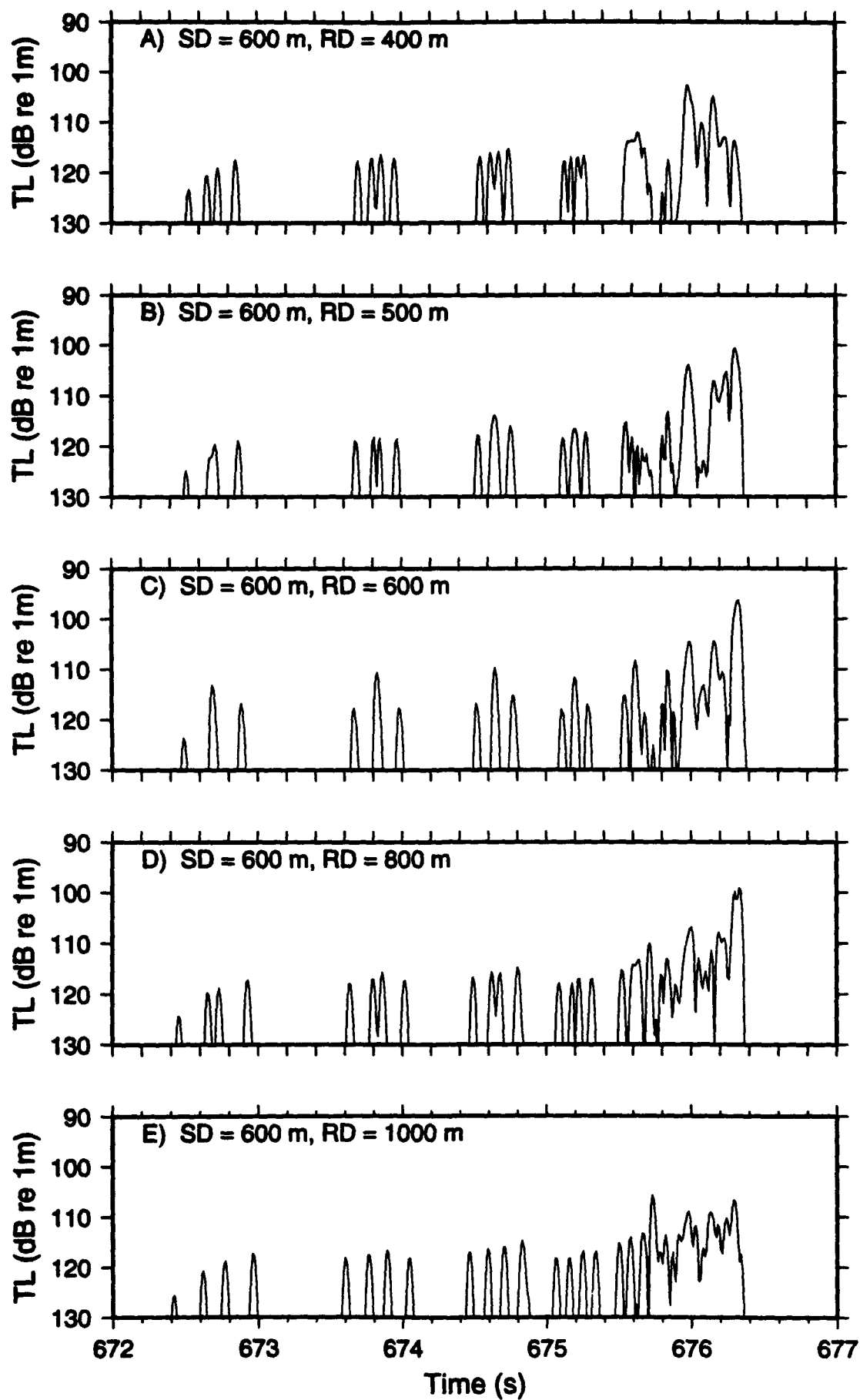


Fig. (3)

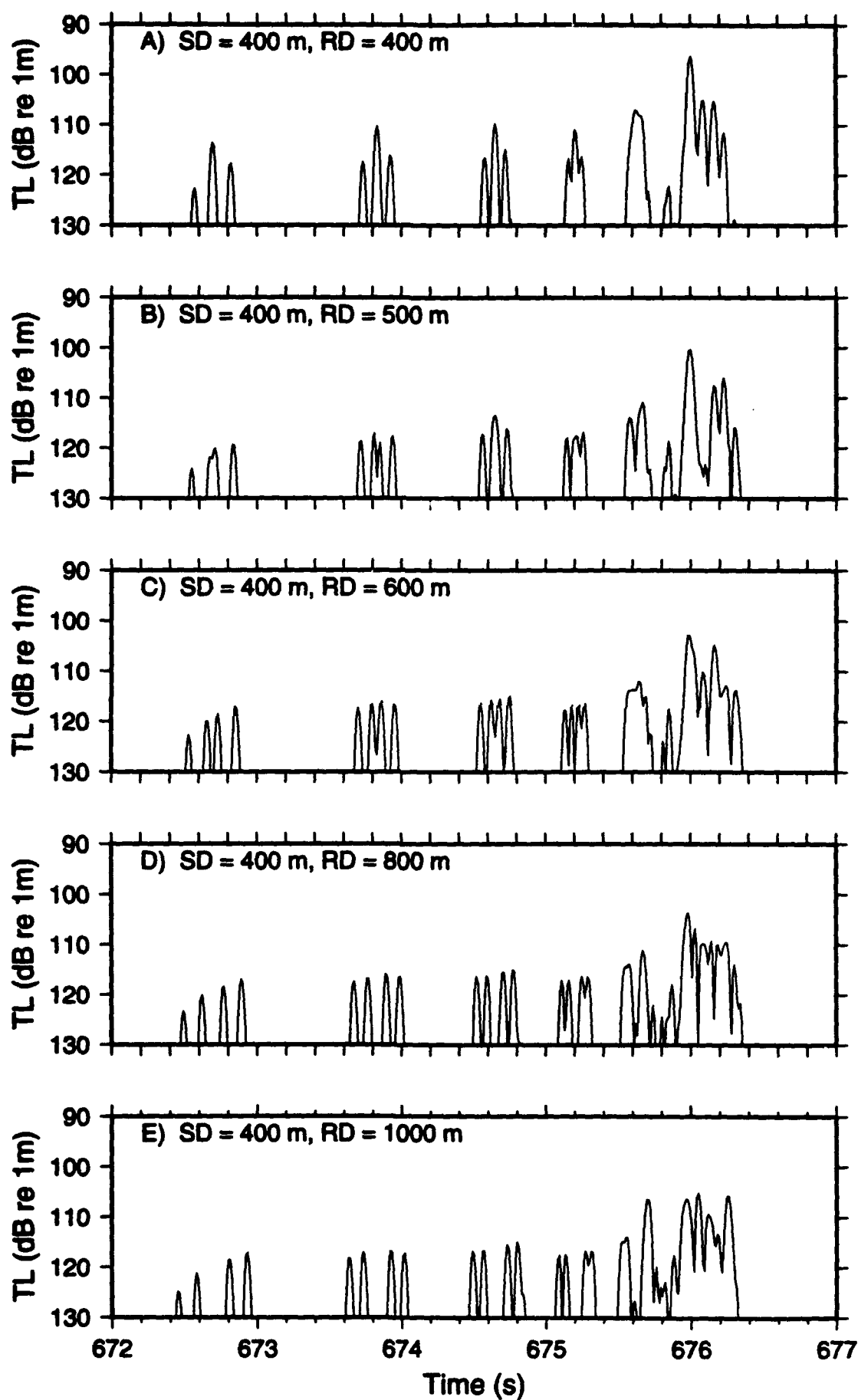


Fig. (4)

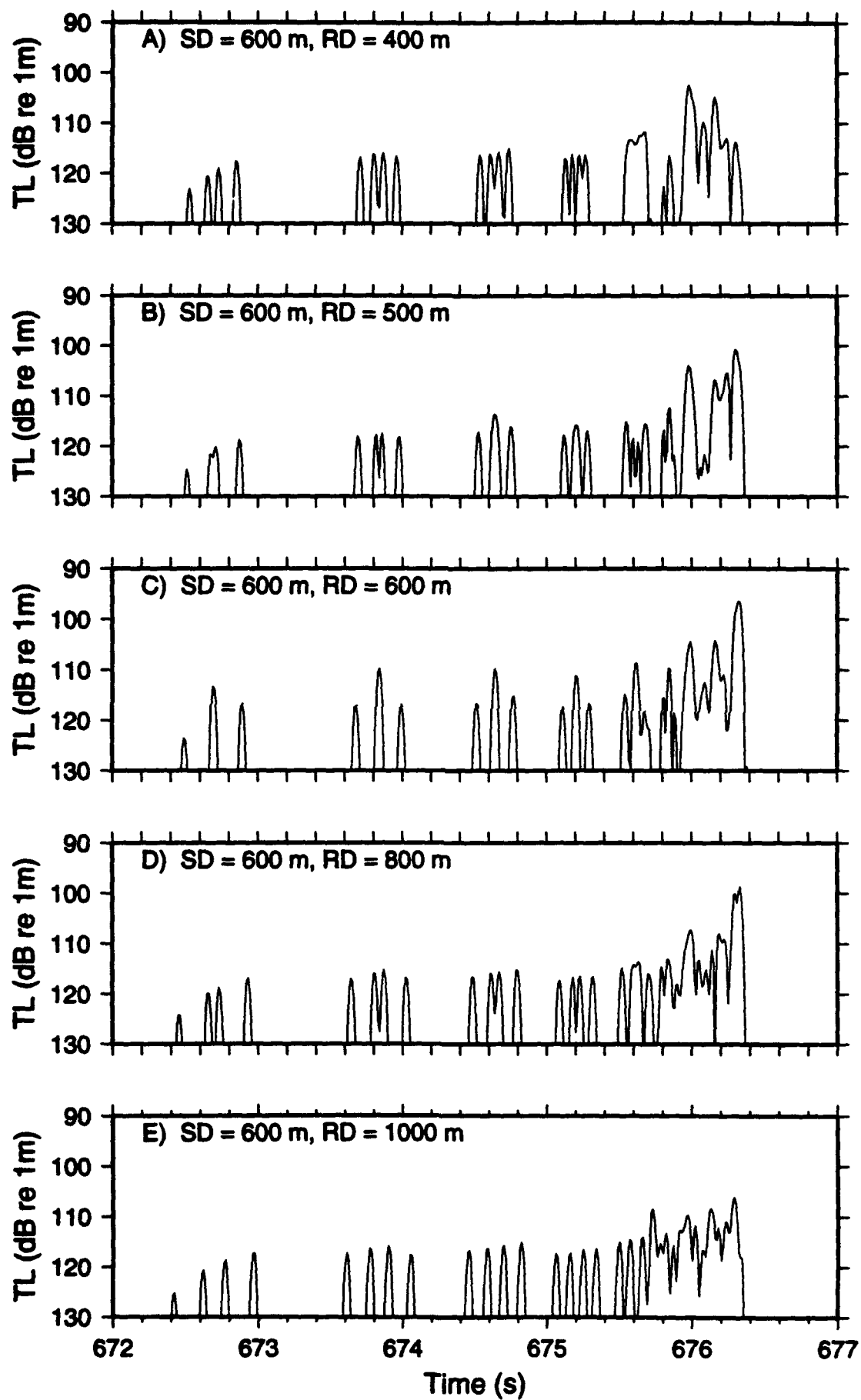


Fig. (5)

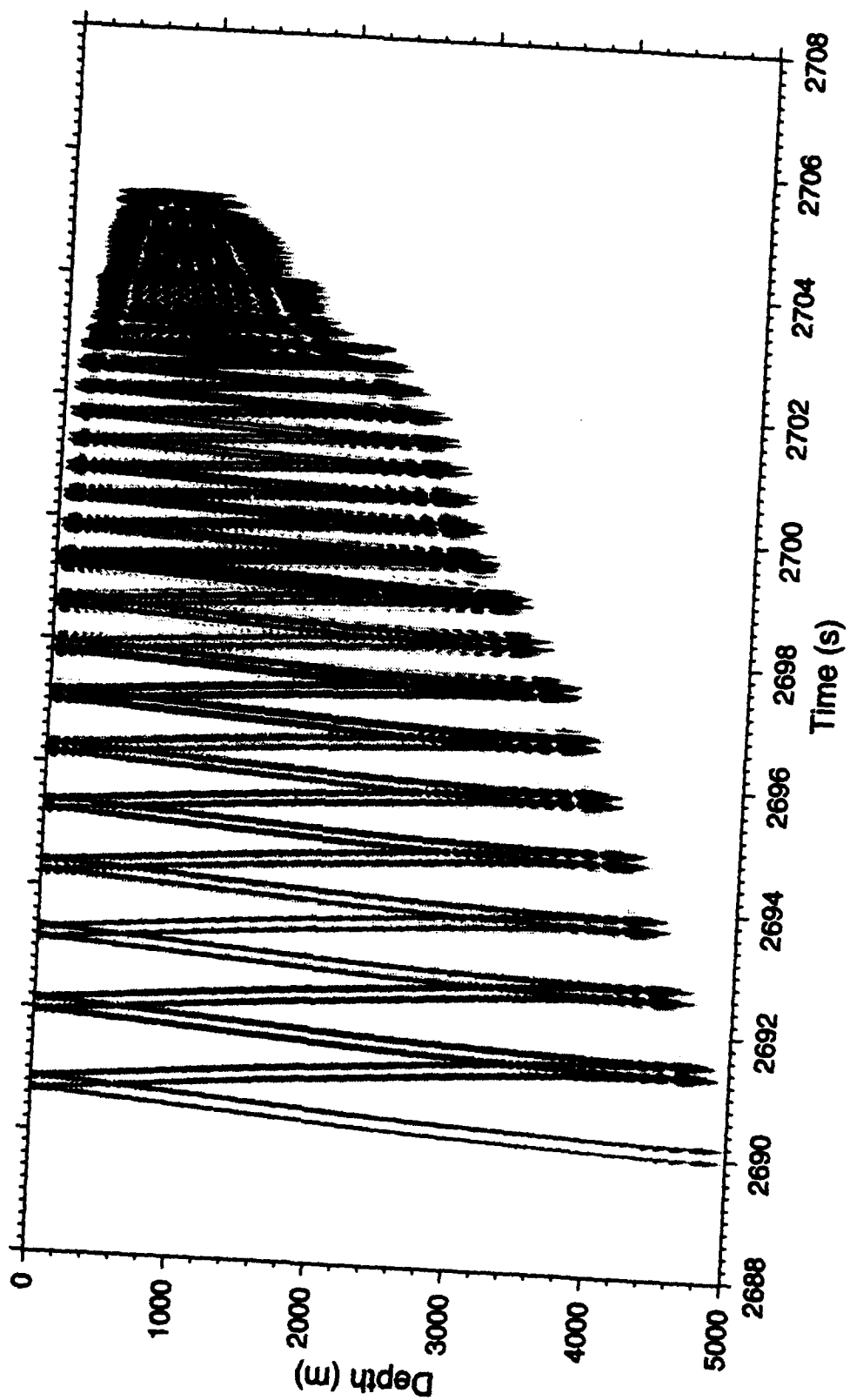


Fig. (6)

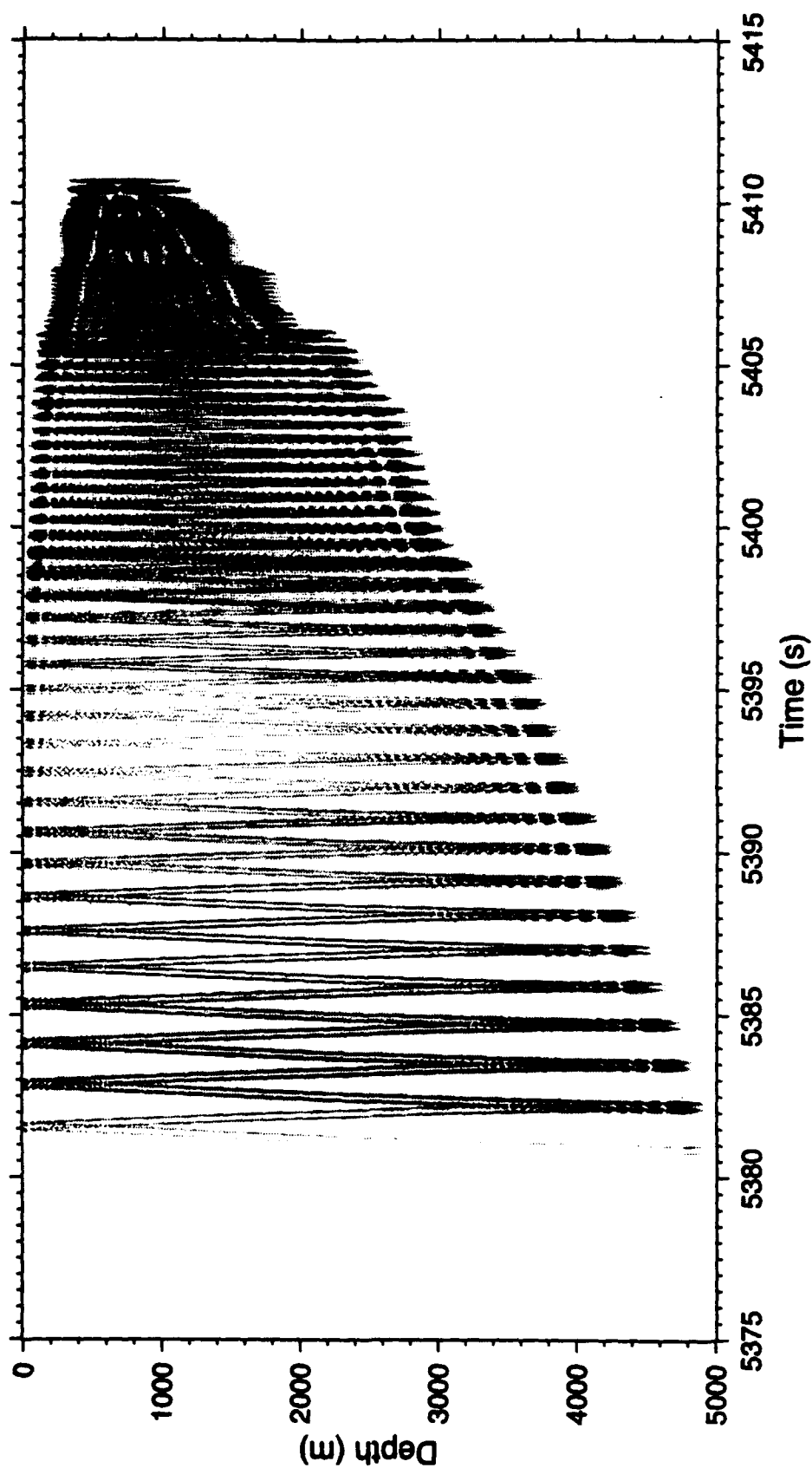
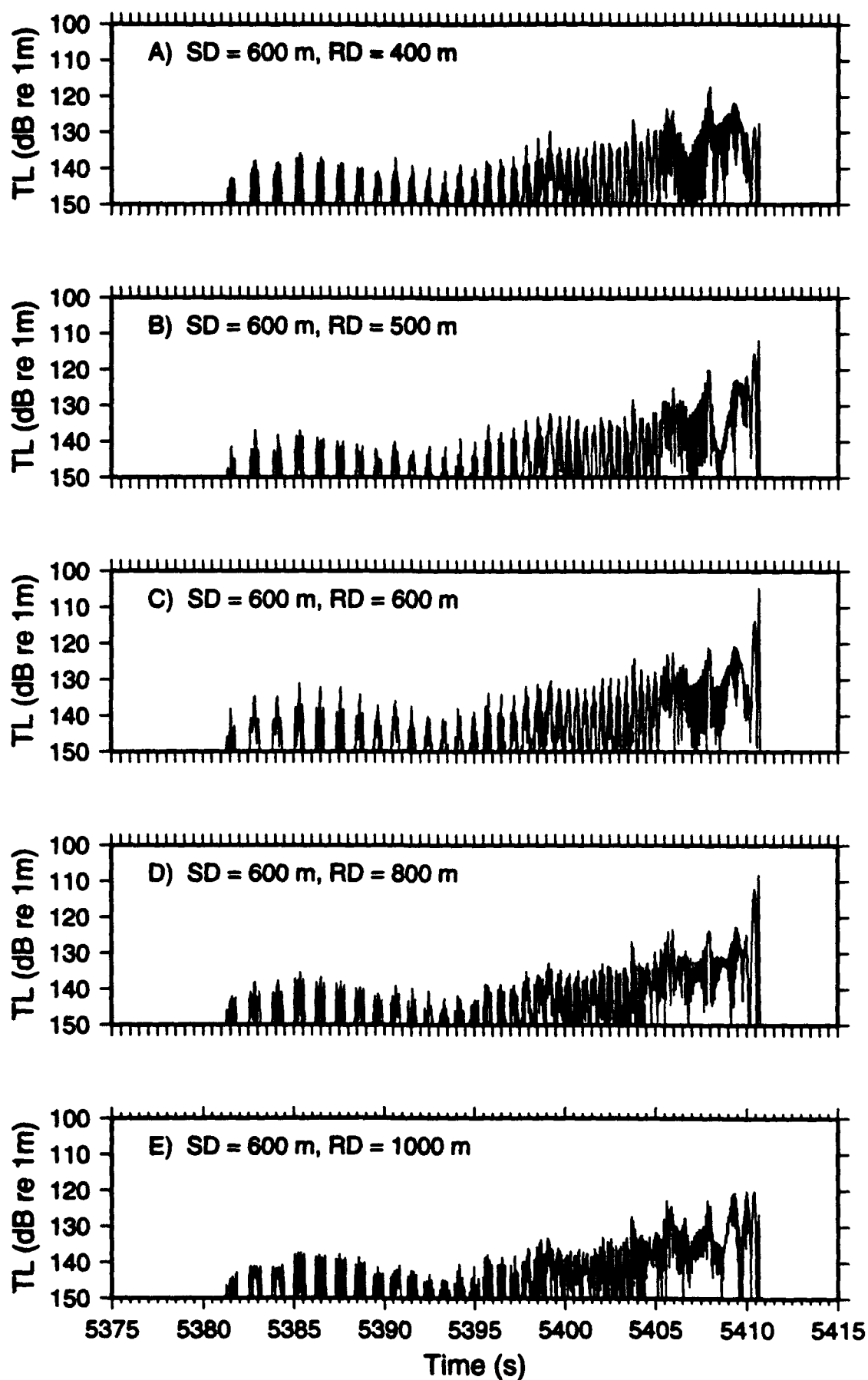


Fig. (7)



GAMOT QUARTERLY REPORT
SECOND QUARTER 1994

FLORIDA STATE UNIVERSITY
PROFESSOR JAMES J. O'BRIEN

I. Summary

The FSU Tasks and Deliverables are now on schedule. We have completed the writing of a manuscript detailing the travel time anomaly (TTA) estimates using a reduced-gravity model (Deliverable B4) of the northeast Pacific Ocean. It is shown that the TTAs over geodesic paths below about 40N have interannual variations controlled mostly by Rossby waves coming off the American coast. Above this latitude, Rossby waves are very weak and the TTA is dominated by sudden changes in wind-stress curl. Additionally, we hypothesize that the 1976-77 climate shift in the Pacific is related to the presence of Rossby waves. This is detailed in a progress report (included herein).

As part of our contribution to Task B5, we have designed an acoustic tomography assimilation scheme for a similar model, but with spatially variable density. An optimal control method is used to assimilate tomographic data into an ocean model with the goal of estimating the time independent density field in the upper northeast Pacific ocean. Coding and testing has already been completed on the forward model and we are in the debugging stage for the adjoint code. A technical summary of the technique is given below. The implementation is primarily being done by graduate student Mr. Ming Liu.

Deliverable B5 - the plan for monitoring the Pacific Ocean for long term change - is incorporated into the reports on Deliverable B4 and Task B5. Additional details should emerge as we gain experience with the new numerical models.

II. Deliverable B4

See attached progress report.

III. Task B5

Data assimilation is a technique combining model dynamics and data to create an output which is more accurate than the model or data alone. Data assimilation schemes may be

classified in three ways: (1) variational (adjoint) methods, (2) optimal interpolation (OI) methods, and (3) successive corrections. They are used extensively in meteorology and increasingly in oceanography. *Anderson and Willebrand [1989]* contains a number of articles on the theory and application of data assimilation in ocean models, using both the variational approach and others. A recent comprehensive article by *Ghil and Malanotte-Rizzoli [1991]* also summarizes the data assimilation in ocean models.

Model

The reduced gravity model of the northeast Pacific (NEP) has been described in our previous reports. For this next stage of research, we shall investigate horizontal variations in the upper layer density $\rho = \rho(\phi, \theta)$ which can be estimated through assimilation of tomographic data using the variational adjoint method. The goal is to reveal the thermohaline structure not included in the reduced-gravity models.

We need to assume that the fluid is Boussinesq which allows us to neglect density variations in the momentum equations, except when coupled with gravitational acceleration. We also assume fluctuations in the density are the result of thermal variations [*Spiegel and Veronis [1960]*].

The variables $U = uh$ and $V = vh$ are the transports in the east and north directions, respectively, where (u, v) are the depth-independent velocity components in the upper layer and h the upper layer thickness (ULT). The density field $\rho(\phi, \theta)$ in the upper layer is treated as a model parameter, which will be determined by the data assimilation process.

The model equations are:

$$E_u = \frac{\partial U}{\partial t} + \frac{1}{a \cos \theta} \frac{\partial}{\partial \phi} \left(\frac{U^2}{h} \right) + \frac{1}{a} \frac{\partial}{\partial \theta} \left(\frac{UV}{h} \right) - 2\Omega \sin \theta V + \frac{c^2}{a \cos \theta} \frac{\partial h}{\partial \phi} - \frac{\tau^\phi}{\rho_o} - A \nabla^2 U - \frac{gh^2}{2\rho_o a \cos \theta} \frac{\partial \rho}{\partial \phi} = 0 \quad (1)$$

$$E_v = \frac{\partial V}{\partial t} + \frac{1}{a \cos \theta} \frac{\partial}{\partial \phi} \left(\frac{UV}{h} \right) + \frac{1}{a} \frac{\partial}{\partial \theta} \left(\frac{V^2}{h} \right) + 2\Omega \sin \theta U + \frac{c^2}{a} \frac{\partial h}{\partial \theta} - \frac{\tau^\theta}{\rho_o} - A \nabla^2 V - \frac{gh^2}{2\rho_o a} \frac{\partial \rho}{\partial \theta} = 0 \quad (2)$$

$$E_h = \frac{\partial h}{\partial t} + \frac{1}{a \cos \theta} \left\{ \frac{\partial U}{\partial \phi} + \frac{\partial}{\partial \theta} (V \cos \theta) \right\} = 0 \quad (3)$$

where A is an eddy viscosity coefficient, a is the radius of the Earth, and Ω is the Earth's

rotation rate. c is defined by

$$c = g' \frac{(H - h)h}{H}$$

where $H = H(\phi, \theta)$ is the total depth of ocean, the reduced gravity $g' = g\Delta\rho/\rho_2$. c can be easily recognized as the local phase speed of the baroclinic mode.

Acoustic travel time anomalies

The estimate of acoustic travel time anomalies (ATTA) using a reduced-gravity model has been discussed in our previous reports. We summarize that the ATTA at time $t = t_j$ due to anomalies in ULT over path i is to first order

$$\begin{aligned} T_{i,j} &\approx T_{i0} - \int_i \frac{\delta c}{c_o^2} ds \\ &= T_{i0} - \frac{1}{c_o^2} \frac{\beta \Delta \rho}{\alpha D} \int_i (h - h_o) ds \\ &= T_{i0} - c_T \int_i (h - h_o) ds \\ &= \int_i \left[\frac{T_{i0}}{\Gamma_i} - c_T (h - h_o) \right] ds \\ &= \int_{\Sigma_i} \left[\frac{T_{i0}}{\Gamma_i} - c_T (h - h_o) \right] \Delta^i(\mathbf{x}) d\sigma \\ &= T_i[t_j] \end{aligned} \tag{4}$$

where $c_T = \frac{1}{c_o^2} \frac{\beta \Delta \rho}{\alpha D}$, c_o is the unperturbed sound speed, $\Gamma_i = \int_i ds$ is the arc length of the path i , Σ_i indicates the space domain, $\Delta^i(\mathbf{x}) = \delta(\phi - \phi_i) \cos \theta_i \frac{d\theta}{d\sigma}$ is the delta-like function along the i the path where tomography data exists, T_{i0} is the mean travel time and $\alpha, \beta, \text{ and } D$ are constants.

Unfortunately there will be no long-term ocean tomographic data available until 1995, so we choose to perform so-called *identical twin* experiments. Given a density distribution ρ_o , such as climatologic data, we run the model with ρ_o and calculate the ATTAs with [Eq. (4)]; reinitializing the initial ρ by adding a perturbation $\delta\rho$, we run minimization scheme in an effort to recover the original ρ_o .

Variational analysis

A cost function must be defined which measures the distance between the observation and the corresponding model outputs to apply the optimal control method. In this study, the

oceanic tomography data will be used. The density field $\rho(\phi, \theta, t)$ in the upper layer is treated as a model parameter, which will be determined by the data assimilation process.

In a least-square sense, the cost function J is chosen as:

$$\begin{aligned} J(T, \rho) &= \frac{K_T}{2} \sum_i \int_0^T [(T_{i,j} - T_{i,j}^o)]^2 dt + \tau \int_{\Sigma_s} \frac{K_\rho}{2} [\rho(\mathbf{x}) - \tilde{\rho}(\mathbf{x})]^2 d\sigma \\ &= \frac{K_T}{2} \sum_i \int_0^T \left[\int_{\Sigma_s} \left(C_T(h - h_o) + \left[\frac{T_{i,j}^o - T_{i,o}}{\Gamma_i} \right] \Delta^i(\mathbf{x}) d\sigma \right)^2 dt \right. \\ &\quad \left. + \tau \int_{\Sigma_s} \frac{K_\rho}{2} [\rho(\mathbf{x}) - \tilde{\rho}(\mathbf{x})]^2 d\sigma \right] \end{aligned} \quad (5)$$

where the subscript i denotes a section between the i th pair between a source and a receiver, the superscript o observed data, T_i^o corresponding to T_i and $T_{i,o}$, and the tilde \sim estimated values. K_T is the inverse of the observation *rms* error if the errors in the data are uncorrelated and equally weighted and K_ρ is a computational weight.

The momentum equations and the conservation of mass, which are the strong constraints can be enforced by introducing the *Lagrange* multipliers. This leads to the formulation of the associated *Lagrange* function:

$$L(S, \Lambda, \rho) = J(T, \rho) + \int_{\Sigma} \Lambda^T E(S, \mathbf{x}, t, \rho) d\sigma \quad (6)$$

where

$$\begin{aligned} S(\mathbf{x}, t) &= (U, V, h)^T \\ \Lambda &= (\lambda_u, \lambda_v, \lambda_h)^T \\ E(S, \mathbf{x}, t, \rho) &= (E_u, E_v, E_h)^T \end{aligned}$$

λ_u, λ_v , and λ_h are the *Lagrange* multipliers for the strong constraints, E_u , E_v and E_h are [Eq. (1), Eq. (2)] and [Eq. (3)].

The first variations of L [Eq. (6)] with respect to λ s give the original model transport equations. Letting the first variations of L [Eq. (6)] with respect to U , V , and h vanish, give the adjoint equations:

$$\begin{aligned} & -\frac{\partial \lambda_u}{\partial t} - \frac{1}{h} \left[L_u \lambda_u + \frac{V}{a \cos \theta} \frac{\partial \lambda_v}{\partial \phi} \right] + 2\Omega \sin \theta \lambda_v \\ &= \frac{1}{a \cos \theta} \frac{\partial \lambda_h}{\partial \phi} + A \nabla^2 \lambda_u \\ & -\frac{\partial \lambda_v}{\partial t} - \frac{1}{h} \left[L_v \lambda_v + \frac{U}{a \cos \theta} \frac{\partial}{\partial \theta} (\cos \theta \lambda_u) \right] - 2\Omega \sin \theta \lambda_u \end{aligned} \quad (7)$$

$$= \frac{1}{a} \frac{\partial \lambda_h}{\partial \theta} + A \nabla^2 \lambda_v \quad (8)$$

$$\begin{aligned} & \frac{\partial \lambda_h}{\partial t} + \frac{c^2}{a \cos \theta} \left[\frac{\partial \lambda_u}{\partial \phi} + \frac{\partial}{\partial \theta} (\cos \theta \lambda_v) \right] + \frac{gh}{\rho_o a \cos \theta} \frac{\partial \rho}{\partial \phi} \lambda_u + \frac{gh}{\rho_o a} \frac{\partial \rho}{\partial \theta} \lambda_v - \left(\frac{U}{h^2} L \lambda_u + \frac{V}{h^2} L \lambda_v \right) \\ & = K_T C_T \sum_i \left[\left(C_T (h - h_o) + \left[\frac{T_i^o - T_{io}}{\Gamma_i} \right] \right) \Delta^i(x) \right] \end{aligned} \quad (9)$$

where

$$\begin{aligned} L_u &= \frac{1}{a \cos \theta} \left[2U \frac{\partial}{\partial \phi} + V \frac{\partial}{\partial \theta} (\cos \theta) \right] \\ L_v &= \frac{1}{a \cos \theta} \left[U \frac{\partial}{\partial \phi} + 2V \frac{\partial}{\partial \theta} (\cos \theta) \right] \\ L &= \frac{1}{a \cos \theta} \left[U \frac{\partial}{\partial \phi} + V \frac{\partial}{\partial \theta} (\cos \theta) \right] \end{aligned}$$

The adjoint equations are similar to the model equations, except that the diffusion terms in the adjoint equations has the opposite sign and the adjoint equations correspond to an evolution backward in time with forcing by the misfit of the model to the data. The *Lagrange* multipliers serve to collect information from the data and propagate it back to the initial time.

The condition that the gradient of cost function J respect to the control variable ρ vanishes is:

$$\nabla_\rho J = K_\rho [\rho(x) - \tilde{\rho}(x)] + \frac{g}{2\rho_o a \cos \theta} \left[\frac{\partial}{\partial \phi} (h^2 \lambda_u) + \frac{\partial}{\partial \theta} (h^2 \lambda_v \cos \theta) \right] = 0 \quad (10)$$

In order to obtain the optimal distribution of ρ , the model equations and corresponding adjoint equations are performed iteratively with a descent algorithm on [Eq. (10)]. The iteration sequence is: (i) starting from $\rho'(x) = \rho_o(x) + \delta\rho$, integrate the model equations forward from $t = 0$ and calculate the ATTAs; (ii) integrate the adjoint equations backward in time from τ to 0; (iii) find a new distribution of ρ which minimizes the gradient of the cost function [Eq. (10)]; (vi) check if the optimal solution has been found. If not, repeat the iterative process until a satisfactory solution has been found. A sufficient number of iterations should recover $\rho_o(x)$.

Since our problem has a large degree of freedom (a large number of control variables $\approx 10^7$), conjugate-gradient methods and limited-memory quasi-Newton methods [Navon and Legler, 1987] and Zou et al. [1993] are the most efficient algorithms and will be used in this work.

References

- Anderson, D. L. T., 1991: Data assimilation in ocean models. Strategies for future climate research, M. Latif, Ed., Max-Planck-Institut für Meteorologie, Hamburg, Germany, 193-225.
- Ghil, M., and P. Malanotte-Rizzoli, 1991: Data assimilation in meteorology and oceanography. *Adv. Geophys.*, **33**, 141-266.
- Navon, I. M. and D. Legler, 1987: Conjugate-gradient methods for large-scale minimization in meteorology. *Mon. Wea. Rev.*, **115**, 1479-1502.
- Røed, L. P. and O. M. Smedstad, 1984: Open boundary conditions for forced waves in a rotating fluid. *J. Sci. Stat. Comput.*, 414-426.
- Zou, X., I. M. Navon, M. Berger, K. H. Phua, T. Schlick, and F. X. Le Dimet, 1993: Numerical experience with limited-memory quasi-Newton and truncated Newton methods. *SIAM J. Optimization*, **3**, No.3, 582-608.

**NRL - SSC
QUARTERLY REPORT
APR - JUN, 1994**

A revised paper on the discovery of a decadal impact of the 1982-83 El Nino on the northern Pacific was completed and is now in press in Nature. In an invited talk H. Hurlburt presented these results at the Earth System Modeling Workshop sponsored by the U.S. Global Change Research Program. This was a multi-agency science policy oriented workshop. They were also presented at a meeting of multinational North Pacific Marine Science Organization (PICES) Working Group on Modeling of the Sub Arctic of the North Pacific circulation and in a seminar at the Pennsylvania State University. While at Penn State, H. Hurlburt had discussions with several GAMOT project members.

The five-year tracks of 194 SSAR's simulated by the $1/8^\circ$ NRL Pacific Ocean model were plotted. The simulated SSAR's extended to 550m depth and covered 1985-90. They were released in the region $20-50^\circ\text{N}$ and east of 160°W . All of the drifting SSAR's stayed in this general region for at least one year. Those released $35-45^\circ\text{N}$ or east of 140°W stayed in the region for all 5 years. However, the northernmost were caught up in the Alaskan Stream and the southernmost in the North Equatorial Current and travel trans-basin distances in 5 years. Paula Taliancich, a very bright engineering student, was hired for the summer to perform more detailed analyses on the statistics of SSAR movement within a year and some initial results were produced.

Complete model output from two $1/8^\circ$ NRL Pacific model simulations (run 1981-93) were sent to Mark Johnson at the University of Alaska and Robert Moorhead from Mississippi State visited NRL-SSC to show and discuss their visualization efforts on the $1/8^\circ$ NRL Pacific Ocean model simulations.

Work funded by Navy sponsors which benefits GAMOT (Apr- Jun 94).

A paper on the $1/8^\circ$ NRL Pacific Ocean model simulations and the dynamics of the Kuroshio/Oyashio current system was completed and submitted to JGR-Oceans. The NRL model is unique in having $1/8^\circ$ resolution and in realistically simulating the mean path of the Kuroshio/Kuroshio Extension and its separation from the coast of Japan.

The NRL "DART" data assimilation group performed a 3-month demonstration of data assimilative version of the $1/8^\circ$ NRL Pacific model north of 20°S . This is the first ever such demonstration for an eddy-resolving model over a basin-scale domain. Satellite IR frontal locations, satellite

altimetry from ERS-1 and TOPEX/POSEIDON, and wind and head flux forcing were the data types assimilated. The final output product was 4-D temperature, salinity, currents and sound speed at high horizontal & vertical resolution. When verified against about 1000 independent (unassimilated) contemporaneous hydrographic profiles, overall the results were 8% better than climatology in nowcast mode and forecasts of the axis of the Kuroshio Extension were better than persistence (a forecast of no change) for 6 days. Based on this first attempt, numerous opportunities for improvement were noted.

The wind-driven only versions of the $1/8^\circ$ NRL Pacific model run 1981-93 were verified using monthly IGOSS sea level time series from 66 locations. The correlations were generally high in the GAMOT region of interest (sea level stations along the North American coast from California to the Aleutian peninsula of Alaska). Simulation of interannual variability was verified by using a 1-year running mean on the time series. The 1982-83, 1986-87, and 1991-92 El Ninos were evident in the 1-year running means as far as the Aleutian peninsula in both the data and the model. The highest correlation in each category was .90 for Neah Bay, Washington using the 30-day means and .92 for Petropavlovsk, Russia on the Kamchatka peninsula for the 1-year running means.

TASK B

OCEAN MODELING

Interannual Variability

The University of Alaska effort has been driven by the hypothesis that coastal Kelvin waves propagating poleward along the U.S. west coast leave it and propagate westward as Rossby waves at the interannual time scale of El Niño and significantly alter the temperature structure of the upper ocean in a way detectable to acoustic thermometry. Offshore propagating Rossby waves were found, using EOF's as basis functions, to account for as much as 60% of the observed pattern in temperature distributions in the northeastern Pacific (Shriver *et al.*, (1991). To extend this work, a quantitative relation is needed between the reduced gravity model variable Upper Layer Thickness (ULT) and the observed temperature at 300m. With such a relation, we can begin to subtract natural variability and increase data sensitivity toward detection of climate change.

We assume that temperature at 300m is related to the relative temperature in the upper kilometer for low frequency dynamics. The Kelvin-Rossby wave solution from the reduced gravity model of Johnson and O'Brien (1990) has been extended through 1989 at Florida State University, and we have now analyzed it from 1960 through 1989 to quantify the relationship between the model's ULT and observed ocean temperature at 300m.

We have used observed temperatures at 300m from XBTs launched between June 1976 and November 1984 and the model ULT along three geodesic paths (tracks 1, 2, and 3 in Figure 1). Each path was analyzed independently to find the linear relation between temperature and ULT. After subtracting the long-term monthly means to remove the annual signal, we found similar linear relationships for all three tracks. ULT from the reduced gravity model was converted to temperature anomaly using this linear relationship for the central eastern Pacific bounded by the geodesic tracks. We selected the tracks and this region because we wanted to compare model predicted temperature changes with the travel time experiments done in the late 1980's that have been discussed by Spiesberger and Metzger (1992).

We find that the temperature anomalies predicted by the reduced gravity model using the linear function to map ULT to temperature produces anomalies at 300m ranging between 0.02 to 0.06°C. The acoustic thermometer data from Spiesberger and Metzger (1992) shows the integrated ocean temperature change

expected in the upper km to be between 0.031 and 0.058°C. Figure 2 shows contour plots of the predicted temperature anomaly from the reduced gravity model for the times surrounding the largest change in observed travel times from the travel time experiments (January through May, 1988). The Kelvin wave solution alone accounts for a very significant portion of the change in temperature observed during the acoustic experiments.

This result is important because it strengthens one of the early suggestions about the physics modifying ocean temperature and the associated changes in travel times. If this hypothesis is true, it also links the Kelvin wave-Rossby wave dynamics of El Niño to first order changes in travel times. Further, if the model results explain a significant portion of the observations from the acoustics work, then we can begin to subtract these known signals to clarify underlying signals that may be related to climate change.

This result needs to be refined and extended beyond the straightforward physics of the reduced gravity model. To that end, we have obtained the multi-layer model data from NRL and are beginning to analyze it. Our effort with this data has two areas of focus. First, we will extend and refine the relation found between ULT and ocean temperature. Second, we will begin to run acoustic "experiments" in the model itself to determine whether climate shifts and dynamical changes in the ocean can be predicted based upon the acoustic travel times. This approach is crucial to understanding the strength of acoustics as a predictor of climate change, and important in determining where to place future sources and receivers. This effort is in agreement with the SERDP objective to support environmental change research and establish enhanced strategies for detecting such changes.

Seasonal Variability

One data source common to the acoustics work and their analyses is the historical ocean data set of Levitus. This data set includes long-term means of ocean variables including temperature. For the northeastern Pacific, it contains historical profiles of temperature across the basin. The data are often used to constrain certain models to the historically observed temperature, and it is also used by acousticians to compute certain parameters related to observed or expected travel times. Because this data set is key to these computations, we compared it to the XBT temperatures at 300m described above. Figure 3 shows the relation between temperature extracted from Levitus at 300m versus the observed temperature at 300m based on XBT data for two tracks for four seasons. The plots show the seasonal means from the Levitus

data versus the appropriate bi-monthly mean from the XBTs. The deviation in historical temperature can be as much as 3°C different from that observed during the summer in warmer latitudes. This difference has implications for both the models and the acoustic calculations.

This difference between historical and observed temperatures highlights the need for accurate models to predict seasonal changes so that these and longer time scale variability can be removed. The remainder is the signal that should contain a true indicators of global change. This approach satisfies the SERDP objective of developing forecast systems and models to enhance prediction of environmental events.

Johnson, M., J.O'Brien, 1990, The northeast Pacific Ocean response to the 1982-1983 El Niño, *J. Geophys. Res.*, 95, 7155-7166.

Shriver, J., M.Johnson, J.O'Brien, 1991, Analysis of remotely forced oceanic Rossby waves off California, *J. Geophys. Res.*, 96, 749-757.

Spiesberger, J., and K.Metzger, 1992, Basin-scale ocean monitoring with acoustic thermometers, *Oceanography*, 5, 92-98.

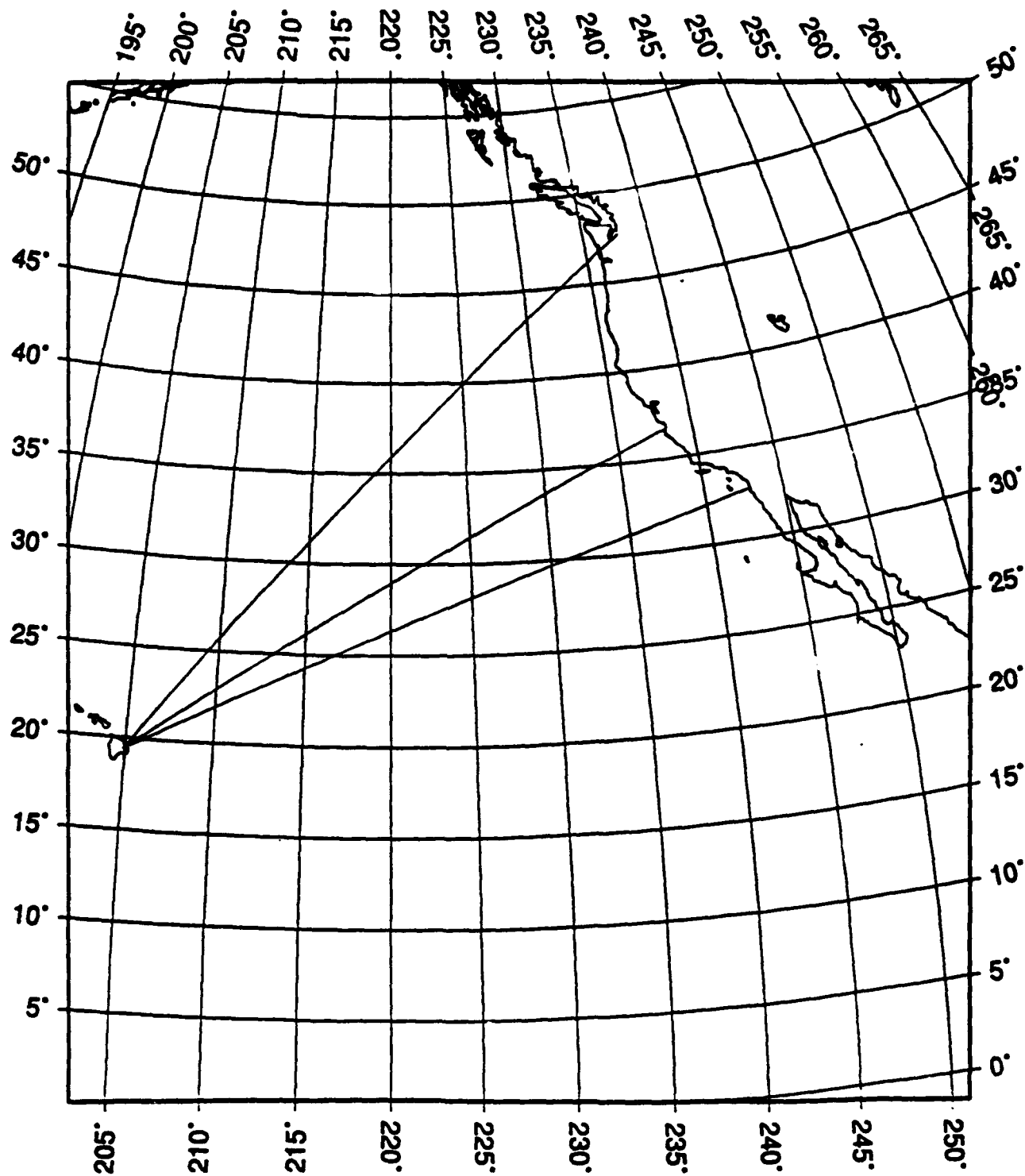


Figure 1. Map of the northeast Pacific with three geodesics tracks analyzed for the relation between the reduced gravity model Upper Layer Thickness and temperatures at 300m

Predicted Temperature Anomaly at 300 (meter)

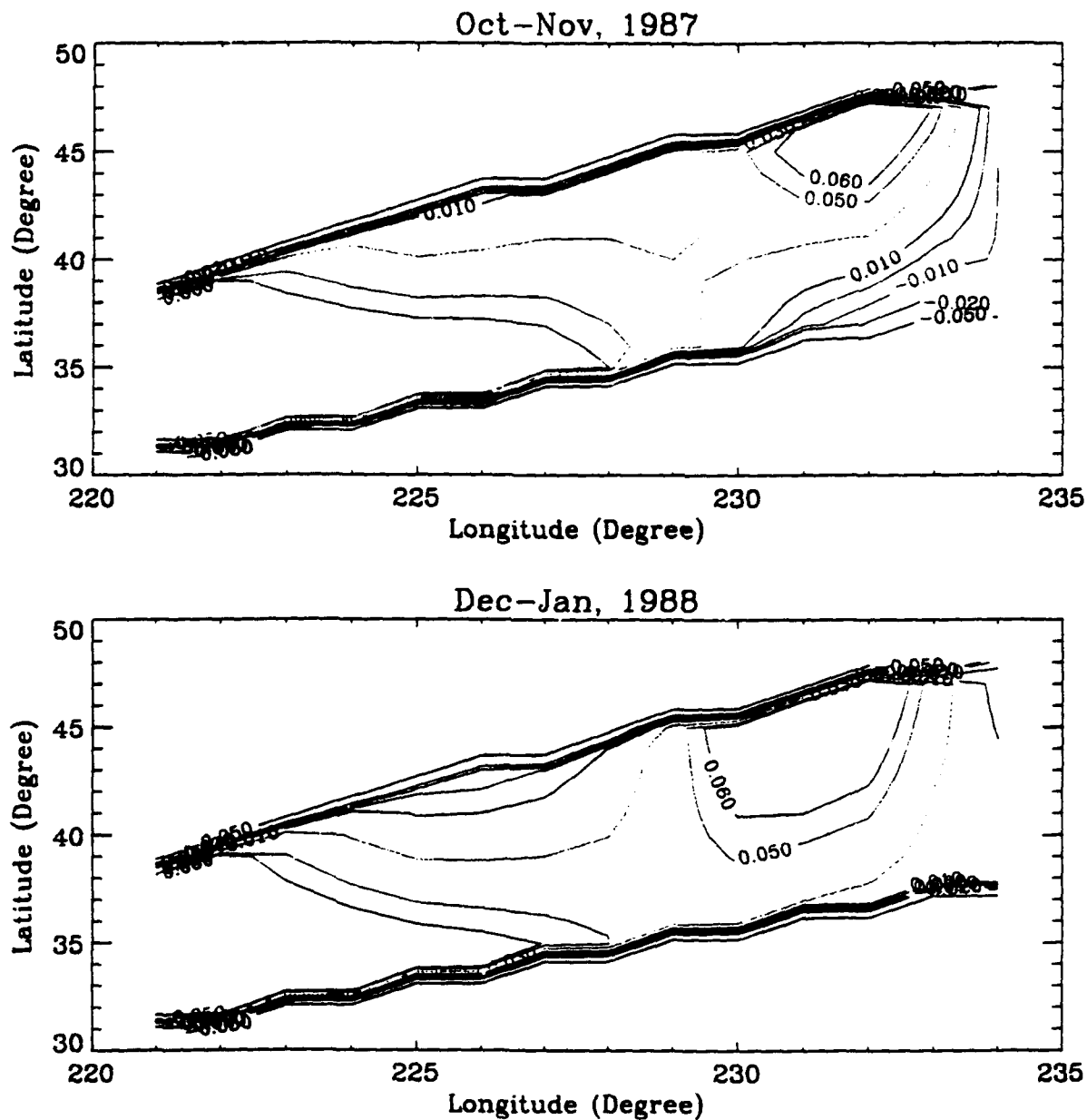
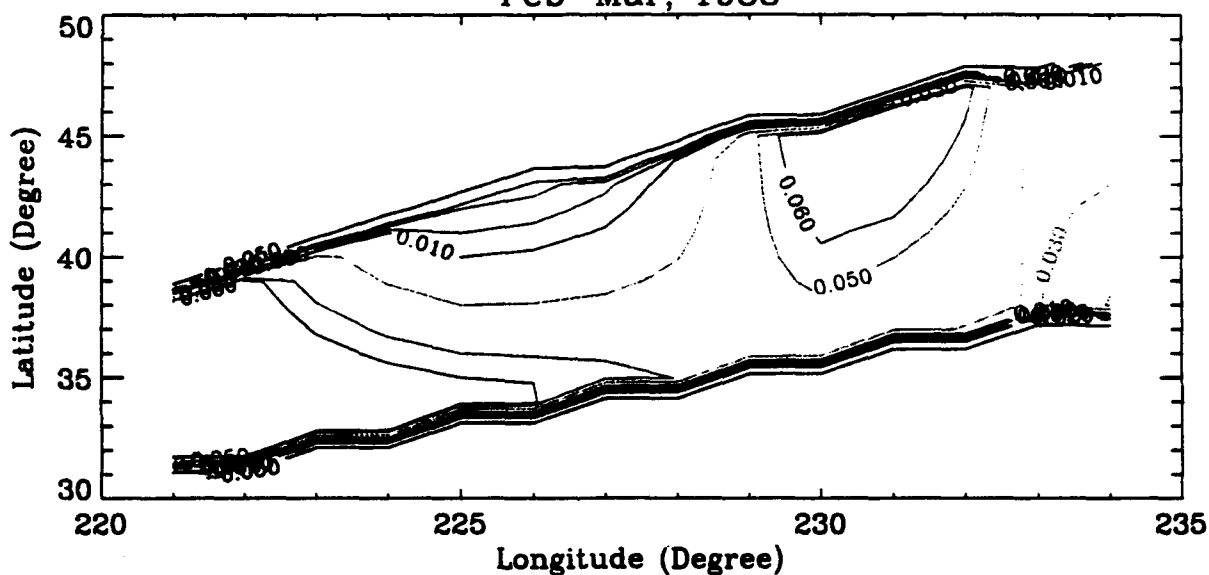


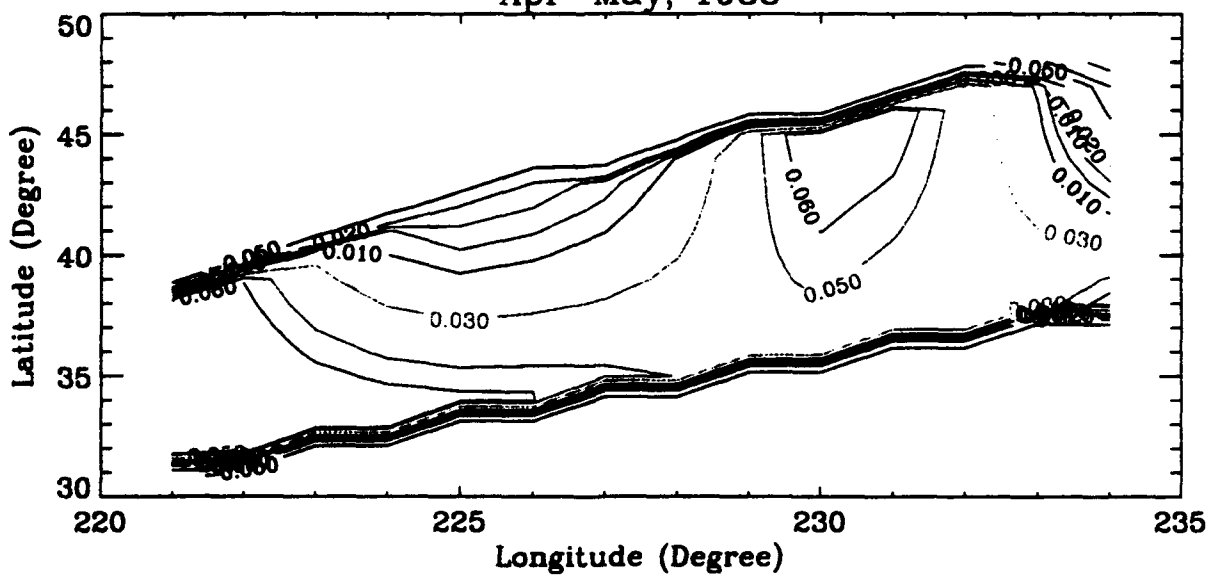
Figure 2. Contour of temperature anomalies predicted from the reduced gravity model and using the linear relation between ULT and temperature at 300m. Selected times correspond to the travel time experiments discussed by Spiesberger and Metzger (1992).

Predicted Temperature Anomaly at 300 (meter)

Feb-Mar, 1988

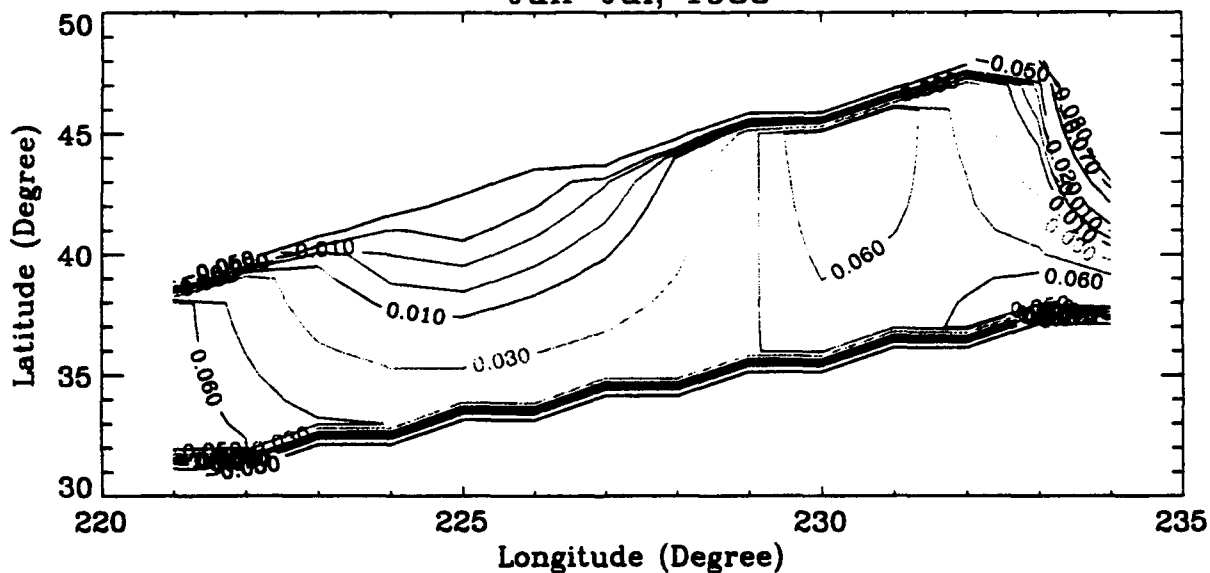


Apr-May, 1988

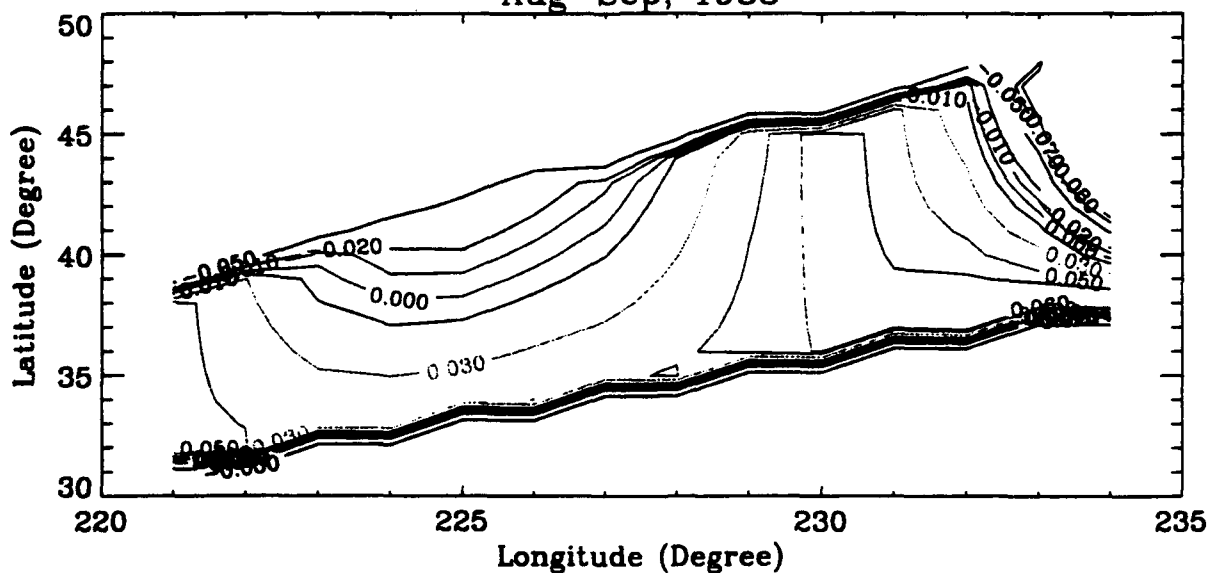


Predicted Temperature Anomaly at 300 (meter)

Jun-Jul, 1988



Aug-Sep, 1988



Levitus & Field Temperature Cross-Plot, Track 1

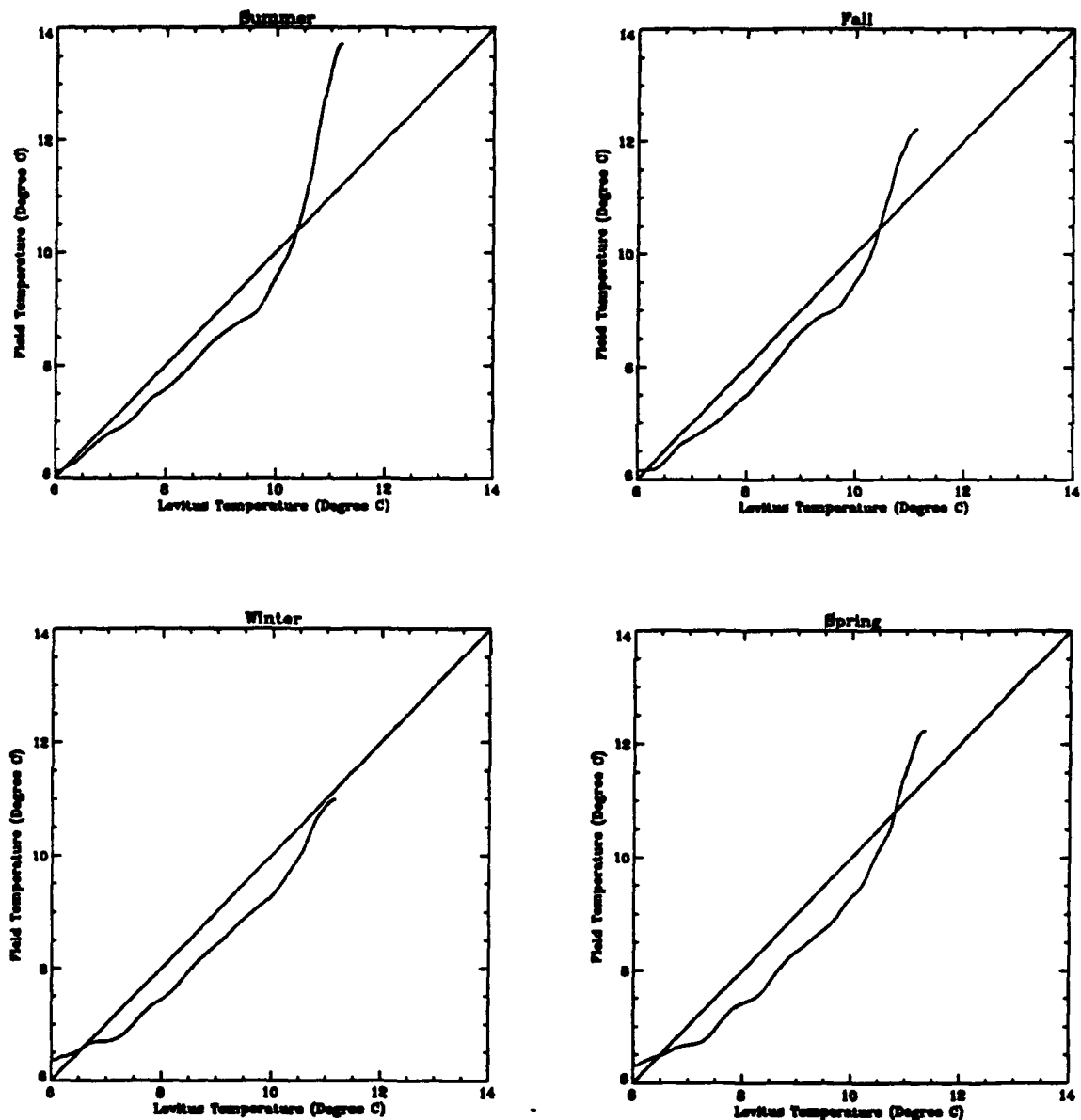
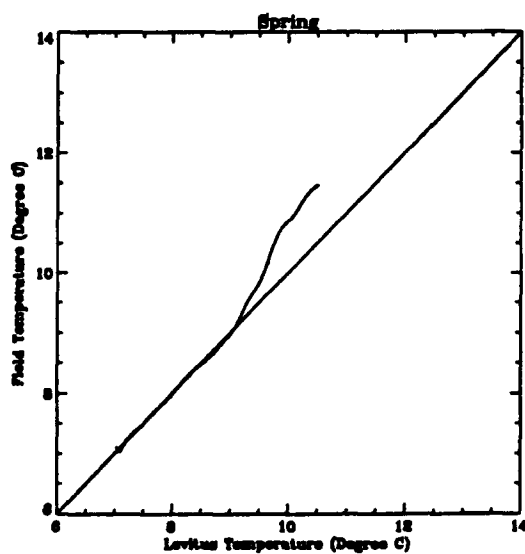
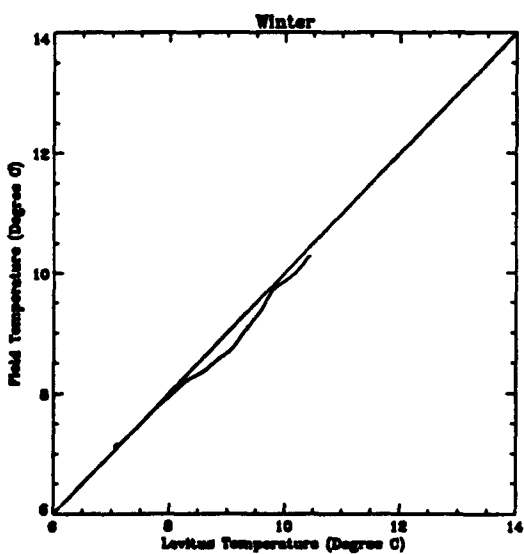
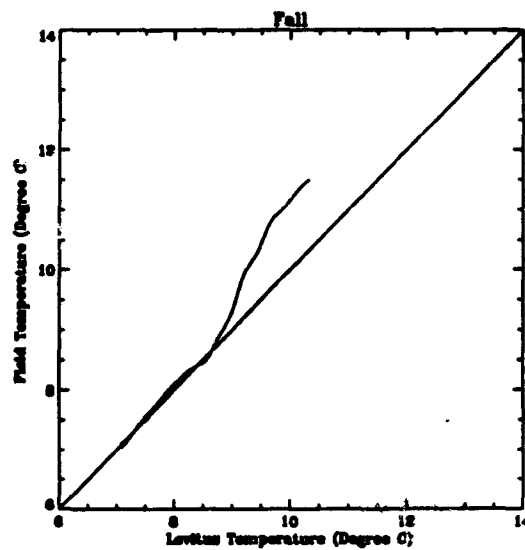
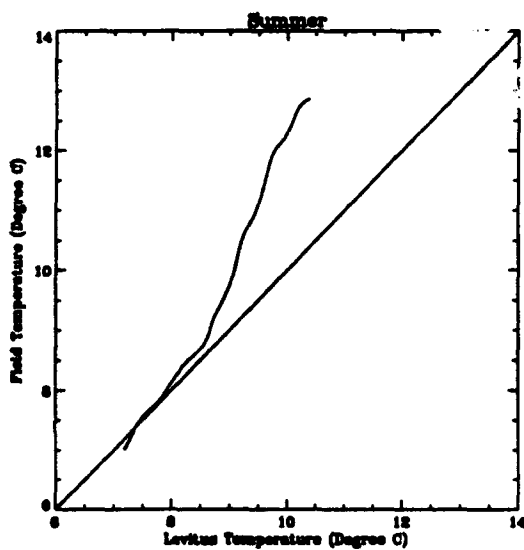


Figure 3. Comparison of temperatures from the historical Levitus data set with the observed temperatures at 300m from XBTs. The difference between the historical and observed underscores potential bias in using these data for predicting travel times and for constraining ocean models.

Levitus & Field Temperature Cross-Plot, Track 2



PROGRESS REPORT

**Interdecadal variability in a numerical model of the
northeast Pacific Ocean. 1970-1989.**

**This research is supported by the Advanced Research Projects Agency grant SC25046 managed
by Dr. Ralph Alewine and the Strategic Environmental Defense Program (SERDP) headed by
Dr. John Harrison.**

ABSTRACT

Variations in the thermocline depth of the northeast Pacific ocean during 1970-1989 are investigated using a reduced-gravity numerical model forced with local windstress and a coastal Kelvin wave signal. Three experiments are presented: wind only, Kelvin wave only, and combined. The wind forcing generates an anticyclonic gyre circulation with mostly annual variations. The Kelvin waves excite Rossby waves near the coast that propagate into the basin interior, producing upper layer thickness anomalies that last for years after the Kelvin signal has passed. The role of the Rossby waves on travel time anomalies for acoustic signals (ATTA) on geodesic paths from Hawaii to the north American coast are calculated using the scheme of Roed [1994]. The wind forcing produces mainly annual variations in the ATTAs, except for the high latitude paths above 40°N that exhibit sudden shifts in ATTA. The Rossby waves are primarily responsible for interannual variations. Two sequential upwelling Kelvin waves in 1973 and 1975 produce Rossby waves that reduce the mean upper layer by approximately 10-20 m during 1976 until the early 1980s. It is suggested that the previously known climate shift observed in winter SST is caused by changes in the depth of the permanent thermocline due to Rossby waves and not due to local air-sea interaction.

INTRODUCTION

Oceanic quantities such as temperature, current velocity, salinity and biological productivity have variations over time scales from fractions of a second to decades – the length of the longest observational records. Oceanic processes with interdecadal duration are particularly important and have received increased attention in recent years because long-term cycles can mask (or masquerade as) anthropogenic climate change. A review of interdecadal climate variability (ICV) in the ocean-atmosphere system is given in an UNESCO-IOC review (1992). ICV in the oceans has important implications for human activity and is believed to influence droughts in Africa, the Asian monsoon cycle, droughts in the western United States [Cayan et al., 1989], extremes in the El Nino/Southern Oscillation (ENSO), hurricane frequency in the Atlantic [Cook et al., 1991] and Arctic sea ice [Mysak et al., 1990], to name some of the physical phenomenon so far investigated. Effects on the biosphere include changes in phytoplankton and the migration pattern of fish [UNESCO, 1992]. The physical mechanisms behind these and other long-term variations are not well understood and are not predictable with current General Circulation Models (GCMs). As climate change becomes an increasing topic of scientific concern, it is important to distinguish the long-term variability of the ocean and atmosphere from any possible climatic shifts.

The north Pacific Ocean has well documented ICV. During 1977-86 the northern central Pacific Ocean experienced a period of decreased winter sea-surface temperature (SST). This time period is also associated with increased winter SST in the eastern Pacific, temperature changes over the North American continent and a decrease in winter sea-level pressure over the north Pacific [Trenberth, 1990; Graham, 1994]. An EOF analysis of SST by Salmon [1992] suggests this cooling in the central Pacific began in 1967 and lasted until 1987, whereas the northeast Pacific ended a cold period and warmed from 1976 to the early 1980s. It will be shown later that the seasonal aspect is crucial for understanding the underlying physical mechanism driving the SST anomalies.

Numerical studies have investigated the relationship between the atmosphere and ocean during these years. Kitoh [1991] and Graham [1994] both used atmospheric GCM's driven by SST to successfully simulate anomalies over the northern Pacific

Ocean. Graham [1994]; Miller et al. [1994] used isopycnal thermodynamic models driven by observed winds and heat fluxes. Their results have supported the idea that the 1976 oceanic climate shift was primarily driven by atmospheric dynamics. Those studies were limited in several ways such as their coarse spatial resolution that greatly distorts the Kelvin waves necessary for the development of El Nino (warm) or El Viejo (cold) events [O'Brien and Parham, 1992]. Additionally, the thermodynamic equation in the eastern Pacific is dominated by the heat flux term [Miller et al., 1994] so the rate of change of SST is largely constrained by observational values. It is therefore not surprising that they obtain results that closely match real SST anomalies. Since there was no feedback of the ocean into the heat flux term, the influence of the ocean on this term was concealed.

The use of a reduced-gravity model trades the explicit numerical representation of thermodynamic processes for increased resolution of oceanic planetary waves, eddies and currents. In particular, ENSO events are correctly represented. Thermodynamic variables that are not directly computed can often be represented indirectly using the hydrodynamic variables. It has been shown that a relationship exists between the model layer thickness and temperature variations in the upper ocean Roed [1994]. A complete numerical representation of the atmosphere-ocean system at appropriate resolution is not likely to be realized for several years. Until then improved understanding of future interdecadal climate variability can only come from an increased quantity of long-term observations.

Monitoring of the ocean is the focus of the GAMOT/ATOC (Global Acoustic Mapping of Ocean Temperature/Acoustic Thermometry of Ocean Temperature) project. Integrated changes in ocean characteristics will be inferred by monitoring the changes in acoustic travel time over basin scales. Pilot projects have been completed [Baggeroer and Munk, 1992; Spiesberger and Metzger, 1991; Spiesberger et al., 1992] and persistent monitoring will begin in the near future.

There are no previous continuous multi-year acoustic observations of the ocean. The observations of Spiesberger et al. [1992] were done discontinuously from 1987-1989 and limited to intervals of, at most, a few months. The only means to recapture the behavior of the ocean in years past and fill-in the observational gaps is through the use of numerical models. Doing so also aids in the understanding of future measurements by yielding an approximate historical record.

We use a high resolution reduced-gravity model of the northeast Pacific (NEP) Ocean to estimate the travel time anomalies for 1970-1989 over paths roughly corresponding to those in Spiesberger et al. [1992]. The model is forced three different ways: Experiment E1 with observed surface winds; E2 with a coastal Kelvin wave from an equatorial model that is forced with observed winds; E3 with both surface winds and the Kelvin wave. Similar experiments were done by Pares-Sierra and O'Brien [1989] for the years 1961-1979 and Johnson and O'Brien [1990a] for 1975-85. They observed coastally-trapped Kelvin waves moving poleward, separating from the coast of North America as Rossby waves and propagating into the Pacific basin. Analysis of altimetry and ocean temperature records has demonstrated the significance of these Rossby waves [White et al., 1990; Shriver et al., 1991]. Recently, the Rossby wave associated with the 1982-83 El Nino has been observed in both a multilayer numerical model and altimetry data to cross the Pacific basin and influence the Kuroshio in 1993 [Jacobs et al., 1994].

A preliminary investigation into the variations in acoustic travel time over paths similar to those planned for GAMOT/ATOC is done for all three model cases. Variations in sound speed are estimated according to the method of Roed [1994]. Interdecadal climate variability occurs in the travel time variations, with the details depending upon the specific path.

Section 2 describes the model and ATTA estimation procedure. The results are described in Section 3 and discussed in Section 4. Of particular interest is the dominant influence on the ocean climate of Rossby waves propagating off the North American coast. They are shown to play a central role in determining the long-term acoustic properties of the upper North Pacific Ocean and are probably involved in the 1976 climate shift.

NUMERICAL MODEL AND ATTA ESTIMATION

The northeast Pacific model

A numerical model of the northeast Pacific ocean is used. The model domain is a spherical section shown in Fig. 1. An Arakawa C-grid is used with a horizontal spacing of $1/12^\circ$ in both latitude and longitude. There is one active upper layer atop an inert lower layer. Realistic topographic effects are included by modification of the local phase speed [Cushman-Roison and O'Brien, 1983]. This is included

since the coastal sea-floor topography has a strong influence on the local evolution of Rossby waves [Liu and O'Brien, 1994]. The eastern boundary has a no-slip condition along the North American continent and elsewhere the boundary condition is open, according to the scheme in Camerlengo and O'Brien [1980].

The model contains three dynamic variables: the upper layer thickness $H(\theta, \phi, t)$ and upper layer zonal and meridional velocities $u(\theta, \phi, t)$ and $v(\theta, \phi, t)$ respectively. The equations describing the model are written in transport form:

$$\frac{\partial U}{\partial t} + \frac{1}{a \cos \theta} \frac{\partial}{\partial \phi} \left(\frac{U^2}{H} \right) + \frac{1}{a} \frac{\partial}{\partial \theta} \left(\frac{UV}{H} \right) - (2\Omega \sin \theta)V = -\frac{g'}{2a \cos \theta} \frac{\partial H^2}{\partial \phi} + \frac{\tau^\phi}{\rho_1} + A \nabla^2 U \quad (1)$$

$$\frac{\partial V}{\partial t} + \frac{1}{a \cos \theta} \frac{\partial}{\partial \phi} \left(\frac{UV}{H} \right) + \frac{1}{a} \frac{\partial}{\partial \theta} \left(\frac{V^2}{H} \right) + (2\Omega \sin \theta)U = -\frac{g'}{2a \cos \theta} \frac{\partial H^2}{\partial \theta} + \frac{\tau^\theta}{\rho_1} + A \nabla^2 V \quad (2)$$

and

$$\frac{\partial H}{\partial t} + \frac{1}{a \cos \theta} \left[\frac{\partial U}{\partial \phi} + \frac{\partial}{\partial \theta} (V \cos \theta) \right] = 0. \quad (3)$$

where $U = uH$ and $V = vH$. Equations (1) and (2) are the equations of motion and (3) is continuity. Model parameters are given in Table 1.

The windstress is $\tau(\phi, \theta, t) = (\tau^\phi(\phi, \theta, t), \tau^\theta(\phi, \theta, t)) = C_d \rho_a \|\mathbf{u}_w\| \mathbf{u}_w$, where $\mathbf{u}_w(\phi, \theta, t)$ is the surface wind, C_d is a drag coefficient and ρ_a is the air density. Monthly average pseudostress was obtained from COADS winds and interpolated to the model grid and a linear temporal interpolation was used between each monthly value. Further details on the numerical scheme, boundary conditions and wind forcing can be found in Pares-Sierra and O'Brien [1989]. The major difference in numerical schemes is our inclusion of realistic sea-floor topography, as mentioned above.

The Kelvin wave for experiments E2 and E3 is input in the following way. The H value of the NEP model on the southern boundary at the easternmost grid point, $H_{eq}(t)$, was taken from an overlapping equatorial model described in Kamachi and O'Brien [1994]. This is called the remote signal and is shown in Fig. 2. Bussalacci and O'Brien [1981] used an essentially identical equatorial model and found it closely reproduced observational sea level near the eastern boundary. The ULT along the

southern boundary is prescribed to be

$$H_{in}(x, t) = H_{eq}(t) \exp\left(\frac{x - x_e}{L_D}\right) + H_0 \quad (4)$$

where $x - x_e$ is the longitudinal distance from the eastern boundary x_e , H_0 is an initial layer thickness and L_D is the radius of deformation, about 50 km at the equator based on the model parameters. The exponential envelope in (4) which defines the region of input is limited to 1° (six H grid points). The input velocities at the corresponding points are, $u_{in} = 0$ and v_{in} is estimated from the inviscid quasigeostrophic equation

$$-g \frac{\partial H_{in}}{\partial y} = u_{in} \frac{\partial v_{in}}{\partial x} + v_{in} \frac{\partial v_{in}}{\partial y} + \frac{\partial v_{in}}{\partial t}, \quad (5)$$

where x and y represent the zonal and meridional distances respectively. These properties are consistent with the coastal Kelvin waves in Moore [1968], Anderson and Rowlands [1976] and Clarke [1983].

Acoustic travel time estimation

Sound speed c in the ocean is controlled by density ρ which is a function of temperature T , salinity S and pressure P , but the dominant variable in the upper ocean is temperature. However, we use a layered model without salinity structure or thermodynamics which cannot directly yield an estimate of c . This handicap of the isopycnal model was overcome by Roed [1994], who provided a means to estimate variations in c as a function $c(H)$. The essence of his argument is now reproduced.

The first-order Taylor expansion of sound speed is $c(T, S, P) \simeq c_0 + \beta(T - T_0) + \gamma(p - p_0) + \kappa(S - S_0)$, where c_0 is a reference speed (typically around 1542 m/s for water at 20°C), and β , γ and κ are constant coefficients. β should not be confused with the gradient of the Coriolis parameter. Since the temperature term of the expansion is known to be the most significant, we can write

$$c = c_0 + \beta(T - T_0). \quad (6)$$

Density is also a function of temperature to first order,

$$\rho = \rho_0 - \alpha(T - T_0). \quad (7)$$

α is the constant coefficient of thermal expansion. The connection to the layered model is now introduced. There is evidence that in many regions of the ocean

variations in thermocline are related to variations in density. In the context of a layered ocean Roed [1994] finds

$$\rho = \rho_0 - \frac{\Delta\rho}{D}(H - H_0), \quad (8)$$

where $\Delta\rho$ is the difference in density between the upper and lower layer. D is a reference depth which is set to a constant 1000 m.

Combining (6), (7) and (8) yields

$$c = c_0 + \frac{\beta\Delta\rho}{\alpha D}(H - H_0). \quad (9)$$

Since the time it takes for sound to travel from a source to a receiver is inversely related to c , we examine c^{-1} using (9) which we denote as $c = c_0 + c'$ where c_0 is the unperturbed speed. Then, assuming $c' \ll c_0$,

$$c^{-1} = \frac{1}{c_0} \left(1 + \frac{c'}{c_0}\right)^{-1} \simeq \frac{1}{c_0} \left(1 - \frac{c'}{c_0}\right). \quad (10)$$

The total acoustic travel time is $\int c^{-1} ds$, with the integral taken over the travel path. Using (10) the integral can be separated into two terms, a mean and an anomaly. The anomaly term which represents the variations in total travel time over the path due to changes in upper layer thickness (ULT) is then

$$T_1 = - \left(c_0^{-2} \frac{\beta\Delta\rho}{\alpha D} \right) \int (H - H_0) ds. \quad (11)$$

Downwelling raises ocean temperature anomalies and increases c' , reducing T_1 . The opposite effect occurs for upwelling. This dependence of temperature anomalies on thermocline depth variations is well known in the tropics [e.g., Bussalacci and O'Brien, 1981] where a strong permanent thermocline exists. It does not necessarily hold for SST anomalies in mid-latitudes where the seasonal thermocline cycle has a significant effect on SST. This is detailed further in the discussion.

MODEL RESULTS AND ANALYSIS

The models are initially spun-up using monthly climatological conditions for seven years. The forcing switches to observational COADS winds and/or the Kelvin signal from the equatorial model. Case E2 does not undergo a spinup. The model input corresponds to years 1961-1989, but only the period 1970-1989 is discussed in detail because the model 1960's appear to be dominated by the adjustment from climatological to observational forcing due to the rather slow propagation of Rossby waves in the mid-latitude ocean.

Winds only (E1)

One difference between the study of Pares-Sierra and O'Brien [1989] and those discussed here is the ULT entrainment level. The ocean model requires a mechanism to prevent layer outcropping. When the ULT drops below a threshold value, the H at that point is slowly increased until it is greater than the threshold. In Pares-Sierra and O'Brien [1989] the threshold for entrainment was 100 meters. We use 60 m. This difference manifests along the coast and northern boundary. Since only ULT anomalies play a role in the analysis, this difference in ULT is not a significant concern.

The ocean currents in this region are dominated by the subtropical gyre centered near the western model boundary (Fig. 3) with relatively small seasonal variations. Examination of the ULT anomaly field show no indication of large-amplitude Rossby waves. No westward propagating features are seen in Fig. 4. Some weak propagating features are seen to travel along the southern model boundary, but do not live more than a few months. There is only weak variation about the mean circulation and seasonal changes.

Some measurements of ATTA are in Fig. 5. The annual signal is clearly the strongest component in the southern paths. There is strong correlation between neighboring paths, due to the large-scale nature of the ocean currents. Surprisingly, paths 9 (not shown) and 10 have almost no annual variations and the TTA is jagged in appearance, suggesting sudden shifts in the integrated H trend. Sudden changes in the sign of $\partial H / \partial t$ are probably due to changes in the sign of the wind stress curl in the northern latitudes.

One possible source for these sudden changes is changes in atmospheric circulation associated with ENSO phenomenon. However, the timing of these changes suggests they are not closely related to ENSO. El Nino and El Viejo events defined according to sea-level at Galapagos [Meyers and O'Brien, 1994] are indicated in Fig. 5a. No consistent relationship between changes in ATTA and ENSO is apparent. Power spectra (not shown) of the ATTAs have a steep power law ω^α , where α is between 2 and 3, with a single large peak at the annual frequency. The amplitude of this peak diminishes with latitude and vanishes for paths 9 and 10.

Remote only (E2)

In this case there is no windstress and the model is driven only by the remote Kelvin signal. The Kelvin waves travel poleward along the coast at speed $c = \sqrt{gH}$ and propagate into the Pacific basin as mid-latitude Rossby waves [Enfield and Allen, 1980; Johnson and O'Brien, 1990a, 1990b]. The dynamics of coastal Kelvin waves have been studied elsewhere [e.g., Moore, 1968; Anderson and Gill, 1975; Anderson and Rowlands, 1976; McCreary, 1976; Clarke, 1983] and will not be discussed in detail, except where it relates to the properties of the ATTA estimates.

Kelvin waves are nondispersive and can incorporate all frequencies; whereas, Rossby waves are dispersive and have a high-frequency cut-off, ω_c . Only the low-frequency part of the Kelvin signal can be converted to Rossby waves. The dispersion of linear mid-latitude quasi-geostrophic Rossby waves [e.g., Gill, 1982] is given by

$$\omega = \frac{-\beta k}{k^2 + l^2 + f^2/c^2} \quad (12)$$

where f is the Coriolis parameter, k is zonal wavenumber and l is meridional wavenumber. The negative sign implies westward phase propagation. See Fig. 6.

From (12), only Rossby waves with small wavenumber can propagate energy westward. The amplitude of the transmitted Rossby wave has been studied analytically by several authors, including White and Saur [1983], Grismshaw and Allen [1988] and McCalpin [1994]. They show a rapid decline in the westward propagation of energy around ω_c , falling to zero for frequencies near or above this critical frequency.

The critical wavenumber, where the group velocity of Rossby waves equals zero, is $k_c = fc^{-1}$. (For brevity, $l = 0$ is assumed.) The Rossby response loses progressively lower-frequency components at higher latitudes because $\omega_c = \cot(\theta)$. Over the model domain ω_c goes from roughly $4.2 \times 10^{-7} \text{s}^{-1}$ (175 d) at 20°N to roughly $1.8 \times 10^{-7} \text{s}^{-1}$ (390 d) at 50°N . The annual cycle of $\omega_a = 2 \times 10^{-7} \text{s}^{-1}$ is reached near 45°N .

The mean circulation for experiment E2 is shown in Fig. 7. A very different structure is seen than in the wind only case. There is no large-scale gyre but regions of cyclonic vorticity are found pinned to the coast at eddy-formation sites [Liu and O'Brien, 1994].

Some examples of instantaneous ULT anomalies are in Fig. 8. Changes in H are induced by Rossby waves from the coast whose meridional structure is the result of topographic influences [Liu and O'Brien, 1994]. Propagation of these waves is clearly

seen in the longitude-time diagram of Fig. 9. Additional discussion of the Rossby features can be found in Pares-Sierra and O'Brien [1989] and Johnson and O'Brien [1990a]. Comparison to observations of ocean temperature at 300 m [Shriver et al., 1991] shows that these waves account for almost 50% of the temperature variance in the NEP.

The relation of ULT perturbation to $H_{eq}(t)$ is investigated through sample time series of ULT from points A, B and C in Fig. 1. The cross-correlations of ULT at these points to $H_{eq}(t)$ are in Fig. 10. The maximum correlation occurs at a time delay, τ_m , that corresponds to the time it takes for the Rossby signal to propagate to the point in question. Point A, the southernmost point, has $\tau_m \simeq 1.3$ years with a correlation near 0.7. Point C has a $\tau_m = 2.3$ years with a correlation of 0.5. Point B is so far from the coast that dissipation has significantly decreased the wave amplitude. Nevertheless, there is a correlation peak of over 0.4 at $\tau_m \simeq 6$ years. This confirms that the Rossby waves survive for years after their separation from the coast while retaining the essential form of $H_{eq}(t)$. Therefore, unusually strong or long-lasting ENSO events can have repercussions at large oceanic scales years after the official event termination through oceanic teleconnection. (See also Jacobs et al. [1994]). Similar events are presumed to occur in the southern ocean, but this is beyond the scope of this study. Los Ninos do not die, they move to mid-latitudes.

The ATTAs estimated according to (11) for E2 are in Fig. 11. Most of the paths have small separations compared to the size of the Rossby waves in Fig. 8 and neighboring path ATTAs are strongly correlated. The average linear correlation of an ATTA measurement with the nearest path to the north is 0.94 ± 0.03 . Each path samples ocean characteristics only slightly different from its neighbor. The nearest northern path anomalies lag their southern neighbor by an average of 2-3 months, based on the average maximum cross-correlation. This lag is probably due to the slower group-velocity of Rossby waves at higher latitudes indicated as dashed lines in Fig. 1.

Power spectra of the travel time anomalies are in Fig. 12. They have no significant peaks, even at the annual frequency. Irregular interannual variations clearly dominate the signals so the broad spectra are probably due to the aperiodic nature of the ATTAs.

The ATTA signals exhibit a mean shift near 1976 towards positive values in the

lower paths (the shift occurs in 1978 in path 10, see Fig. 11) and a positive ATTA is maintained until roughly 1983. This is coincident with the Pacific climate shift of 1976-1982 as discussed below.

Combined winds and remote (E3)

Both surface windstress and the Kelvin signal drive the circulation in this case. The average ULT for E3 based on the years 1970-89 is shown in Fig. 13. The circulation is dominated by the large-scale gyre as in E1. The evolution of the California current system and its representation in this model is discussed in [Pares-Sierra and O'Brien, 1989].

A comparison of the circulations induced in E3 to those induced in E1 and E2 demonstrate the high (annual) frequency variations in this experiment are largely the result of direct wind forcing and the long-term variations largely result from the remote boundary forcing. Removal of the mean ULT and seasonal signal (which are dominantly wind-driven) leaves a response that closely matches the ULT in experiment E2, suggesting the a linear regime with the Rossby waves superposed on the wind-driven circulation. This is demonstrated by comparing the ULT anomalies in Fig. 15 to those in Fig. 8. They are almost identical in pattern and relative amplitude. The absolute amplitude is not the same because of the different background conditions. This implies that the calculations based on (11) will have properties of both E1 and E2.

Some ATTAs for E3 are in Fig. 16. They are, roughly, superpositions of cases E1 and E2, having strong annual and interannual variability very similar to that seen in Fig. 5 and Fig. 11 respectively. The longer term changes in Fig. 16a match those in Fig. 11a and the annual variations match those in Fig. 5a. The high latitude paths primarily show the same jagged structure as in case E1, except for a few multi-year periods when the Rossby signal is strong in the upper latitudes. There is a decrease in the higher frequencies at higher latitudes, as in both the previous cases. See Fig. 17.

E3 captures the essential physics that controls the depth of the permanent thermocline in the NEP. Understanding how SST relates to thermocline depth yields an indirect method for hindcasting SST using a reduced-gravity ocean model. This allows for an oceanic explanation for the anomalously warm SST field in the NEP in

the late 1970s and early 1980s, that is an alternative to the atmospheric explanations mentioned above.

The observed SST anomaly has a warming trend of winter values from the early 1970s to the late 1970s and early 1980s. This was first shown by differencing multi-year SST averages. A similar analysis is made of model ULT. The ULT change in Fig. 18 shows a mean raising of the permanent thermocline roughly coincident spatially and temporally with the change in SST. The SST does not relate to thermocline depth due to the presence of the seasonal thermocline. How the model ULT shift translates to an SST shift is discussed in the next section.

DISCUSSION

Acoustic travel time anomalies and Rossby waves

Interannual and interdecadal variability in the NEP model is driven mostly by Rossby waves coming off the coast of North America which are triggered by coastal Kelvin waves from the equatorial Pacific Ocean. ENSO extremes are particularly important since they generate strong coastal Kelvin waves that effect the Pacific basin for years after the official termination of an ENSO event.

The influence of the Rossby waves is easiest to understand when their effect is isolated (E2). Warm El Nino and cold El Viejo events defined by sea-level anomalies [Meyers and O'Brien, 1994] are shaded in Fig. 11a. The changes in thermocline depth associated with these events directly translates to changes in ATTA according to (11). Most of the strong ATTA declines are associated with warm events (related to a downwelling Kelvin wave) and rapid ATTA increases are associated with cold events (related to an upwelling Kelvin wave). The ATTA increases of 1975-76 and 1980-82 are not shaded due to our definition of El Viejo based on observational sea-level, which is not necessarily identical to events in the $H_{eq}(t)$ input.

The features of the ATTAs are easily understood. Consider path 1 in Fig. 11. In 1970 the decay of a previous cold event slowly increases the overall ATTAs towards zero. The 1972 El Nino creates a downwelling Rossby wave that decreases ATTA, but it is rapidly followed by a cold event that cancels its effect. Late 1974 to mid-1975 is a stable period as the Rossby waves slowly decay. A large El Viejo in mid-1975 feeds into the previous event and further decreases the overall ULT, increasing the ATTA. The 1976 El Nino is too weak to have a significant effect. The subsequent

two El Viejos are also weak, but are sufficient to maintain an overall thin ULT. The thin ULT anomalies begin to significantly decay in 1979 until the cold event of 1980-1981.

The large 1982-1983 El Nino produces a rapid decline in ATTA, in spite of the fact that downwelling Rossby waves still exist in the model basin. Its effect on the ATTA of path 1 is dominant until 1986 when the slowly decaying Rossby wave along the southern boundary begins to propagate outside the model domain. The 1987 El Nino is very weak and has no significant effect for path 1. The El Viejo of 1988 rapidly shifts the ATTA back toward zero.

Similar scenarios occur for each path, but due to spatial variations in the Rossby wave field important differences in ATTA occur over different paths. For example, the ATTA of path 5 in Fig. 11 is characterized by one broad peak from mid-1976 to 1980 and one trough from 1985 to mid-1987. Otherwise the ATTA hovers near zero. There is no effect of the 1977 warm event, the 1980 cold event, the large 1982-83 warm event or the 1987 cold event. The ATTA of path 5 lacks much of the structure of the ATTA for path 1 because path 5 connects to the coastline at a region of cyclonic eddy production. Near that location, the circulation associated with the Rossby waves are generally suppressed.

In the combined E3 case, the type of variations due to the Kelvin signal are superposed upon the somewhat weaker wind-driven variations. Over paths that avoid the Kelvin-Rossby signal, wind induced variations dominate. For instance, the higher latitude ATTAs are largely governed by the wind-driven ocean circulation. Only some ENSO events appear to be able to penetrate into higher latitudes and effect the ATTAs along these particular paths.

Kelvin generated Rossby waves are believed to be responsible for almost 50% of the variance of 300 m water off the coast of North American [Shriver et al., 1991]. That estimate was made by comparing observations of temperature to calculations from case E2. Understanding the Rossby wave variability will be important for interpreting acoustic measurements from the GAMOT/ATOC project. We anticipate that variations similar to those presented in Fig. 16 will be found, implying observations must be made over many years in order to correctly sample the long-term variability that is intrinsic to this region of the ocean.

Much of the interannual variability in the GAMOT observations should be pre-

dictable up to several years in advance from knowledge of the equatorial Pacific sea-level. The strong correlation between $H_e q(t)$ and H at mid-basin points (Fig. 10) shows that for paths that sample regions where the Rossby response is strong, the thermocline depth closely follows the equatorial signal.

Climate shift

Many authors including Graham [1994] and Miller et al. [1994] attribute the climate shift in the northern Pacific to atmospheric forcing. They can reproduce observational SST anomalies by specifying heat flux terms in numerical models. However, the ocean's role in creating these terms is ignored since they had no feedback from the ocean to the heat flux. Examining the hydrodynamic properties of the NEP in a high-resolution model driven by observational winds yields information on the thermocline depth and the increased horizontal resolution allows for correct representation of equatorial Kelvin waves that are the underlying physical mechanism of ENSO phenomenon in the ocean. These Kelvin waves impact the western coast of the Americas, propagate poleward along the coast and back into the Pacific basin as mid-latitude Rossby waves. Some Rossby waves appear to significantly influence the mean thermocline depth for several years.

A shift in the model ULT coincides with the observed shift in SST in the mid-1970s. The mean ULT from 1976-1981 minus the mean ULT from 1970-1975 is shown in Fig. 18. A thinning of the upper layer occurs over these years. This thinning corresponds to an upwelling of the permanent thermocline (PT). Above the permanent thermocline is a seasonal thermocline (ST) supporting the mixed layer. In the summer the ST is strong, but in the winter it is destroyed by atmospheric cooling and vertical mixing that transports the heat in the mixed layer down towards the PT [White and Walker, 1974]. If the PT is unusually deep, the heat from the mixed layer is spread over an especially large volume, creating anomalously low SST values. Conversely, if the PT is shallow then the SST anomaly is large. This is consistent with the model results that the ULT is thinner in the late 1970s than the early 1970s. It also explains the importance of winter observations since only in winter when the ST is weak is the depth of the PT important. No SST shift similar to that seen for the winter months is seen during the other seasons.

Whether this simple representation of the ocean can account for the mid-Pacific

SST shift remains unclear, since the western model limit is 155W and most of the Rossby energy is reduced by viscous action to very small values by the time it reaches 140W. A fully coupled ocean-atmosphere model that resolves the ENSO signals and includes a more complete representation of both the hydrodynamics and thermodynamics should be used to investigate this issue further. This will probably not be practical for several years and observations remain the final validator of these ideas.

The changes in SST off the American coast will have an effect on weather over the American continent. Other climatic changes in the Pacific are associated (though the causal connections are not fully understood) with a variety of weather changes in inhabited regions. It should lend a measure of predictability to annual to decadal climate forecasts if it can be shown that observational SST is predictable based on the state of the equatorial Pacific.

Acknowledgments. The Mesoscale Air-Sea Interaction Group acknowledges funds from the Secretary of the Navy Chair awarded to J.J.O. and from NOAA-OGP for TOGA. This research is supported by the Advanced Research Projects Agency grant SC25046 managed by Dr. Ralph Alewine and the Strategic Environmental Defense Program (SERDP) headed by Dr. John Harrison. Thanks for Mark Johnson for his important input on the model operation and ocean dynamics and to Detlev Muller for many useful discussions.

REFERENCES

- Anderson, D.L.T. and P.B. Rowlands, The role of inertia-gravity waves in the response of a tropical ocean to the incidence of an equatorial Kelvin wave on a meridional boundary. *J. Mar. Res.*, **34**, 295-312, 1976.
- Anderson D. and A.E. Gill, Spin-up of a stratified ocean with applications to upwelling. *Deep-Sea Res.*, **22**, 583-596, 1975.
- Baggeroer, A. and W. Munk, The Heard Island feasibility test. *Phys. Today*, **45**, 22-30, 1992.
- Bussalacchi and O'Brien. Busalacchi, A.J. and J.J. O'Brien, Interannual variability of the equatorial Pacific in the 1960's. *J. Geophys. Res.*, **86C**, 10901-10907, 1981.
- Camerlengo, A. L., and J. J. O'Brien, Open boundary conditions in rotating fluids, *J. Comp. Phys.*, **35**, 12-35, 1980.
- Cayan, D.R. et al. Introduction in *Geophysical Monograph 55: Aspects of Climate Variability in the Pacific and the Western Americas*, edited by D.H. Peterson, pp. xi-xvi, AGU, Washington D.C., 1989.
- Clarke, A.J., The reflection of equatorial waves from oceanic boundaries, *J. Phy. Oceanogr.*, **13**, 1193-1207, 1983
- Cook, E. et al., Climatic change in Tasmania inferred from a 1089-year tree-ring chronology of Huon pine, *Science*, **253**, 1266-1268, 1991.
- Cushman-Roisin, B. and J.J. O'Brien, The influence of bottom topography on baroclinic transports, *J. Phys. Oceanogr.*, **13**, 1600-1611, 1983.
- Enfield D. and J.S. Allen, On the structure and dynamics of monthly mean sea level anomalies along the Pacific Coast of North and South America. *J. Phys. Oceanogr.*, **10**, 557-578, 1980.
- Grimshaw R. and J.S. Allen, Low-frequency baroclinic waves off coastal boundaries, *J. Phy. Oceanogr.*, **18**, 1124-1143, 1988.
- Gill, A.E. *Atmosphere-Ocean Dynamics*. Academic Press, New York, 1982.
- Graham, N.E., Decadal scale variability in the 1970's and 1980's: Observations and model results, *Clim. Dyn.*, **10**, 60-70, 1994.
- Inoue, M. and J.J. O'Brien, The trends in sea level in the western and central equatorial Pacific during 1974/75-1981, *J. Geophys. Res.*, **92C**, 5045-5051, 1987.
- Jacobs, G.A. et al., A decadal impact of the 1982-83 El Nino. submitted *Nature*, 1994.
- Johnson, M. and J.J. O'Brien, The northeast Pacific Ocean response to the 1982-1983 El Nino. *J. Geophys. Res.*, **95C**, 7155-7166, 1990a.
- Johnson, M. and J.J. O'Brien, Modeling the Pacific Ocean. *Int. J. Supercom. App.*, **4**,

37-47, 1990b.

Kamachi, M. and J.J. O'Brien, Continuous data assimilation of drifting buoy trajectory into an equatorial Pacific Ocean model, submitted to *J. Mar. Sys.*, 1994.

Kitoh, A., Interannual variations in an atmospheric GCM forced by the 1970-1989 SST.

Part II: Low frequency variability of the wintertime northern hemisphere extratropics, *J. Meteor. Soc. Japan*, 69, 169-181, 1991.

Liu M. and J.J. O'Brien, personal communication.

McCalpin, J.D., Rossby wave generation by poleward propagating Kelvin waves: the mid-latitude, quasigeostrophic approximation, submitted to *J. Phy. Oceanogr.*, 1994.

McCreary, J., Eastern tropical ocean response to a changing wind system: with application to El Nino, *J. Phy. Oceanogr.*, 6, 632-645, 1976.

Meyers, S.D. and J.J. O'Brien. The influence of ENSO on Mauna Loa carbon dioxide and a prediction for 1994, submitted to *Nature*, 1994.

Miller, J.A., et al., Interdecadal variability of the Pacific Ocean: model response to observed heat flux and wind stress anomalies. *Clim. Dyn.*, 9, 287-302, 1994.

Moore, D.W., Planetary-gravity waves in an equatorial ocean. PhD thesis, Harvard University, 1968.

Mysak, L.A. et al., Sea-ice anomalies observed in the Greenland and Labrador Seas during 1901-1984 and their relation to an interdecadal Arctic climate cycle, *Clim. Dyn.*, 5, 111-133, 1990.

Oceanic Interdecadal Climate Variability, (United Nations Educational, Scientific and Cultural Organization, Paris, 1992).

Pares-Sierra, A. and J.J. O'Brien, The seasonal and interannual variability of the California Current system: A numerical model, *J. Geophys. Res.*, 94C, 3159-3180, 1989.

O'Brien, J. J. and F. Parham, Equatorial Kelvin waves do not vanish, *Mon. Wea. Rev.*, 120, 1764-1766, 1992.

Roed, L.P., personal communication, 1994.

Salmon, D., On the interannual variability and climate change in the north Pacific, PhD. thesis, University of Alaska, 1992.

Shriver et al., Analysis of remotely forced oceanic Rossby waves off California, *J. Geophys. Res.*, 96C, 749-757, 1991.

Spiesberger, J.L. and K. Metzger, Basin-scale tomography: A new tool for studying weather and climate, *J. Geophys. Res.*, 96C, 4869-4889, 1991.

Spiesberger et al., Listening for climatic temperature change in the northeast Pacific: 1983-1989, *J. Acous. Soc. Amer.*, 92, 384-397, 1992

- Trenberth, K.E., Recent climate changes in the Northern hemisphere, *Bull. Ameri. Meteor. Soc.*, **71**, 988-993, 1990.
- White, W.B. and A.E. Walker, Time and depth scales of anomalous subsurface temperature at ocean weather stations P, N and V and in the north Pacific. *J. Geophys. Res.*, **79**, 4517-4522, 1974.
- White, W. and J. Saur, Sources of interannual baroclinic waves in the eastern subtropical north Pacific, *J. Phy. Oceanogr.*, **19**, 531-544.
- White et al. Annual Rossby wave characteristic in the California current region from the GEOSAT exact repeat mission. *J. Phy. Oceanogr.*, **20**, 1297-1311, 1990.

FIGURE CAPTIONS

Fig. 1. The domain of the numerical model. The arcs are great circle paths (geodesics) over which acoustic properties are estimated. They are close to those that will be used in the early GAMOT/ATOC field observations. The final latitudes of each are (1) 21.23 (2) 22.84 (3) 24.66 (4) 26.46 (5) 28.47 (6) 30.75 (7) 33.25 (8) 35.91 (9) 40.00 (10) 47.15. The dashed lines mark the estimated yearly propagation of a 1000 km Rossby wave starting from the right-most dashed line, assuming $l = 0$ and $c = 3$ m/s. The indicated points A, B and C are specifically sampled as described in the text.

Fig. 2. The heavy line is the input anomaly from the equatorial model, $H_{eq}(t)$. The thin line is a five month running mean. The dark shaded regions denote cold ENSO events and the light shaded regions are warm ENSO events defined by sea level anomaly.

Fig. 3. The 1970-1989 mean upper layer thickness for E1. The contour levels are in meters.

Fig. 4. A longitude-time diagram along 20°N of H with the mean and seasonal signals removed. From E1. The contour levels are in meters.

Fig. 5. The travel time anomalies from (11) for the E1 experiment. The travel paths are shown in Fig. 1.

Fig. 6. The dispersion diagram for mid-latitude Rossby waves. The circles are lines of constant frequency. The dotted line demarks the local maximum frequency where $c_g = 0$.

Fig. 7. The 1970-1989 mean upper layer thickness for E2. The contour levels are in

meters.

Fig. 8. The ULT for case E2 on two different days. The mean H_0 has been removed. (a) During an El Nino. A strong downwelling Kelvin wave has propagated up the coast and is beginning to separate. (b) one year later, the Rossby wave has entered the Pacific basin.

Fig. 9. As in Fig. 4 but for case E2.

Fig. 10. The cross-correlations of $H_e q(t)$ with the time series from the three points in Fig. 1. (a) point A, (b) point B, (c) point C.

Fig. 11. As in Fig. 5 but for the remote-only case (E2).

Fig. 12. The power spectrum for the ATTA from Fig. 11. Pre-whitening was used and the linear trend and mean were removed before the analysis.

Fig. 13. The 1970-1989 mean upper layer thickness of the E3.

Fig. 14. As in Fig. 4 but for case E3.

Fig. 15. ULT anomalies for the E3 case with the mean H field removed. Dates and conditions are as in Fig. 8.

Fig. 16. As in Fig. 5 but for the remote and wind case (E3).

Fig. 17. As in Fig. 12 but for E3.

Fig. 18. The mean 1976-1981 ULT minus the mean 1970-1975 ULT. Contour levels are in meters. ***northern boundary

TABLES
Model Parameters

Parameter	Symbol	Value
radius of Earth	a	$6.3784 \times 10^6 \text{ m}$
eddy viscosity	A	$400 \text{ m}^2/\text{s}$
drag coefficient	C_D	1.5×10^{-3}
mean ULT	H_0	175 m
reduced gravity	g'	0.03 m/s
phase speed	$c = \sqrt{g'H}$	2.3 m/s
grid size	$\Delta\phi, \Delta\theta$	$1/12^\circ$
time step	Δt	10 min
Earth's rotation	Ω	$7.29 \times 10^{-5} \text{ s}^{-1}$

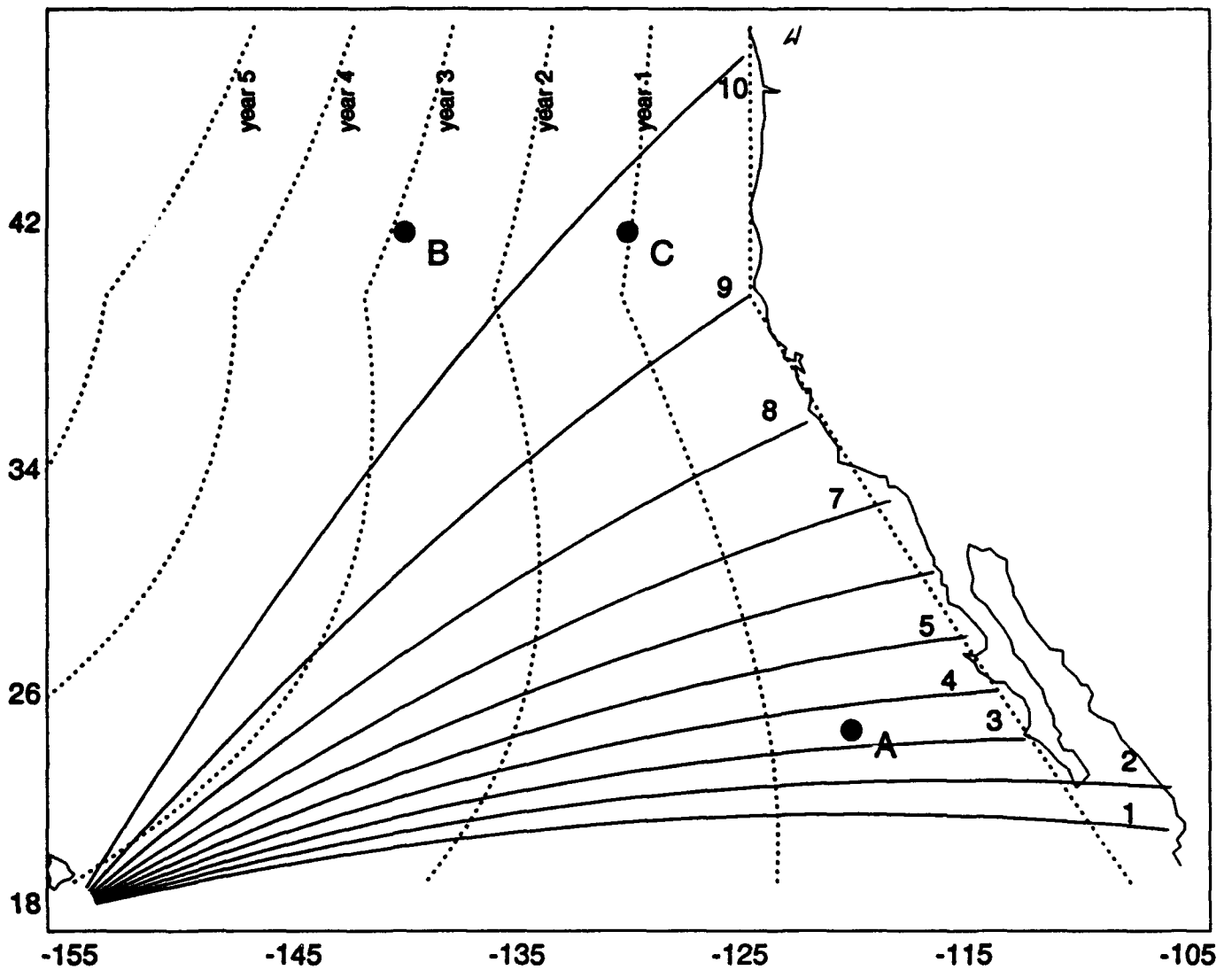


Fig. 1. The domain of the numerical model. The arcs are great circle paths (geodesics) over which acoustic properties are estimated. They are close to those that will be used in the early GAMOT/ATOC field observations. The final latitudes of each are (1) 21.23 (2) 22.84 (3) 24.66 (4) 26.46 (5) 28.47 (6) 30.75 (7) 33.25 (8) 35.91 (9) 40.00 (10) 47.15. The dashed lines mark the estimated yearly propagation of a 1000 km Rossby wave starting from the right-most dashed line, assuming $l = 0$ and $c = 3$ m/s. The indicated points A, B and C are specifically sampled as described in the text.

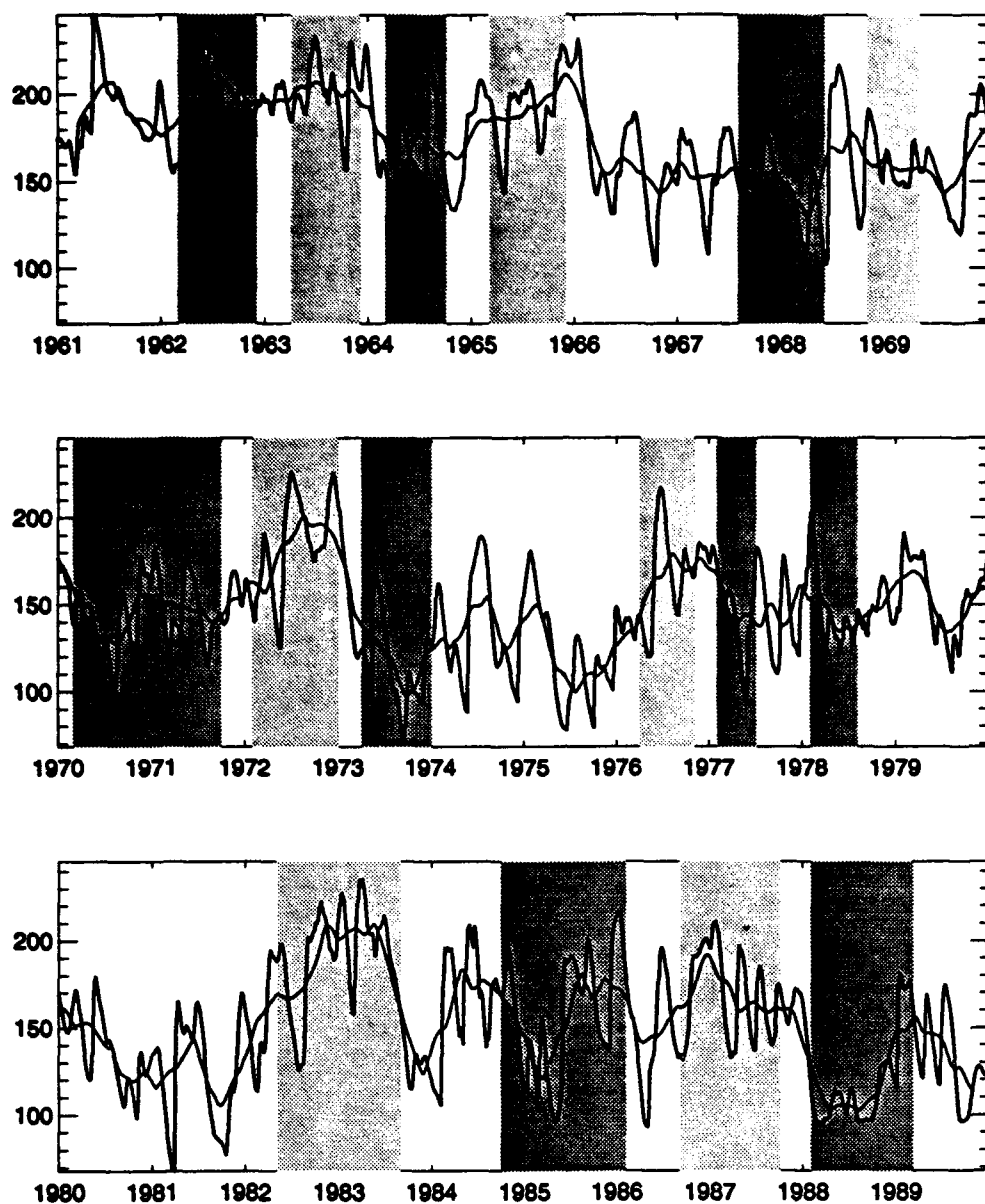


Fig. 2. The heavy line is the input anomaly from the equatorial model, $H_{eq}(t)$. The thin line is a five month running mean. The dark shaded regions denote cold ENSO events and the light shaded regions are warm ENSO events defined by sea level anomaly.

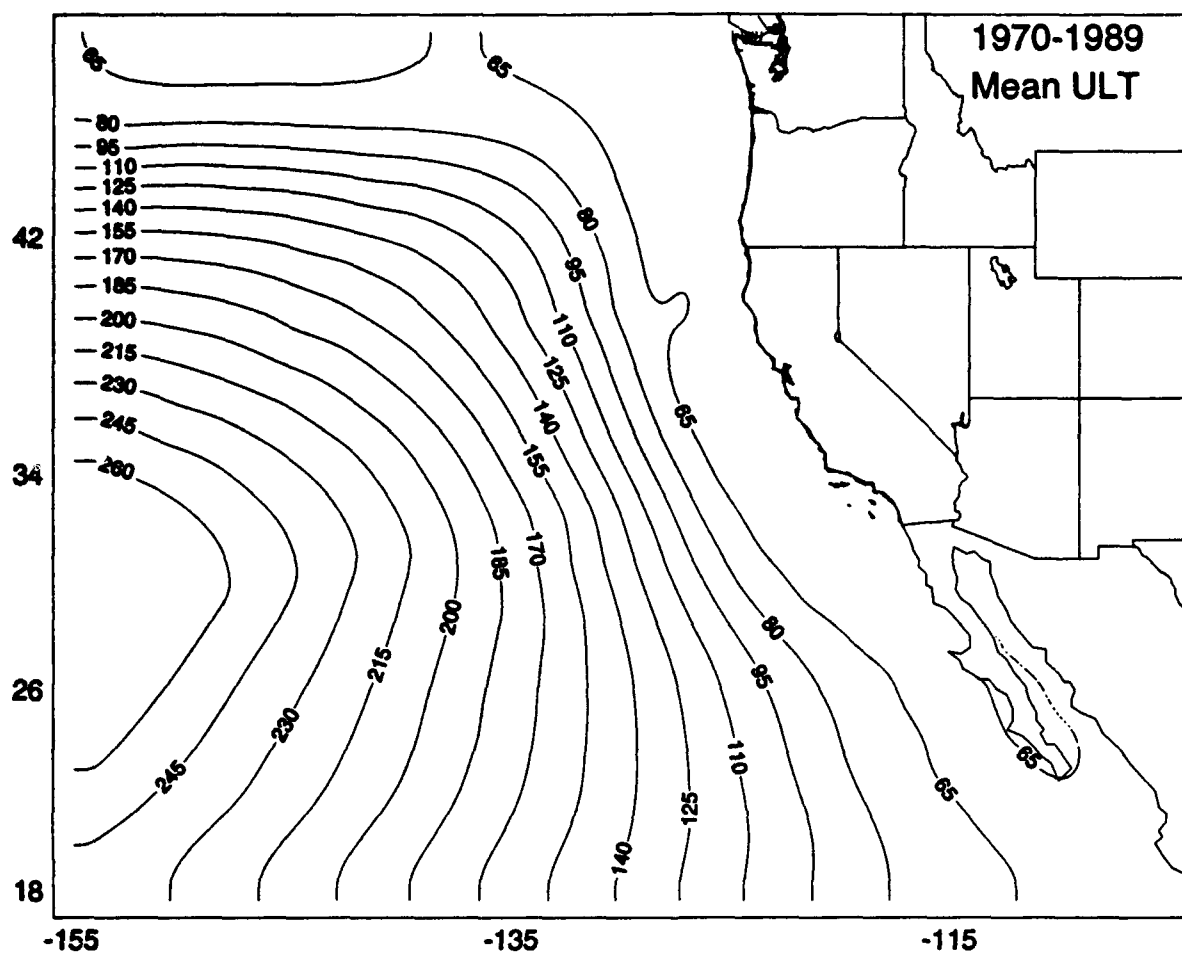


Fig. 3. The 1970-1989 mean upper layer thickness for E1. The contour levels are in meters.

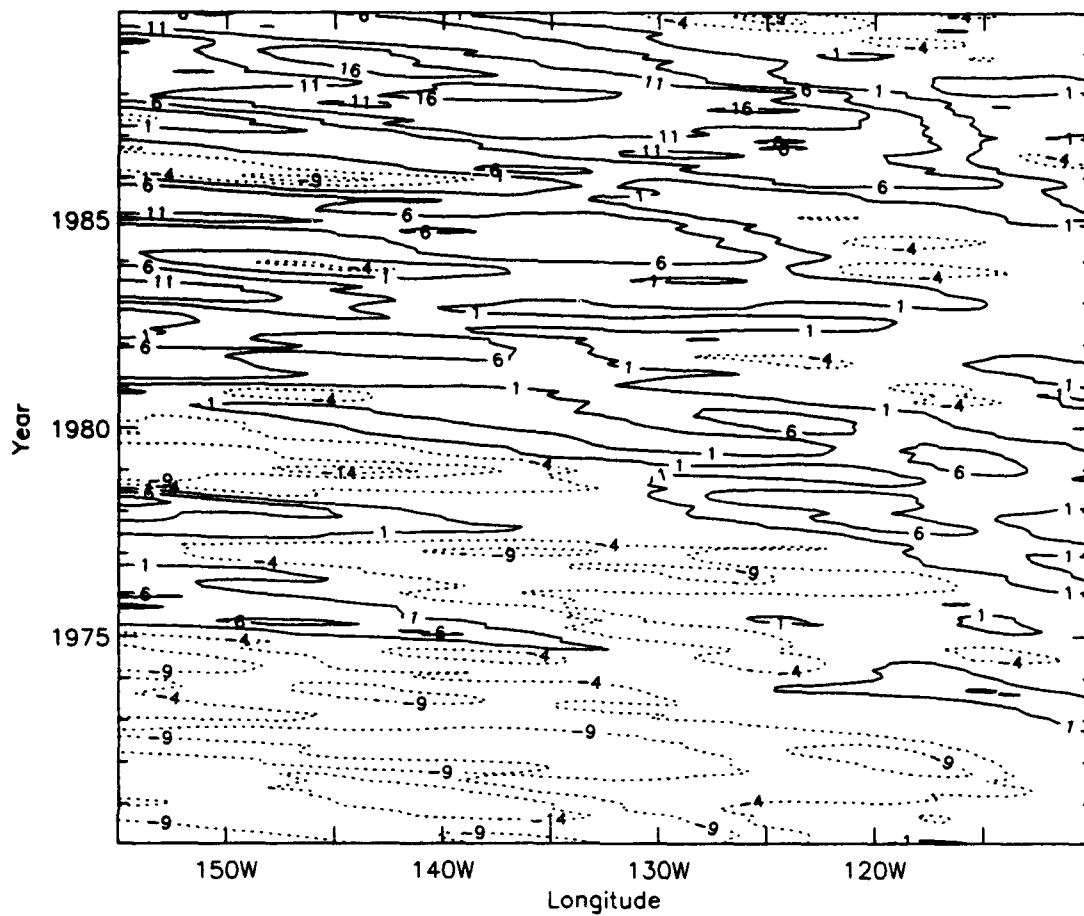


Fig. 4. A longitude-time diagram along 20°N of H with the mean and seasonal signals removed. From E1. The contour levels are in meters.

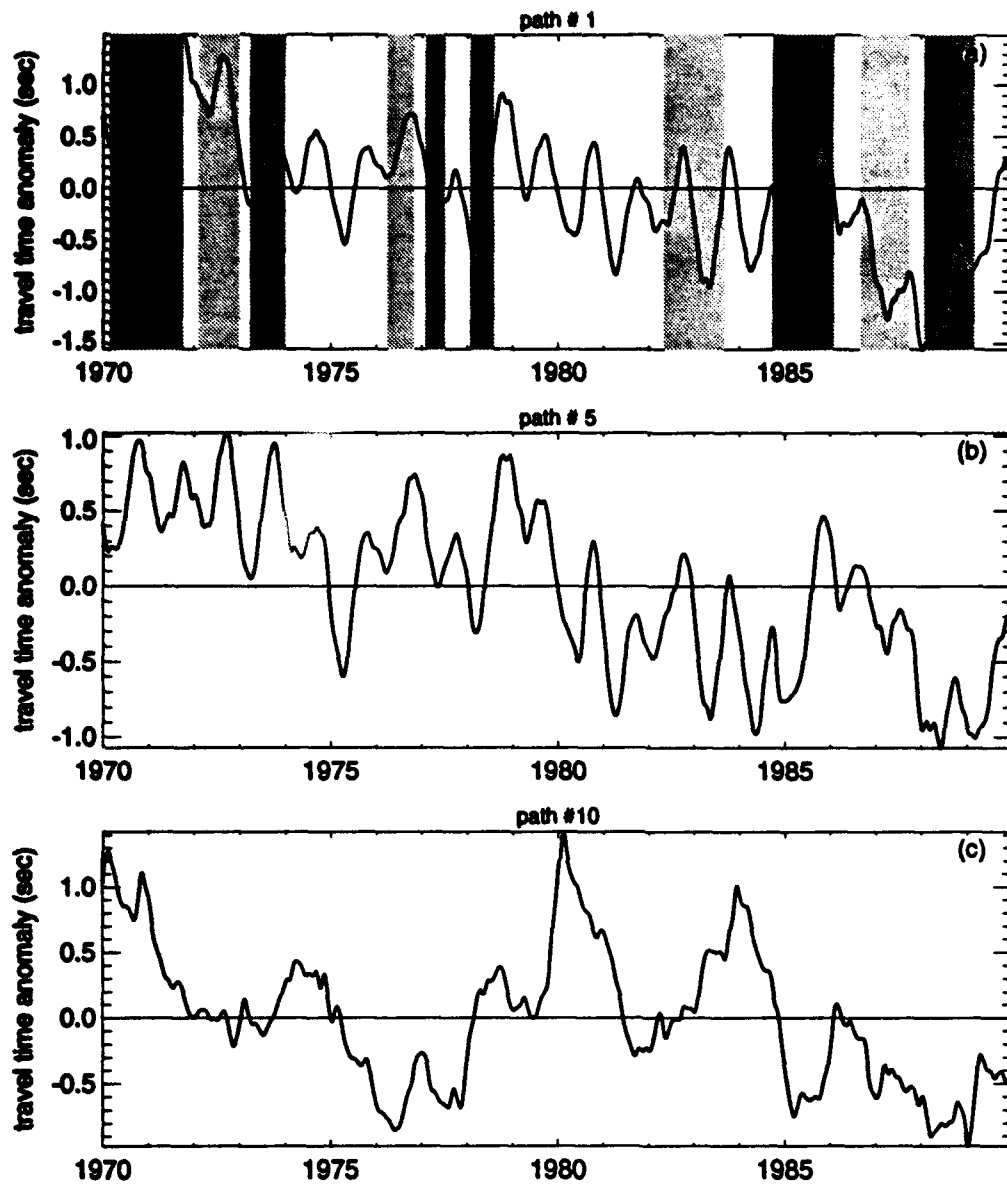


Fig. 5. The travel time anomalies from (11) for the E1 experiment. The travel paths are shown in Fig. 1.

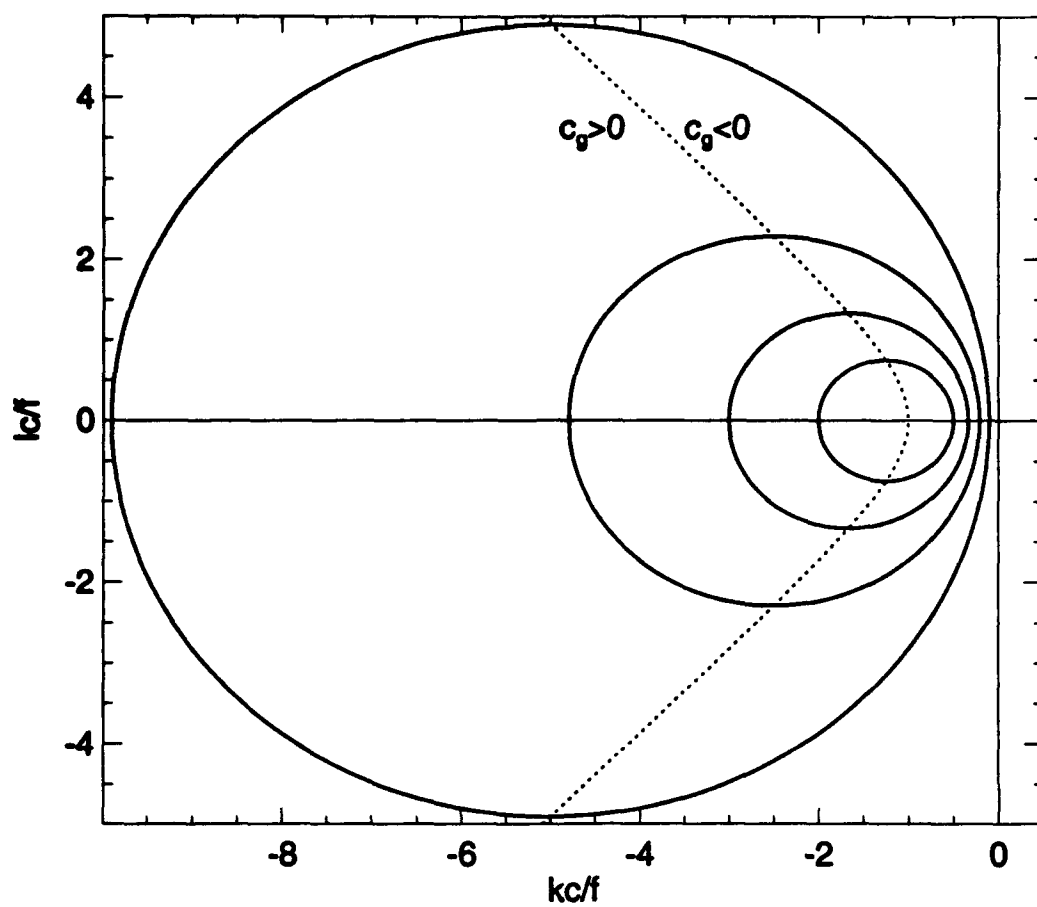


Fig. 6. The dispersion diagram for mid-latitude Rossby waves. The circles are lines of constant frequency. The dotted line demarks the local maximum frequency where $c_g = 0$.

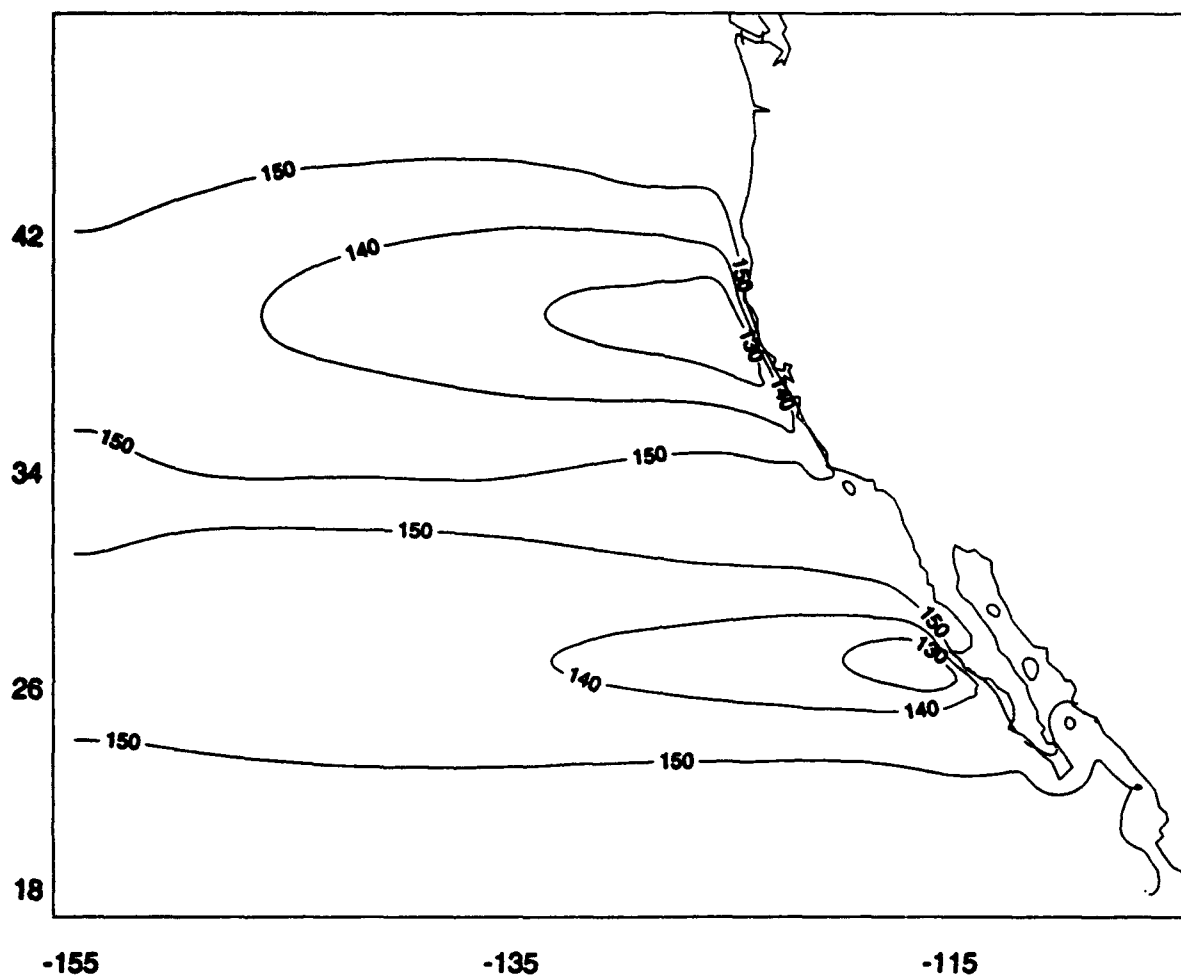


Fig. 7. The 1970-1989 mean upper layer thickness for E2. The contour levels are in meters.

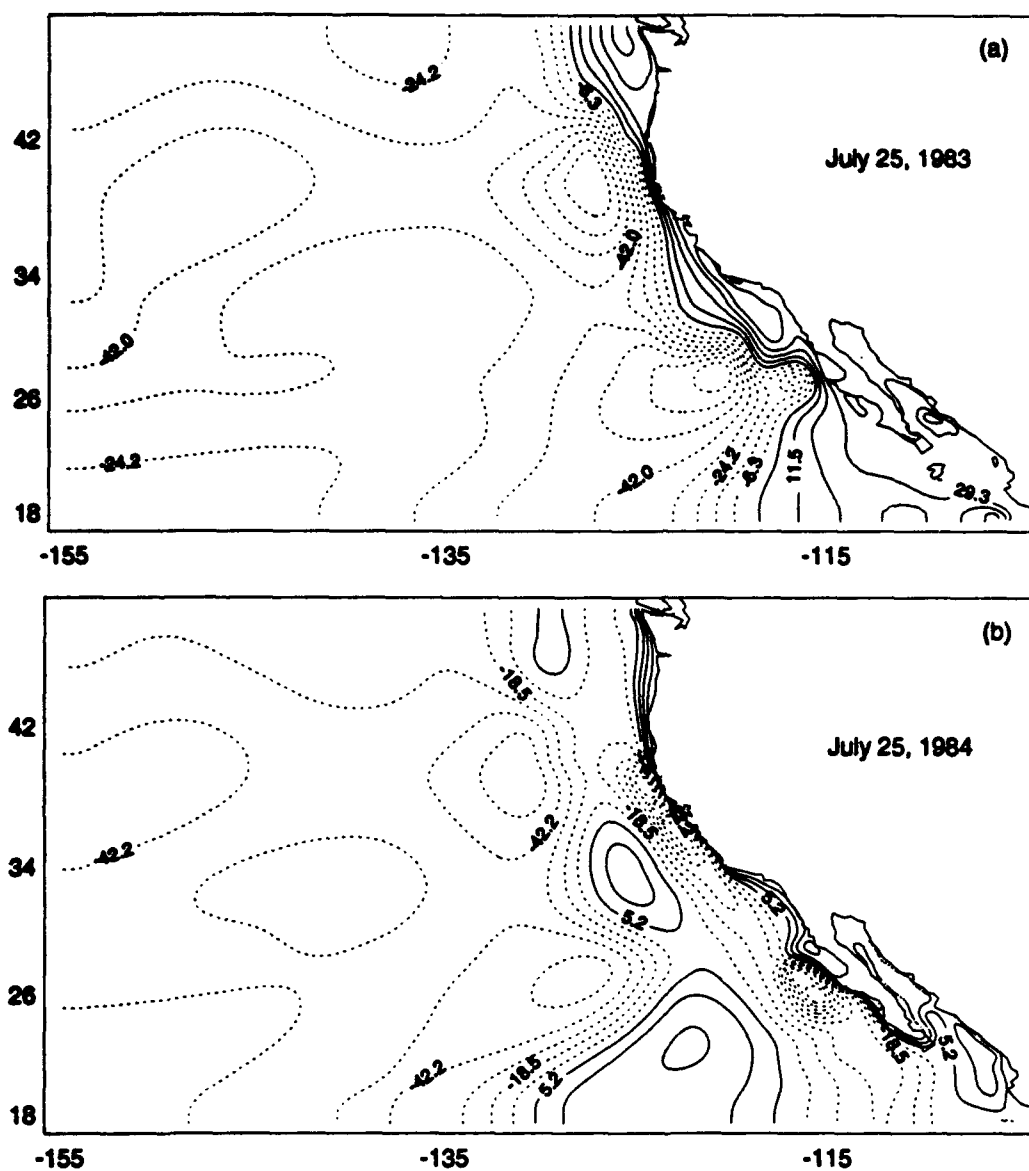


Fig. 8. The ULT for case E2 on two different days. The mean H_0 has been removed. (a) During an El Niño. A strong downwelling Kelvin wave has propagated up the coast and is beginning to separate. (b) one year later, the Rossby wave has entered the Pacific basin.

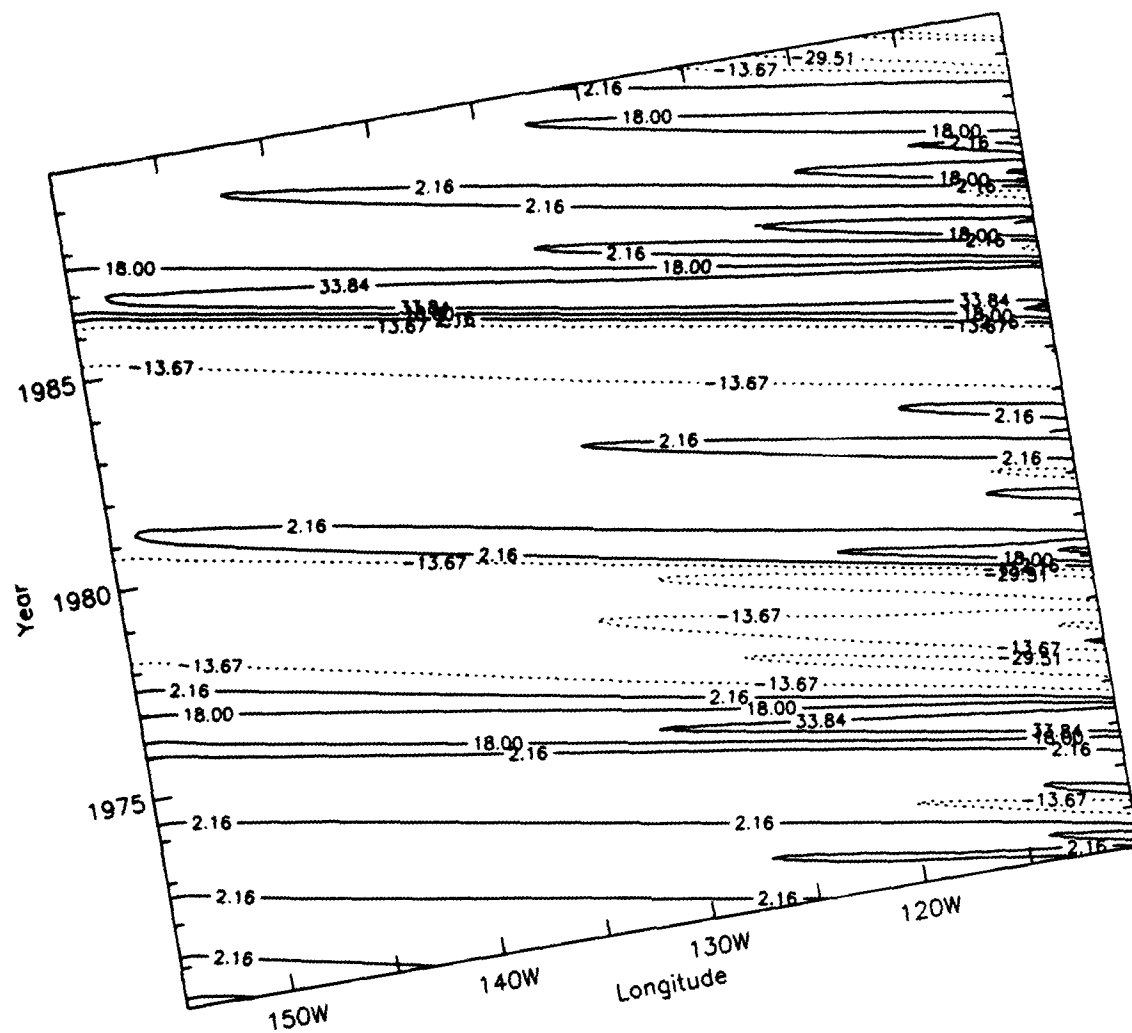


Fig. 9. As in Fig. 4 but for case E2.

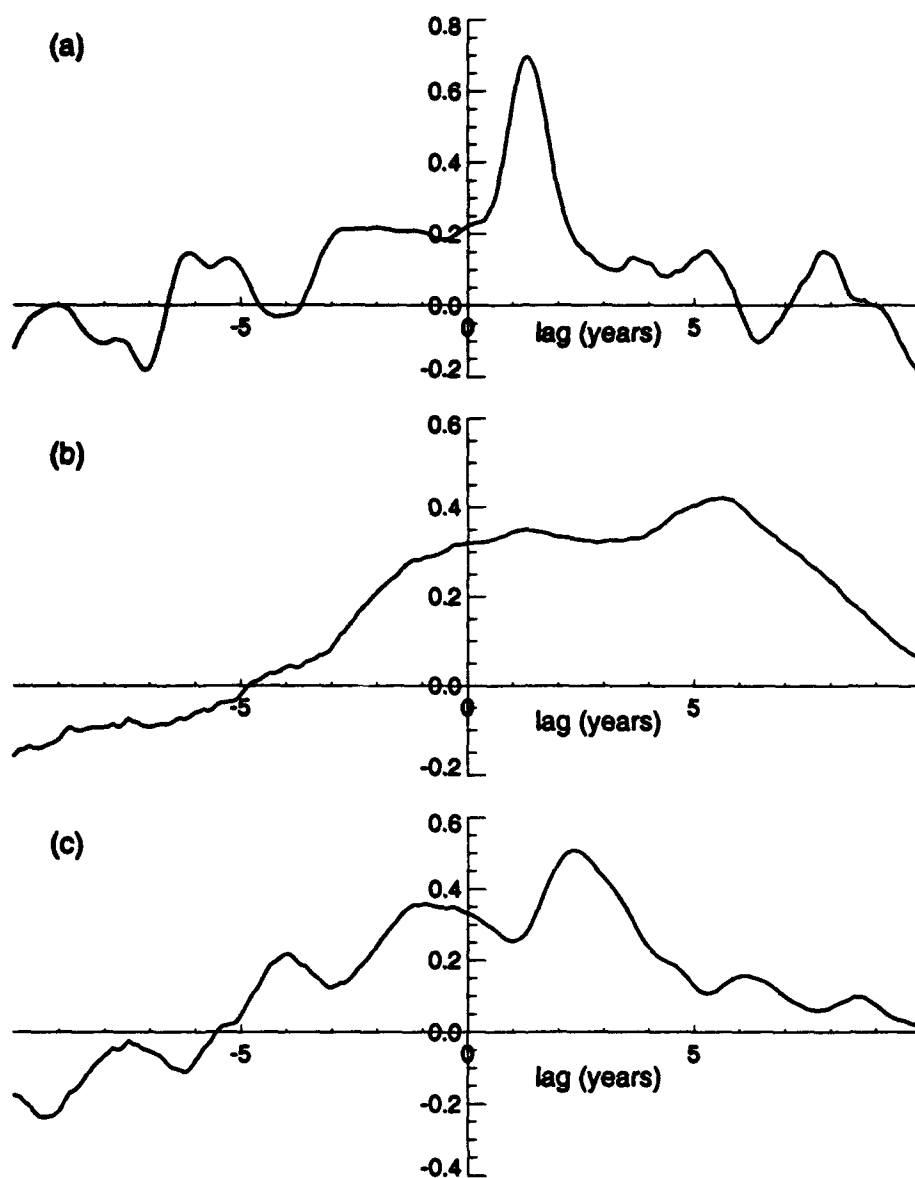


Fig. 10. The cross-correlations of $H_{eq}(t)$ with the time series from the three points in Fig. 1. (a) point A, (b) point B, (c) point C.

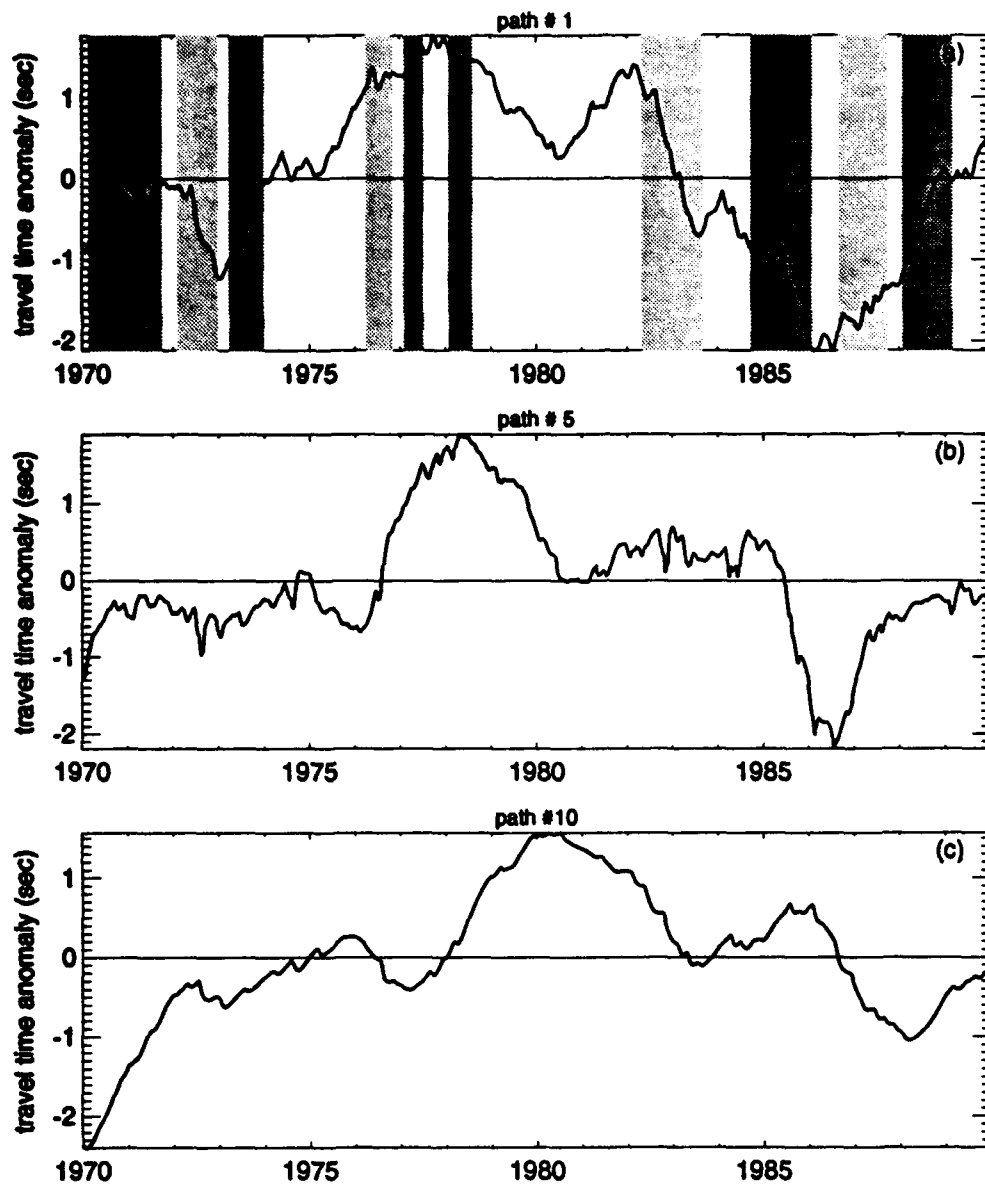


Fig. 11. As in Fig. 5 but for the remote-only case (E2).

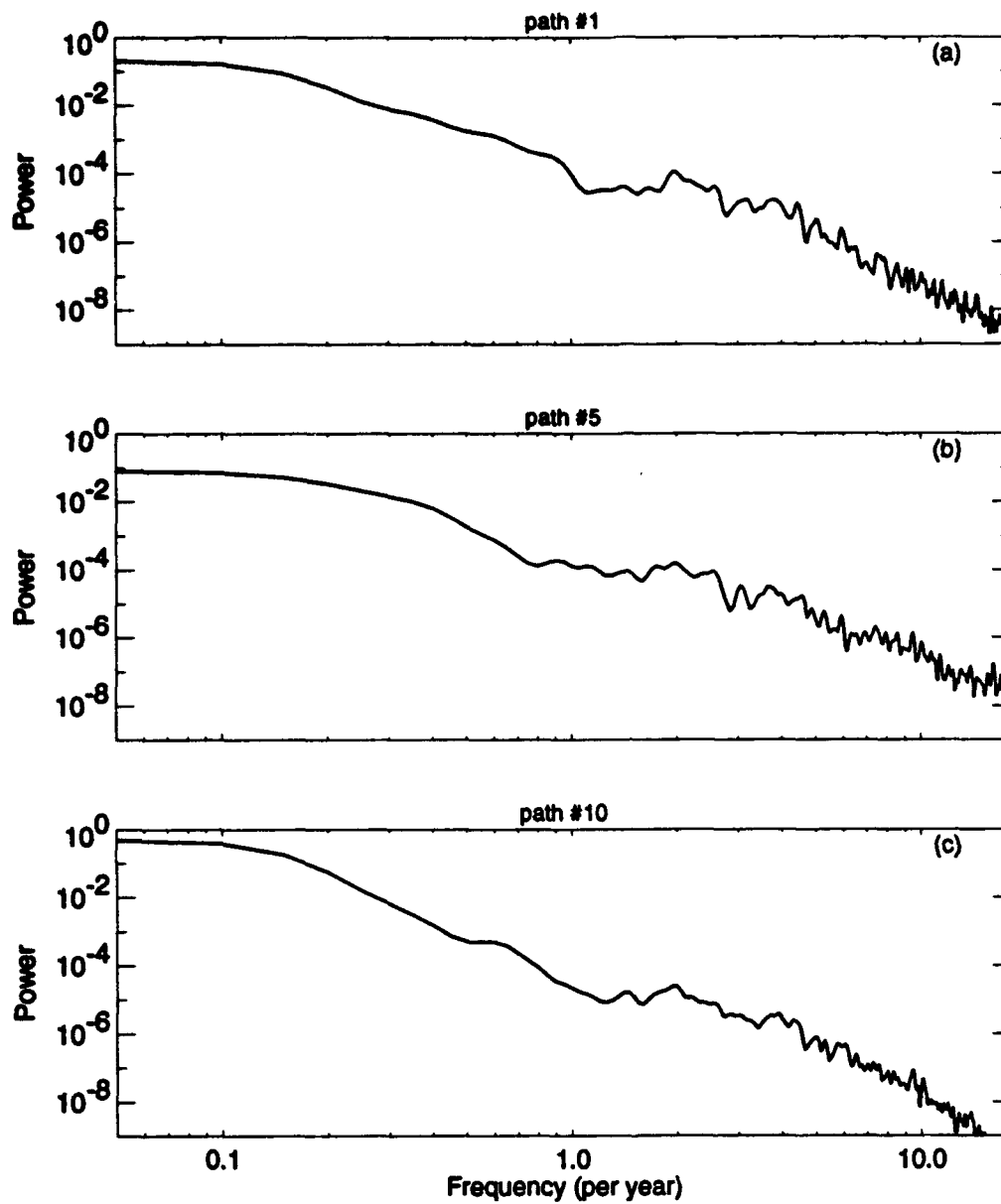


Fig. 12. The power spectrum for the ATTA from Fig. 11. Pre-whitening was used and the linear trend and mean were removed before the analysis.

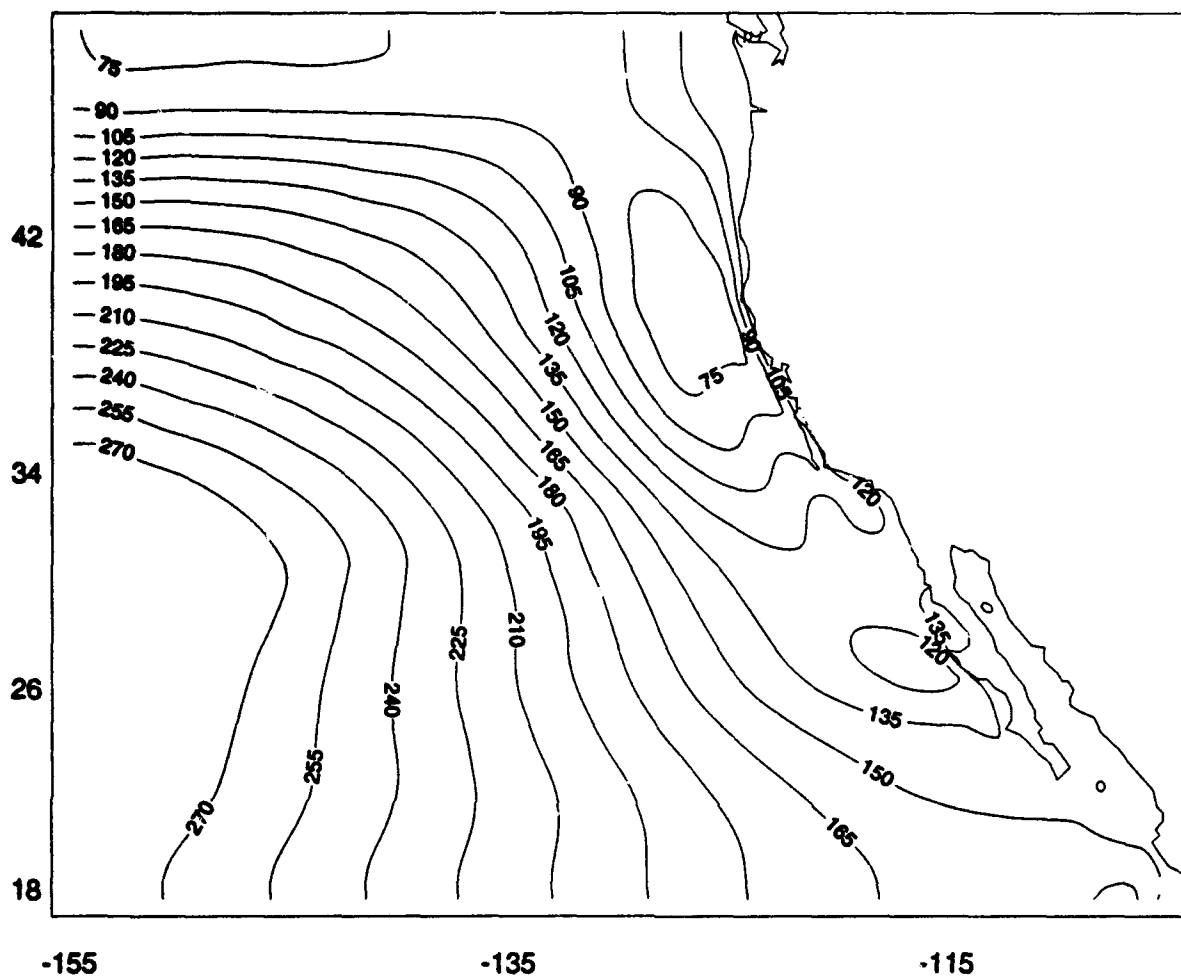


Fig. 13. The 1970-1989 mean upper layer thickness of the E3.

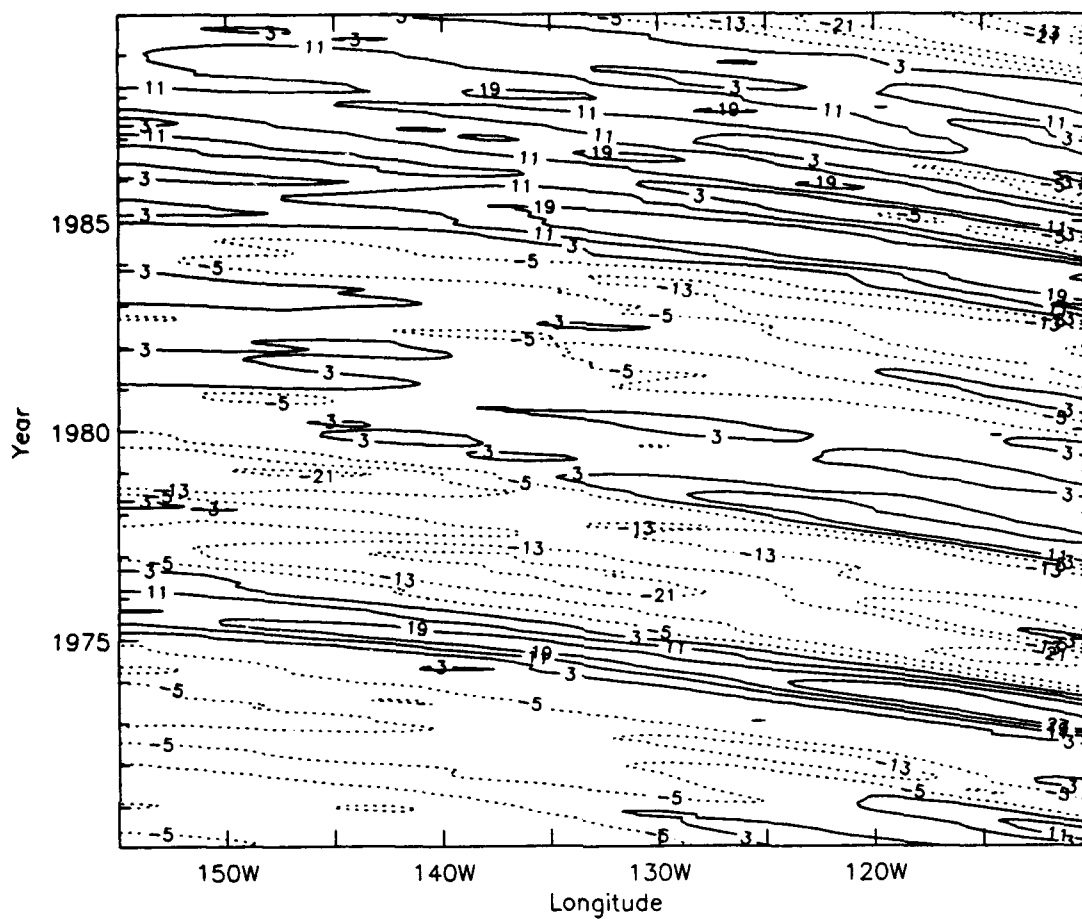


Fig. 14. As in Fig. 4 but for case E3.

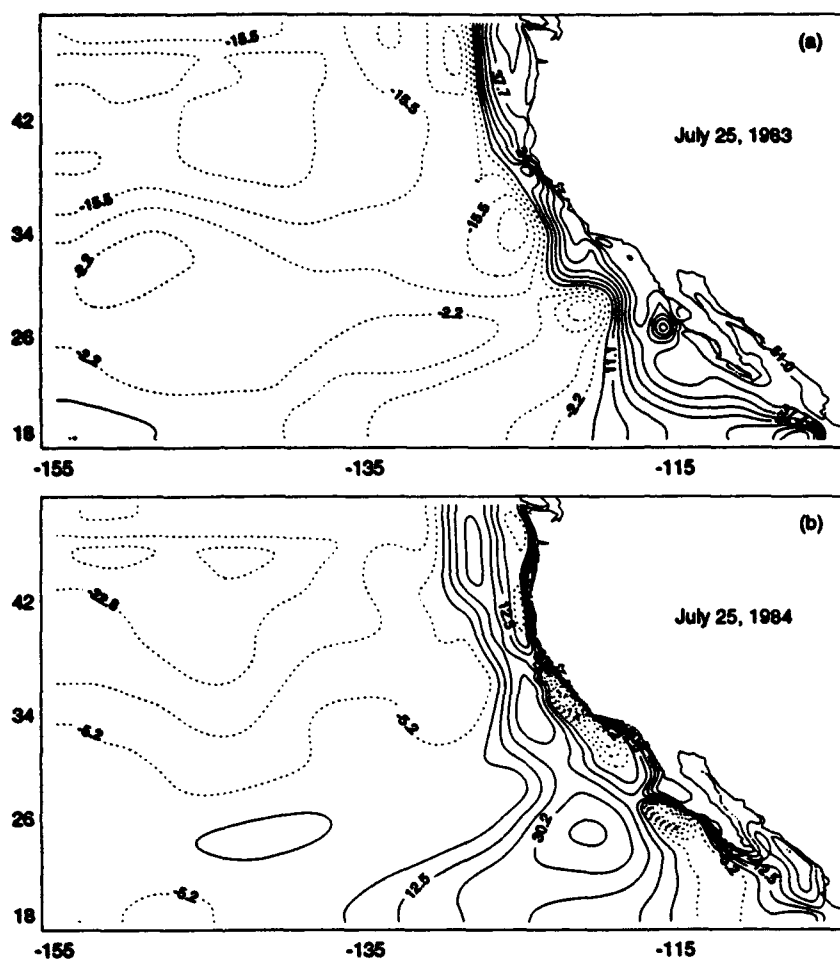


Fig. 15. ULT anomalies for the E3 case with the mean H field removed. Dates and conditions are as in Fig. 8.

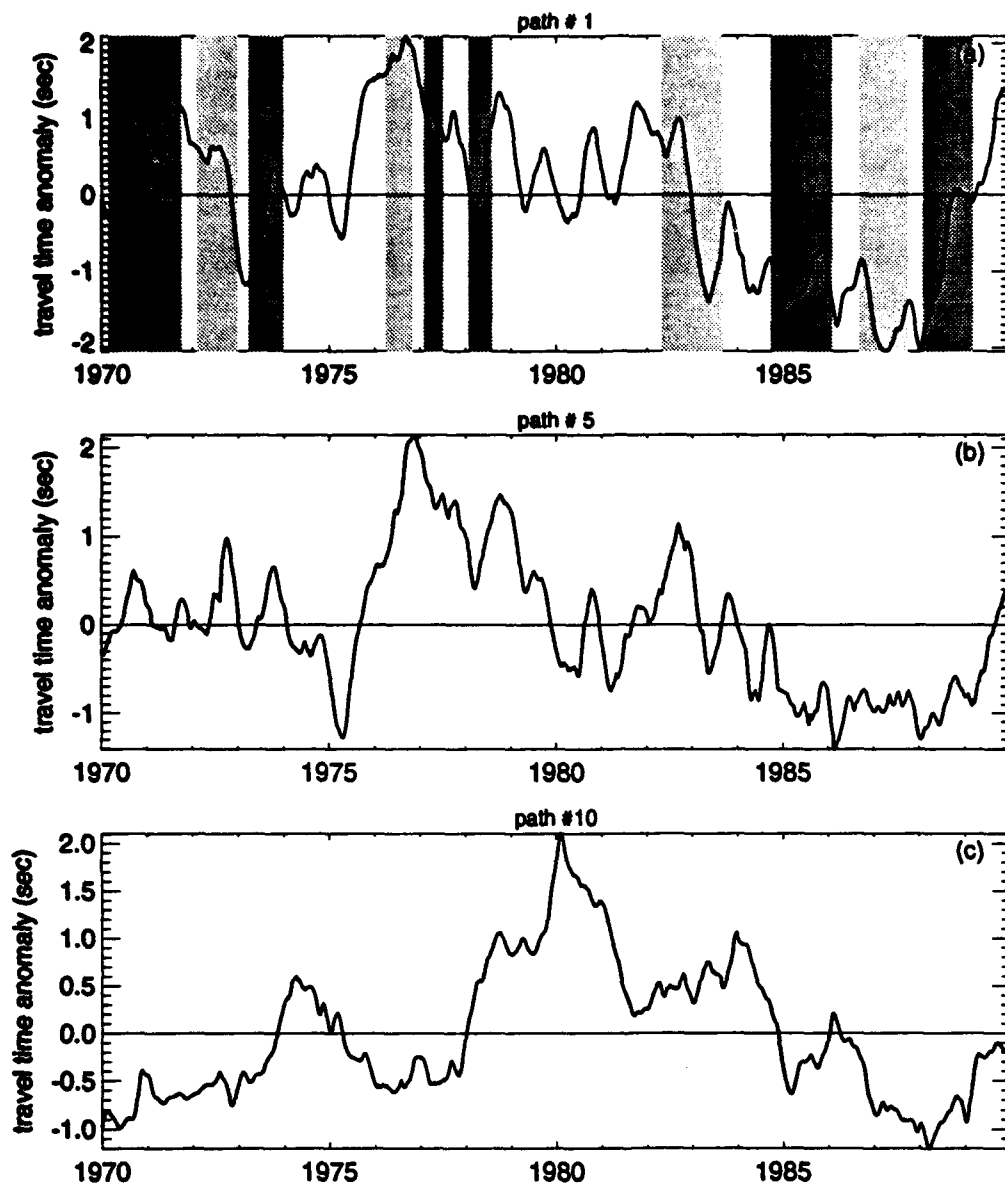


Fig. 16. As in Fig. 5 but for the remote and wind case (E3).

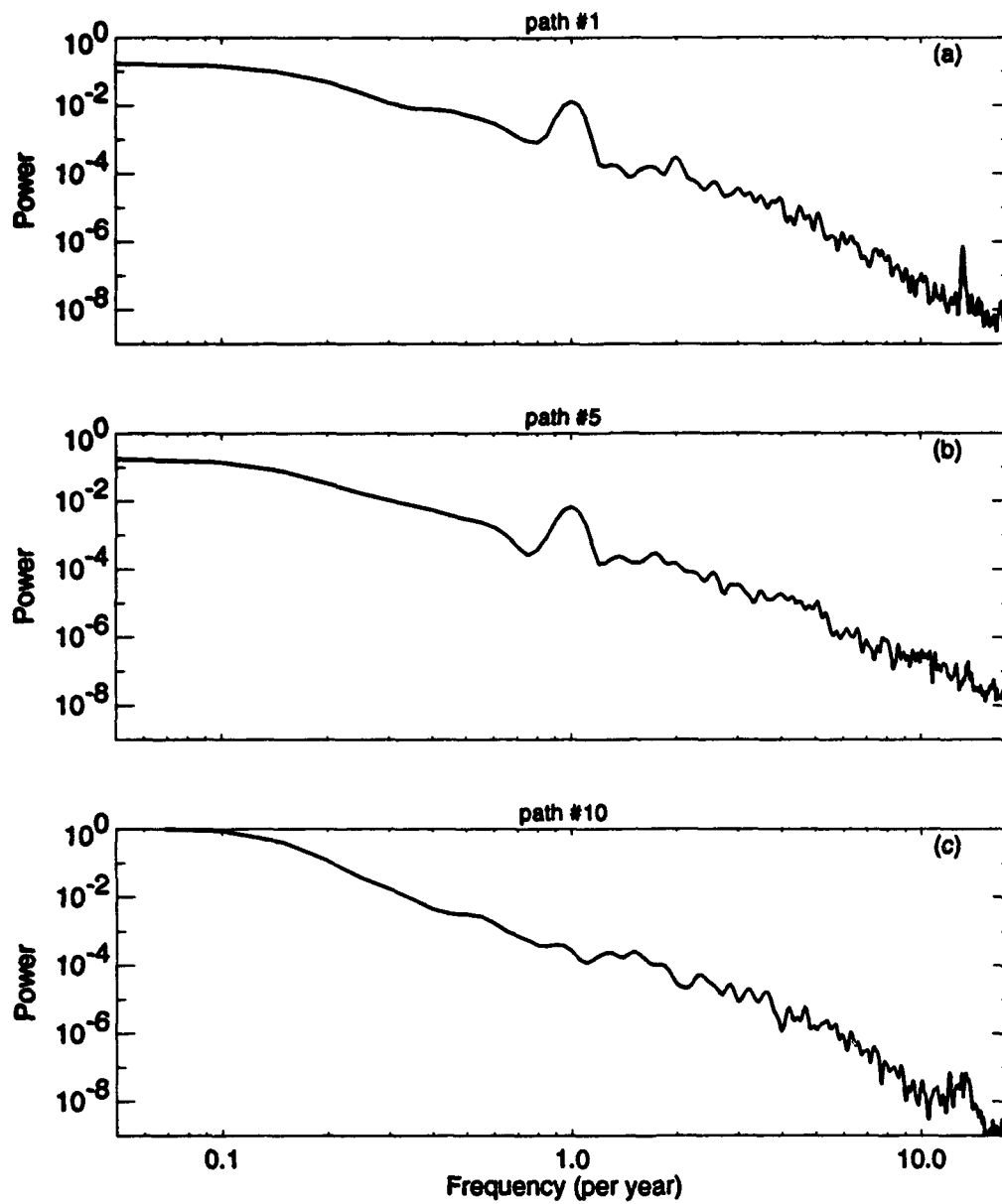


Fig. 17. As in Fig. 12 but for E3.

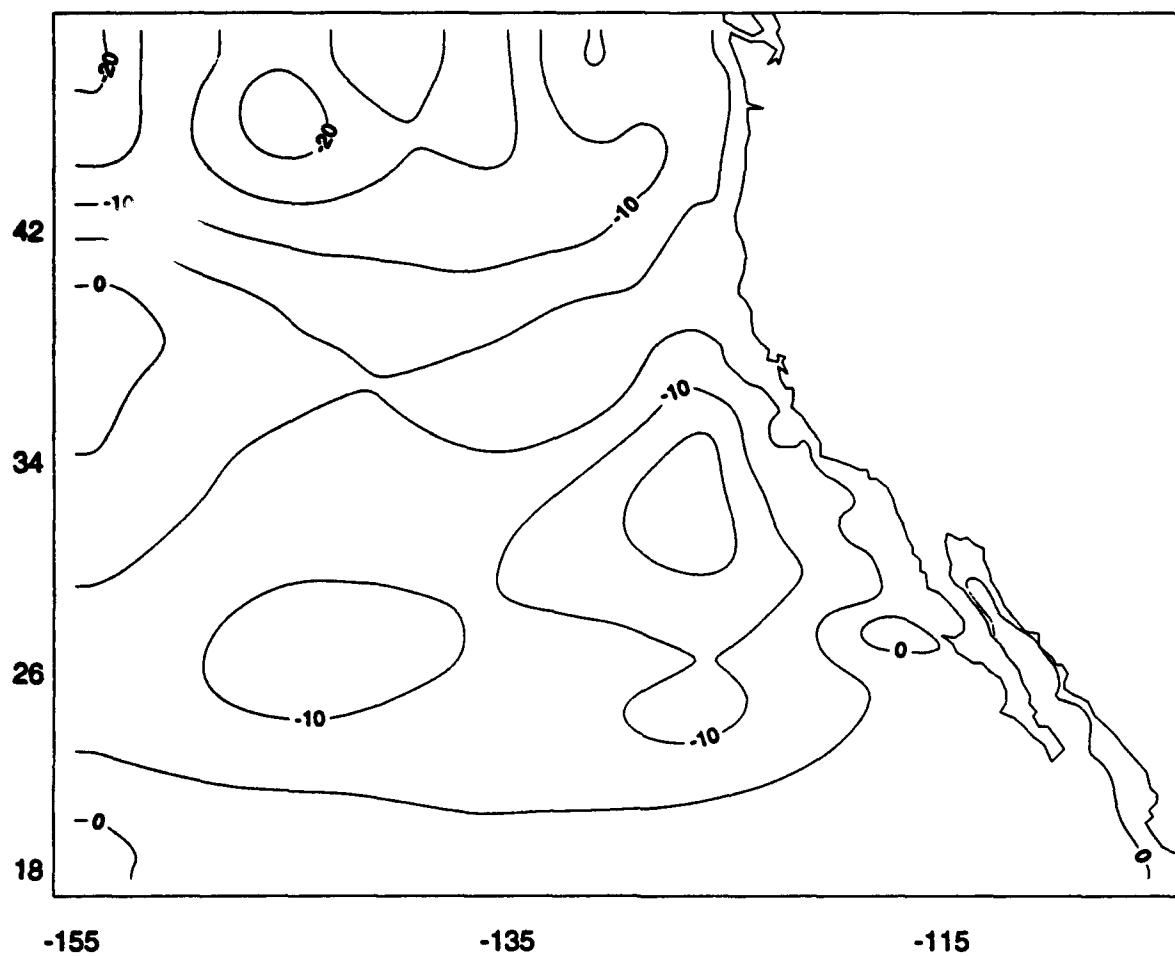


Fig. 18. The mean 1976-1981 ULT minus the mean 1970-1975 ULT. Contour levels are in meters. ***northern boundary

[illegible]

TASK C: SSAR DEVELOPMENT

New Conductor Assemblies For SSAR Hoses

Following the conductor failure experienced by the SSAR deployed offshore Bermuda in March 1994, two new conductor assemblies have been investigated. The first design, shown in Figure C.5 in the last Quarterly Report, used a combined stop rope and conductor assembly. It was built in prototype form, but was judged to be too inflexible to avoid the potential for abrasion on the inner hose wall. The second design, which eliminates the stop rope entirely (Figure C.1), uses a coiled conductor with a heavy reinforced rubber jacket. The coiled portion of the conductor provides the slack needed to accommodate hose stretch while the straight portion is long enough to run the length of the unstretched hose. The coiled section, which can extend to five times its retracted length, is designed to have sufficient length to allow up to 40% hose stretch. Gravity and the elastic memory of the coiled cord's vulcanized rubber jacket repositions the surplus conductor length into its coiled condition during hose contraction. The outer coil diameter measures at least 60% of the hose inner diameter to avoid tangling or kinking during the retraction.

The cord construction uses six AWG #20 stranded and heavily insulated conductors which are twisted around a central polyester strength member, and are protected by an outer neoprene rubber jacket. A portion of the finished cord is wrapped around a mandrel to form the coiled section. Through steam vulcanization, the coiled and the straight configuration is permanently formed. The coil cord configurations allow at least 40% hose elongation; at this stretch the calculated hose tension is 2955 lbs for the *Snubber* and 3660 lbs for the *Standard* hose. The maximum tension measured during the 4 month *Standard* SSAR sea trial was 1,500 lbs. It is possible to eliminate the stop rope because the new hoses (which were redesigned based on the TMT fatigue tests) have enough inherent strength in their nylon reinforcement layers to limit stretch even under the most severe wave conditions. By eliminating the stop rope, it is possible to take advantage of the coil cord technology.

A simple test of the coil cord design was set up at WHOI in a 9m section of clear wall tubing (Figure C.2). This facility simulates the service conditions of a coil cord subjected to stretching and relaxing inside a hose. An off-the-shelf coil cord with a straight pull cord was assembled inside the vertical, transparent water-filled PVC tubing. A gear motor drive lifts the pull cord 1m and allows it to retract again in 3 second cycles. The unit has run 24 hours per day for 6 weeks at the time of this writing, subjecting the coil cord to 1.2 million stretch and retraction motions. The assembly shows no signs of tangling or other geometric changes under the cycling tests and only small, reductions in elastic retraction. Continuity is monitored continuously and no conductor breaks have been experienced. Only slight abrasion has been observed on the coil cord jacket, which so far has logged

2.2 million meters (= 1,374 miles) of rubbing displacement against the hose wall. Custom test samples for the test facility are currently being manufactured, using SSAR coil cord cable material. These samples will be subjected to the same service simulating fatigue testing in the near future.

Hydrophone Array Tests

A technical memo is included in this section as Appendix A which describes in detail the methodology and results of the hydrophone array tests. In these tests a sonobuoy test fixture at Hazeltine Corporation's test facility was used to measure the effects of vertical motion on the hydrophone output. The effectiveness of the SSAR filtering was then examined. By extrapolating these 2 meter tests; it was verified that a 10-meter surface buoy excursion produces a heave signal attenuated by at least 40 dB which is well below the system clipping level.

In the process of conducting this test, however, it was discovered that the hydrophone array was sensitive to mechanical impacts propagating down the array cable. These broadband vibrations are in band and will require mechanical isolation of the hydrophones from the cable. A new design for attaching hydrophones to the cable is being implemented and will be tested during the AUTECH cruise in August.

Fatigue Testing of Hose Assemblies

As discussed in the last Quarterly Report, a test hose section with conductors in the hose sidewall was tested to destruction at Tension Member Technology (TMT). In order to better understand the failure mechanism a series of x-rays were taken to look at the conductors in situ.

During the fatigue tests at 710,590 bend cycles, the hose increased its length by about 0.8cm. An additional slow length increase was measured before and after the initial length change. The x-ray photo, Figure C.7, reveals that the hose body had pulled partly off the steel nipple of the coupling being subjected to flexing. The dislocation is shown by the appearance of the binding wire end, which is located slightly to the right of the coupling. This wire was wrapped over the reinforcement layers and terminated about 2.5cm to the left of the coupling end during the hose building process. The shift eventually resulted in a 5cm length increase of the hose.

The dislocation ruptured the conductor wires at the end of the coupling and broke individual stranded wires (Figure C.8). Further along the free length of the hose (Figure C.9) the conductors show signs of Z-kinking, indicating excessive conductor length most likely after some yielding. The Z-kinking appears not to have broken the conductor path.

On the hose end subjected only to tension cycles the conductors look normal (Figure C.4). This x-ray photo also shows the position of the binding wire to be unchanged from its original position. It should be noted that the conductors are all arranged in one twist direction inside the hose wall, though the x-ray photos also show the backside of their path, giving the false impression of conductors arranged in both left hand and right hand spiralling conductor paths.

While we believe that the embedded conductor design has merit, we do not have time to perfect it at the moment and therefore have decided to use the coil cord design mentioned above for the first 10 operational SSARs.

Ultrashort Baseline Navigation System Tests

The USBL navigation system was tested at the AUTEK Range in April by comparing the relative positions obtained from acoustic pingers located at the surface buoy and the lower pressure case with offsets obtained from the USBL. A portion of this data is shown graphically in Figure C.5. While the typical errors in the USBL data are within the overall SSAR specification, i.e. $\pm 30\text{m}$ for all error sources, we are not totally satisfied with the results of the test. Because the AUTEK range pinger was mounted to the side of the lower pressure case and offset from the center line, it unbalanced the lower pressure case resulting in both an average tilt and a fairly complex dynamic motion. While there is a compass and a tilt sensor in the lower pressure case to correct for tilt and to measure the case orientation, the motion was such that some spurious data was recorded. Thus, the USBL system functioned very well in some instances (Figure C.5) and more erratically in others. We plan to repeat these tests at the AUTEK Range in August with the AUTEK pinger hung in line below the lower pressure case. This should better mimic the true SSAR motions and reduce the high frequency, irregular rotations.

Fabrication and Testing

Fabrication of the operational SSARs is underway and on schedule. A few components have yet to be delivered including coil cords and a few mechanical items. Modifications to the hydrophone array cables to isolate the phones from the cable are being done by the manufacturer. No serious problems are anticipated. The first four operational units should be completed in August. The last six units will be completed this Fall.

Bench and dock tests of each of the operational units is underway and will be documented in detail in the Design and Test Report to be submitted next month. Additional testing of complete SSAR systems is being planned for the AUTEK Range in August and in the Pacific in the Fall. The AUTEK test will provide additional verification of the SSAR navigation system operation and of the acoustic array data collection and processing algorithms. The AUTEK test, however, is

limited to short ranges and cannot completely test the SSAR tomographic capability. These tests will have to be done over long range with an operational source. The AUTECH Range Test Plan is attached as Appendix B. It will use one drifting SSAR and one moored SSAR (Figure C.6) to compare results of a drifting and fixed receiver array. Both arrays will be navigated and equipped to record raw data on hard disk.

Other Tasks

In addition to completing the fabrication and testing of the ten operational SSARs, ARPA requested that we prepare an operational test plan to fully verify SSAR usefulness in detecting ocean warming. Plans for the August AUTECH cruise, and for one or more Pacific test cruises are the result. Appendix C is a letter to ARPA describing our initial recommendations for these tests. The revised ATOC plans to use FLIP to suspend the Alliant Tech source offshore San Diego will impact these tests. We are working with ATOC and ARPA on new plans for these Pacific tests. In addition to the SSAR tests, it was suggested that a low power version of the SSAR receiver be designed and built to eliminate the need for advance scheduling of the SSAR receiver. With the low power receiver a SSAR can listen all the time and adapt its processing schedule in real time to accommodate changes in the source transmission schedules. Planning for these activities is ongoing.

List of Figures and Tables

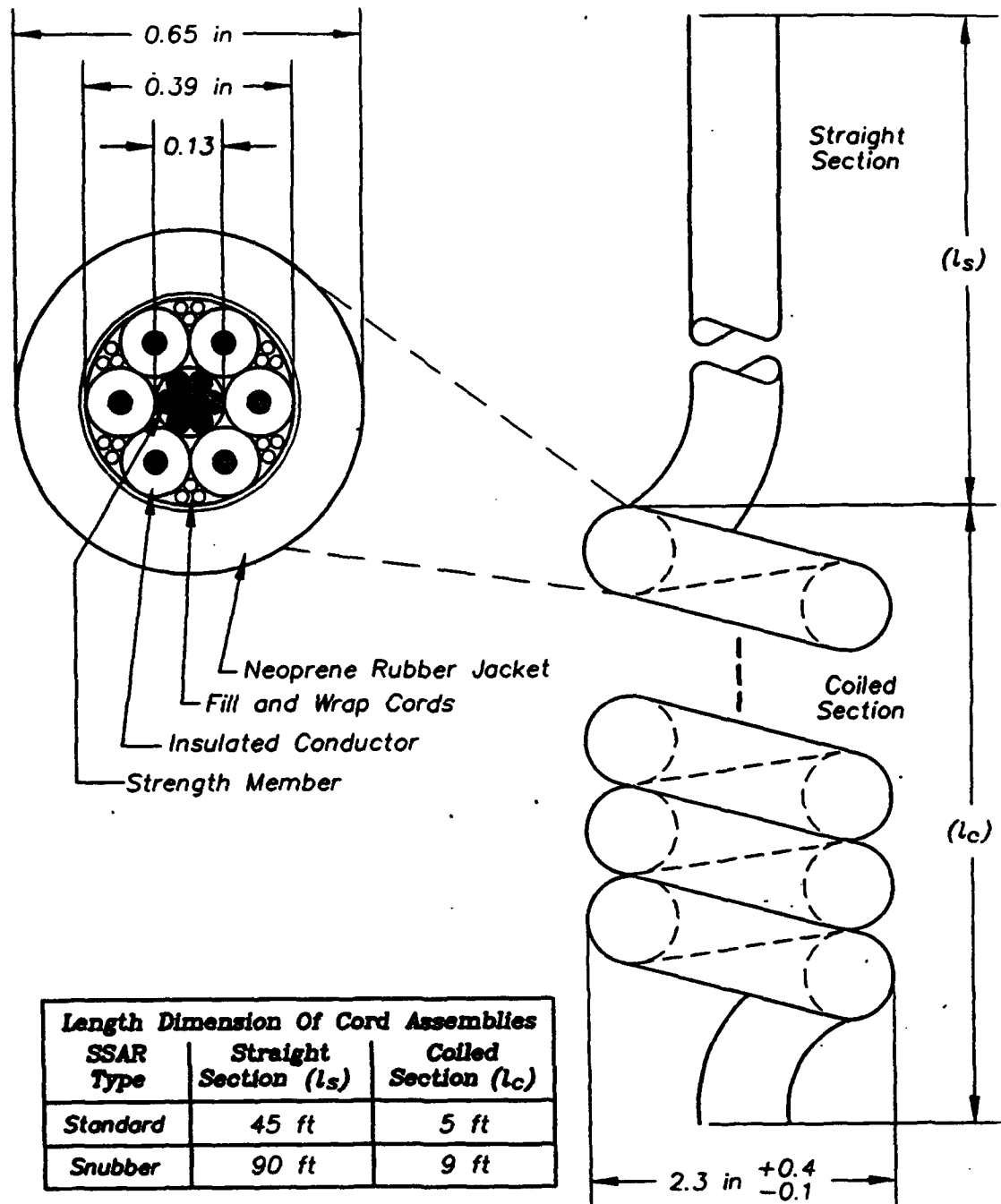
Figure

- C.1 Coil cord assembly for SSAR stretch hose.**
- C.2 Coil cord fatigue test facility.**
- C.3 X-ray photo of conductor path in hose near coupling subjected to bend cycles.**
- C.4a X-ray photo of conductor path in free stretch hose length.**
- C.4b X-ray photo of conductor path near coupling at tension cycle end.**
- C.5 Relative x-y position of the subsea array with respect to the surface buoy. The solid line is the AUTECH tracking data and the "+" are the SSAR USBL data. The surface vessel was used to pull the buoy in order to create this offset.**
- C.6 Moored acoustic array with SSAR processing and recording electronics planned for deployment during the August AUTECH test cruise.**

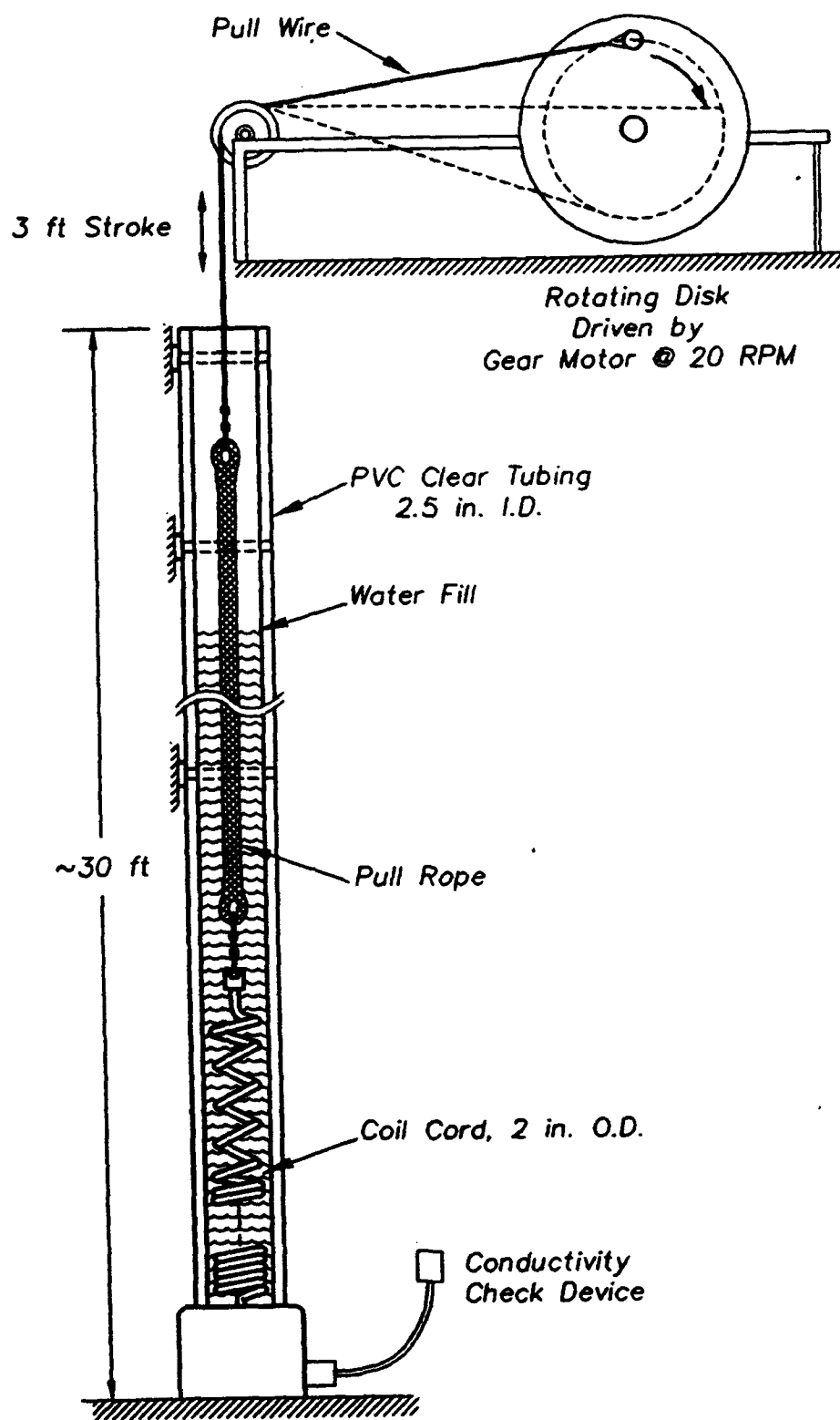
Appendices

- A. SSAR Array Heave Response Test memos**
- B. SSAR Engineering Test Plan: AUTECH**
- C. Letter to Dr. Alewine summarizing the Operational Test Plan**
- D. Walter Paul, Alessandro Bocconcelli, and Paul R. Boutin "The SSAR drifting buoy system; A new approach for a reliable telemetry link to a suspended sensor package," Submitted, Proceedings, MTS '94.**

Coil cords for SSAR Hose Assemblies

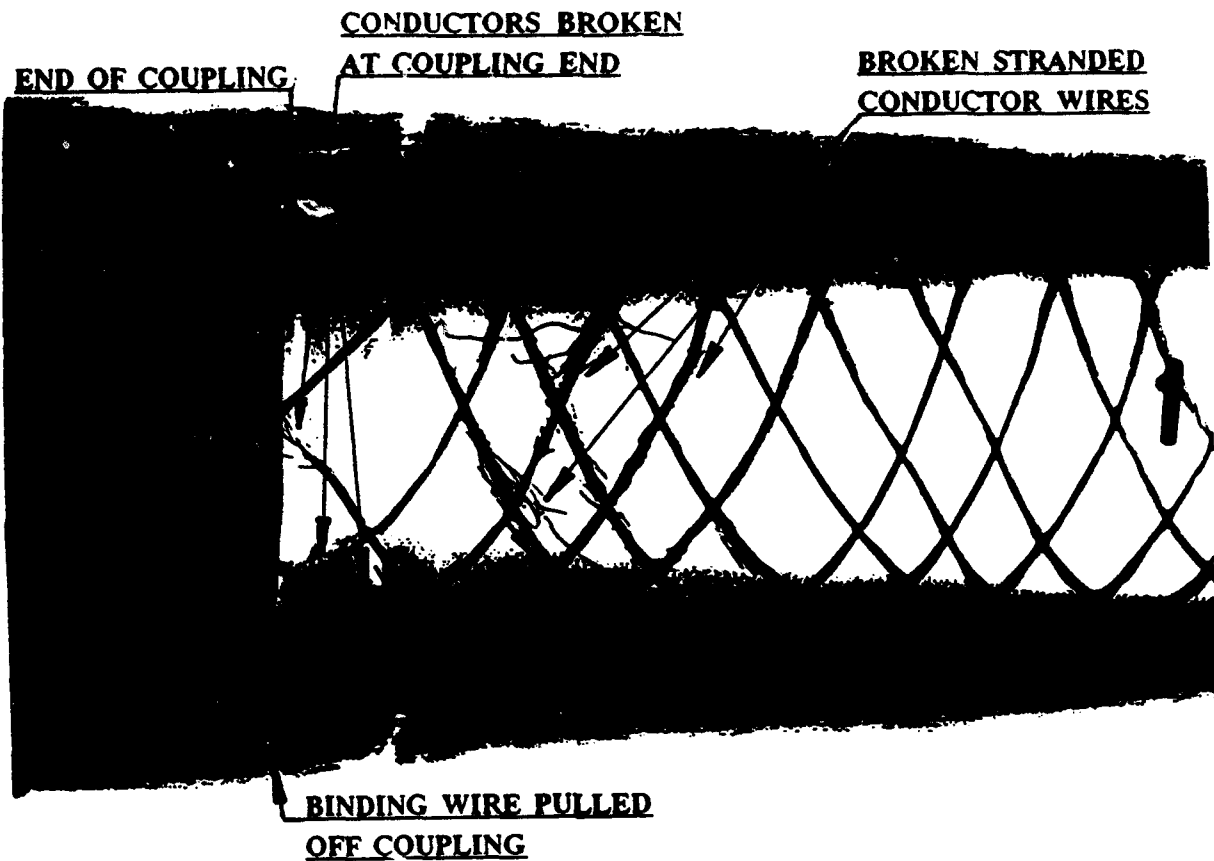


C.1 Coil cord assembly for SSAR stretch hose.



C.2 Coil cord fatigue test facility.

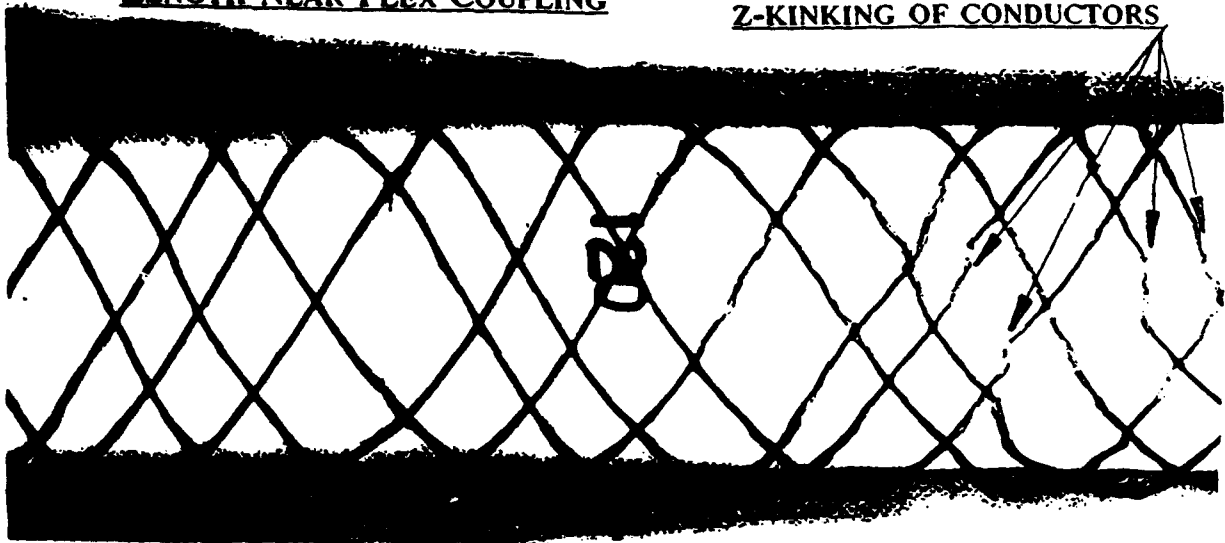
HOSE AND COUPLING END SUBJECTED
TO BEND AND TENSION CYCLES



C.3 X-ray photo of conductor path in hose near coupling subjected to bend cycles.

SECTION OF FREE STRETCH HOSE
LENGTH NEAR FLEX COUPLING

Z-KINKING OF CONDUCTORS

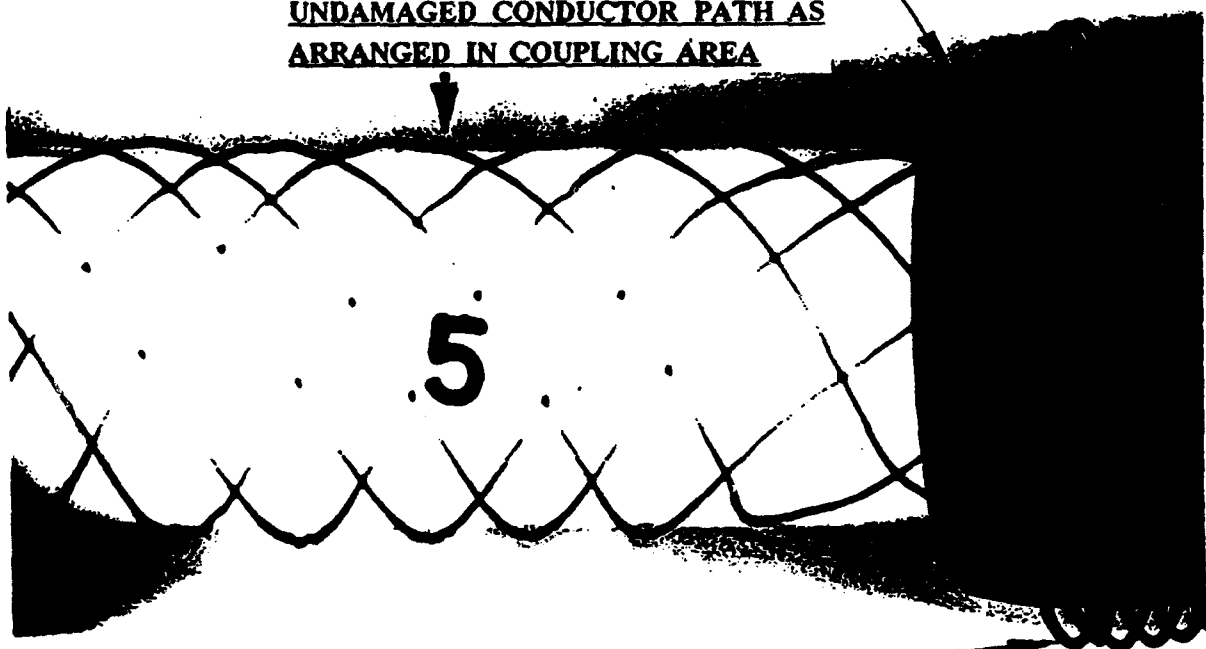


C.4a X-ray photo of conductor path in free stretch hose length.

HOSE AND COUPLING END ONLY
SUBJECTED TO TENSION CYLES

UNDAMAGED CONDUCTOR PATH AS
ARRANGED IN COUPLING AREA

END OF COUPLING



BINDING WIRE, UNCHANGED FROM
ORIGINAL POSITION AFTER TEST

C.4b X-ray photo of conductor path near coupling at tension cycle end.

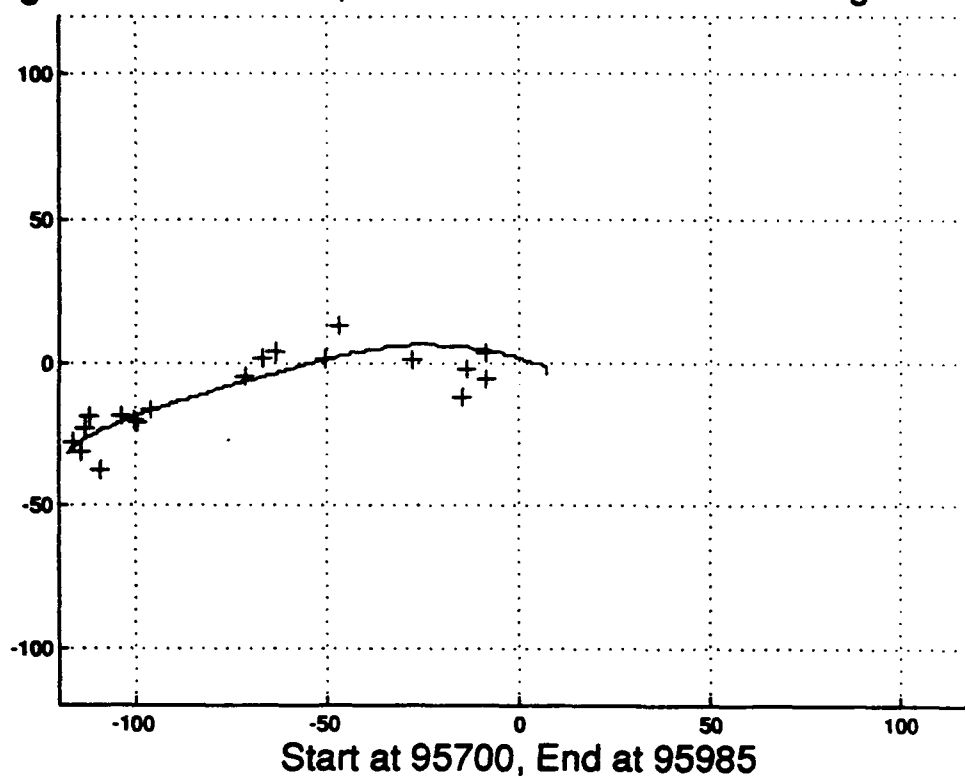
Array Rotation -135.0 deg Y Sign -1

Pitch offset -2.80 deg Roll Offset 0.50 deg Roll Sign -1

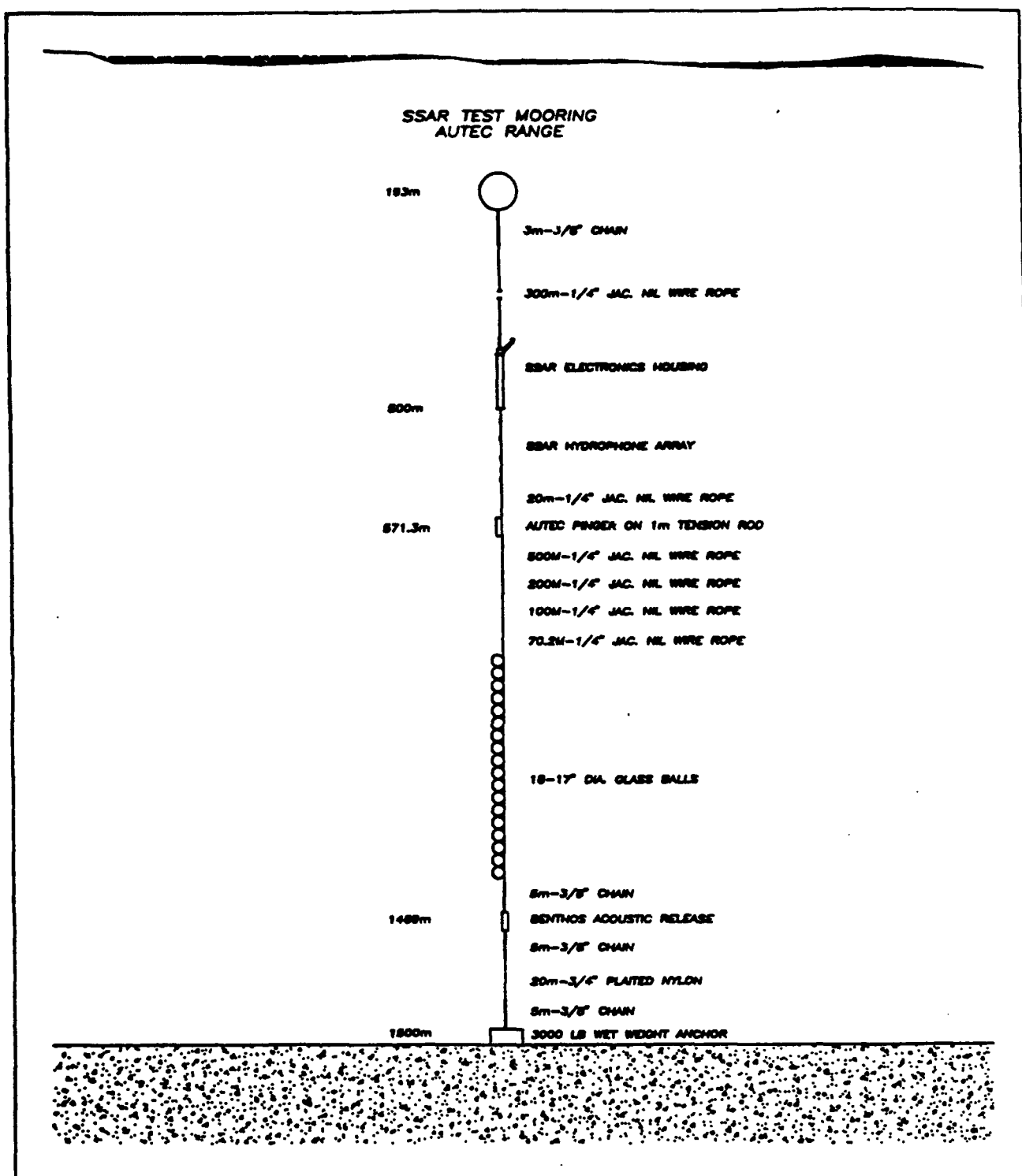
Mag. Inc. 7.00 deg

Hyd x offset 0.0159 Hyd y Offset 0.0135 Outliers Removed: 1

Range data is solid line, SSAR Final = +. No Smoothing or Averaging



C.5 Relative x-y position of the subsea array with respect to the surface buoy. The solid line is the AUTECH tracking data and the "+" are the SSAR USBL data. The surface vessel was used to pull the buoy in order to create this offset.



C.6 Moored acoustic array with SSAR processing and recording electronics planned for deployment during the August AUTEC test cruise.

SSAR Array Heave Response Test

May 25, 1994 at Hazeltine Corp. Braintree, Mass

Setup

The array was attached to a rope which was coupled to a DC motor using a rotating bar on the shaft of a reduction system. The rotation speed could be observed with a spectrum analyzer. Both 3 and 6 foot excursions were tested. The table at the end of this document summarizes the data from the experiment.

Summary of Important Results

The heave of the hydrophone introduces a large signal which was calculated in an earlier note. This test was performed to verify previous calculations and to ensure that the signal out of the hydrophone was as expected given the manufacturers specified response. We also wished to make sure that the filtering in the analog front-end was correct. The calculations of the heave signal are attached (memo of Jan 25, 1994). In summary, a 10 meter excursion would produce 0.28 volts directly at the hydrophone output at 0.1 Hz. Thus for a 2 meter excursion 0.056 volts would be observed. An excursion of 1.83 meters (6 feet) should yield 0.051 volts.

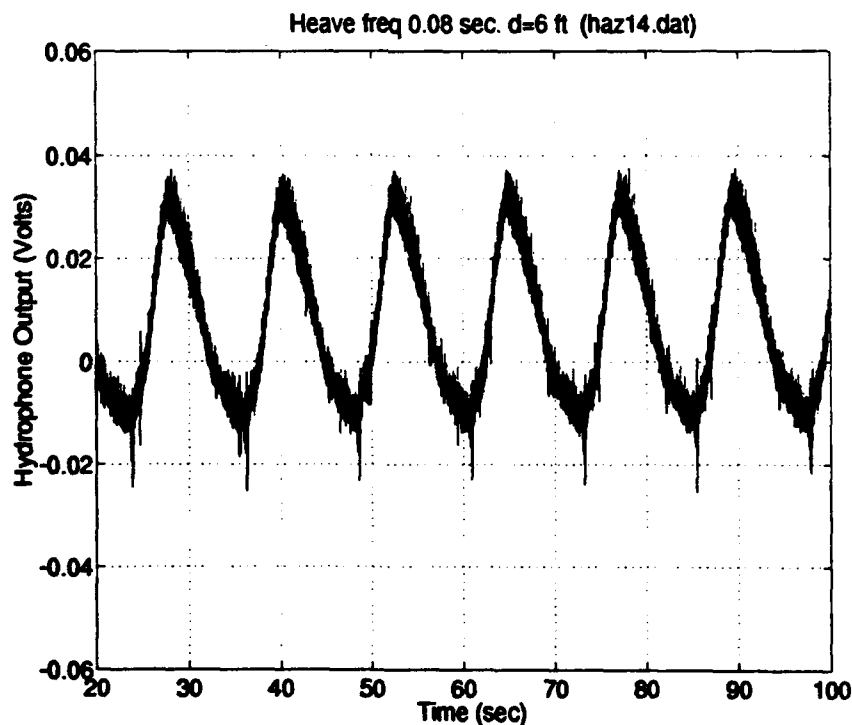


Figure 1. Direct hydrophone output from the array during displacement test. High frequency noise is due to motor vibration coupling down the cable. A slight jerk in the system causes the noise spike at the bottom of each stroke.

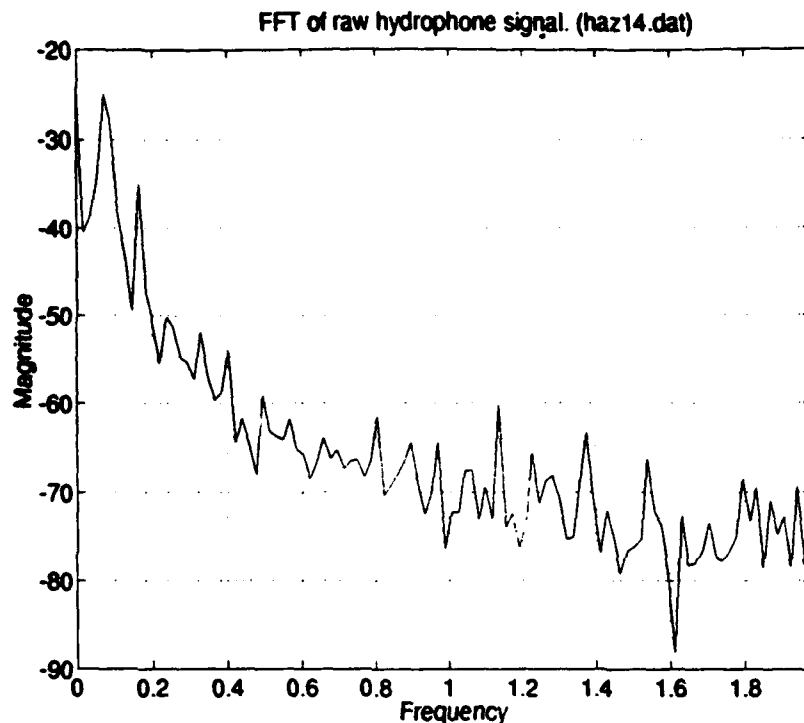


Figure 2. Frequency domain plot of hydrophone data.

The signal in Figure 1 was taken at 6 feet displacement at 0.08 Hz. The peak to peak magnitude is approximately 0.05 volts which matches the output calculated from the response of the EAI hydrophone. The Fourier transform of this signal is shown above. The heave signal is about -25 dB re volt.

The next two stages in the front end are (1) low-noise transistor amplifier with 20 dB gain and 1 high pass pole, (2) op-amp stage with an additional high pass pole and another 30 dB of gain. Clearly, if the large low frequency signal is not attenuated before the gain is added the output will clip when the heave signal is large.

At the output of the first stage the heave signal is -37 dB re volt (Figure 3). This is after 20 dB of gain. The total attenuation is thus 12+20 or 32 dB after this stage. The net attenuation is 12 dB. A 10 meter signal (0.28 volts or -11 dBV) would be at -23 dBV (well below the clipping level).

At the output of the second stage the heave signal is -62 dBV (Figure 4). This is after a total of 50 dB of gain. The total attenuation is thus 37+50 or 87 dB after this stage. The net attenuation is 37 dB. A 10 meter signal (0.28 volts or -11 dBV) would be at -48 dBV (well below the clipping level).

The next stages in the system are the bandpass filters and variable gain. The maximum gain from the variable gain stage is 48 dB. The most likely amplification value for this stage is about 20 dB, depending on the ambient noise level. Even if the full 48 dB of gain were used, the heave signal would be brought to 0 dBV after this stage. However, an additional 2 poles of high pass filtering is

in the circuit before the A/D converter. This provides well over 40 dB of additional attenuation to reduce the heave signal to very small levels before sampling.

An additional bench test will be done to determine the exact level at which the system will clip, but by extrapolating the numbers from this test it appears as though 10 meters heave at 0.1 Herz is not at all a problem for the analog front-end.

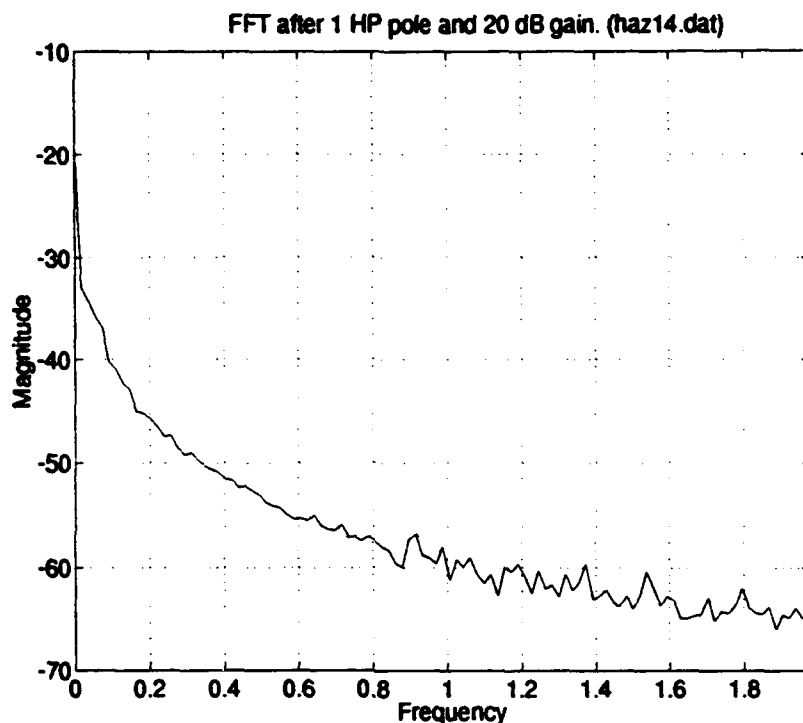


Figure 3. Output after the transistor amplifier stage in the front-end for the 0.08 Hz signal at 1.83 meters displacement. The heave signal is reduced to about -37 dB re volt.

A number of other data sets were taken at different displacements and frequencies. They will be used as reference to check the calculations for heave signals at the hydrophone and through the front-end.

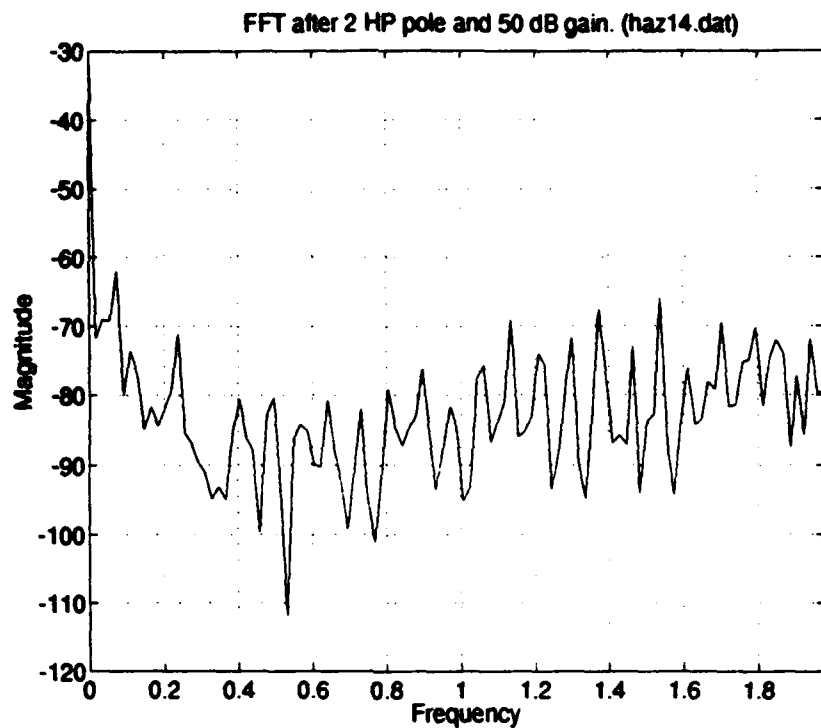


Figure 4. Output after the op-amp stage in the front-end for the 0.08 Hz signal at 1.83 meters displacement. The heave signal is reduced to about -62 dB re volt at this point. While there is still fixed gain after this, there are 2 more high-pass poles before the A/D converter to keep any residual heave signal to very small levels

Prototype (AUTECH) Array Testing

The array used at AUTECH was tested after the new array testing was complete. It was suspended with 20 lbs of weight hanging about 15 feet below it. The response of the hydrophones used for this array is -168 dB as opposed to -185 dB for the new hydrophones. While the heave response of the array will be examined, of more importance was the discovery of a very high sensitivity to light taps on the array cable.

The top plot in the figure below is the raw hydrophone output. An impulse is followed by high frequency signals that slowly decay. It should be noted that this waveform is probably aliased because it is sampled at 300 Hz without low-pass filtering. When an oscilloscope was used to examine the signals they were found to contain some relatively high frequency components up to 600 Hz. However, most of the energy is between 20 and 40 Hz. The bottom plot is the output of the final stage. It is clipped in amplitude and has a duration of about 0.3 seconds.

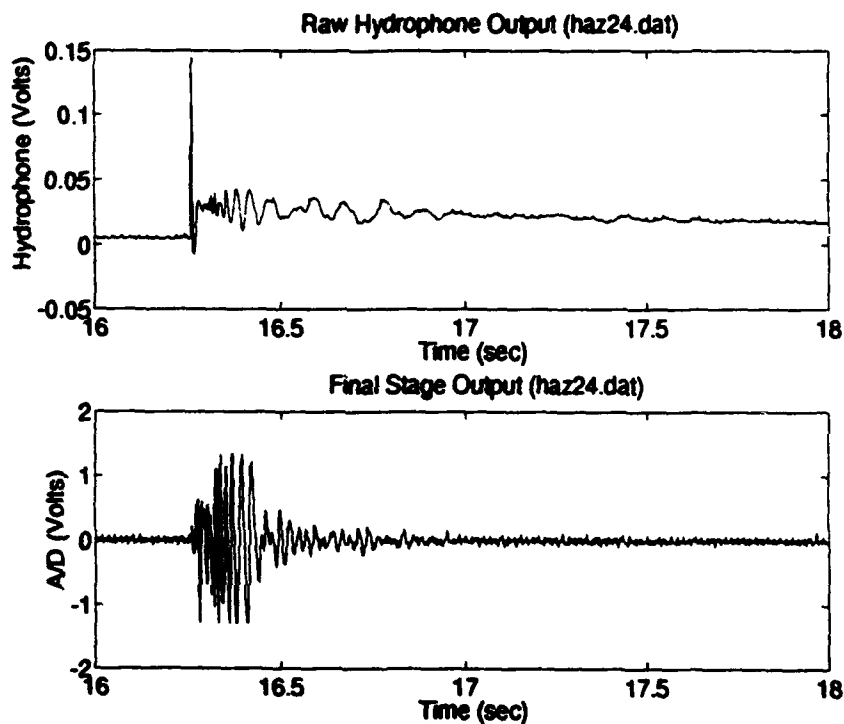


Figure 5. Output during tap test. The array was held still and the cable was tapped lightly with a pen.

The construction of this array is such that the hydrophones are mounted by their acceleration canceling nibs at their longitudinal midpoints. A ring is used to hold them to a PVC tube which was attached to the Kevlar strength member by lacing cord. An Ace bandage was wrapped around the entire assembly and held in place with tape. It appears that this provides very little damping from impulse signals on the cable (despite the acceleration canceling mounts). While in many applica-

tions this may not be important (moorings without a surface expression for example), for the SSAR the hydrophones must be very robust with respect to motion of the cable.

This noise may be the same as that observed in the AUTECH data. Frequency domain plots of the tap test data are shown below.

The noise observed in the AUTECH data will be re-examined in light of this.

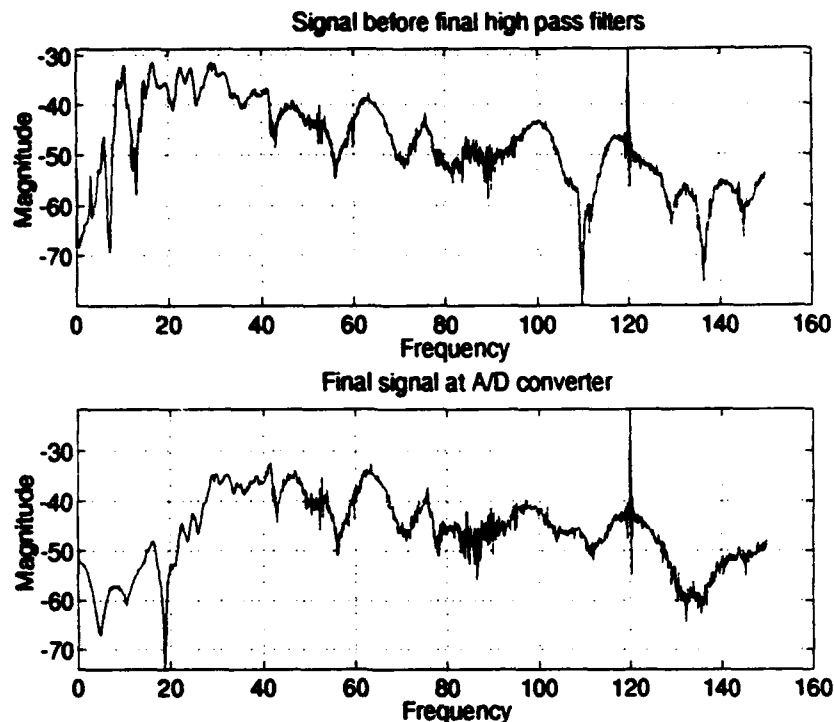


Figure 6. Frequency domain plot of the impulse signal at both the final output stage and just before the last high pass filter stage. Note that the dominant energy is between 10 and 40 Hz, but that the high pass filters reduce that significantly before it is sampled. The AUTECH data showed large amounts of noise energy at about 40 Hz.

Summary of Test Data Taken

0745	Arrive and begin setup			
0845	Setup complete with final SSAR array (C & M Tech with EAI Hydrophones).			
Time	File	Blocks	Disp/Freq	Comments
0846	haz1	2	3'/0.3 Hz	
0857	haz2	2	"	Grounded case and racks to water
0903	haz3	10	"	Ground from F.E. case to water.
	Equipment rack ground removed.			
	With 10 pound weight below the array found that a large 24 Hz signal was generated at the bottom of the stroke.			
0925	haz4	10	"	Changed array weight to 20 lbs.
0945	haz5	10	"	
	Removed hydrophone from PVC tube and wrapped directly to the cable with an ace bandage to see if the hydrophone is jostled inside the tube during the direction reversal at the bottom of the stroke.			
1050	haz6	10	no motion	
	Added ground inside F.E. case to allow observation of DC signals on scope.			
	Disconnected monitor cables during data collection.			
	Some 20 Hz signals are caused by hitting the cable.			
1136	haz7	10	3'/0.3 Hz	
	Changed service loop to hold cable clear. Moved array off aluminum catwalk over hole in barge. Found that just walking on the catwalk with the array on it would transmit noise down to the hydrophone by jostling the array cable.			
	All channels were clipped (bipolar). Hydrophone output was clipped at V+.			
1202	haz8	10	3'/0.1 Hz	
	Disconnected channel 4 from A/D mux to try to fix above problem. Saturating mux on one channel causes data from other channels to appear clipped as well (IC takes time to recover)			
1216	haz9	10	"	Removed 10 lbs off counterweight
	Added 2.4 kohm resistor in series with input to mux on channel 2, and 5.1 kohms for channel 4.			
1242	haz10	10	"	
	Restored hydrophone mounting, changed attachment a little. Wrapped ace bandage around the element before putting into the PVC tube. Used ace bandage to attach tube to cable. Tie-wraps had been used to hold element into tube and tube to cable. Put mesh over tube as before, but tried to puff it out as much as possible before taping ends down.			
1302	haz11	10	3'/0.3 Hz	
	Hydrophone signal is now much cleaner than in data set 9.			
1336	haz12	20	6'/0.06 Hz	

Note that some jerkiness is felt on cable during downward swing. Vibration is different after changing counterweight, but is still present.

1356	haz13	20	6'/0.09 Hz	
	Sprayed some WD40 on knot in center of pull rope. Doesn't seem to change jerkiness at all.			
1435	haz14	20	6'/0.08 Hz	
	Changed to pulley so that center knot would not slip. Not a big difference.			
1444	haz15	20	6'/0.147 Hz	
1448	haz16	20	6'/0.22 Hz	
1455	haz17	20	6'/0.29 Hz	
1502	haz18	~47	6'/0.29 Hz	Sample freq is 600 Hz
1512	haz19	20	3'/0.29 Hz	
1520	haz20	20	3'/0.48 Hz	Very jerky at this speed.

Changed to prototype array used at AUTECH

1540	haz21	20	3'/0.26 Hz	Not connected yet, no data.
1546	haz22	20	3'/0.26 Hz	
1555	haz23	20	3'/0.15 Hz	
1605	haz24	20	not moving	

Tapped cable several times with different intensity. Also lifted a few inches and dropped.

TECHNICAL MEMORANDUM
Advanced Engineering Lab
Woods Hole Oceanographic Institution

TO: Pierre Tillier, Seascan
FROM: Lee Freitag
SUBJECT: Response of hydrophone array to low-frequency heave
(Revised to reflect input from Tom Ensign at EAI on correct preamplifier response.)
DATE: Jan 25, 1994
CC: Tom Ensign (EAI), Dan Frye, John Spiesberger

The frequency response of the hydrophone preamplifier and the vertical motion of the array directly affect the listening capability of the SSAR. The following summary shows the estimated affect of the heave signal on the output.

$1 \text{ Pa} = 1.02 \times 10^{-4} \text{ m}$ of differential pressure
 $10^8 \text{ uPa} = 1.02 \times 10^{-2} \text{ m}$ (1 cm)
and so $2 \times 10^{10} \text{ uPa} = 2 \text{ m}$
 $2 \times 10^{10} \text{ uPa} \rightarrow 206 \text{ dB re uPa}$ (for 2 meters)

Most of the time most of the waves will be less than or equal to 10 meters in height, and close to 8-10 seconds. For a 10 meter displacement the sound pressure due to the differential pressure is 220 dB at the frequency of motion.

The sensitivity of the selected hydrophone (EAI-101-R) is -185 dB re uPa. The output of the preamplifier is:

$$SL - 185 - A_{pa}(f)$$

where $A_{pa}(f)$ is the frequency dependent attenuation of the preamplifier. Obviously in the passband this is 1.

For the EAI-101-R the response is: 3 dB down at 20 Hz, sloping 6 dB/octave below 10 Hz.

At the wave frequencies expected, (approximately 0.1 Hz) $A_{pa}(f)$ is:

$$A_{pa}(0.1) = 46 \text{ dB} \quad (\text{from Tom Ensign at EAI})$$

The low-frequency signal due to the maximum heave motion (10 meters peak to peak) is then:

$$\text{for } 0.1 \text{ Hz} \quad 220 - 185 - 46 = -11 \text{ dB re Volt} \quad (0.28 \text{ volts})$$

Tom Ensign calculates that the preamplifier output will clip at 2.4 V peak to peak. This corresponds to 8 times the 10 meter estimated heave. Thus the pre-amplifier is capable of delivering the signal even in the presence of large vertical excursions, however filtering at the input to the next stage must be set up appropriately to avoid clipping the tomography signal when the system gain is added.

The current ATOC signal is 2 cycles per digit and centered at 75 Hz. The closest the 3 dB points of any filters in the system should be placed to the center frequency is 75 ± 35 Hz or 40 Hz (HPF) and 115 (LPF). However, the self-noise of the preamplifier-ceramic combination will increase when the cut-off point is increased so it is not desirable to move the cutoff beyond 20 Hz. The fact that the cutoff is at 20 Hz and not at 10 Hz as in the EAI-101 already increases the equivalent self noise to 46-47 dB.

Thus the cutoff should be left at 20 Hz and the second stage amplifier set up to handle the 0.28 volt low-frequency signal. A single additional pole at 40 Hz before the next gain stage reduces this level by over 40 dB. A second pole is probably required in order to avoid saturation before the main gain stage and the high-pass filter section.

TECHNICAL MEMORANDUM

Advanced Engineering Lab
Woods Hole Oceanographic Institution

TO: Pierre Tillier, Seascan
FROM: Lee Freitag
SUBJECT: Response of hydrophone array to low-frequency heave
 (Revised to reflect input from Tom Ensign at EAI on correct preamplifier response.)
DATE: Jan 25, 1994
CC: Tom Ensign (EAI), Dan Frye, John Spiesberger

The frequency response of the hydrophone preamplifier and the vertical motion of the array directly affect the listening capability of the SSAR. The following summary shows the estimated affect of the heave signal on the output.

1 Pa = 1.02×10^{-4} m of differential pressure
 10^8 uPa = 1.02×10^{-2} m (1 cm)
 and so 2×10^{10} uPa = 2 m
 2×10^{10} uPa \rightarrow 206 dB re uPa (for 2 meters)

Most of the time most of the waves will be less than or equal to 10 meters in height, and close to 8-10 seconds. For a 10 meter displacement the sound pressure due to the differential pressure is 220 dB at the frequency of motion.

The sensitivity of the selected hydrophone (EAI-101-R) is -185 dB re uPa. The output of the preamplifier is:

$$SL - 185 - A_{pa}(f)$$

where $A_{pa}(f)$ is the frequency dependent attenuation of the preamplifier. Obviously in the passband this is 1.

For the EAI-101-R the response is: 3 dB down at 20 Hz, sloping 6 dB/octave below 10 Hz.

At the wave frequencies expected, (approximately 0.1 Hz) $A_{pa}(f)$ is:

$$A_{pa}(0.1) = 46 \text{ dB} \quad (\text{from Tom Ensign at EAI})$$

The low-frequency signal due to the maximum heave motion (10 meters peak to peak) is then:

$$\text{for } 0.1 \text{ Hz} \quad 220 - 185 - 46 = -11 \text{ dB re Volt} \quad (0.28 \text{ volts})$$

Tom Ensign calculates that the preamplifier output will clip at 2.4 V peak to peak. This corresponds to 8 times the 10 meter estimated heave. Thus the pre-amplifier is capable of delivering the signal even in the presence of large vertical excursions, however filtering at the input to the next stage must be set up appropriately to avoid clipping the tomography signal when the system gain is added.

The current ATOC signal is 2 cycles per digit and centered at 75 Hz. The closest the 3 dB points of any filters in the system should be placed to the center frequency is 75 ± 35 Hz or 40 Hz (HPF) and 115 (LPF). However, the self-noise of the preamplifier-ceramic combination will increase when the cut-off point is increased so it is not desirable to move the cutoff beyond 20 Hz. The fact that the cutoff is at 20 Hz and not at 10 Hz as in the EAI-101 already increases the equivalent self noise to 46-47 dB.

Thus the cutoff should be left at 20 Hz and the second stage amplifier set up to handle the 0.28 volt low-frequency signal. A single additional pole at 40 Hz before the next gain stage reduces this level by over 40 dB. A second pole is probably required in order to avoid saturation before the main gain stage and the high-pass filter section.

SSAR Engineering Test Plan: AUTECH

NUSC AUTECH Range

Preliminary

Test Goals

The specific goals for the AUTECH test are detailed below. They essentially include all engineering elements of the SSAR.

1. Perform final test of ultra short baseline tracking system by using the AUTECH range to measure the exact locations of the buoy and subsurface package.
2. Perform final test of GPS navigation system at-sea by comparing de-jittered GPS data with range-supplied positions.
3. Test collection and processing of 70 Hz m-sequence signals using the tomography array. Raw acoustic data will be stored to disk. Processed data will be loaded into the argos transmitter and stored to disk.
4. Collection of tension data, statistics as well as time series.

Special Requirements for the Test

1. The source vessel must be kept as quiet as possible during the source transmissions. It is proposed that an inverter be used on the ship in order to reduce generator noise. A system is available that could provide about 4 hours of source operation. This is approximately 12 15 minute transmissions plus one hour of backup.
2. Tracking is needed for the drifting SSAR, the moored array and the source. Because the AUTECH pingers are high power sources, they cannot be used at the same time the low-frequency array is being used except perhaps at a very low duty cycle. The pingers can be equipped with sequencers that turn them on for a specific, programmable, period and then off for a second period.

A total of four WATT pingers will be used, two on the drifting SSAR, one on the moored array, and a fourth on the acoustic source.

The mooring pinger can be at a much lower rep rate than the others because its motion will be small.

The two pingers on the drifting SSAR will be synchronized with the pinger on the source. This is required to yield accurate positions for travel time estimation. Desired synchronization is a few seconds over the course of the experiment.

3. A mooring with one of the SSAR arrays and subsea data acquisition package will be deployed along the edge of the range. It will be placed within about 2 miles of the fixed mooring where the source vessel will tie up during transmissions.

Summary of AUTECH Equipment/Facilities Required

1. R/V Ranger or R/V Rover rigged for quite ops with inverter for power
2. MAXISATS acoustic source with WATT pinger for tracking exact source location.
3. 2 WATT pingers for the buoy and subsea package that will be free drifting.
4. 1 WATT pinger for the moored acoustic array.
5. Staging area such as the RUB 4 building.

Notes: All WATT pingers require sequencers.

SSAR Equipment

1. Snubber Buoy with batteries
2. Snubber Hose and subsurface buoy
3. E/M cable
4. Subsea pressure case, ultra-short baseline acoustic array and batteries
5. Acoustic array
6. Array weight
7. Strong-back for WATT pinger to allow it to be placed in-line below the acoustic array, but above the weight.

Mooring Equipment

1. Mooring flotation (subsurface buoy)
2. Subsea pressure case
3. Acoustic array
4. Strong-back for WATT pinger to allow it to be placed in-line below the acoustic array, but above the weight.
5. Wire rope
6. Release and deck box
7. Mooring anchor
8. Glass balls
9. Mooring hardware and deck gear

Schedule and Calendar

August 4th	Last day to ship heavy gear to Port Canaveral to make Aug 12 barge
August 19	Personnel Arrive
August 20-21	Preparations on shore
August 22	Load R/V Ranger
August 23	24 hours of operations at sea with MAXISATS and range tracking for about 4 hours in that period
August 24	Contingency, continued operations if required.
August 25-26	On-shore data analysis
August 27	24 hours of operations at sea with MAXISATS and range tracking for about 4 hours in that period
August 28	Contingency, continued operations if required.
August 29	Depart

Overall Test Schedule

Day 1 - Deploy Mooring and Perform First Test

0800	Depart
1000	Arrive fixed array deployment site
1200	Place fixed array
1600	Arrive SSAR deployment site
1700	Begin deployment
1900	Transit to mooring location
2000	Secure on deep-water mooring. Prep for quiet ops.
2100	Transmissions begin
0100	Transmissions end
0200	Begin transit to SSAR for pickup
0300	Start SSAR retrieval
0600	Return to AUTECH port
0800	In port

Day 2 is contingency for weather or other delay

Day 3-4 On shore for data analysis

Day 5 Repeat test above. Also retrieve fixed array.

0800	Depart
1000	Arrive SSAR deployment site
1100	Begin deployment
1300	Transit to mooring location
1400	Secure on deep-water mooring. Prep for quiet ops.
1500	Transmissions begin
1900	Transmissions end
2000	Begin transit to retrieve SSAR
2100	Start retrieval of SSAR
2300	SSAR on-board
0000	Transit to moored array
0100	Begin retrieval of moored array
0500	Return to AUTECH port
0700	In port

Day 6 is contingency for weather or other delays

Detailed Test Summary During Transmissions

The test will involve transmitting from the source vessel at specific intervals. The number of transmissions per hour will be 2 or 3, depending on the total time to complete a reception sequence on the SSAR. The schedule below is for two transmissions per hour.

Minute	Source	SSAR
58		GPS/SBL localization active
0	Source transmission start	SSAR reception start
10	Source transmission end	
11		SSAR reception ends (last min. for noise check)
12		SSAR in situ processing
20		SSAR data processing complete and sent to surface.
28	Sequence above repeats again	

During the tests the transmitter source power should be varied at 2-3 settings. If 3 power levels are chosen then full power, -6 dB and -12 dB would provide simulated ranges of 4 and 12 times the nominal. This allows for testing of the capability of the SSAR to provide maximum processing gain. Transmissions at 160, 154 and 148 dB could be done at both close and far ranges.

Advanced Engineering Laboratory
Woods Hole Oceanographic Institution
Woods Hole, Massachusetts 02543



May 3, 1994

Ralph Alewine
Advanced Research Projects Agency
3701 N. Fairfax Drive
Arlington, VA 22203

Dear Ralph:

We are preparing a detailed operational test plan to verify SSAR operating characteristics and to provide objective evidence that the SSAR is capable of measuring small changes in acoustic travel times over ocean basins. Before we go too far down the road in preparing this document, we wanted to give you a summary of its salient points and get your response to the proposed approach. The summary plan is attached.

On a second subject, we are interested in designing a low power acoustic receiver for the SSAR which could be used for both acoustic thermometry and nuclear monitoring projects. For acoustic thermometry a low power receiver would allow the SSAR to adapt on the fly to modified source transmission schedules. This would make the SSAR a more flexible instrument and minimize the potential for wasting SSAR resources. The development time for this receiver is about six months, so depending on the ATOC source schedule it might (or might not) be available for use with the operational SSARs. A short description of the low power receiver design is attached.

As you will see in the summary plan, we are recommending that two of the ten operational SSARs be deployed in the Pacific in September this year to test their long term reliability. They will be fully operational so that when the ATOC sources begin operating, they will start collecting real data. In the interim, they will collect ambient acoustic data and provide needed long term test data. The other eight operational SSARs will be held for deployment after the ATOC sources are operating.

I will call you in a few days to discuss these ideas.

Regards,

Daniel E. Frye

DEF/wwl
Enc.

SUMMARY OF THE SSAR OPERATIONAL TEST PLAN

Test I: A complete test of the SSAR system including reception, processing, navigation and telemetry will be performed at the AUTECH Acoustic Test Range in July or August 1994. This test will utilize an AUTECH provided 70 Hz source deployed from an AUTECH ship and suspended at 350 feet. It will transmit an M-sequence at 160 dB source level. A fully operational SSAR will receive those signals at ranges from .5 to 10 Km or more and the data will be processed in the SSAR and telemetered to satellite. Raw data will also be recorded in the SSAR to verify the in situ processing algorithms. GPS and ultrashort baseline navigation systems will be used to determine SSAR positions and these will be compared to positions determined independently by the AUTECH tracking system.

A moored SSAR receiver array will be installed using a sub-surface mooring and will also receive and record the source signals. This will allow a comparison to be made between data collected by a fixed receiver and data from a drifting receiver in close proximity. These tests will be performed several times over several days with time for data analysis scheduled between test runs.

The general goals of this test are listed below. The specific tests and analyses will be detailed in the Operational Test Plan document.

1. Verify SSAR positioning accuracy to $\pm 30\text{m}$ by comparing the internally derived position (with GPS correction) to the positions determined independently by the AUTECH tracking system.
2. Verify the sensitivity and noise rejection of the acoustic array. This will be done by receiving the source signal at an SNR equivalent to that anticipated for the ATOC source at 4000 Km distance under typical oceanic conditions.
3. Verify the receiver processing algorithms by comparing results processed in situ and telemetered via the Argos transmitter to raw data stored in the SSAR and post-processed in the lab.
4. Verify the overall SSAR performance by comparing data collected by the SSAR, which moves with the waves and currents, to data collected by the moored array.

Test II: To verify the long-term reliability of the SSAR we need to get experience with operating systems in the open ocean. To make best use of time we are recommending that two of the operational SSARs (one Snubber and one Standard) be deployed in the Pacific in September 1994. When ATOC sources come on line, these SSARs will receive and process these signals. Until then, they will receive and process ambient noise and provide data on system reliability needed to prove the SSAR concept. We plan to deploy these SSARs a few hundred miles offshore and recover them six months or one year later, if feasible, to check their mechanical condition. The goal of the test is to verify that the SSAR

design is capable of operating one year without mechanical or electrical failure. This verification is, of course, an ongoing process, but the earlier we begin, the more information we can get.

Test III: A SSAR test with an active source in a large ocean basin is a highly desirable test. When an appropriate source is available, whether it is cabled, moored, or ship lowered, a test similar in design to the AUTECH test should be performed in the Pacific over 100s or 1000s of Km. The goal of this test is to verify that acoustic signals propagated over basin scales and measured with the SSAR are interpretable and comparable to those measured by fixed arrays. Unambiguous tracking and identification of acoustic multipaths, comparison with acoustic models, and comparison with data from fixed arrays will be used in the verification.

**THE SSAR DRIFTING BUOY SYSTEM
A NEW APPROACH FOR A RELIABLE TELEMETRY
LINK TO A SUSPENDED SENSOR PACKAGE**

Walter Paul, Alessandro Bocconcelli, and
Paul R. Boutin
Woods Hole Oceanographic Institution
Applied Ocean Physics & Engineering Department
Woods Hole, MA 02540 USA

INTRODUCTION

The Global Acoustic Mapping of Ocean Temperatures (GAMOT) project is a multi-institutional effort funded by the Advanced Research Project Agency (ARPA) with the goal to establish techniques to measure and analyze changes in the heat content of the ocean [1]. In support of the GAMOT project the Woods Hole Oceanographic Institution developed a new type of free drifting buoy system called SSAR (Surface Suspended Acoustic Receivers). They are designed to make very accurate measurements of acoustic travel time between a sound source and the hydrophone array suspended from the drifting buoy and to transmit these data via satellite. Earlier publications of the engineering development of the SSAR buoy systems are found in [2][3]. This paper summarizes the earlier work and describes results from recently performed sea trials and laboratory fatigue tests.

SSAR BUOY SYSTEM DESCRIPTION

The SSAR function is that of a sonobuoy with a significantly expanded capability and service life. A short vertical acoustic array is suspended

from a surface buoy at a depth of 500 meters and transmits acoustic and engineering sensor output data via telemetry to a satellite. Two SSAR configurations, called *Standard* and *Snubber* have been built and are shown in Figure 1. In the *Standard* SSAR the hydrophone array and electronics pack are suspended directly from the surface buoy through a 15 meter elastic shock absorber and a 500 meter long electro-mechanical cable. In the *Snubber* SSAR configuration a subsurface buoy is included which supports most of the weight of the suspended electro-mechanical cable and its payload. An 80 meter elastic shock absorber forms the connection to the surface buoy. The purpose of the subsurface buoy in the *Snubber* configuration is to keep the static tension in the shock absorber low, and to more effectively decouple the motions of the wave following surface buoy from the suspended acoustic array.

**REINFORCED RUBBER HOSE
INTRODUCED AS SHOCK ABSORBER**

Tire cord reinforced compliant rubber hose assemblies were developed as elastic shock absorbers for the SSAR

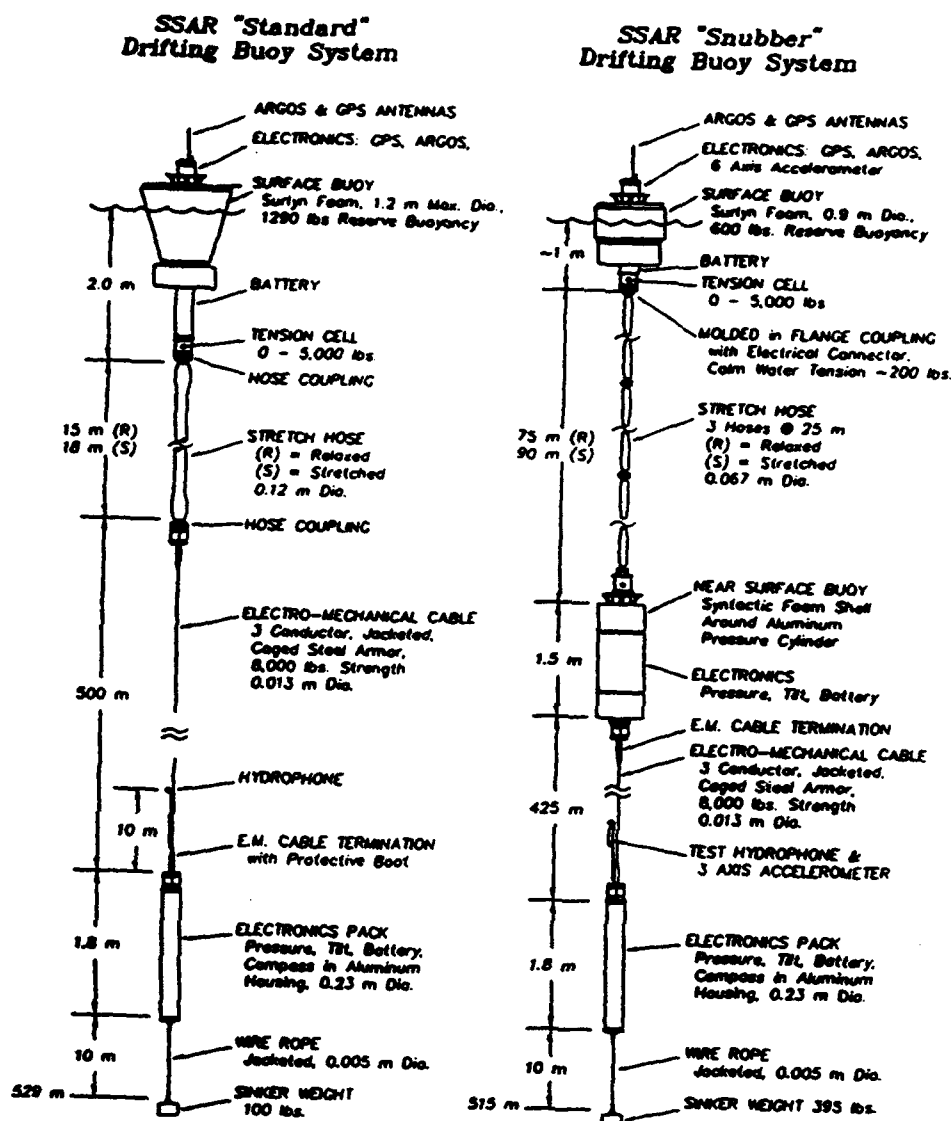


Figure 1: Schematic Illustration of Standard and Snubber Drifting Buoy System

program, forming a protected conduit for the passage of electrical conductors. The hoses are designed to respond with significant stretch to the tensions generated by the displacement of the surface buoy relative to the suspended array while following the surface waves. The hose design combines techniques developed for towed array vibration isolation modules

and offshore oil transfer hoses. Inside the hose is the electrical link between sensors and surface buoy. In addition a stop rope may be used to limit the stretch and loading of the rubber hose.

AT SEA DEPLOYMENT

Both the Standard and the Snubber prototype designs were deployed offshore Bermuda for

an engineering test in September 1993. The Snubber system was recovered after a few days when engineering data telemetered through Argos suggested a loss in system buoyancy. During retrieval it was discovered that the lower 10 - 15 meter of the 80 meter long Snubber hose was compressed flat due to low density fill fluid's upward migration. The lower flattened hose portion caused less displacement and thereby the buoyancy loss. Data flow was not affected, and the hose returned to its original round shape after retrieved. The Standard SSAR was recovered unharmed and redeployed for an endurance test some 50 km southeast of the island.

In early December 1993 the Standard SSAR had drifted to a position close the southwest reef of the island. It was recovered and redeployed a few days later 87 km from Bermuda's northeast corner. After 4 months at sea the Argos transmission reported an interrupted electrical path between the surface buoy and the suspended electronics package. The decision was made to terminate the engineering/endurance test and the SSAR was recovered from its position some 100 miles north of Bermuda in order to determine the cause of failure. All components appeared to be in excellent shape and no visible damage was found during recovery at sea.

RESULTS FROM SEA TESTS

Conductor Failure

Investigation: Once ashore all system components were carefully inspected and

dissected. An open circuit was found inside the elastic hose. The hose was drained and disassembled in order to extract the conductor cable/stop rope assembly.

The failure investigation found the conductor path inside the hose interrupted. The conductor assembly was attached in 1 meter intervals to the separate stop rope with 16% extra length, so that the conductor path would not be in tension until the polyester stop rope neared its breaking point. The excess conductor rope length formed a loop just above the stitched connection points to the stop rope, see Figure 2. The small diameter loops rubbed against the smooth inner hose wall. Abrasion first consumed the outer protective braided polyester jacket. Once this outer containment braid was locally destroyed, the single layer of helically wrapped conductors formed a sharp loop by untwisting. The deformed conductor layer started rubbing against the hose wall in a small sharply bent area, first abrading the thin insulation and subsequently the looped conductors. Outside of the loop or snarl areas the conductor rope looked like new with no sign of wear or electrical damage.

Natural Frequency of Drifting Buoy System: The period of one tension cycle lasted about 3 seconds for the Standard SSAR, close to the natural period of its spring mass system. Since a 3 second period is associated with light weather waves, the drifting buoy system is in damped resonance while amplifying a benign sea state.

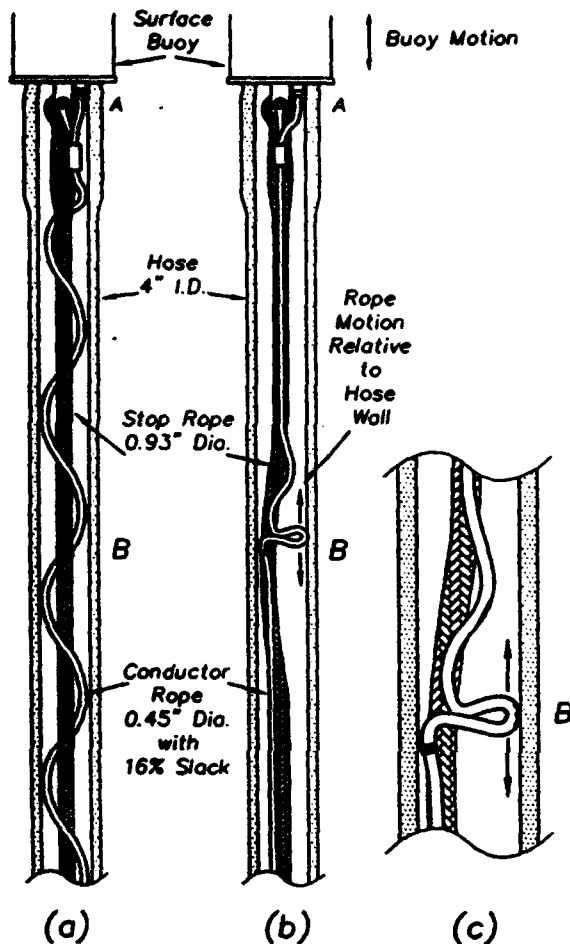


Figure 2: Harness of stop rope and conductor rope inside Standard stretch hose:

- (a) as built with 6 inch slack of conductor rope between attachment points to stop rope
- (b) configuration after 4 months at sea; conductor rope migrates down towards point B and forms loop
- (c) detail of abrasion area of conductor rope loop, abrasion destroyed conductors after 4 month at sea

At higher sea states, the system acts like a wave follower with decreasing amplification of the surface buoy's wave motions and tensions acting on the suspended electronics pack and bottom end of the stretch hose. It is impractical to design the drifting buoy system with a natural frequency lower than the destructive high energy storm wave frequencies (<0.7 Hz) to obtain a true vibration isolation, since it would require either a much longer shock absorbing hose (softer spring) or a much higher suspended mass. This would increase the service loading and thereby increase the size and cost of the system substantially. The main function of the stretch hose is therefore to act as a shock absorber, not a wave oscillation isolator.

Recorded Tension Levels:

During the sea test the Standard SSAR transmitted its position and its engineering sensors' outputs. The recorded loads never exceeded 1,600 lbs. On many days the tensions measured at the surface buoy cycled between 900 lbs and 300 lbs around the static downward weight load of 650 lbs (Figure 3). The Standard hose with 4 inch inner diameter is stressing its load carrying nylon counterhelical cord layers between 2 and 11% (at 1,600 lbs) of its breaking strength without stop rope load sharing. However above 1,100 lbs the stop rope engaged to share the load, reducing the peak hose reinforcement loading. As a design goal, a maximum cord loading of 10% of its breaking strength was

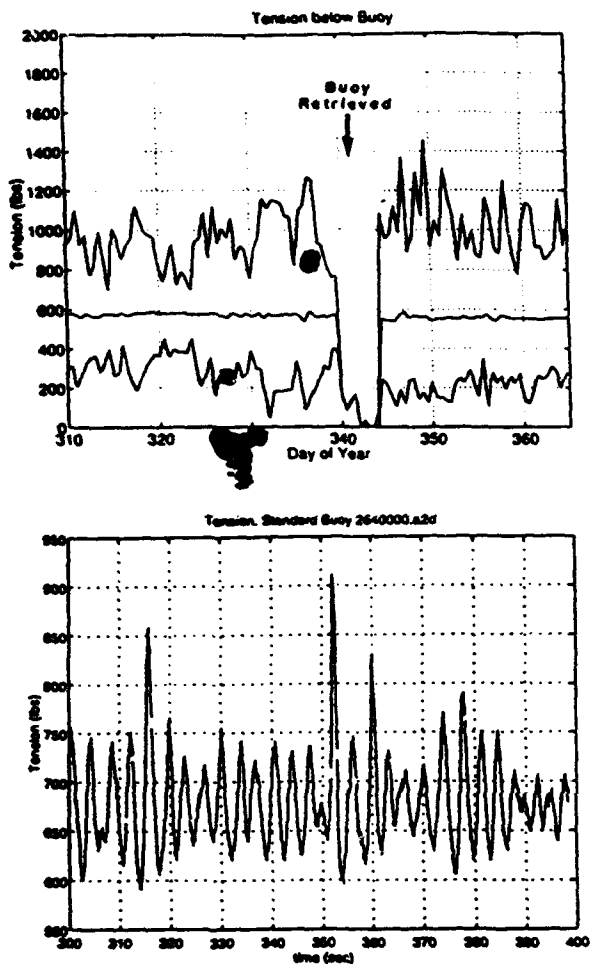


Figure 3: Tension records transmitted from Standard SSAR

considered the upper limit for long term fatigue endurance. The Standard hose loading meets this goal approximately even without a stop rope.

Other Engineering Data:

Besides the tension the depth of the bottom electronics and its vertical acceleration and tilt were recorded and telemetered as well as the surface buoy tilt and the battery

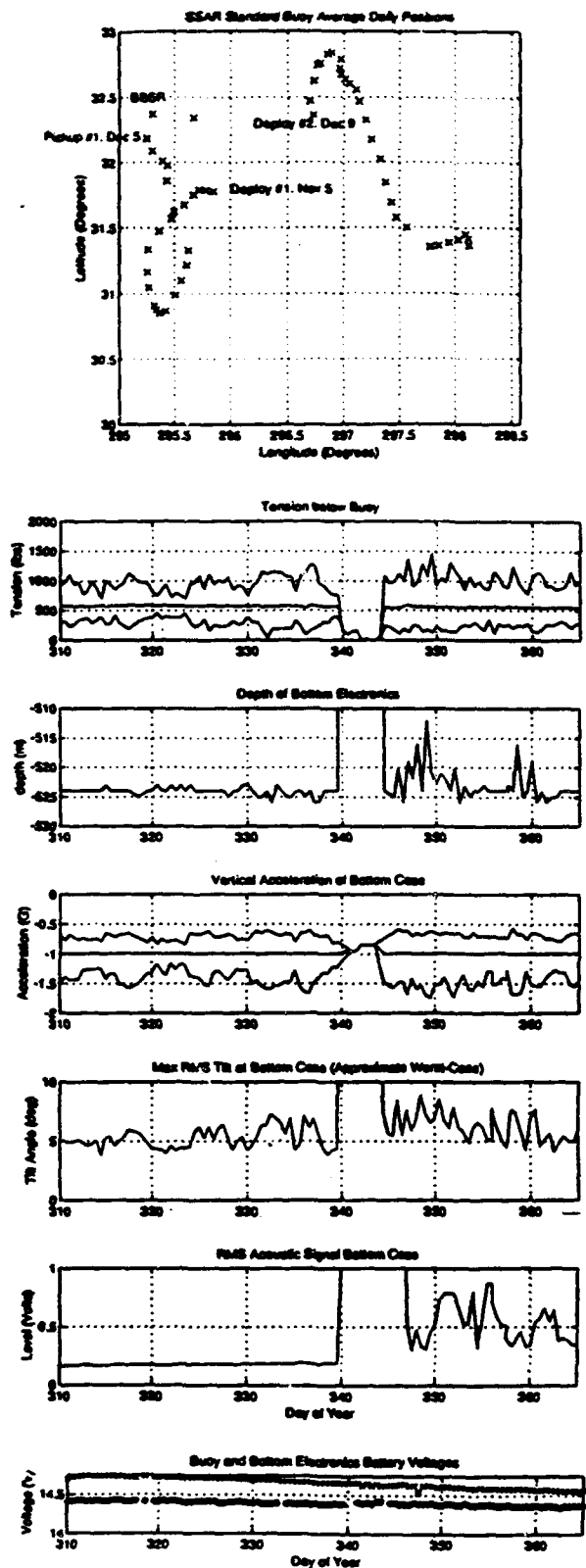


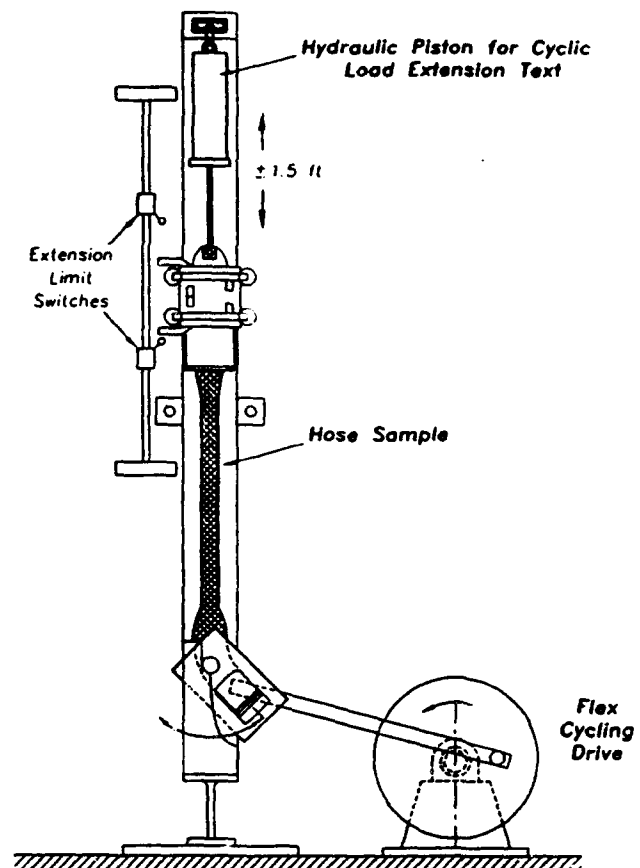
Figure 4: Data recording output from Standard SSAR test buoy on 2/21/94

voltage at the buoy and electronics package. A daily test data record including position of the Standard SSAR is found in Figure 4.

Evidence of Shark Attack: The upper hose section had been subject to shark attack. Long thin razorblade-like straight cuts were found on one hose side, the other hose side showed impressions of the lower jaw's teeth. The cuts do not penetrate beyond the fishbite protective layer of Kevlar tire cord fabric located about 2.5 mm beneath the hose surface. However at one location, the bite punctured through the Kevlar fabric but could not tear any further. A small tooth tip was found at that spot as evidence of the attack. The main load carrying counterhelically arranged nylon tire cord fabric layers and the inner hose wall were not damaged.

HOSE FATIGUE TESTING

In order to investigate the stretch hose behavior in its function as a shock absorber under wave excitation a fatigue test program was undertaken at a commercial test facility. A special test machine was built which simulates wave action on short stretch hose assemblies (Figure 5). The test machine flexes one hose end to a predetermined angle, while subjecting the other end to tension cycling, and records all pertinent test data, which are summarized in Table 1. All test hoses were 2 meters long with molded in end flanges, installed termination hardware and stop rope, and were fluid filled. The hose inner diameter was 5.1 cm. In



HOSE CYCLIC TENSION AND FLEX TESTER

Figure 5: Hose fatigue tester simulates wave action stresses

all tests the duration of a tension cycle was 9 to 10 seconds, which a flex cycle was repeated every 2.5 to 3.5 seconds. First Hose Fatigue Test: This test was performed

with a $\pm 45^\circ$ flex angle and a tension cycle between 50 lbs and 1,800 lbs. At 1,800 lbs the hose stretches 50%, and stresses the hose reinforcement to 30% of its breaking strength, with additional stress exercising the flexing hose end. This

flex-tension cycle combination simulated the hose response in a chaotic storm without support of a stop rope. During each load peak the tensioned, counterhelical arranged nylon reinforcement generates choking pressure in the fill fluid of 220 psi. The hose failed at the flexing end. The highly pressurized fill fluid penetrated through the hose wall rupturing the outer hose rubber jacket after 13,761 flex cycles. The load supporting nylon reinforcement stayed intact. The failure location was at the point where the hose assembly left the steel coupling section, where the steel pipe end forming the coupling ruptured the rubber hose wall, thereby starting the burst failure.

Second Hose Fatigue Test: A second test was performed on a new test hose assembly, with a $\pm 25^\circ$ flex angle and the tension reduced to 1,300 lbs. This tension is stressing the hose nylon reinforcement to $\pm 25\%$ of its breaking strength and elongated the hose to 42.5%. Under 1,300 lbs load the fill fluid pressure was 105 psi. The hose failed at the flexing end after 39,546 bend cycles but away from the coupling. A tiny burst hole developed in the area near the coupling where the elongation under peak load increased from 5% to 42.5% in less than 5 inches.

Lessons Learned: From the above two tests it was learned that excessive test loads lead to fairly rapid hose wall bursting due to high fill

fluid pressure, and that a more gradual staggered decrease in extra bend limiting reinforcement had to be employed. The loading of the tire cords of 30% and 25% is much higher than a practiced safety factor of 10 for nylon rope. The more staggered decrease in extra bend limiting reinforcement avoids short hose length sections with too large elongation differentials under load. The thin hose wall in the stretch section of only about 0.25 inch should be increased to provide more shape stability and burst resistance. It was also concluded that test tensions should be more in line with actual operating loads in order to determine life expectancy in service.

Third Fatigue Test, Hose with Electrical Conductors: A third test sample was built which had a more gradual reduction in extra reinforcing tire cord end layers, and a hose wall thickness increased from about 0.25 inch to 0.5 inch. This hose was also equipped with electrical conductors spiralled inside the hose wall cross section in a no-stretch helical path to test a different solution for a survivable conductor path near the sea surface. The cyclic tensions were initially set between 50 lbs and 800 lbs, but later increased to 1,300 lbs, and a stop rope shared the higher tensions with the hose through about 60% of the test.

This third test hose performed well in mechanical fatigue tests. It passed one million flex cycles and about 600,000 tension cycles at different load levels. After 641,200

flex cycles the internal stop rope was removed. The tests without stop rope were first operated with about 800 lbs peak tension and later with 1,300 lbs tension. At 800 lbs tension the load level in the supporting nylon cords is 7%, at 1,300 lbs about 13% of its breaking strength in this test hose built with a heavier wall.

During the test, in particular after removal of the stop rope and increase of tension to 1,300 lbs, the hose developed permanent stretch and seemed to have pulled slightly off the end of its flexing coupling, but stayed physically intact. The electrical conductors did not survive the test. Initial changes in resistance were noticed after 632 bend cycles, and the last conductor failed at 143,920 bend cycles under 800 lbs peak loading. A subsequent x-ray test of the hose showed that the conductors had parted near the coupling at the flexing hose end, but showed additional signs of Z-kinking and damage in other locations near the flexing coupling. The x-ray image of the conductors looked undamaged near the hose end subjected to straight tension-cycling. The conductors were stranded AWG#16 copper wire. The low elasticity of standard copper conductors is insufficient to accommodate the flexure caused by hose elongation. More compliant stretchable conductor materials have to be devised which can take the abuse of a fatigue or sea test.

CONDUCTOR ISSUES FOR STRETCH HOSES

The relentless cyclical extension and relaxation of a stretch hose hanging from a wave following surface buoy and tensioned by the weight and inertia of the payload suspended from its bottom end presents a significant challenge for electrical conductors which have to be supported in this environment. The advantage of arranging conductors inside the fluid filled hose cavity with sufficient extra length to accommodate for the hose stretch is their mechanical protection. The disadvantage is that the conductors have less than 1/2% elastic stretch, and are subject to yielding and Z-kinking. Inside the hose they are also subject to dynamic tensions generated by the lifting and tugging of a vertical cable assembly due to the surface buoy motion and hose stretch. The conductors have to permit up to 30% cyclical hose stretch and relaxation while oscillating with the wave frequencies. This is made possible by coiling strength member supported conductor assemblies inside the hose cavity. The strength member is tied off to the hose coupling bulkheads to take any tension off the electrical conductors and connectors.

Our prototype designs included an initially slack stop rope, which starts load sharing with the stretch hose beyond a predetermined hose elongation. In the prototype Standard SSAR a stop rope was arranged in combination with a longer conductor rope. In the proto-

type Snubber SSAR a single unit served both as a stop rope and a conductor carrier. The prime reason for a stop rope is to have an elongation limiter for the stretch hose to prevent the loading of the hose reinforcement above safe limits.

The vertical suspension of conductor assemblies generates weight and inertia tensions at the top end. Unless the coiled assembly can maintain its shape in a truly elastic manner or can be made weightless in the fill fluid by adding distributed flotation material it will tend to migrate to the bottom of the hose assembly due to gravity. This will add dynamic tension in the upper portion of the cable assembly and possible entanglement at the bottom of the hose, or can lead to snarling of excessive conductor rope length above attachment points to the stop rope.

The simplest stretch cable is the coiled telephone cord, which can typically increase its length five fold and can therefore easily accommodate the 20 to 30 percent cyclical length change of the stretch hose in a severe sea state. If such a cord is able to retract to its coiled configuration even after a large number of extension cycles, and if it is sized to fit into the hose cavity without entanglement, it should form a reliable conductor path. In support of this approach a 10 meter high vertical conductor fatigue test facility was constructed from transparent PVC tubing. A coil cord assembly, slightly smaller than the inner diameter of the

water filled tubing, is being lifted 3 ft every 3 seconds, and is passing the 1 million cycle count at the time of this writing. So far no noticeable abrasion or snarling has been observed.

IMPROVED CONDUCTOR ASSEMBLIES IN NEW SSARS

For a currently ongoing assembly of five Snubber and five Standard production SSARs we will not use stop ropes. Due to the inherent strength of the hose assemblies, they are able to support the service loads without overstressing the nylon tire cord reinforcement. This facilitates the incorporation of custom made heavy jacketed coil cord assemblies into the hose cavity, since they do

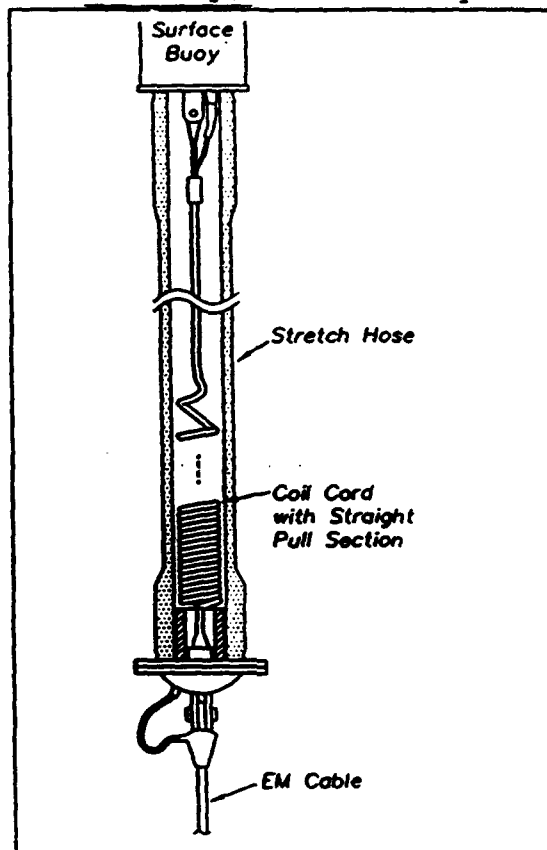


Figure 6: Coil cord assemblies prevent snarling inside hose

Table 1: Conditions and results of hose flex and tension fatigue cycling tests

TEST RESULTS	HOSE SAMPLE #1	HOSE SAMPLE #2	HOSE SAMPLE #3** with Conductors	
Min and Max Load	0-1,800 lbs	0-1,300 lbs	0-800 lbs	0-1,300 lbs
Load Cycle Duration	10 sec	9.5 sec	9 sec	10 sec
Elongation* at Max Load	50%	42.5%	31	40
Flex Angle	45°	25°	30°	30°
Duration of Flex Cycle	3 sec	2.5 sec	3	3.5
Fill Fluid Pressure at Max Tension*	220 psi	105 psi	36	62
Load Cycles till Failure	4,152	9,878	671,500 without failure (conductors 1,478-70,980)	
Flex Cycles till Failure	13,761	39,546	1,000,000 without failure (conductors 3,500-143,920)	
Failure Type and Localization	Burst failure at end of steel coupling. Reinforcement intact.	Small burst hole at taper of extra reinforcement; hose otherwise intact.	Hose survived 6 weeks of fatigue cycling without failure. Some changes observed at flex coupling, dissection of hose is planned.	

*Elongation and fill pressure in compliant section of test hoses at load cycle 100.

** Hose was built with twice the wall thickness than samples 1 and 2.

not have to share the space with a separate stop rope (Figure 6). The coil cords are manufactured with a heavy neoprene outer jacket, which is steam vulcanized into its required coil configuration. The survival of these highly elastic coil cords for a year's mission is expected based on the cord fatigue test results.

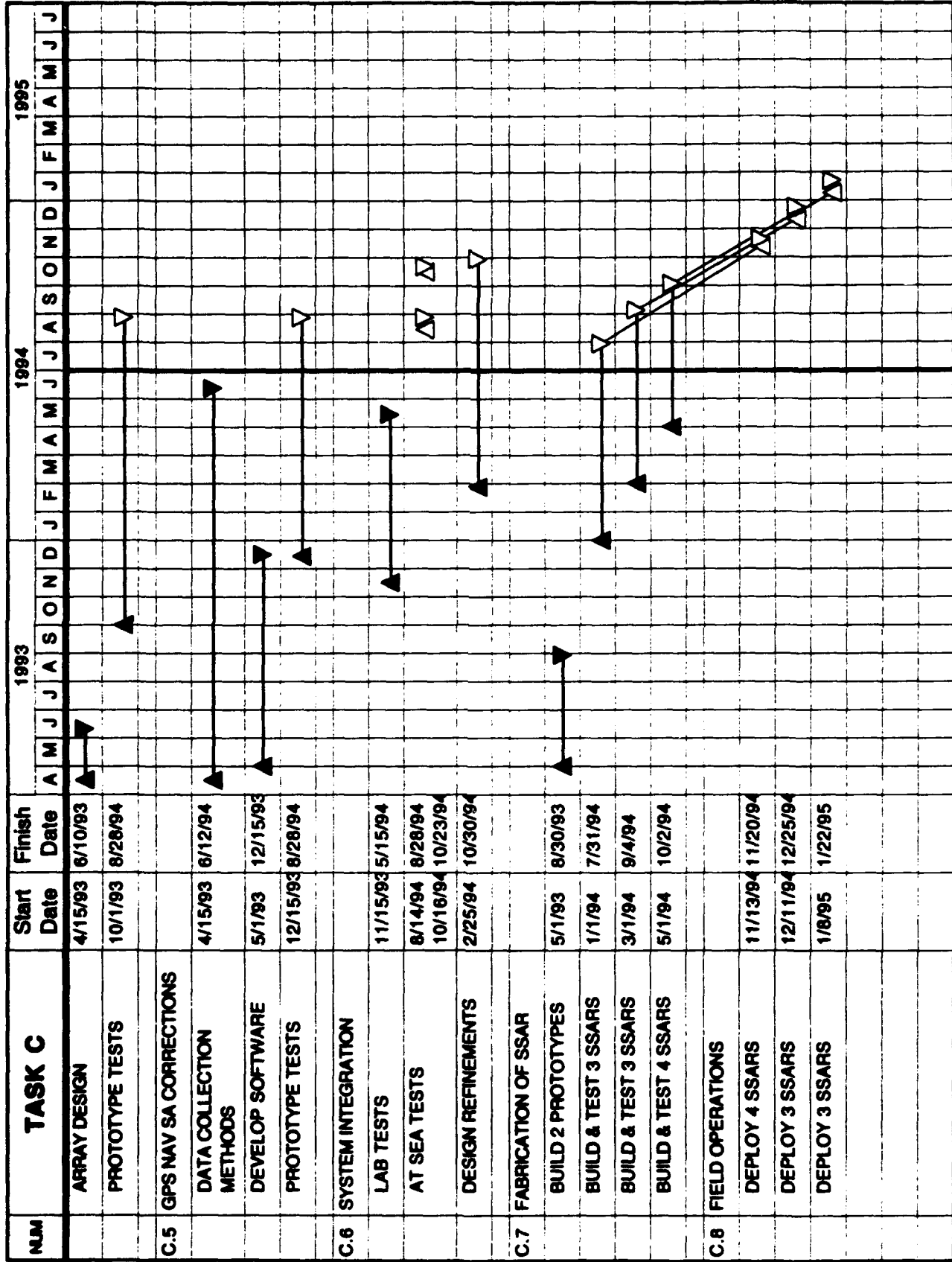
ACKNOWLEDGEMENTS AND SUMMARY

The SSAR development program is sponsored by the Advanced Research Projects Agency (ARPA) as part of the Global Acoustic Mapping of Ocean Temperatures (GAMOT) project under the direction of Dr. Ralph Alewine. This work relates to ARPA Grant MDA972-93-1-0004 issued by the Contract Management Office and is funded by the Strategic Environmental Research and Development Program (SERDP). The United States Government has a royalty-free license throughout the world in all copyrightable material contained herein. The SSAR Program is a multi-institutional effort. The authors acknowledge the guidance and leadership of John Spiesberger and John Kenny of the Pennsylvania State University, and of Daniel E. Frye from the Woods Hole Oceanographic Institution. We also express our appreciation to the W.H.O.I. supporting staff and to the suppliers which have made the SSAR progress possible.

We are near the end point of the development of the SSAR drifting buoy systems for the GAMOT program. Through system modeling as well as modeling and fatigue testing of the newly developed compliant stretch hoses and compliant conductor assemblies we seek to gain at least one year electrical and mechanical survival of the buoy system.

REFERENCES

- [1] J.L. Spiesberger, D.E. Frye, J.O. O'Brien, H. Hulburt, J.W. McCaffrey, M. Johnson, and J. Kenny: "Global Acoustic Mapping of Ocean Temperatures (GAMOT)"; IEEE Oceans'93 Proceedings, I-253-I-257, 1993.
- [2] D.E. Frye, L. Freitag, W. Paul, M. Grosenbaugh, J. Spiesberger: "Surface Suspended Acoustic Receiver (SSAR) for Mapping Ocean Temperatures"; Oceanology International'94 Conference Proceedings, Volume 1, 1994.
- [3] W. Paul, A. Bocconcelli, M. Grosenbaugh: "Drifting Buoy Systems Using Elastic Rubber Stretch Hoses"; to be published in the BOSS'94 (Behavior of Offshore Structures) proceedings, Cambridge, MA, July 1994.



QUARTERLY PROGRESS REPORT NO. 5

Contract: SC25048
Sponsor: Woods Hole Oceanographic Institution
Project Leader: Mark Leach
Report Period: April, May, June 1994

Applied Research Laboratories, The University of Texas at Austin (ARL:UT), is tasked to provide Woods Hole Oceanographic Institution (WHOI) with a method and system for determining accurate positions of free floating Surface Suspended Acoustic Receivers (SSAR). ARL:UT is to provide guidance in the selection of Global Positioning System (GPS) equipment, and determine the best method of obtaining SSAR positions. During this quarterly period, the following progress was completed.

Subtask 3: Develop Receiver Control Software

As part of the GPS-based buoy positioning system, ARL:UT developed, tested and delivered software to control the GPS receiver onboard the buoy. This software is designed to initialize the GPS receiver, collect positions at system-specified times, and prepare a data table containing buoy position and GPS satellite information for ARGOS transmission. During this report period, ARL:UT completed several software refinements requested by WHOI and Applied Research Laboratories, Pennsylvania State University (ARL:PSU). These enhancements were required to support the system interface, and to provide additional diagnostic information during system operation. Final software testing was performed over a period of 8 weeks to insure functionality and robustness. There have been no problems or anomalies observed by ARL:UT during testing. The receiver control software is now considered fully operational, and has been delivered to WHOI to support system testing. This subtask is considered complete with the exception of any modifications that may be identified during final system integration.

Subtask 7: Integrate and Test the Position Correction Facility

During the previous report period, the system design for the Position Correction Facility (PCF) was completed, and integration of the components into a deliverable system was begun. The first portion of the PCF consists of three software components that combine data from the SSAR with GPS satellite ephemeris data obtained from the Defense Mapping Agency (DMA). The functionality of the three components are 1) automated downloading of ephemeris data from DMA; 2) decompression of the DMA data and generation of ephemerides in the proper format for data processing; and 3) reading ARGOS decoder output, reconstruction of GPS observables from the buoy positions, and formatting the data for removal of Selective Availability (SA). The software that performs the functions in Item 1 was completed during the previous report period.

During this report period, the software for functions described in Item 2 was completed, and ARL:UT conducted a 12 week test and evaluation shakedown of the software. The software successfully operated on a daily bases over the three month period, with only four observed anomalies. The first three anomalies occurred after GPS week roll-overs. The source of the

problem was identified in the decompression routine and corrected. There have been no further occurrences of this problem since the corrective action was implemented. The fourth anomaly was attributed to receiving a modem call from an unknown source. Apparently the calling party used incompatible communication settings that caused the communication software to lock. The software was restarted, but the subsequent data transfer that night from DMA was unsuccessful. The GAMOT computer was rebooted, and further transfers were completed normally. No further occurrences were observed. ARL:UT is continuing to monitor the software performance on a daily basis.

The program within the PCF software which performs the functions of Item 3 was completed during this report period, and is currently undergoing a test and evaluation period. As this segment of the PCF software utilizes the coded ARGOS data message, program validation cannot be completed until the ARGOS message format has been finalized.

Additional Activity:

Phase I Extension Proposal

ARL:UT responded to a GAMOT Program Office request for an initial assessment of cost and effort required to support an extension of Phase I. ARL:UT identified four principal areas that would support the GAMOT program beyond the original scope. The areas identified are additional PCF software support, processing corrected buoy positions in the event that ARL:PSU's requests for processing approvals are not granted prior to buoy deployment, assessment of viable unclassified methods for obtaining buoy positions with required accuracy, and evaluation of improved GPS OEM receiver technology and subsequent integration.

Security Procedure Information and Guidance

ARL:UT provided additional information and guidance to ARL:PSU regarding facility and system security requirements, and procedures for conducting the classified portion of the PCF processing.

Shawn Furgason
Research Engineer Associate

ISSUES AND CONCERNS

Three issues are addressed:

- Acoustic interaction of cabled sources with the bottom slope, and
- Identification of a source for the autonomous mooring.
- An at-sea test with a suitable source transmitting M sequences over long range is desirable to fully verify SSAR operation. A short range tomography test will be performed at the AUTECH Range in August, but a long range test in the Pacific should be scheduled following the AUTECH work.

CABLED SOURCES ON THE BOTTOM

As previously discussed, bottom interaction may be a problem for the SSARs because the transmission paths change for each different SSAR position and the bottom interactions are typically not known well enough to accurately predict its effects. The Kauai and Pt. Sur sources will be bottom mounted. Detailed bottom surveys of the source locations have been conducted as part of the ATOC program and when that survey information is received from ATOC it will be used to develop an analytical understanding of the expected bottom interactions prior to the deployment of the SSARs.

In November 1994, ATOC will conduct the AET test which should provide valuable information about signal to noise ratios, stability of multipaths, and possible bottom interactions. GAMOT will participate in that test.

IDENTIFICATION OF A SOURCE FOR THE AUTONOMOUS MOORING: TASK D

The autonomous mooring work is delayed because a source has not been identified for the mooring and the long term source is not appropriate to complete this important aspect of GAMOT's work prior to June 30, 1995.

ARPA will provide the more information regarding the GAMOT proposal to build a 70 Hz source at a meeting at WHOI on 26 August 1994.

AT SEA TEST

In addition to ATOC's AET, we have developed an at sea test of the SSARs using the HLF-6A source suspended from a ship. There is sufficient funding to conduct this test. The test is described in the attached letter from the GAMOT Program Manager to NMFS. NMFS has given permission to GAMOT to conduct

this test. This is a significant breakthrough in that this is the first permission that any group (in this ARPA program) has received to put sound in the water.

Appendices:

A. Ltr fm John M. Kenny /Penn State to Ken Hollingshead /NMFS dtd 13 July 1994

B. Ltr fm William Fox /NMFS to John M. Kenny /Penn State dtd 10 August 1994



July 13, 1994

Dr. Ken Hollingshead
NMFS
1335 East West Highway
Silver Spring, MD 20910

Dear Dr. Hollingshead,

Thank you for talking with me today about the feasibility of an experiment which would test the signal reception and signal processing of the SSAR (Surface Suspended Acoustic Receiver) using a source (HLF-6A) suspended from a ship.

Here is a rough outline of the experiment:

- The duration of the test would be five days. This duration does not include the transit time to and from the selected transmission site.
- The transmission schedule would be six times per day with a signal duration of ten minutes. The signal duration does not include the ramping up of the signal to the test source level.
- The center frequency would be 75 Hz with a bandwidth of 30 Hz and a source level of 197 dB. The code would be an m sequence.
- The crew onboard the research vessel would include a marine biologist who would terminate or delay the test if there was evidence of marine activity.
- During the transmission, the source would be in the sound channel at a depth between 500 and 800 meters.
- The test would take place during the last two weeks in October 1994.
- The location of the test will be determined by the NMFS scientist and most likely will occur in an area of low density marine life. The source and support ship are located in Port Hueneme, California.

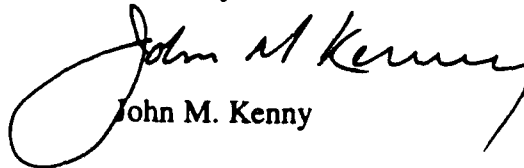
We will rely on you and your scientists to recommend the best location for this test as well as possible modifications to the signal frequency, duration, and source level. This test is not meant to be an alternative to the ATOC sources. Rather it would be a one time test designed specifically to test the SSAR.

FAX TRANSMITTAL		# of pages 2
To K HOLLINGSHEAD	From JOHN M. KENNY	
Co. NMFS	Co. ARL / PENN STATE UNI.	
Dept.	Phone # (814) 863-9401	
Fax # 301-713-0276	Fax # (814) 863-9527	



I look forward to working with you to design an experiment which meets the criteria of providing a robust test of the SSAR while at the same time not harming the marine environment. If you have any questions or comments please do not hesitate to call me.

Sincerely,

A handwritten signature in cursive script, reading "John M. Kenny". The signature is fluid and stylized, with a large loop at the beginning and a long, sweeping tail.

John M. Kenny

cc:
Spiesberger
Frye
Cheaure



UNITED STATES DEPARTMENT OF COMMERCE
National Oceanic and Atmospheric Administration
NATIONAL MARINE FISHERIES SERVICE
Silver Spring, Maryland 20910

AUG 10 1994

Dr. John M. Kenny
Pennsylvania State University
527 Walker Building
University Park, PA 16802-5013

Dear Dr. Kenny:

This is in response to your July 13, 1994, letter concerning the potential for an incidental take of marine mammals while testing the signal reception and signal processing of the Surface Suspended Acoustic Receiver (SSAR), using an acoustic source (HLF-6A) suspended from a ship. I understand that this test is to determine the feasibility of using this receiver in the future as a part of Project GAMOT (Global Acoustic Mapping of Ocean Temperatures). In your letter, you request that National Marine Fisheries Service (NMFS) scientists recommend the best location for this one-time test in order to avoid areas with marine mammals.

The duration of the acoustic test would be 5 days with a transmission signal 6 times per day and a signal duration of ten minutes, not including ramp-up time to reach the test source level. The transmission time therefore, would be approximately one hour per day. The center frequency would be 75 Hz with a bandwidth of 30 Hz and a source level of 197 dB (re 1 μ Pa) at 1 meter (m). During the transmission, the source would be in the sound channel at a depth of between 500 and 800 m and would take place during the last two weeks in October, 1994. Based upon a March 14, 1994, letter describing the GAMOT project, we assume that the 120 dB isopleth would be approximately 10 kilometers (km) (5.4 nautical miles (nm)) from a 197 dB source. At the surface, the signal will attenuate to less than 120 dB within a few km.

NMFS has reviewed your proposed activity and has determined that provided the test is conducted within an oceanic gyre at the time period proposed, and is only for the short duration mentioned in your letter, no incidental takings of marine mammals are likely to occur, and, therefore, a Small Take Authorization under section 101(a)(5) of the Marine Mammal Protection Act is not necessary. NMFS scientists have identified two gyres within the North Pacific Ocean where your research could be conducted with little likelihood of encountering marine mammals. One area is a few hundred miles north of Hawaii and the other is approximately 1,000 miles west of San Diego, CA. At the time of the year you propose conducting this calibration test, mysticete (baleen) whales and sperm whales would be expected to be in more northerly waters and not in the vicinity of the test.



As avoidance behavior by marine mammals has been observed to occur at decibel levels greater than 120 dB for continuous noise, efforts should be undertaken to ensure that marine mammals are neither within, nor on a course that will intercept, the 120 dB isopleth of the transmitter when in operation. In the event that a marine mammal is sighted within 6 nm of the source, because you are not authorized to incidentally take a marine mammal, you should terminate activities until the marine mammal has left the vicinity of the test. In addition, as some marine mammals may exhibit a startle response at the onset of high noise levels, it is important that the source be powered up slowly to avoid this type of taking by harassment. Your letter notes that you have agreed to this procedure.

Finally, it is recommended that the marine biologist onboard the vessel be a trained marine mammal observer. Although a marine biologist would be able to recognize a marine mammal or a sea turtle, and therefore terminate or delay transmitting the acoustic signal, a trained marine mammal observer would be able to identify marine mammals to the species level and would be able to recognize and record any changes in behavior that the acoustic signal may generate. Also, if at all possible, the biological observer should be provided with a pair of 25-power pedestal-mounted binoculars mounted on an upper level of the vessel. The binoculars would allow the observer to detect marine mammals up to 6 nm (11.1 km) from the vessel.

Sincerely,



William W. Fox, Jr., Ph.D.
Director, Office of Protected
Resources

DELIVERABLES

Three deliverables were due this quarter:

1. A detailed plan for implementing the investigation of more complex ocean models and providing a prototype design of an experiment for monitoring the North Pacific for climate change and natural variability. This deliverable is contained in the Task B section.
2. SSAR design and test report. This report will not be completed until the results of the August AUTECH tests has been incorporated.
3. Delivery of SSARs 1 through 3. As reported in the Task C section, the delivery of these SSARs has been delayed pending the completion of the AUTECH tests.

Two deliverables are due during the next quarter:

1. SSAR design and test report.
2. Delivery of SSARs 1 through 3.

Figure:

Fig. 1 GAMOT Deliverable Master Schedule

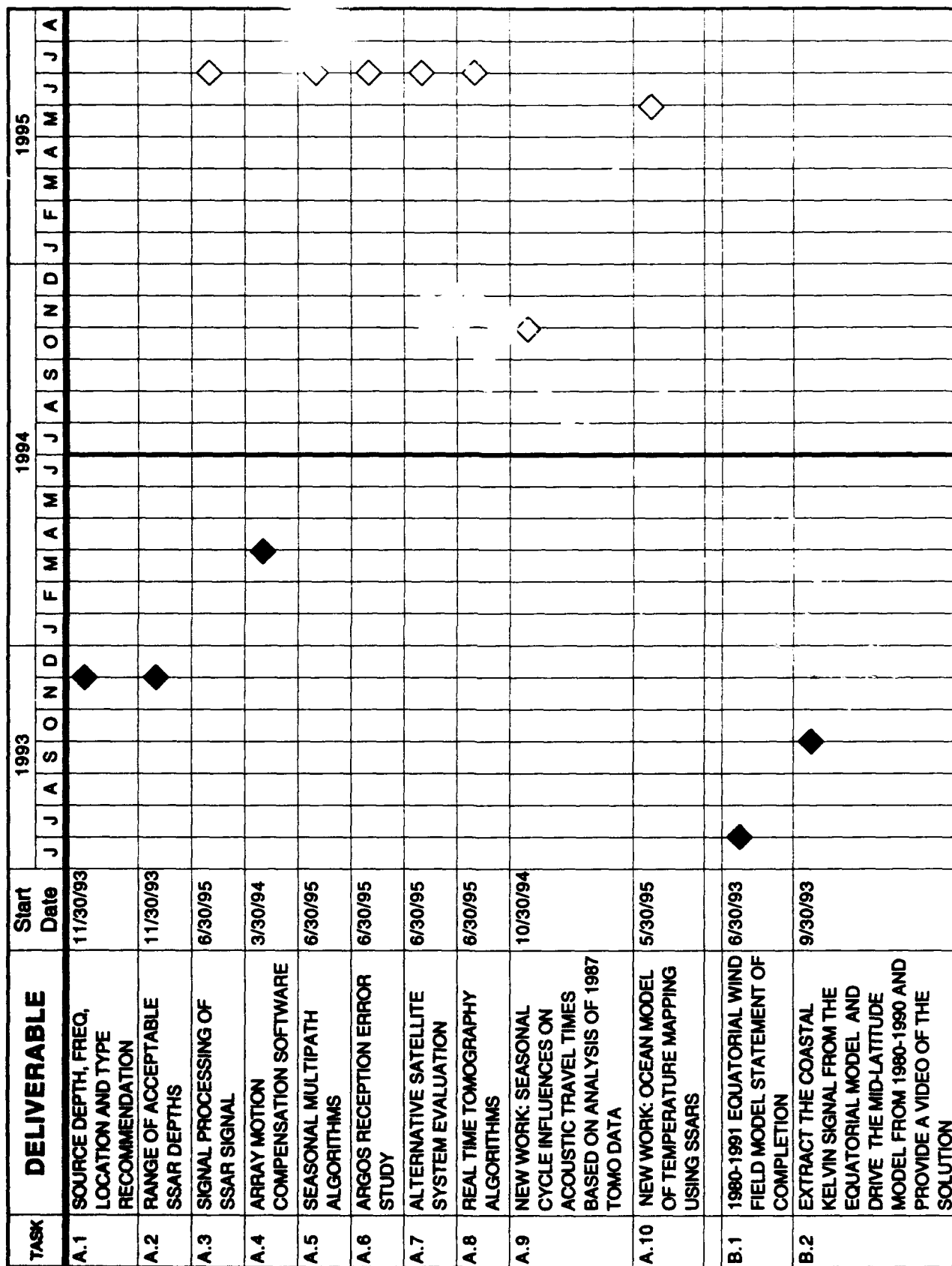


Figure 1: GAMOT Deliverable Master Schedule

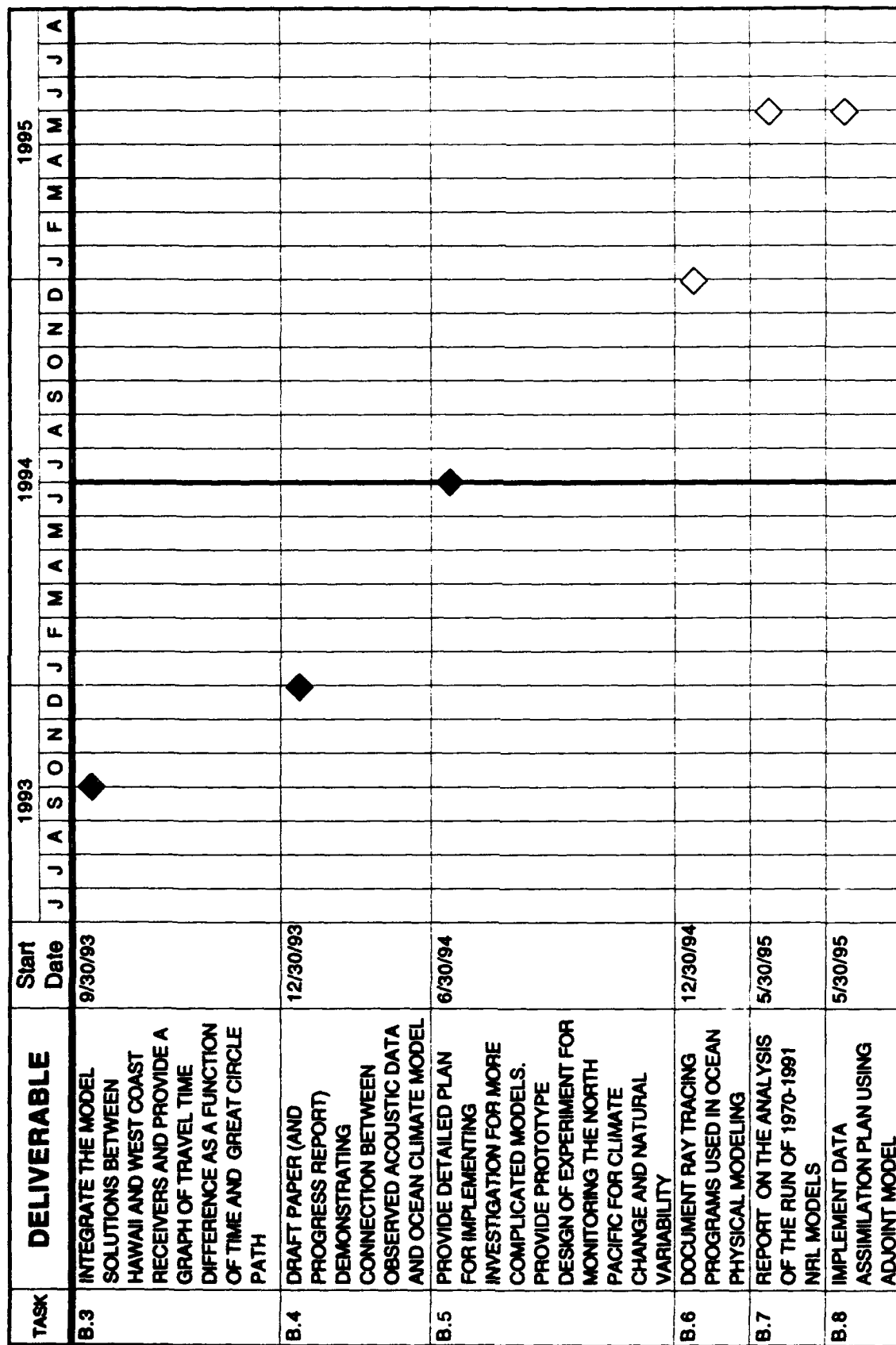


Figure 1: GAMOT Deliverable Master Schedule

TASK	DELIVERABLE	Start Date	1993												1994												1995																																																																																																																																																																																																																																																																																																																																																																																																																																																																																																																																																																																																																																																																																																																																																																																																																																																																																																																																																																																																																																																																																																																																																																																																																																																																																																																																													
			J	J	A	S	O	N	D	J	F	M	A	M	J	J	A	S	O	N	D	J	F	M	A	M	J	J	A																																																																																																																																																																																																																																																																																																																																																																																																																																																																																																																																																																																																																																																																																																																																																																																																																																																																																																																																																																																																																																																																																																																																																																																																																																																																																																																																											
D.3	MOORING DEPLOYMENT CRUISE REPORT																																																																																																																																																																																																																																																																																																																																																																																																																																																																																																																																																																																																																																																																																																																																																																																																																																																																																																																																																																																																																																																																																																																																																																																																																																																																																																																																																																							</

Figure 1: GAMOT Deliverable Master Schedule